NECESSARY AND SUFFICIENT CONDITIONS FOR TROPICAL CYCLOGENESIS

by

Jonathan Andrew Zawislak

A dissertation submitted to the faculty of
The University of Utah
in partial fulfillment of the requirements for the degree of

Doctor of Philosophy

Department of Atmospheric Sciences

The University of Utah

August 2013

The University of Utah Graduate School

STATEMENT OF DISSERTATION APPROVAL

The dissertation of **Jonathan Andrew Zawislak**

has been approved by the following supervisory committee members:

Edward J. Zipser	, Chair	**4/15/2013** Date Approved
Steven K. Krueger	, Member	**4/15/2013** Date Approved
Zhaoxia Pu	, Member	**4/15/2013** Date Approved
William James Steenburgh	, Member	**4/15/2013** Date Approved
Jeffrey Halverson	, Member	**4/28/2013** Date Approved

and by **Kevin D. Perry**, Chair of the Department of **Atmospheric Sciences**

and by Donna M. White, Interim Dean of The Graduate School.

ABSTRACT

This dissertation attempts to detail the necessary and sufficient conditions for tropical cyclogenesis; specifically those environmental, convective, and thermodynamic properties that may determine the fate of disturbances with apparent genesis potential. Unlike previous observational case studies which evaluate a few cases with limited spatial and temporal resolution in-situ and satellite data, this study examines 12 developing and four nondeveloping cases from recent (since 2005) tropical cyclone field campaigns using dropsonde data from multiple agency aircraft, as well as data from infrared and multiple passive microwave satellite platforms.

Results, composited for all developing cases, indicate that the inner core of developing disturbances prior to genesis exhibits a midlevel moisture that is greater than the surrounding environment, high relative humidity, a warm temperature anomaly at upper levels that progressively lowers through genesis, and a cool, dry anomaly at low levels. Likewise, the vertical alignment of the low- and midlevel vorticity centers is necessary for formation. The midlevel moisture content only shows a slight "progressive moistening" during the pregenesis stage, while the total precipitable water does not apparently increase among the cases studied. Consistent with conclusions from previous observational and modeling studies, the cool, dry anomaly and increased static stability at low levels in the composite, perhaps as a result of persistent convective precipitation near the center within 1–3 days of genesis, appears to be a necessary condition for formation;

this genesis pathway suggests that an initially stronger midlevel vortex precedes primarily low-level spin-up within a day of formation.

Among the convective properties examined using the satellite datasets (raining area, convective intensity, area of intense convection, duration, and proximity), the results suggest that the proximity and duration of precipitation within three degrees of the center are the most important properties for formation. However, the developing cases studied do not exhibit any common distinguishing convective characteristics during the pregenesis stage; not all developing cases exhibit widespread, intense convective episodes, and although some of the cases exhibit their most "favorable" convective episodes (in terms of intensity, area, and proximity to the center) around 30–36 hours prior to formation, in a few cases that episode occurs as many as 3 days before formation.

TABLE OF CONTENTS

ACKNOWLEDGMENTS

The GRIP field program and subsequent research is under the leadership and support of Dr. Ramesh Kakar, NASA Headquarters. This research has been supported by NASA grant NNX09AC44G. A special thanks to my advisor and committee chair, Dr. Ed Zipser, whose continual teachings and guidance over the years have been invaluable. I also extend my gratitude to the rest of the dissertation committee, Drs. Steve Krueger, Zhaoxia Pu, and Jim Steenburgh of the University of Utah and Jeffrey Halverson of the University of Maryland Baltimore County, for many valuable conversations, as well as their recommendations that have improved this dissertation. Much appreciation goes to all of the members of the Zipser Tropical Convection Group, including Dr. Chuntao Liu, for their support, as well as for the numerous conversations and recommendations that have improved the methodology and figures in the dissertation.

Many other people have directly contributed data and advice that has been included or considered for the dissertation: Simone Tanelli and Steve Durden (NASA APR2), and Svetla Hristova-Veleva and Joe Turk (IR) of NASA JPL; Paola Salio of the University of Buenos Aires (IR) and Ken Knapp of NOAA (IR); Mark Boothe of NPS (pouch tracking); and the NCAR/NSF PREDICT and NOAA HRD IFEX science teams (dropsondes). Also a very special thanks to members of the NASA Hurricane Science Research Program, NASA Airborne Science Program, and NASA Earth Science Project Office who have been integral to obtaining these important in-situ datasets of pre- and

developed tropical cyclones, have offered invaluable research advice, and have been a part of three unforgettable field experiences in NAMMA, GRIP, and HS3.

Finally, this dissertation has not been possible without the support of many friends — many of which have been fellow graduate students — and my incredible family, including my parents, Priscilla and Tom, and brother, Chris.

CHAPTER 1

INTRODUCTION

1.1 Motivation

The need for an improved prediction of tropical cyclogenesis and understanding of the underlying processes is well accepted, especially when considering since 2004, 13 tropical cyclone landfalls have each resulted in greater than $1 billion in damage (NCDC; online at http://www.ncdc.noaa.gov/oa/reports/billionz.html#chron). This startling figure may be related to population increases along the United States coastlines commonly affected by hurricanes. A U.S. Census Bureau report (Wilson and Fischetti 2010) reveals that the population along the Atlantic coastline between 2000 and 2008 increased approximately 2.3 million (10% of the total population increase in the U.S. for the same period, and 45% of the total increase among all U.S. coastline counties), while the Gulf of Mexico has seen a 1.5 million increase (6% of the total population increase in the U.S. for the same period, and 25% of the total increase among all U.S. coastline counties). The report notes some particularly concerning numbers for U.S. coastline counties frequently impacted by hurricanes; for the 11 coastline counties that experienced 11 or more hurricanes between 1960 and 2008, the population and housing units in those counties increased nearly 179% and 255%, respectively. Likewise, the report notes that the 10 strongest hurricanes since 1960 affected a total of 51 million people, but in 2008, those same hurricanes would impact 70 million people. Hurricane Donna (1960), which

affected 11.7 million people along the entire stretch of the eastern seaboard from Florida to Maine, would affect over two times that population, 24.1 million, in 2008. Counties impacted by category 5 Hurricane Andrew (1992), and category 4 Hurricane Opal (1995), have seen 20% increases in population since each event. These statistics provide unquestionable evidence that a greater portion of the population of the United States is at risk to the potentially devastating effects of a tropical cyclone.

Though difficult to ascertain, estimates for evacuation are often quoted as a "million dollars per mile." Whitehead (2003) disputes this figure and instead determines the average evacuation cost per household; the author estimates that the cost per household to evacuate is approximately $211, $233, $273, $256, and $292 for hurricanes categories 1–5, respectively. As an example, they compute an approximate evacuation cost for households in the eight ocean counties of North Carolina; they estimate that under voluntary evacuation, costs are approximately $1 to $26 million depending on the category of the hurricane, and for mandatory evacuation, $15–$50 million. Though the continued advancements in satellite technology and other observational platforms has greatly improved hurricane detection and risk awareness, the implications of genesis and intensity prediction are still great considering the increases in population along the coastlines and estimated costs of evacuation. While the slow progress in improving tropical cyclone intensity prediction, such as the rapid intensification of a mature tropical cyclone, has been well documented (DeMaria and Gross 2003; DeMaria et al. 2005), the genesis stage has been similarly stagnant in progress.

An understanding of physical processes related to tropical cyclone formation, as well as the detection and definition of a genesis event, has long suffered from the lack of

routine observations over the ocean. Conventional geosynchronous satellite observations provide detailed 30-minute infrared and visible imagery; however, these data are not without limitations. Visible imagery is not available during the diurnal maximum in precipitation over the ocean (night) when important convective processes may impact the disturbance, while in infrared imagery, widespread cold brightness temperatures associated with cirrus outflow can be misinterpreted for active deep convection, or if convection is active, mask the convective organization underneath the cold cirrus shield. Passive microwave sensors offer significantly more relevant information related to convective intensity and organization, but suffer from limited temporal continuity (any given instrument will only pass over a disturbance at most twice each day) and viewing area. Though numerical models are convenient for exploring the problem, they are subject to error due to limited horizontal and vertical resolution, insufficient observations for data assimilation and initial conditions, and errors associated with parameterizations (such as those for boundary layer, turbulence, microphysical and convective processes). Perhaps most lacking is information on the vertical thermal and wind structure of the developing disturbance; in the absence of in-situ measurements, the few daily rawindsondes available in the main development regions (MDR) cannot provide this information at either sufficient spatial or temporal resolution. Field campaigns offer opportunities for more detailed spatial and temporal observations, but as will be described later in Section 1.3, until recently, genesis cases have received disproportionately less attention during field efforts than mature tropical cyclones; even those relatively well-documented genesis cases still suffer from limited aircraft resources (in number and altitude coverage of aircraft). Studies that rely on any one of these

satellite or aircraft platforms individually to analyze intensification processes face a near impossible task — temporal and spatial continuity is just too poor — but by strategically combining *multiple* satellite platforms with in-situ data from *multiple* aircraft penetrations of a developing disturbance, formation processes may be better elucidated.

1.2. Background

1.2.1. Conditions Favoring Tropical Cyclone Formation

During the genesis process, a disturbance experiences a complex interplay between synoptic-scale (~10^3 km) and mesoscale (~10^1–10^2 km) processes. On the synoptic-scale, waves that possess concentrated areas of lower tropospheric relative vorticity and convergence are favorable for vortex formation and intensification (McBride and Zehr 1981). Likewise, increased upper-tropospheric divergence (outflow) over top of the low-level convergence will aid the formation process (Gray 1968; McBride and Zehr 1981; Riehl 1948). Key variables that determine the "environmental" characteristics of the incipient disturbance include the sea surface temperatures (SSTs), latitude (must be sufficiently away from equator for increased Coriolis effect), vertical wind shear, relative humidity, and moisture (often defined by total precipitable water, specific humidity, or water vapor mixing ratio). Accompanying African easterly waves (AEW) exiting northern Africa, the Saharan Air Layer (SAL) has recently received attention as a potential inhibitor for tropical cyclogenesis due to the increased vertical wind shear and dry (low relative humidity and moisture) air mass that suppresses deep convection (Dunion and Velden 2004).

An environment containing large cyclonic relative vorticity (generally referred to as the "preexisting disturbance") in the low troposphere, high SSTs (>26.5°C), low

vertical wind shear (850–200 hPa magnitude <10 m s^{-1}), and high moisture content and relative humidity is considered favorable for tropical cyclone formation. However, given the high frequency that such favorable environmental conditions exist in the tropics, tropical cyclogenesis is not guaranteed; in fact, it is a relatively rare event. Whether genesis occurs is most often linked to how deep convection evolves within the disturbance; characteristics of the deep convection that must be considered are the area, intensity (including the fraction of convective/stratiform rainfall), persistence, and the location of the convective systems relative to the disturbance center. To further complicate matters, the environmental characteristics not only influence the initiation and attributes of the convective events, the large-scale environment is subsequently modified by the convective events themselves. Although the importance of deep convection in the genesis process has long been recognized, hypotheses pertaining to the specific role of deep convection in genesis continue to be contested through numerous observational and numerical modeling experiments.

1.2.2. Past Tropical Cyclogenesis Field Campaigns

A number of field programs over the past couple of decades have not only emphasized investigating the mature tropical cyclone structure, but also the mesoscale and synoptic-scale processes involved in tropical cyclogenesis. While detailed datasets of mature tropical cyclones have existed for decades, extensive spatial and temporal observations in the developing tropical cyclone environment have been obtained only recently. Given that some of the cases will be included in analyses presented in the dissertation, the following section reviews field programs that have sought to investigate tropical cyclone formation within the past couple of decades.

In the mid-1970s, NOAA purchased two customized WP-3D (P-3) aircraft for use in tropical cyclone observation. Through 2005, the two P-3s were deployed in 134 total storms (Aberson et al. 2006). Equipped with dropsondes, Doppler radar, in-situ microphysical probes, and the Stepped Frequency Microwave Radiometer (SFMR; for surface winds and rain rate), the NOAA P-3s, as well as the NOAA G-IV (acquired in 1996) have been workhorses for both surveillance and research missions into tropical cyclones since 1976. As will be a theme in a few recent field programs, cooperation between NOAA and other agency aircraft (such as those belonging to NASA and NCAR/NSF) has been integral in acquiring remarkable datasets in all stages of the life cycle of a tropical cyclone. In addition to tasked surveillance missions, NOAA's Hurricane Research Division (HRD) has deployed, annually, NOAA aircraft on research missions for the Hurricane Field Program, and most recently, the Intensity Forecast Experiment (IFEX; 2005–current). The overarching objectives of IFEX are to sample the various stages of a tropical cyclone life cycle, including formation, in hope to better represent tropical cyclone structure in numerical models, and ultimately improve tropical cyclone intensity predictions (Rogers et al. 2006). However, given that 90% of missions with NOAA aircraft were in *mature* tropical cyclones, rather than the pregenesis stage, during the 30 years of service before 2005 (Aberson et al. 2006), IFEX project scientists have recently placed more emphasis on sampling the predepression and tropical depression stages.

Staged in the eastern Pacific in July-August 1991, the Tropical Experiment in Mexico (TEXMEX) was a joint effort between NOAA and NCAR to specifically study tropical cyclogenesis processes, in particular as they pertain to the evolution of the

thermodynamic environment at low and midlevels within mesoscale convective systems (MCS) (Bister and Emanuel 1997). Using the NOAA P-3 and the NCAR Electra, six flights (three by each) investigated the evolution of an MCS embedded in an easterly wave that eventually became Hurricane Guillermo. Though the sequence of flights (over the course of 4 days) into Guillermo was, at the time, unparalleled in continuity, flight levels were confined to 3 km and below, limiting in-situ sampling of the thermodynamic environment at the important midlevels of the pre-Guillermo vortex. Likewise, the stair-step flight pattern employed, though providing greater spatial coverage, sacrificed temporal resolution in the developing inner core (Reasor et al. 2005).

The Tropical Cyclone Motion 1992 (TCM-92) mini-field experiment, staged in the western Pacific, sought to observe structure and processes occurring within MCSs, in particular those associated with tropical cyclones. One disturbance, Typhoon Irving, was the focus of three United States Air Force (USAF) WC-130 (equipped with omega dropwindsondes) missions over the course of 9 days in the precursor disturbance (Ritchie and Holland 1997). Likewise, TCM-93, in addition to evaluating how MCSs adjacent to tropical cyclones impact track deflection, sought to observe the role of MCSs in tropical cyclone formation. One case, pre-Tropical Storm Ofelia, was particularly well sampled in two aircraft missions (Harr et al. 1996). Also in 1993, NASA deployed the DC-8 and ER-2 in a joint effort with NOAA (P-3s) and NCAR (Electra) in the Tropical Ocean-Global Atmosphere (TOGA) Coupled Ocean-Atmosphere Response Experiment (COARE). The overall project goal of TOGA-COARE is to understand the role of the oceanic tropical warm pool in the western Pacific on atmospheric processes occurring on a wide range of time and spatial scales. Though the project goals were broad, NASA

assets were used to investigate the formation of Tropical Cyclone Oliver (Simpson et al. 1997). Although continuity was limited (two flights by the NASA ER-2 and DC-8 were dedicated to Oliver), Oliver's formation in proximity of Willis Island, Australia meant unique coverage from ground-based radar and rawindsondes.

In preparation for the launch of the Tropical Rainfall Measuring Mission (TRMM) satellite, NASA conducted a series of field campaigns seeking to examine the performance of airborne and surface-based instrumentation in precipitation as a validation tool for satellite products to be developed for TRMM; the ultimate goal was not only to improve future satellite remote sensors and their precipitation algorithms, but also to further understand the precipitation processes themselves and better represent those processes in numerical models. The successful deployment of a unique set of active and passive remote sensors on NASA aircraft (medium-altitude DC-8 and high-altitude ER-2) during the Convection and Moisture Experiment (CAMEX) -1 (1993) and -2 (1995) field campaigns (based at NASA Wallops Flight Facility, Virginia) paved the way for their application in future tropical cyclone studies, CAMEX-3 (1998) and -4 (2001). Based in Florida, and in close collaboration with NOAA (the successful coordination between NASA and NOAA aircraft would prove to be an auspicious collaboration for future field efforts), CAMEX-3 and CAMEX-4 deployed numerous airborne in-situ and remote sensors, as well as ground-based radar and profilers, to obtain observations of tropical cyclone intensity change (including formation), motion, and rainfall (Kakar et al. 2006). Though CAMEX-3 and -4 would investigate eight tropical cyclones (Bonnie, Danielle, Earl, and Georges in 1998; Chantal, Gabrielle, Erin, and Humberto in 2001), and offer one of the most comprehensive datasets of the tropical cyclone structure to-

date, no pre-cyclone disturbance was investigated.

Following in the footsteps of CAMEX-4, the NASA Tropical Cloud Systems and Processes (TCSP, 2005; based in San Jose, Costa Rica), in collaboration with NOAA IFEX, sought to investigate tropical cyclone structure and intensity change, specifically targeting convective systems within developing disturbances using a wide array of satellite and aircraft remote sensors (Halverson et al. 2007). Though the NASA ER-2 primarily spent time in developed cyclones (Hurricanes Dennis, Emily, and Tropical Storm Gert), some missions (in coordination with dropsonde-equipped NOAA P-3s) were focused on genesis: one, a mesoscale complex in the East Pacific that may have eventually became Tropical Storm Eugene, and a second, an easterly wave that may have served as a precursor to Tropical Storm Gert.

The NASA African Monsoon Multidisciplinary Analyses (NAMMA; 2006) campaign, based at Sal, Cape Verde in the East Atlantic investigated seven consecutive African easterly waves; one specific objective of NAMMA was to observe AEWs undergoing tropical cyclogenesis (Zipser et al. 2009). NAMMA was, however, limited to one aircraft (DC-8) and any single disturbance was flown at most two times. Two genesis events occurred in the NAMMA region, Tropical Storms Debby and Helene; unfortunately, the only mission flown into Debby was well after genesis, and while the flight into Helene was during genesis, the flight had limited dropsonde coverage. Three other events may have originated from a previously investigated NAMMA AEW (Ernesto, Florence, and Gordon), but uncertainty remains (Zawislak and Zipser 2010), and continuity of observation prior to genesis was severely lacking. Although the genesis-related objectives were less successful, the NAMMA dataset provides the most

detailed observations of AEWs in the East Atlantic since the GARP Atlantic Tropical Experiment (GATE; 1974), and has provided (in association with NOAA SALEX [Saharan Air Layer Experiment]) an unprecedented dataset focused on the SAL structure and composition.

In the summer of 2008, multiple agencies deployed aircraft to the West Pacific with a goal of obtaining in-situ observations during the entire life cycle of a tropical cyclone, with a particular emphasis on the dynamic and thermodynamic processes occurring during the formation stage. Participating aircraft (equipped with dropsondes) included the Naval Research Laboratory (NRL) P-3 and a USAF C-130. One particular genesis case, Typhoon Nuri, was well sampled. An impressive six flights by the P-3 and C-130 (coincident; one each day) over the course of 3 days was accomplished, providing much needed day-to-day continuity.

Though the previously described field campaigns achieved varying success in sampling tropical cyclogenesis, the tri-agency effort during the summer of 2010 served as a culmination of all previous attempts at sampling genesis processes. NASA's Genesis and Rapid Intensification Processes (GRIP) field campaign, based at Ft. Lauderdale, Florida, sought to obtain high temporal and spatial resolution observations in nondeveloping, developing, and rapidly intensifying disturbances located in the Atlantic basin and Gulf of Mexico (Braun et al. 2013). Multiple NASA aircraft participated in GRIP: the medium-altitude DC-8 (based in Ft. Lauderdale), high-altitude WB-57 (based at Ellington AFB in Houston, TX), and for the first time, the unmanned high-altitude Global Hawk UAV (based at Edwards AFB in Palmdale, CA). St. Croix, U.S. Virgin Islands, provided a forward operations base for DC-8 flights to achieve a greater range in

the Central Atlantic. GRIP also worked in close coordination with NOAA's IFEX (participating aircraft include the P-3s [NOAA42/43] and the G-IV [NOAA49]), the USAF (C-130s), and NSF/NCAR Pre-depression Investigation of Cloud Systems in the Tropics (PREDICT) campaign (NSF/NCAR G-V). The unique observing strategies involved consecutive and coordinated aircraft missions including, for the first time, the over flight of a hurricane by an unmanned aircraft (NASA Global Hawk). PREDICT-GRIP-IFEX (P-G-I) observations ultimately provide an unprecedented dataset of nondeveloping disturbances, and developing and rapidly intensifying tropical cyclones, specifically, in-situ observations of the large-scale environment and meso-convective events involved. Investigations during P-G-I include two rapid intensification periods during Hurricane Earl; the non-redevelopment of Tropical Storm Gaston; the genesis of Tropical Storm Matthew; and perhaps most impressive, the entire lifecycle of Hurricane Karl starting 4 days before genesis.

1.3. Objectives

As introduced previously, the interaction of multiple spatial scales must be considered when describing tropical cyclogenesis. On the mesoscale, deep convection, often organized in MCSs, is invariably identified as a requirement for tropical cyclogenesis. A fundamental question to be addressed in this dissertation is: *what environmental conditions, at multiple scales, are required to organize intense low-level rotation?* Critical to answering this question is characterizing the time evolution of not only relevant vortices at low and midlevels, but also the associated convective systems and the thermodynamic state of the environment.

Distinguishing among hypotheses related to tropical cyclogenesis requires a

collection of near-continuous measurements of precyclone disturbances from aircraft, ground-based, and satellite platforms. Though previous studies have analyzed tropical cyclogenesis using data from individual infrared and passive microwave satellite instruments, few have sought to incorporate data from multiple platforms and field campaigns. Given the unprecedented continuity of observations achieved during the tri-agency (P-G-I) field campaigns during the summer of 2010, as well as the availability of data from some of the recent field programs outlined in 1.2.2, this is arguably the best opportunity to date to synthesize observations to describe the evolution of the pregenesis environment.

Using an extensive aircraft and satellite dataset collected on developing and nondeveloping disturbances, *this dissertation seeks to advance our understanding of the necessary and sufficient conditions for tropical cyclogenesis; specifically those kinematic (environmental), convective, and thermodynamic properties that may determine the fate of disturbances with apparent genesis potential.* By analyzing the temporal evolution of *multiple* genesis cases, one goal will be to offer *quantitative* information on the convective and thermodynamic properties observed in developing and nondeveloping disturbances; such information may have important implications in an operational forecast setting.

To achieve the main goals, the following questions will be addressed in the context of an historical dropsonde dataset, and detailed case studies of developing and nondeveloping disturbances:

1) How do developing disturbances differ thermodynamically from nondeveloping disturbances?

2) What is the thermodynamic evolution of the developing inner core? Does the inner core of a developing disturbance progressively moisten as a result of deep convective events?

3) What are the properties of the wave organization that are favorable for formation? In particular, is the presence of a midlevel vortex, in an already moist environment, a necessary condition for cyclogenesis?

4) What are the properties of convective systems prior to formation of a tropical cyclone? Given those properties, which characteristic (areal coverage, intensity, and proximity to the pouch/vorticity center) is most influential in determining the fate of the disturbance?

The synthesis of dropsonde data, as well as IR and microwave satellite overpasses, offers a unique opportunity to observe the time evolution of MCSs, their timing as it relates to intensification, and the thermodynamic environments in which they are embedded. The unprecedented, near-continuous dropsonde coverage achieved by tri-agency and USAF aircraft is crucial for not only documenting the evolution of vorticity maxima on all scales, but also the thermodynamic changes occurring in the environment (question 1 and 2 above). By analyzing the thermodynamic evolution, the role of convection in priming the environment for genesis can be elucidated. As such, a specific emphasis is placed on critically evaluating the hypothesis that deep convection is responsible for the progressive moistening of the inner core, as well as the hypothesis that high relative humidity (near saturation) through the troposphere is necessary for genesis (question 2 above). Given that P-G-I datasets offer continuity for as many as 4 days before formation, one may also critically evaluate a recent hypothesis which states that

low-level spin-up requires a midlevel vortex in an environment characterized by high moisture content and relative humidity; this scenario results in a favorable thermodynamic environment for deep convection to intensify low-level rotation through increased low-level mass flux and convergence (question 3). Answers to question 3 should also provide additional information on what large-scale properties of the "preexisting disturbance" are necessary for formation. Question 4 is an attempt to identify what convective properties may distinguish developing disturbances from nondeveloping, and which property may be most important for genesis. Likewise, question 4 can corroborate evidence for or against the hypothesis that deep convection, organized in intense convective towers ("hot towers") is necessary for genesis.

This dissertation will synthesize information from model analysis, in-situ dropsonde data, and satellite data for 12 developing and four nondeveloping disturbances from recent field programs (15 total as Gaston counts as both developing and nondeveloping). Hurricane Karl will be the primary genesis case study in the dissertation as this case offers the most continuous observation by the P-G-I campaigns. Although the observational continuity is not as impressive as Karl, the pregenesis stages of developing Matthew will offer additional insight for the questions posed and offer a comparison with Karl, while non-redeveloping ex-Gaston will offer an opportunity to contrast developing from nondeveloping disturbances. Given the extensive temporal and spatial coverage accomplished by the considerable number of platforms/instruments, the careful synthesis of data is critical to success. The dissertation is organized as follows: Chapter 2 will provide some background literature on the ingredients and pathways for tropical cyclogenesis; Chapter 3 will briefly describe the cases included, methodologies related to

the pregenesis disturbance tracking, and in-situ and satellite datasets utilized in the dissertation; Chapter 4 will describe results from a historical dropsonde dataset; Chapter 5 will present results from individual case studies that have synthesized model analysis, in-situ, and satellite data; and finally, Chapter 6 will summarize key findings and offer final conclusions.

CHAPTER 2

LITERATURE REVIEW

2.1 Large-scale Genesis Factors

Riehl (1954) and Gray (1968, 1975) outlined a set of necessary conditions that must be met for tropical cyclogenesis to occur: a preexisting disturbance with enhanced low-level vorticity must be present over high sea surface temperatures (> 26.5°C), away from the equator, contain low vertical wind shear, a deep moist layer, and persistent deep convection. Though not sufficient for formation alone, persistent cloud clusters (2 or more days) may increase the probability for formation (Zehr 1992). Gray (1968) also notes that, as a consequence of the moisture convergence and release of latent heat by cumulus at low levels, compensating upper-level divergence (outflow) must develop. This idea disputes that of the earlier Riehl (1948) study on typhoon formation, which concludes that upper-level divergence may *trigger* low-level convergence. McBride and Zehr (1981) agree that increases in both low-level cyclonic vorticity and upper-level anticyclonic vorticity are necessary during formation.

Low vertical wind shear, which prevents ventilation of latent heat produced from condensation and freezing from deep convective clouds within the inner core, has been a well-known necessary condition for genesis to occur (Gray 1968; Gray 1984a; Shapiro 1987). Molinari et al. (2004), however, suggest that while strong shear (greater than 10–15 m s^{-1}) is certainly detrimental to genesis, moderate shear (5–10 m s^{-1}) may in fact

contribute positively to the genesis process. The authors provide support for this conclusion in an observational case study of the genesis of Hurricane Danny (1997). Using lightning data, satellite imagery, and reconnaissance aircraft data, they show that convection downshear of a vortex center developed a new, stronger vortex that became the dominant center (and absorbed the original center). These conclusions support the result from Reasor and Montgomery (2001) which, using idealized numerical simulations, similarly argued that vertical wind shear is not necessarily a negative factor.

While many studies focus on the internal aspects (i.e., convection and latent heating) of tropical cyclogenesis and intensification, others have focused on external influences, such as upper-tropospheric interactions. Intensification of mature cyclones has been linked to the establishment of an outflow channel (such as from a Tropical Upper Tropospheric Trough [TUTT]; Wu and Cheng 1999), which evacuates mass and invigorates convection in the inner core (Holland and Merrill 1984), while other studies have focused on the favorable organization of upper-level eddy flux convergence of angular momentum (DeMaria 1993; Molinari and Vollaro 1989; Pfeffer and Challa 1981). Regardless, the development of low inertial stability in the outflow layer (Holland and Merrill 1984) appears to be a requirement for upper-level environmental conditions to positively contribute to tropical cyclone intensification. While mature tropical cyclones have received much of the attention regarding the relationship between upper-level environmental conditions and intensification, proportionately less attention has been paid to the relationship during the genesis process.

Although upper-level environmental interactions in tropical cyclogenesis will not be examined in this dissertation, Sears (Masters Thesis, University of Wisconsin, 2011)

investigated the role of the upper levels in developing and nondeveloping systems for PREDICT cases — the same disturbances investigated in this dissertation — using 3-D variational analyses incorporating satellite cloud-track winds and dropsondes from the PREDICT G-V. In the study, the author identifies the development of outflow channels (or ventilation ducts) and strong divergence aloft in developing disturbances, critical conditions not observed in nondeveloping disturbances. Outflow channels were identified to extend both north (turning northeast; often due to southwesterlies from transient upper-level troughs) and south (turning southwest; often found near the ITCZ). They also suggest another important effect of stronger outflow, the reduction of subsidence near the inner core, which would otherwise potentially entrain dry air into the inner core that may suppress deep convection (Braun 2010).

The incipient vortex for a tropical cyclone can be traced to a number of phenomena present over the tropical oceans. Although cyclone formation has been linked to upper-level troughs (Sadler 1976, 1978), wind surges (Lee 1989a, Zehr 1992), and ITCZ breakdown (Guinn and Schubert 1993), the monsoon trough and easterly waves have generally received the most attention as sources of a "preexisting disturbance." The monsoon trough is characterized by elevated background cyclonic vorticity due to the convergence of cross-equatorial westerlies and trade wind easterlies.

Identified as the most frequent precursor to tropical cyclogenesis in the Atlantic, the African easterly wave (AEW) is a westward propagating disturbance with a mean wavelength of 2500 km and mean period of 3.5 days (Reed et al. 1977). AEWs were identified as precursors to tropical cyclogenesis even before their detailed structures were documented (Carlson, 1969b; Erickson, 1963; Frank, 1970). Two primary AEW tracks

are commonly recognized. One, a relatively cloud and precipitation free low-level vorticity maxima track north of the midlevel African easterly jet (AEJ) at approximately 20°N, and another track south of the AEJ in the rainy zone centered at 10°N (Burpee, 1974; Carlson, 1969a; Pytharoulis and Thorncroft, 1999; Reed et al. 1977, 1988a). Thorncroft and Hodges (2001) find that the maximum track density of 600 and 850 hPa vorticity maxima is observed to be in the southern track and co-located with part of the main development region (MDR) for Atlantic tropical cyclones (Hopsch et al. 2007 and Kerns et al. 2008). Likewise, this maximum in genesis extends eastward downstream to the Guinea Highlands; these genesis events are attributed to an increase in vorticity due to latent heating from orographically-induced rainfall over the Guinea Highlands, as well as the merging of subsynoptic PV anomalies (generated by convection) (Berry and Thorncroft 2005; Hopsch et al. 2007). Although various numbers exist, up to 60% of Atlantic basin tropical cyclones are linked to AEWs (Landsea 1993).

2.1.1. Developing vs. Nondeveloping Disturbances

For Atlantic and Pacific nondeveloping and developing cloud clusters, McBride and Zehr (1981) outline some important conditions that differ between those cloud clusters that develop and those that do not. They find that the developing clusters generally exhibit a more pronounced warm core at upper levels, stronger easterlies north of the center (in fact overall, stronger tangential winds at low levels), a warmer atmosphere over a large horizontal scale, large values of low-level relative vorticity (twice as large as nondeveloping clusters), zero or near-zero vertical wind shear directly over the system center, and characteristically anticyclonic vertical shear (positive zonal shear to the north and negative zonal shear to the south). The latter is an important

condition in which an anticyclone develops directly over the low- and midlevel cyclonic circulation, and thus as defined in their paper, a higher daily genesis potential (DGP; the magnitude difference in relative vorticity between 900 and 200 mb); the vertical alignment of positive relative vorticity at low levels and negative at upper levels may be fortuitous for system intensification. Although the authors ultimately see variability in the large-scale parameters at horizontal scales beyond that of the cloud cluster, they do not address the importance of mesoscale processes that interact with those on the synoptic-scale.

Lee (1989) investigated a larger sample of cloud clusters than McBride and Zehr (1981) and documented not only the differences between developing and nondeveloping clusters, but also their lifecycles using 1–2 times per day satellite imagery. The main conclusions are that cloud clusters (both developing and nondeveloping) develop in areas of initially lower surface pressure and low-level convergence, while developing clusters exhibit a few important characteristics that differ from nondeveloping; developing clusters moisten the middle levels (although the authors state that the link to cyclogenesis is not clear), develop a convective burst, exhibit stronger middle- to low-level cyclonic circulation (which may exist due to a strong large-scale wind surge or southwest monsoonal surge which concentrates cyclonic vorticity), have stronger anticyclonic vertical wind shear, and stronger low-level inflow. The strength of the upward vertical motion (peaks at approximately 100 mb day^{-1} at 400 hPa) is, however, not appreciably different between developing and nondeveloping cloud clusters.

A more comprehensive satellite study on developing and nondeveloping differences is presented by Wang et al. (2008). The authors investigated 13

nondeveloping and 30 developing disturbances in the South China Sea using derived moisture variables from the Special Sensor Microwave / Imager (SSM/I) satellite platform. The authors find that the total column water vapor and liquid water, as well as the latent heat release (TLHR) are all statistically different between developing and nondeveloping disturbances. They note that though nondeveloping disturbances can obtain large values of TLHR, the essential ingredient for formation is persistent periods of large TLHR.

More recently, Kerns and Zipser (2009) examined the differences between developing and nondeveloping vorticity maxima that were tracked in 4 years of the ERA-40 in the Atlantic and East Pacific (Kerns et al. 2008). The authors note that large-scale predictors that exhibit the greatest discrimination between developing and nondeveloping include the DGP (difference between 925 and 200 hPa relative vorticity; 0–6° avg.), relative vorticity at 925 hPa (0–6° avg.), divergence at 925 hPa and 200 hPa (0–6° avg.), magnitude of vertical wind shear between 850 and 200 (2–8° avg.), and midlevel moisture (775–400 hPa mean mixing ratio; 0-6° avg.). The best predictor is 925 hPa relative vorticity, while the second is 200 hPa divergence in the East Pacific (EPAC) and midlevel moisture in the Atlantic. Vertical wind shear came in 4th in the Atlantic, but is interestingly the least important in the EPAC. Satellite predictors in the EPAC show greater discrimination than the Atlantic; in fact, combining satellite predictors with large-scale predictors does not enhance predictive skill in the Atlantic. That is not to say that satellite predictors (thus deep convection) are unimportant; rather, this result illustrates the probabilistic, not deterministic, nature of genesis governed by the characteristics of deep convection and their location within the large-scale disturbance.

2.1.2. The Marsupial Paradigm

Distinguishing among disturbances that develop from those that do not has most often been done by evaluating the characteristics of their cloud clusters and vorticity maxima at low and midlevels. Tracking cloud clusters and vorticity maxima are often subjective; for example, cloud clusters can merge or split, while a disturbance such as an AEW may contain multiple vorticity maxima, some of which may have a convective origin and thus do not persist for more than a day. Such tracking techniques are most often based in the Eulerian framework, which offers snapshots of the total flow (background plus wave translation speed). Recent work suggests that viewing the flow in the Lagrangian, or wave relative, framework (hereafter, 'co-moving') makes more sense, and is perhaps necessary to truly appreciate the interactions and transport of moisture, convection, and vorticity throughout the wave.

In the marsupial paradigm (Dunkerton et al. 2009; Montgomery et al. 2010; Wang et al. 2010a,b; Wang et al. 2011), an AEW is likened to the marsupial mother's pouch, in which she carries an infant 'proto-vortex' along until that protected vortex is primed and strengthened to leave the pouch as a self-sustaining entity, the tropical cyclone. The pouch is identified by the closed circulating region (Kelvin's cat eye) around the critical layer of an easterly wave. The critical layer is the region surrounding the critical latitude, the latitude in which the zonal phase speed of the wave is equal to the background zonal flow. The presence of the Kelvin's cat eye, or pouch, is essential as this region is approximately a closed circulation in which the air within *is repeatedly moistened by convection*, and at least to some degree protected from dry air intrusions, such as those originating from the SAL (Montgomery et al. 2010). It is near the center, the intersection

of the trough axis and critical latitude, of the pouch that tropical cyclogenesis has been observed to occur (Dunkerton et al. 2009).

The previous studies advocate that waves be tracked in the co-moving framework as the pouch is considered to be a more reliable representation of the proto-vortex, and does not suffer from the difficulties encountered in tracking short-lived cloud clusters and vorticity maxima. Pouches have since been used extensively in operational forecasting, and planning missions during field campaigns (for example, TCS-08 and PREDICT-GRIP-IFEX [Evans et al. 2012; Montgomery et al. 2012]). In a case study of Hurricane Felix, Wang et al. (2010a,b) show that the location of the pouch most favorably correlates with the concentration of deep convection and formation location of Felix; however, in the earth-relative perspective, the wave is open with the characteristic inverted-V pattern, and most importantly, no closed circulation is apparent. One caveat of the marsupial paradigm is that the identification of a pouch is predicated on the phase speed of the wave to be approximately that of the background flow; low-amplitude waves, or waves that exhibit high or low phase speeds, may not exhibit a recirculating region. Likewise, the wave trough phase speed is computed using a Hovmöller diagram of the wave's "v=0" line; the line in which meridional southerlies east of the AEW trough axis switch to northerlies on the west side (Dunkerton et al. 2009; Montgomery et al. 2010). The meridional "v=0" line is difficult to track, for example, in situations where the easterly wave trough axis is horizontally tilted. Wang et al. (2012) have since modified the phase speed of the wave to represent both the zonal and meridional movement of the wave, as well as the vorticity centroid rather than the "v=0" line.

2.2. Convective Events in Genesis

The essence of the tropical cyclogenesis problem lies in the inherent difficulties of connecting processes occurring on many scales; synoptic, mesoscale, and cloud scales. Tropical cyclogenesis can be summarized into two stages: 1, the synoptic-scale preconditioning, and 2, mesoscale organization (Karyampudi and Pierce 2002; Tory and Montgomery 2006). While many early studies focused on the large-scale preconditioning, more recent focus has been placed on the mesoscale organization that occurs during the genesis process. As Ooyama (1982) notes, the composites of large-scale conditions observed in developing systems, such as those outlined by Gray (1968), do not necessarily provide causality with tropical cyclogenesis; composites may only indicate a disturbance is undergoing formation. It is now well accepted that mesoscale convective systems and their associated dynamics and thermodynamics must play a role in intensification processes such as genesis. An essential component of the secondary circulation, latent heat released by condensation in deep convection provides an increase in the vertical mass flux and a subsequent concentration of inflow into disturbance center; a process that will then intensify the primary circulation (Ooyama 1982). In one case during GATE in the East Atlantic, Zipser and Gautier (1978) observed that the upward mass flux from cloud systems within a single MCS can alone account for nearly the entire net mass flux of the synoptic-scale depression. Houze et al. (2009), using the ELDORA radar on the NRL P-3 during RAINEX (Hurricane Rainband and Intensity Change Experiment), similarly identified an MCS with a deep, wide, intense updraft that appeared to directly contribute to the intensification of Hurricane Ophelia.

Two primary pathways related to meso-convective scale processes have been

argued in tropical cyclogenesis literature; the top-down and bottom-up hypotheses. In essence, the top-down pathway describes the process by which, in a environment characterized by elevated midlevel cyclonic vorticity, anticyclonic vorticity (divergence) observed at low levels in the stratiform region of an MCS (Houze 2004) is replaced by cyclonic vorticity (convergence); such a transition is linked to moistening of the troposphere to saturation which encourages downdraft-free convection. The bottom-up pathway describes a process by which, in an environment with elevated low-level cyclonic relative vorticity, vertical vorticity produced within deep convective updrafts aggregate and results in an upscale intensification of the vortex; downdraft-free convection is not required in this pathway (Tory and Montgomery 2006). The following sections will describe, in more detail, each pathway as well as review studies that investigate the theories behind the thermodynamics of tropical cyclogenesis.

2.2.1. Top-down Hypothesis

Holland (1995) notes that when favorable environmental conditions exist, vortices on the mesoscale scale play a crucial role in tropical cyclogenesis; such conditions are found in monsoon trough regions. In the top-down route, it is hypothesized that low-level vorticity intensification can be linked to cyclonic midlevel convective vortices (MCV), such as those commonly produced about the melting layer of a stratiform raining area of a mesoscale convective system (Holland 1995; Ritchie and Holland 1997; Simpson et al. 1997); however, a consensus on how midlevel vorticity concentrates at low levels has yet to be reached.

One thought as to how the midlevel vortex extends to the surface is through MCS merger that would extend the region of circulation both horizontally and vertically

downward (Ritchie and Holland 1997; Simpson et al. 1996). Ritchie and Holland (1997) examined the development of Typhoon Irving during the Tropical Cyclone Motion (TCM-92) experiment using objective analyses, satellite data, and sounding data. Although their observations do not unambiguously support that MCSs occurring within Irving follow the MCV merger pathway, they reference baroclinic modeling results, which suggest that merging, midlevel vortices may enhance the circulation at both midlevels and the surface. Similarly, Simpson et al. (1997) use aircraft data from the NASA DC-8 and ER-2 in developing Tropical Cyclone Oliver during TOGA COARE (1993), as well as IR information, to investigate how MCSs and their subsequent midlevel vortices may interact in the formation process. The authors conclude that, in an environment characterized by a reduced deformation radius and low vertical wind shear, the merger of convective systems and their vortices allows midlevel vortices to extend downward and subsequently increase low-level rotation.

Another explanation is provided by Bister and Emanuel (1997); the authors conclude that the formation of a low-level vortex is supported in the cool, moist environment of the stratiform rain region. This pathway requires that initially anticyclonic low-level rotation be replaced by cyclonic rotation originating from the midlevels. Their hypothesis suggests that midlevel cyclonic vorticity is advected downward in sustained stratiform precipitation, and once the low levels are sufficiently cooled and saturated, the low-level equivalent potential temperature (θ_e) recovers and new downdraft-free convection acts to intensify the vortex.

Regardless, persistence is an essential requirement for any MCV to aid in development of a tropical cyclone; the MCV must be resistant to weakening due to

destructive environmental shear, and the lack of forcing during the diurnal minimum in deep convection. In evaluating the role of multiple MCVs in the development of Tropical Storm Ofelia (West Pacific), Harr et al. (1996a) find that the most persistent MCV becomes Ofelia. They relate the vertical penetration of the MCV to low levels to the persistence of the MCV, due in part to its location in the favorable cyclonic shear side of strong low-level confluent flow; the low-level penetration of the MCV, as well as the persistence of deep convection in its vicinity during the expected diurnal minimum are linked to the formation of Ofelia. In another well-documented case from TCM-93, Harr et al. (1996b) note that the remnant midlevel vortex of an MCS located on the eastern edge of the monsoon trough in the west Pacific concentrates large-scale vorticity from the monsoon trough and provides a focal point for subsequent MCS activity; genesis proceeds once favorable thermodynamic conditions are met. The authors note that at low levels, intensification is aided by transport of cyclonic angular momentum into the disturbance and removal of anticyclonic angular momentum by the outflow circulation at upper levels. The subsequent depression is then characterized by high θ_e at the inner core, as well as a clear separation of the inner core from the outer large-scale monsoon trough environment.

Repeated convective bursts occurring within an environment characterized by a midlevel MCV, high relative humidity, and a favorable (reduced) local Rossby radius of deformation, will result in low-level vorticity intensification due to the low-level convergence and stretching imparted by the height changes from midlevel latent heating (Chen and Frank 1993; Rogers and Fritsch 2001). By reducing the Rossby radius of deformation, warming due to latent heat release will remain confined to the inertially

stable MCV and encourage further stability and heating efficiency due to localized increase in vorticity (Ooyama 1982; Schubert and Hack 1982). Although Rogers and Fritsch (2001) modeled an MCV over land, the results can be applied to the tropics; due to the smaller Coriolis and thus larger Rossby radius of deformation, intensification will likely only occur when the MCV is coincident with elevated background cyclonic vorticity, such as that associated with an easterly wave. Likewise, the weaker cold pools observed in the Tropics may allow increased low-level penetration of the midlevel cyclonic vorticity.

2.2.2. Bottom-up Hypothesis

In contrast to the top-down theory, the foundation of the bottom-up theory is deep, intense, cyclonically rotating convective cores known as vortical hot towers (VHTs). The deep convective tower is not only an important source of latent heating, but its vortical nature may amplify preexisting vorticity by orders of magnitude. In modeling the formation of Hurricane Diana (1984), Davis and Bosart (2001) support the bottom-up pathway as they describe the transformation of a weak baroclinic disturbance into a warm-core tropical cyclone. The authors conclude that low-level potential vorticity (PV) anomalies generated by condensational heating from deep convection advects inwards to the center of the disturbance then, as the disturbance moistens, latent heat fluxes from the ocean dominate as the tangential wind increases. Likewise, in an idealized numerical modeling framework, Montgomery et al. (2006) hypothesize that, in the presence of a preexisting midlevel cyclonic MCV with a weak surface circulation, VHTs acquire intense vertical vorticity through tilting and stretching of horizontal vorticity generated by the MCV, by intense latent heating in the VHT, and the multiple vortex merger from

neighboring towers (Hendricks et al. 2004; Montgomery and Enagonio 1998; Moller and Montgomery 2000). Even in simulations at lower resolution (~15 km), thus requiring convective parameterizations, Tory et al. (2006a,b) suggest that convective updrafts on the order of 60 km enhance low- to midlevel vorticity in a similar way to how VHTs organize low-level rotation through aggregation in finer resolution cloud-resolving models (Hendricks et al. 2004; Montgomery et al. 2006). Though seemingly unrealistic, Tory and Montgomery argue that convective areas at such a scale have been recognized by studies under the top-down pathway (described in Chapter 2.2.1). Supporting the conclusions of Tory et al. (2006a,b), Braun et al. (2010) find, in a simulation of Tropical Storm Gert (2005), that the aggregation of cyclonic PV from VHTs is a necessary step in the formation process, as such a conglomeration results in increased vorticity and low- and midlevel inflow (enhanced secondary circulation).

Though the bottom-up hypothesis has gained recognition as the more sensible route to genesis, the basis of the hypothesis, VHTs, has lacked observational support. An accepted definition of a VHT does not exist, and is most often identified as coherent structures resolved in cloud-resolving and mesoscale simulations. In an effort to support that VHTs both exist in the real atmosphere and play an important role in genesis, Reasor et al. (2005), in compositing tail Doppler radar data from two NOAA P-3 flights into developing Dolly (1996), show results that indicate low-level vortices coincident with deep convection (VHTs) in an already elevated cyclonic vorticity environment (at midlevels, from an MCV), may be instrumental (though not solely responsible) for the formation of a depression-like surface vortex. Likewise, with observations from the TCS-08 field campaign in the Pacific, Bell and Montgomery (2010) confirmed, with the

ELDORA radar, coherent VHT-like structures in a vertically sheared environment in predepression Hagupit (3-4 days before genesis) that are characteristically similar to those resolved in the idealized (no shear) numerical modeling studies of Montgomery et al. (2006). The authors note a strong (~100 times greater than the background) positive vertical vorticity core up to 6 km (maximum at 4 km) and mid- to upper-level vorticity dipoles, consistent with tilting and stretching of preexisting vorticity by the convective updraft. The authors conclude that even in a vertically sheared environment that tilts updrafts, VHTs form and contribute strong low-level vorticity that enhances a preexisting low-level circulation, and repeated bursts of this nature are responsible for building the tropical depression. Finally, in examining the formation of Tropical Storm Allison, Sippel et al. (2006) identify convective-scale vortices in Doppler radar data at the scale of 1.5–5 km. These studies suggest that both stratiform (meso-B scale; 10–100 km) and convective (meso-gamma scale; 1–10 km) processes occur coincidentally (Tory and Montgomery 2006).

2.2.3. Thermodynamics of Genesis

Similar to rapid intensification of developed cyclones (Rogers 2010), cyclogenesis is closely linked to the horizontal and vertical distribution, as well as the magnitude, of latent heating. The vertical distribution of latent heating is determined by the relative proportions of convective and stratiform precipitation. Though much of the recent modeling and observational work suggests the bottom-up hypothesis to be the more likely route to genesis, it is naïve to focus only on the contributions from convective raining areas in tropical cyclogenesis; both stratiform and convective regions must participate in the genesis process. Using high-resolution ELDORA radar during the

genesis stages of Hurricane Ophelia during RAINEX, Houze et al. (2009) identify important contributions from convective and stratiform regions. The high resolution Doppler radar wind fields indicate small-scale positive vorticity perturbations at middle to upper levels connected to the remnants of old vortical convective updrafts that have since weakened (in an extreme case, one such convective updraft was observed to be a deep [~17 km], wide [~10 km], intense [vertical velocity 10–25 m s^{-1}], and vortical). Such remnant vortical elements populate the stratiform region and contribute to spin-up at middle to upper levels. While the authors observe similar convective-scale vortical elements as described by previous modeling studies, they also note that even within stratiform regions, upward vertical mass flux is always observed and is bi-modal; the vertical profile of mass flux exhibits a large gradient at low levels (below 3 km; related to the population of weaker convective updrafts) and a secondary maximum at higher altitudes (6–9 km; due to latent heat release from freezing); since PV production is directly proportional to the vertical gradient of latent heating, this result implies PV generation from low to midlevels. So, although Houze et al. (2009) conclude that they observed similar convective-scale vortical elements as identified in the aforementioned bottom-up studies, the authors extend an important hypothesis regarding the role of stratiform regions; while individual convective elements generate low-level PV, stratiform areas of MCSs contain weakened vortical updrafts from previous convective cells and contribute to a PV increase at midlevels.

It is also worth noting that Houze et al. (2009) find that, unlike ordinary MCSs, the raining areas in pre-Ophelia are nearly absent of significant downdrafts as there is no evidence of downdraft gust front convergence below the updraft. Rather, strong inflow,

which may obtain a high θ_e and steep lapse rate (nearly dry adiabatic) through wind-induced mixing in the PBL with the ocean surface, is lifted above the rain-cooled air above the level of free convection and subsequently produces the strong updraft observed. Such a conclusion confirms an earlier study by Zipser and Gautier (1978) of a depression formation during GATE in which, in the dominant MCS, convective-scale downdrafts play a relatively unimportant role in modifying the boundary layer θ_e, and while mesoscale downdrafts exist, they do not appreciably dry the subcloud air.

In a WRF modeling study of the genesis of Hurricane Dolly (2008), Fang and Zhang (2010), examine whether top-down or bottom-up process are at work. The numerical modeling results suggest that both convective and stratiform dynamics are important at all phases, but a downward extension of midlevel vorticity in the stratiform region is not observed. Rather, subsequent low-level spin-up is coincident with deep convection and its associated low-level convergence and stretching, as well as the aggregation of vorticity anomalies, the foundation of the bottom-up hypothesis.

Raymond et al. (1998) summarize cases investigated during the TEXMEX (1991) program. The authors identify a relationship between high humidity in the mid-troposphere and a lower elevation of the maximum in vertical mass flux, an indicator of a more convective-type heating profile. They hypothesize that as the midlevel relative humidity increases, the vortex transitions from that characterized by stratiform dynamics (midlevel convergence with low-level divergence in the subsidence region below), which increases midlevel rotation, to that characterized by convective dynamics (low-level convergence, upper-level divergence), which results in low-level vortex intensification. Such an increase in humidity, and in particular, reduction of the midlevel minimum in

moist static energy (MSE), is a requirement for the WISHE (wind-induced surface heat exchange) mechanism for intensification. The WISHE mechanism involves the positive feedback between the magnitude of the surface winds and the latent heat flux from the ocean; the subsequent increase in MSE below cloud provides an environment favorable for the intensification of the warm core through deep convective processes. The WISHE mechanism is only efficient when cooling and drying due to downdrafts do not offset an increase MSE at the surface; downdraft activity can be reduced when the midlevel humidity is increased.

A decade later, Raymond et al. (2010, 2011) analyze genesis cases during TCS-08 and further explore the possibility that, although the bottom-up hypothesis makes more sense dynamically than the top-down hypothesis, genesis may be best described as having elements of both hypotheses. Raymond et al. (2010) in an observational study of Tropical Cyclone Nuri during the TCS-08 experiment documents the evolution of the vorticity budget and its implications for genesis. During its 'tropical wave' phase, Nuri exhibited a vertical mass flux profile peaked at upper levels, and thus a maximum inflow and spin-up at midlevels. During intensification to tropical storm strength, the vertical mass flux instead peaked at midlevels and showed a rapid increase from the surface to 4 km. This profile is subsequently associated with strong inflow at low levels, and thus vorticity convergence and circulation spin-up at low levels. Raymond et al. 2011 points out that dynamically, the vertical vorticity at midlevels can not be transported downward to low levels. Montgomery and Smith (2012) also question the downward advection of vorticity and relate the process to the downward advection of absolute angular momentum. They assert that downward advection of absolute angular momentum is

associated with horizontal divergence, and since absolute angular momentum is conserved and is directly proportional to absolute circulation, the circulation cannot increase. The only way to have low-level spin-up is convergence at the surface, which most certainly comes from convection ('an increase in vertical mass flux with height at low levels'). The midlevel vortex alters the thermodynamic environment to favor convection and low-level convergence. That is, in the presence of the midlevel vortex and high moisture content, strong net upward mass flux at low levels produces low-level mass and moisture convergence, and subsequent vorticity spin-up.

It is generally well understood that genesis requires an environment that is characterized by high moisture and relative humidity, while the core of the disturbance must reach a warm core state; that is, the strongest vorticity and winds are at the lowest levels, below an increasing warm core with height. Many studies have suggested that genesis may not be an instantaneous event in time; rather, for some disturbances, the formation process involves "priming" or "incubation" in which deep convective episodes lead to a gradual moistening of the troposphere to "near saturation." An increase in θ_e and relative humidity is a manifestation of this process occurring. Idealized numerical modeling results by Nolan (2007) suggest that this process, in combination with a deepening and contraction of the midlevel vortex, is followed by the appearance of a small-scale low-level vortex, one that ultimately intensifies as it concentrates vertical vorticity anomalies generated in and around convective towers.

Some research hypothesizes that static stability increases during the formation stage; in other words, developing a cold core at low levels limits the convective inflow layer to low levels and subsequently leads to an environment favorable for spin-up and

the development of a warm core (Bister and Emanuel 1997; Raymond and Sessions 2007; Raymond et al. 2011). Raymond and Sessions (2007) argue that moisturization, although producing more rainfall per unit mass, is not a major factor; the stabilization of the low levels results in concentration of convergence in a shallower layer. Smith and Montgomery (2012) and Montgomery and Smith (2012), using dropsonde data from PREDICT and TCS-08 (Nuri), dispute the claim that a low-level cold core precedes cyclogenesis. The authors show that the system-mean virtual temperature within the developing pouch showed no such cooling at low levels, about 1 K warming at upper levels, an increase in θ_e (moisture) at low and midlevels, and a decrease in the surface to midlevel θ_e minimum deficit during the genesis stages.

CHAPTER 3

DATA AND METHODOLOGY

3.1. Case Descriptions

This dissertation will examine, in detail, 12 developing and four nondeveloping cases (Table 3.1). Case selection is not random; all cases were the focus of recent (since 2005) NOAA, USAF, NASA, NSF/NCAR, and NRL field programs (described in detail in Chapter 1.2.2). Although only a few disturbances, specifically those investigated by the PREDICT-GRIP-IFEX (2010) campaigns, offer extensive sampling more than 2 days before genesis, in most cases critical in-situ information from aircraft missions flown within a day of genesis were available to the National Hurricane Center (NHC) to help identify that formation was nearing, or had already occurred. In the absence of this in-situ information (for example, from dropsonde, SFMR, or radar-derived velocity measurements), NHC forecasters must depend on the appearance of convective organization (Dvorak technique) from satellites to declare tropical cyclone formation; a necessary, but subjective technique. At least in many cases included in this dissertation (Earl and Gaston are exceptions), one can have more confidence in the declared genesis time, given that decisions were made from less subjective in-situ data.

3.1.1. PREDICT-GRIP-IFEX (2010) Cases

The earliest disturbances investigated by the PREDICT program were two obvious nondeveloping pouches, PGI-27 (research flights on 17 and 18 August) and PGI-30 (21 and 23 September). PREDICT then examined a developing case, Fiona. The first investigation into Fiona by the G-V was just prior to genesis on 30 August, and was followed by two flights after genesis on 31 August and 1 September. Those two flights were the only flights by PREDICT into a tropical cyclone.

GRIP also examined a nondeveloping case early in the campaign, ex-TD5 (17 August). The disturbance, located in the northern Gulf of Mexico, is thought to have originated from TD5, which made landfall in the Gulf Coast 6 days earlier. Ex-TD5, however, has been excluded from the dropsonde analyses (Chapter 4) and case studies (Chapter 5) that follow because of two issues; first, the link to the TD5 is weak since GRIP and NOAA research flights sampled the disturbance 5–6 days after TD5 made landfall, weakened, and recurved southward back over the Gulf of Mexico, and second, the disturbance was highly sheared, and was obviously interacting with a frontal boundary over the southeastern U.S.

GRIP followed ex-TD5 with an impressive series of flights into Hurricane Earl. NASA, NOAA, and USAF conducted multiple flights into Earl between 28 August and 4 September; the flights on 29 and 30 August investigated a period in which Earl experienced rapid intensification from a strong tropical storm to category 4 hurricane. The number of flights on September 2, while Earl was recurving northward along the east coast, is considered a record day for hurricane airborne research; up to six aircraft (NASA DC-8, WB-57 and Global Hawk; NOAA P-3, G-IV; USAF C-130) were present

in Earl at the same time. This day also included the very first Global Hawk over flight of a hurricane, as well as the first successful coordination of the Global Hawk with the DC-8.

Following successful missions into Hurricane Earl and Tropical Storm Fiona, GRIP and PREDICT conducted coordinated flights into non-redeveloping ex-Gaston. Declared a tropical depression at 0600 UTC on 1 September (from satellite organization and a satellite scatterometer overpass), Gaston was at tropical depression strength for only 36 hours (reaching tropical storm status for only 12 hours). Although redevelopment initially looked likely, Gaston never redeveloped. Eight total flights by the DC-8 (2), G-V (5) and USAF C-130 (1) sampled ex-Gaston over 3 days, providing unsurpassed continuity by aircraft in a nondeveloping disturbance. Even though genesis was declared without any in-situ evidence, the formation of Gaston still offers an interesting comparison to the other cases included in the dissertation. For this reason, Gaston is treated as both a developing (between 30 August and 3 September, the date that Gaston weakens) and nondeveloping disturbance (from 3 September to the end of the track on 11 September).

The first flights into Karl were conducted by PREDICT on 10 September (two flights); however, over the following days prior to formation, GRIP and IFEX aircraft worked in close coordination with PREDICT. Karl was declared a tropical storm at 1200 UTC on 14 September, and made its first landfall in Mexico on 15 September. After reemerging in the Bay of Campeche on 16 September, Karl underwent rapid intensification to a category 3 hurricane — an event captured by multiple aircraft, including an astounding 20 overpasses by the Global Hawk. Flights into Karl were

concluded by the DC-8 and WB-57 as the hurricane made its final landfall in Veracruz, Mexico on 17 September. In total, 29 flights were conducted in Karl among P-G-I and USAF aircraft; 13 (of which 12 are dropsonde-equipped) prior to genesis (10–13 September), 6 (5 dropsonde-equipped) on 14–15 September, and 10 (7) on 16–17 September. Combined with dozens of overpasses by PMW satellites, as well as conventional visible and IR imagery, Karl may be considered one of the best-observed cases of tropical cyclogenesis in history.

As with Karl, P-G-I aircraft were also able to achieve outstanding continuity during the 2 days before genesis of Tropical Storm Matthew. In the 2 days prior to genesis, the DC-8 and G-V made five flights (one on 20 September; one each on 21 and 22 September) into the pregenesis environment. Following genesis (1200 UTC on 23 September), the G-V, NOAA G-IV and Global Hawk conducted additional flights on 24 September. The Global Hawk would sample Tropical Storm Matthew for eight consecutive hours, providing an opportunity to look in great detail at the storm structure, and specifically at the evolution of convective bursts occurring in the tropical storm just prior to landfall (Braun et al. 2012).

Although GRIP concluded operations after Matthew, PREDICT went on to fly three additional missions in two disturbances, developing Nicole, and nondeveloping pouch PGI-48. The origin of Nicole remains an interesting question; some recently presented work indicates that Nicole not only originated from a large gyre region near Central America and the western Caribbean, but can also perhaps be linked to dissipating Matthew (Bosart, personal communication). Declared a tropical depression on 28 September, two PREDICT flights investigated the pregenesis environment on 27 and 28

September. Although dropsonde data from Nicole will be included in the analysis presented in the next chapter, due to the difficulties encountered in tracking the vorticity maxima (VM) and pouch prior to 27 September, the case will not be included in the case studies presented in Chapter 5.

3.1.2. Non-PGI Cases

Two additional cases from the 2010 season are also included in the analyses, TD2 (6–9 July) and Bonnie (18–25 July). Although occurring before the GRIP and PREDICT campaigns began, NOAA and USAF sampled both disturbances extensively with the P-3s, G-IV and C-130s. In Bonnie, which was declared a tropical depression at 0600 UTC on 22 July, a G-IV flight sampled the disturbance in the pregenesis stage, while one G-IV and four C-130 reconnaissance flights investigated the postgenesis stage as Bonnie progressed northwestward into the Gulf of Mexico, and made landfall in Louisiana. In TD-2, which originated near the Yucatan Peninsula and also tracked into the Gulf of Mexico, NOAA accomplished five consecutive G-IV and P-3 flights into the pregenesis environment. In large part to the in-situ data obtained by the aircraft, NHC had enough evidence to upgrade the disturbance to a tropical depression at 0000 UTC on 8 July.

Danny (24–29 August) is the only 2009 case included in the dataset. Originating near the Lesser Antilles, NOAA dedicated one G-IV and one P-3 flight to the pregenesis stage; data from the P-3 flight provided enough support to upgrade the disturbance to a tropical depression at 0900 UTC on 26 September. Struggling to maintain strength, 11 additional flights by NOAA and USAF assets investigated the postgenesis stage as Danny progressive northwestward towards the east coast of the U.S.

Two cases from the 2008 IFEX campaign are included, Kyle and Fay. The VM in pre-Kyle (20–29 September) originated in the Lesser Antilles. After circumnavigating Puerto Rico and Hispaniola for 3 days, Kyle was upgraded to a tropical depression at 0000 UTC on 25 September north of the Dominican Republic, in large part because of data from two consecutive G-IV and P-3 reconnaissance flights on 24 September. Following genesis, eight additional flights were dedicated to Kyle as the storm progressed northward along 70°W. Fay (10–24 September) originated from an easterly wave that left Africa around 6 August. The disturbance, which is consistently tracked beginning 10 September, was not declared a tropical depression until 5 days later, 1200 UTC on 15 September. Three NOAA P-3 flights investigated the disturbance in the day prior to, and on the day of, formation; an incredible 18 flights followed after formation as Fay continued to track westward through the Caribbean, before turning north making a first landfall in Cuba on 18 September, and a second landfall a day later in southwestern Florida.

The NASA TCSP field campaign (2005) coordinated with NOAA aircraft in developing Tropical Storm Gert (21–25 July). VM tracking in Gert, like TD-2 (2010), originates near the Yucatan Peninsula. Although close to land, two NOAA P-3 missions investigated pregenesis Gert within 18 hours of formation (declared a tropical depression at 1800 UTC on 23 July); NOAA and USAF followed with three additional flights in the 24 hours after genesis, before Gert made landfall in Mexico.

One of the primary cases of T-PARC/TCS-08, Typhoon Nuri (14 – 23 August) was the only Pacific case included in the analysis. The NRL C-130 and USAF C-130 investigated Nuri a total of six times during its westward progression, including three

flights dedicated to the pregenesis stage (a tropical depression was declared by the Joint Typhoon Warning Center at 1800 UTC on 16 August).

Not all disturbances from recent field campaigns are included. For instance, another case from TCSP, Eugene, was not included as it has since been documented that ER-2 and NOAA P-3 flights did not investigate Eugene's incipient vorticity center (Kieu and Zhang, 2008). Likewise, NAMMA cases are also excluded as, in addition to the lack of temporal continuity, a clear link between the waves investigated by the DC-8 and the formation of tropical cyclones downstream have yet to be established (Zawislak and Zipser 2010). Likewise, only one flight investigated a wave during genesis (Helene), and dropsonde data from that flight are limited.

3.2. Vorticity Maxima and Pouch Tracking

For this dissertation, both vorticity maxima (VM) and pouches are *manually* tracked using the National Centers for Environmental Prediction (NCEP) Final (FNL) operational global model analyses. A product of the Global Forecast System (GFS), the NCEP FNL is prepared 1 hour after GFS initialization, every 6 hours on a 1° x 1° grid, and contains 26 mandatory pressure levels from 1000 to 10 hPa. Vorticity fields are spatially smoothed for tracking using a low-pass filter built into IDL ('smooth'). Spatial smoothing removes spurious grid scale vorticity maxima, or "bulls-eye" features, that are most likely not real. Likewise, unlike previous attempts at relative vorticity tracking (such as Kerns et al. 2008), which filter vorticity for a timescale representative of an easterly wave (2–7 days), no time filtering is applied for this study. Since some disturbances investigated in the dissertation do not appear to directly originate from an easterly wave, and since tropical cyclogenesis is often linked to mesoscale circulations

produced by organized convective systems that vary at a time scale less than that of the easterly wave, time filtering has not been applied.

Using the analyses, relative vorticity maxima exceeding a threshold of $2x10^{-5}$ s^{-1} are tracked at four levels; 925, 850, 700, and 600 hPa. VM tracking begins when the VM is consistently seen in the analysis for at least 24 hours, with the initial time of the tracking being the beginning of that period. Tracking ends when the VM drops below the threshold, can no longer be consistently tracked, makes landfall (anywhere but Caribbean islands), or becomes extratropical. Consistent with the marsupial paradigm (Dunkerton et al. 2009), the pouch center is identified at the same pressure levels by evaluating the total wind field in the co-moving (Lagrangian) framework; the co-moving field is computed by subtracting the zonal phase speed of the wave from the zonal (u-) wind field. Whereas the early literature presenting the marsupial paradigm (Dunkerton et al. 2009; Montgomery et al. 2010; Wang et al. 2010a) computes wave phase speed representative of the entire lifetime of the wave, this study updates the phase speed daily. Using a Hovmöller diagram of the meridional (v-) wind, the phase speed is identified as the zonal progression of the wave trough axis (transition between the southerly winds on the east side and the northerly winds on the west side of the trough; 'v=0' meridional wind line) from 0000 UTC – 0000 UTC. Tracking the 'v=0' line becomes increasingly unreliable for waves where there is an apparent horizontal tilt to the wave trough (in other words, the trough axis is not classically oriented north-south). In these scenarios, a wave axis is difficult to deduce because winds on the western side of the trough never turn northerly. At times when the wave axis is not well defined, the phase speed is instead calculated by using locations of the VM at each level. Waves such as those just

described, or waves that have characteristically high phase speeds (~ 10 m s^{-1}), tend to not exhibit a pouch (Wang et al 2012). The pouch location is only identified when a clear recirculating region is present in the co-moving wind field.

3.3 Dropsonde Datasets

Dropsondes from the NOAA P-3, G-IV, USAF C-130s, NSF/NCAR G-V, and NASA DC-8 will be utilized throughout the dissertation. All dropsonde data have been quality controlled using the Atmospheric Sounding Environment (ASPEN) software (online at http://www.eol.ucar.edu/data/software/aspen/aspen). Additional quality control has been manually applied to GRIP and PREDICT dropsondes by staff at the National Center for Atmospheric Research (NCAR) Earth Observational Laboratory (EOL). Manual quality control includes visually examining all profiles of temperature, relative humidity, wind speed, and vertical velocity for outliers (including those outliers as a result of interference from the transmitter antenna and erroneous aircraft initialization), adjusting data for GPS signal loss or PTU oscillations, and identifying dropsonde profiles which may be classified as "fast falls" where the parachute fails to deploy (for "fast falls," wind speed and wind direction are set to missing).

3.4. Satellite Datasets

Describing the temporal evolution of convective systems will be integral to the case studies presented in Chapter 5. Unlike many previous observational cyclogenesis case studies, which employ a single satellite, this dissertation will use data from a collection of multiple satellite platforms. Only then is the temporal resolution adequate enough to describe how the evolution of convective properties, such as intensity, raining

area, and location relative to the center, may be relevant for genesis.

The most frequent satellite observations are provided by standard geostationary IR data. IR data obtained for this dissertation are gridded to 3 km horizontal resolution and are available every 30 minutes. Although IR provides one source for convective intensity information, widespread cold brightness temperatures in IR imagery associated with cirrus outflow can be misinterpreted for active deep convection, or if convection is active, mask the convective organization underneath the cold cirrus shield. For this reason, the satellite dataset will also include passive microwave data (PMW) from polar orbiting satellites; PMW radiometers allow the user to "see through" the upper clouds that otherwise mask the precipitation organization in the IR. Higher frequency PMW channels, such as 85–91 GHz, are sensitive to high-altitude precipitation-sized ice particles, and thus are more reliable indicators for convective intensity than conventional IR (Spencer el al. 1989); convective intensity is inversely proportional to the depression of the 85–91 GHz brightness temperature. Lower frequencies, such as 19 and 37 GHz, are influenced by emissions from liquid hydrometeors lower in the cloud; high liquid water contents result in elevated brightness temperatures in precipitating regions. Due to the emissivity differences between land and ocean, a fundamental problem in an analyzing PMW data are the discontinuities that appear along coastlines. Likewise, due to its low emissivity, the ocean appears at a lower brightness temperature in the 85 GHz horizontal polarization; this can often lead to ambiguity in separating areas with depressed brightness temperatures due to deep convective clouds against the ocean background. The same ambiguity is encountered in lower frequencies over land, due to the similar magnitudes of land emissions and emissions from liquid cloud and raindrops.

To alleviate this problem, Spencer et al. (1989) recommend using the polarized corrected temperature (PCT), rather than brightness temperature. The PCT is a linear combination of the vertical ('v') and horizontal polarization ('h') brightness temperatures:

For 85 GHz:

$$PCT_{85} = 1.8\ T_{85v} - 0.8\ T_{85h} \qquad \text{(Equation 3.1)}$$

For 37 GHz:

$$PCT_{37} = 2.2\ T_{37v} - 1.2\ T_{37h} \qquad \text{(Equation 3.2)}$$

Brightness temperature (PCT) information from the following PMW instruments will be presented in the dissertation: TRMM TMI (85 GHz), AMSR-E (89 GHz), and SSM-I(S) 15 (85 GHz), 16 (91 GHz), and 17 (91 GHz).

The Tropical Rainfall Measuring Mission (TRMM) satellite package was launched in 1997 and contains a suite of instruments that include the first space-borne precipitation radar (PR), a microwave imager (TMI), a visible and infrared scanner (VIRS), as well as a lighting imaging sensor (LIS). The PR provides vertical profiles of reflectivity at a horizontal resolution of 4.3 km at nadir (about 5 km at swath edge) and swath width of 250 km, while the TMI (a conical scanner) has an 850 km wide swath and measures upwelling radiance at five frequencies: 10.7, 19.4, 21.3, 37.0, and 85.5 GHz. The footprint at 37 GHz is 16 x 9 km^2 and at 85 GHz, 7 x 5 km^2. Rainfall statistics are computed from the level-3 TRMM 3B42 TMI merged-IR product, available 3-hourly at 0.25° resolution.

The Special Sensor Microwave Imager (SSM/I) and next generation, Special

Sensor Microwave Imager/Sounder (SSM/IS), is a suite of microwave instruments flown on the Defense Meteorological Satellite Program (DMSP) satellites (F8-F15 and F16-F17, respectively). SSM/I and SSM/IS sensor data records (brightness temperature) are obtained from the NOAA Comprehensive Large Array-Data Stewardship System (CLASS; http://www.class.ngdc.noaa.gov/). SSM/IS is a 24 channel (frequencies ranging from 19 to 183 GHz), sun-synchronous, conically scanning, PMW radiometer that samples a swath width of approximately 1700 km. The footprint is 16 x 13 km^2 at 85 and 91 GHz (12.5 km spatial sampling), and 38 x 30 km^2 at 37 GHz (25 km spatial sampling). Such a large frequency range facilitates the sensor packages unique goal; the retrieval of atmospheric temperature and moisture soundings at 15 mandatory pressure levels from 1000 to 10 hPa (Northrop Grumman Technical Report; "Algorithm and Data User Manual for the Special Sensor Microwave Imager / Sounder [SSM/IS]).

The Advanced Microwave Scanning Radiometer (AMSR-E) is a conically scanning, PMW radiometer aboard the Aqua satellite (launched in 2002). The swath width of AMSR-E is approximately 1500 km, and although it has less channels (12) than SSM/IS, the instrument samples at greater spatial resolution; the footprints are comparable to that of TMI, 6 x 4 km^2 at 85 GHz (mean spatial resolution of 5.4 km), 14 x 8 km^2 at 37 GHz (spatial resolution of 12 km) and 27 x 16 km^2 at 19 GHz (spatial resolution of 21 km). AMSR-E level-2 brightness temperature data are obtained from the National Snow and Ice Data Center (NSIDC; http://nsidc.org/data/ae_l2a.html).

In addition to swath brightness temperatures, derived total precipitable water (TPW) data from AMSR-E, TMI, and SSM-I(S) have been acquired from Remote Sensing Systems (REMSS, online at http://www.ssmi.com). Temperature, humidity, and

TPW data have also been acquired from the Atmospheric Infrared Sounder (AIRS) profiles. AIRS data are obtained from the Goddard Earth Sciences Data and Information Services Center (GES DISC; http://disc.sci.gsfc.nasa.gov/AIRS/data-holdings). AIRS (also on the Aqua satellite) is a high resolution spectrometer, which scans across track at 2378 bands in the thermal infrared (3.7–15.4 μm) and four bands in the visible (0.4–1.0 μm). The horizontal resolutions vary from 13.5 km at nadir, to 41 km at swath edges. In the vertical, temperature is measurable at 1 km thickness at an accuracy of 1°C and relative humidity, in layers 2 km thick at an accuracy of 20% (from the AIRS Instrument Guide, online at http://disc.sci.gsfc.nasa.gov/AIRS/data-holdings/by-data-product-v5/documentation/airs_instrument_guide.shtml). Because AIRS data are considered unreliable in precipitating regions, only data flagged as reliable – outside of cloudy, precipitating regions – are included.

Table 3.1
Summary of cases and the number of dropsondes included in the dataset

YEAR	TRACK DATES (GENESIS)	PROGRAM/AGENCY	NAME	PGI #	DEV/NDEV	FLIGHTS	NUMBER OF DROPSONDES			
							NDEV	PRE-GENESIS	POST-GENESIS	TOTAL
2010	-	PREDICT/GRIP	Misc.	-	-	2	*35*			35
2010	8/16 - 8/21	PREDICT	-	27	NDEV	2	47	-	-	47
2010	-	GRIP/NOAA	ex-TD5	29	NDEV	2	*62*	-	-	62
2010	8/17 - 8/23	PREDICT	-	30	NDEV	2	28	-	-	28
2010	8/23 - 9/4 (25/06Z)	GRIP/NOAA/USAF	Earl	34	DEV	35	-	0	607	607
2010	8/27 - 9/4 (30/12Z)	PREDICT/USAF	Fiona	36	DEV	7	-	8	96	104
2010	8/29 - 9/11 (01/06Z)	PREDICT/GRIP/USAF	Gaston	38	DEV/NDEV	8	144	-	-	144
2010	9/9 - 9/18 (14/12Z)	PREDICT/GRIP/NOAA/USAF	Karl	44	DEV	24	-	242	189	431
2010	9/20 - 9/25 (23/18Z)	PREDICT/GRIP/USAF	Matthew	46	DEV	9	-	105	48	153
2010	9/29 - 9/30	PREDICT	-	48	NDEV	1	26	-	-	26
2010	9/27 - 9/30 (28/12Z)	PREDICT/USAF	Nicole	50	DEV	5	-	23	40	63
2010	7/6 - 7/9 (08/00Z)	NOAA	TD02	-	DEV	5	-	109	8	117
2010	7/18 - 7/25 (22/06Z)	NOAA/USAF	Bonnie	-	DEV	6	-	33	30	63
2009	8/24 - 8/29 (26/09Z)	NOAA/USAF	Danny	-	DEV	13	-	26	60	86
2008	8/10 - 8/24 (15/12Z)	NOAA/USAF	Fay	-	DEV	22	-	44	252	296
2008	9/20 - 9/29 (25/00Z)	NOAA/USAF	Kyle	-	DEV	11	-	14	52	66
2008	8/14 - 8/23 (16/18Z)	NRL/USAF	Nuri	-	DEV	7	-	40	102	142
2005	7/21 - 7/25 (23/18Z)	NOAA/USAF	Gert	-	DEV	5	-	23	53	76
						Total	245	667	1537	2546

CHAPTER 4

ANALYSIS OF DEVELOPING AND NONDEVELOPING THERMODYNAMIC PROPERTIES USING A HISTORICAL DROPSONDE DATASET

4.1. Introduction

Progress towards understanding the underlying processes of tropical cyclogenesis continues to be challenged by the relative sparsity of observations available over the ocean. As described previously, field campaigns, as well as NOAA and USAF reconnaissance missions, prior to 2010 have achieved some success of high spatial resolution in-situ sampling of the pregenesis environment, but have often lacked the temporal continuity necessary to truly appreciate the kinematic and thermodynamic changes occurring in a disturbance as it progresses toward formation. In achieving a temporal continuity unsurpassed by previous airborne field campaigns, the collection of observations from dropsonde-equipped PREDICT, GRIP, IFEX, and USAF aircraft during the summer of 2010 provides an unparalleled dropsonde dataset covering all stages of a storm's lifecycle, thus providing the best opportunity to date to observe the temporal history of a disturbance undergoing tropical cyclogenesis.

Though dropsondes have previously been used to support observational tropical cyclogenesis studies, little success has been achieved in using them to describe the time evolution in detail. Some initial work by Smith and Montgomery (2012), using

PREDICT and GRIP data, provides evidence that supports a systematic change in moisture and temperature during the formation of Karl, Matthew, and Nicole; in each successive day prior to formation, they observe that the difference between the surface and midlevel equivalent potential temperature minimum is decreased, while in general, equivalent potential temperature and virtual potential temperature increases (primarily at midlevels) in each subsequent flight. In contrast, they conclude that a systematic decrease in midlevel relative humidity in ex-Gaston is the reason for its non-redevelopment. Smith and Montgomery (2012) only, however, include dropsondes from PREDICT and, for Karl only, GRIP; no IFEX dropsondes (totaling 94) are included in the analysis of Karl, and no GRIP dropsondes (totaling 44) are included in the Matthew analysis. Therefore, although all available dropsondes are included for ex-Gaston, of the 347 total dropsonde observations in the pregenesis environments of Karl and Matthew, approximately 40% of the available dropsonde observations are excluded from their analysis. Though the P-3s and C-130s do not offer as much upper-level information as the DC-8 and G-V, they can offer critical information at low levels.

As a step towards accomplishing the overall goal of the dissertation of advancing our understanding of the necessary and sufficient conditions for tropical cyclogenesis, this chapter will analyze an unprecedented collection of dropsonde observations from not only the P-G-I campaigns, but also a number of genesis-related field programs conducted since 2005. Using composite vertical profiles, the dataset will be analyzed to quantify the thermodynamic properties that distinguish developing from nondeveloping disturbances, and characterize the temporal evolution of the developing inner core at all levels in the troposphere. In addition, the dataset will yield valuable information that can corroborate

or disprove a few recent hypotheses: that the inner core of a developing disturbance progressively moistens after each convective episode (to be addressed further through case studies in the next chapter), that the troposphere must achieve near-saturation for genesis to proceed, and that, prior to genesis, the low levels are characterized by a cool temperature anomaly and increased static stability.

The following questions will be addressed with the dropsonde dataset:

1) How do developing disturbances differ thermodynamically from nondeveloping?

2) Is there is a systematic increase in temperature and moisture during the formation of a tropical cyclone? If so, by how much and at what levels?

3) Do the observations support a persistent low-level cold anomaly prior to formation?

4) Is there is a systematic increase in relative humidity, and does the troposphere achieve near-saturation prior to genesis?

Given the extensive use of model analyses in numerical simulation initialization, and reanalyses for research purposes, the dataset also represents a unique opportunity to critically evaluate how well analyses and reanalyses represent the thermodynamic and wind environment before and after genesis; included will be the NCEP FNL operational model analysis, NCEP/NCAR reanalysis, and ERA Interim reanalysis. Therefore, one additional question will be explored using the dataset:

- How well do model analyses and reanalyses represent the environment and inner core properties of developing and nondeveloping disturbances?

This chapter is organized as follows; section 2 will provide an overview of the

dropsonde dataset; section 3 will present the composite differences between developing and nondeveloping systems, describe the time evolution of inner core thermodynamic properties in developing and nondeveloping disturbances, and quantify the differences between the observations and the model analysis and reanalyses; finally, section 4 will summarize the important findings.

4.2. Case Selection and Dataset Description

4.2.1. Case Selection

The dropsonde dataset consists of dropsondes from developing disturbances from 2005–2010 (see Table 3.1), and some nondeveloping disturbances from 2010; all dropsondes from the GRIP, PREDICT, IFEX, and USAF aircraft for cases during August–September 2010 are included in the dataset. For each case in the dataset, dropsondes from flights after genesis are also included. Genesis is defined by the tropical depression classification by NHC. Although the majority of dropsondes in the dataset are associated with developing disturbances (total drops are 667 before development and 1537 after), some well-sampled nondeveloping disturbances investigated by the 2010 field campaigns are included in the dataset. The best-sampled case of nondeveloping is ex-Gaston, in which both the NASA DC-8 and PREDICT G-V were able to sample the potential redevelopment of Gaston over the course of 3 days following its downgrade to a low from a tropical storm. Three other disturbances, P-G-I 27, 30, and 48 were also investigated by the G-V only and are included in the nondeveloping composites. Once again, dropsondes from ex-TD5 (nondeveloping), as well PREDICT and GRIP test flights are not included (italics in Table 3.1). As stated in Chapter 3.1.1., ex-TD5 is excluded due to its close proximity to the Gulf Coast of the U.S. and because of its

unique environment compared to the other developing and nondeveloping disturbances studied; ex-TD5 is located in a highly sheared region associated with a midlatitude frontal zone. With these exclusions, the sample size of nondeveloping profiles is 245.

Prior to 2010, nearly every mission by USAF aircraft was considered for inclusion in the dataset; however, whether the disturbance consisted of a single reconnaissance flight during the pregenesis stage (those flights were often the reason for upgrading the investigated disturbance to a tropical depression or tropical storm) or consisted of multiple C-130 reconnaissance flights, many flights are excluded due to insufficient horizontal and vertical spatial coverage (less than three dropsondes, many confined to low levels) and a lack of temporal continuity. On the other hand, cases in which at least one P-3 or G-IV flight investigated the disturbance prior to TD formation are included, considering that those aircraft fly at a higher altitude and provide a greater sample of dropsondes. While the current dropsonde dataset does not consist of every dropsonde that has sampled the pregenesis environment, many of the historically best-sampled genesis cases are already included. The ultimate goal is to accumulate all well-sampled genesis cases, making the dropsonde dataset the most comprehensive and complete dataset of pregenesis dropsondes available.

4.2.2. Dataset Set-up/variables

For each disturbance, the "center" is defined by the vorticity maximum (VM) and pouch (PCH) manually tracked in the 1°x1° NCEP FNL model analyses (see Chapter 3.2 for more detail on the tracking methodology). Although 925, 700, and 600 hPa VM/pouches are also tracked, the analyses presented are based on the 850 hPa VM/pouch center. The radius separating the "inner core" and "environment" regions will be

identified appropriately for each analysis, when presented. Each dropsonde is interpolated onto 19 vertical pressure levels: 1000, 975, 950, 925, 900, 850, 800, 750, 700, 650, 600, 550, 500, 450, 400, 350, 300, 250, 200 hPa. Greater vertical resolution is required at low levels to better resolve the low-level cold anomaly and static stability. Variables given directly from the sensors on the dropsonde include time, latitude, longitude, temperature, pressure, height, and relative humidity. Derived variables include the u- and v-wind components (and thus, wind speed and wind direction). Other variables are computed and included: potential temperature (θ), equivalent potential temperature (θ_e; computed using Bolton's [1980] formula), saturated equivalent potential temperature (θ_{es}), virtual potential temperature (θ_v), water vapor mixing ratio (w), saturated water vapor mixing ratio (w_s), specific humidity (q), dewpoint temperature (T_d), and virtual temperature (T_v). Likewise, the 'PGI' number (for 2010 cases, represents the P-G-I invest number assigned to pouches of interest to the PREDICT forecast team; for pre-2010 cases, represents the sequential tropical cyclone number assigned by the NHC), and an index that classifies the dropsonde as being associated with a developing disturbance (assigned a '2'), nondeveloping ('1') or neither (i.e., a test flight; '0'), are included. Using the zonal and meridional phase speed of the disturbance, each dropsonde is also co-located with its location in the nearest in time NCEP FNL analysis, NCEP/NCAR reanalysis (2.5° horizontal resolution), and ERA Interim reanalysis (1.5°). Once the dropsonde location is moved the appropriate distance, based on zonal/meridional phase speed and the time difference between the launch time and the closest analysis time, the dropsonde is then assigned the nearest neighbor analysis and reanalysis profile for all previously mentioned thermodynamic and kinematic variables.

Each dropsondes radial distance from the VM/pouch in the nearest analysis time at 925, 850, 700, and 600 hPa are also included. This allows the user to readily differentiate dropsondes at various radial distances from the center. Each dropsonde is also assigned a value, 'hrgen,' which is the time difference between the dropsonde launch time and the genesis time of the disturbance (defined as the time the NHC declares the disturbance to be at least a tropical depression). Nondeveloping disturbances are also assigned this time. However, all times are considered to occur before genesis and the "genesis" time ("zero" hour in the figures) is simply the last tracked time for the disturbance. Therefore, the value has no real relevance for nondeveloping cases. The one exception is ex-Gaston; data appear "after genesis" since all flights were investigating Gaston after it had formed and since weakened to below a tropical depression.

The distribution of samples versus the radial distance from the vorticity maximum for all dropsondes in developing and nondeveloping disturbances is illustrated in Figures 4.1 and 4.2, respectively. In both nondeveloping and developing cases, the samples are distributed equally across all quadrants within 3°, and somewhat biased to the north beyond 3°. Likewise, Figures 4.3 and 4.4 also show the sample distribution for those dropsondes before and after formation, respectively, and indicate that samples are well distributed around the inner core in both stages; not unexpectedly, the postgenesis sample is over two times as large as the pregenesis sample.

4.3 Results

4.3.1. Developing and Nondeveloping Composite Profiles

Figure 4.5 shows the composite θ_e (a), water vapor mixing ratio (b), relative humidity (c), and θ (d) for developing and nondeveloping disturbances in the dataset.

Developing disturbances are further separated by pregenesis and postgenesis stages. This figure clearly illustrates some important differences in the thermodynamic environment among developing and nondeveloping disturbances. For θ, only a small difference is observed below 600 hPa between nondeveloping disturbances and the pregenesis stage of developing disturbances; however, as one should expect, the mean θ in the postgenesis environment is warmer at upper levels than prior to formation. The most distinguishing differences, however, appear in the moisture variables. Although nondeveloping disturbances and developing disturbances exhibit similar moisture (and thus θ_e) profiles at low levels, in the composite, the pre- and postgenesis stages of developing disturbances exhibit a greater midlevel (above 700 hPa) mixing ratio compared to nondeveloping disturbances. The composite relative humidity also illustrates an important difference between nondeveloping and developing disturbances: nondeveloping disturbances have a lower relative humidity in the middle to upper troposphere (above 800 hPa) than developing disturbances.

A t-test was performed on each variable for each level to determine if the means of the developing and nondeveloping samples are significantly different from each other. For all variables (θ, θ_e, water vapor mixing ratio and relative humidity), at all levels, the developing and nondeveloping samples are significantly different at the 95 and 99% level. This result, however, must not be considered conclusive; while the assumption that the samples are normally distributed is somewhat valid, the assumption that the samples are independent is most likely not valid. Dropsondes in each individual flight are likely not independent. Even if each flight is considered to be an independent sample, the sample sizes for developing and nondeveloping disturbances are too small to make any

definitive conclusion. So while the nondeveloping composite water vapor mixing ratio and relative humidity profiles are clearly different from the developing composite profiles at midlevels, given that only four disturbances contribute to the nondeveloping composite (which is much less than the 11 disturbances contributing to the developing composite), one must take caution in generalizing this result for all nondeveloping cases. It seems plausible that nondeveloping disturbances can exhibit inner core thermodynamic characteristics comparable to developing disturbances.

Interestingly, the composite relative humidity in the midlevels in the postgenesis stage is slightly lower than the pregenesis stage (Figure 4.5). This may, however, be a consequence of including soundings located outside the inner core of the tropical cyclone, where subsidence drying is occurring, in the composite profile. This reasoning is supported in Figure 4.6, which presents the same analysis except profiles are separated for the "inner core" (within 3° of the center) from those in the "environment" (3 to 7° from the center). Now the inner core relative humidity profiles in the postgenesis period are, on average, slightly greater than the pregenesis period. More importantly, separating the analysis in this way amplifies the inner core differences between pregenesis and postgenesis in θ_e and mixing ratio; the postgenesis mixing ratio increases by up to 1 g kg^{-1} from the pregenesis average, while the entire θ_e profile has increased approximately 5 K. In addition, the θ_e lapse rate, as well as the difference between the surface θ_e and midlevel θ_e minimum, is reduced after genesis; a sign of stabilization at low levels. As expected, the environment is characteristically drier, less humid, and cooler than the inner core for developing cases; in fact, the environmental properties in developing cases are fairly close to those observed in nondeveloping cases. Not surprisingly, the nondeveloping

cases exhibit the least difference between inner core and environmental characteristics.

4.3.2. Thermodynamic Evolution of Developing Disturbances

Figure 4.7 shows the time evolution of the vertical profile of θ_e anomaly for all genesis cases included in the dropsonde dataset. Data are composited in 1-day periods from 4 days before genesis to 4 days after. The anomaly is defined by the difference between the mean profile of the inner core (0–3°) dropsondes for each 1-day period, and the mean profile of environmental (between 3° and 7° of the VM center) soundings from all flights. Figure 4.7 illustrates an important characteristic of developing tropical cyclones; within the inner core, their mean low- to midlevel (above 900 hPa) θ_e is higher than that of the surrounding environment and increases slightly each day, while the low levels (below 900 hPa) exhibit little increase until after formation. Figure 4.8 similarly illustrates the time evolution of θ and indicates that the warm core is developing at middle to upper levels (above 500 hPa) as many as 3 days before genesis, and extends downward with time. The warm θ anomaly observed 3–4 days before genesis in the composite is primarily from Karl, and reflects that pre-Karl is initially warm core; however, as pre-Karl disorganizes (will be shown in a case study in the next chapter), the disturbance transitions to cold core through the midlevels. The development of the inner core upper-level warm anomaly prior to genesis may be related to latent heating aloft (the composite θ anomaly profile is characteristically stratiform), or may possibly be a consequence of compensating subsidence in the convective region (Fritsch and Chappell 1980). Regardless, through hydrostatic adjustment, warming aloft will produce surface pressure falls; a potentially important step in the genesis process since this will promote low-level convergence and spin-up.

Given the relatively small magnitude of the θ anomaly compared to θ_e, the positive, increasing (albeit slowly) θ_e anomaly at midlevels is mostly attributed to an increase in moisture content. This conclusion is confirmed when looking at the inner core water vapor mixing ratio anomaly (Figure 4.9); the positive low- to midlevel (above 950 hPa) water vapor anomaly increases slightly each day (approximately 0.5 g kg^{-1} per day). Compared to the VM, the pouch inner core (both 1 and 3°) exhibits similar anomalies and patterns, and is therefore not shown.

Figures 4.10–4.12 (θ_e, θ, water vapor mixing ratio) are similar to Figures 4.7–4.9, except the inner core is redefined as 1° from the center (rather than 3°). Although the magnitude of θ_e and θ is similar between the two definitions within 48 hours of genesis, compared to the increase observed in the same period for larger inner core definition (0–3°), there is a more noticeable increase in the inner core θ_e and θ anomaly in the 2–4 days before genesis in the 1° composite (here data are primarily for Karl). Likewise, the mixing ratio anomaly within 1° shows a more noticeable daily increase at midlevels, closer to 1 g kg^{-1} per day, prior to genesis than what is observed in the 3° analysis (0.5 g kg^{-1}). However, is the anomaly's daily increase as a result of an increase in the inner core moisture, or a decrease in the environment? The time series of the dropsonde mean midlevel mixing ratio (700–400 hPa) for dropsondes within 1°, 1–3°, and 3–5° is provided in Figure 4.13. This figure indicates that increase in the anomaly can be attributed to both a slight increase in mean midlevel mixing ratio within the inner core (1°) and a slight decrease of the mean midlevel mixing ratio at outside radii (3–5°).

Figure 4.14 shows the time series of the 3° inner core relative humidity; the inner core relative humidity exhibits little increase each subsequent day prior to, and after

formation, while at no point does the middle troposphere achieve a "near-saturated" state (though "near saturated" is hardly ever defined in the literature, here it will be defined as above 90%). Similar to the water vapor mixing ratio, the analysis for the 1° inner core relative humidity (Figure 4.15) shows an initially drier disturbance 3–4 days prior, which subsequently humidifies as genesis is reached.

Figure 4.16 similarly shows the time series of the inner core wind speed. The figure indicates that the wind speed at middle to upper levels (700–400 hPa) initially exceeds that at low levels (below 700 hPa), and that within 2 days of genesis, the *low levels* gradually increase; the midlevels do not increase substantially until after formation. Likewise, Figure 4.17 shows the time series of relative vorticity from the NCEP FNL within 3° of the center. Consistent with the observed warm anomaly aloft (above 850 hPa) and cool anomaly at low levels (below 850 hPa), the relative vorticity is initially stronger at midlevels (850–600 hPa) 3 days prior to formation. Consistent with the fact that Karl is initially warm core (θ anomaly; Figures 4.8 and 4.11), the relative vorticity is initially maximized at low levels (below 850 hPa) 3–4 days prior to formation. Within 2 days of formation, while the relative vorticity steadily increases at all levels, the low levels (below 850 hPa) increase much more rapidly until the relative vorticity maximum is lowered to the near-surface 24 hours after genesis.

Although Figure 4.16 does not specifically show the tangential wind speed - here the tangential wind speed is approximated by total wind speed - an analysis of the time evolution of the vertical profile of tangential wind speed for three P-G-I (Karl, Matthew, and ex-Gaston) cases has, however, already been presented in Davis and Ahijevych (2012). The authors relate the evolution of the tangential wind profile to the circulation

tendencies and observe that developing disturbances exhibit faster growth in the midlevel circulation initially, while only immediately prior to formation (they approximate within a day) does the low-level circulation begin to rapidly increase. Similar conclusions are presented in Nolan (2007) who, using idealized model simulations of tropical cyclogenesis, emphasized the requirement of having a midlevel vortex already present in a moist, near-saturated environment to trigger low-level spin-up. Depending on the perspective, one can interpret this result as supporting the bottom-up or top-down theory. However, this result must be interpreted more simply; the midlevels exhibit the stronger vortex prior to formation and low-level spin-up is required for genesis.

Another important observation from Figures 4.8 and 4.11 is the persistent cool anomaly (~1–1.5 K) at low levels. The anomaly, which extends from the surface to 900 hPa, is a common feature for the VM and pouch and both inner core definitions (1 and 3°). A negative (dry) anomaly is even apparent in θ_e (Figures 4.7 and 4.11) and mixing ratio (Figure 4.9 and 4.12). The anomaly reaches its greatest vertical depth a day before genesis, and then gradually shallows until it is confined only to the near-surface after genesis. Subsequently, one should expect increased static stability at low levels; the mean vertical profile of temperature lapse rate in the 4 days prior to genesis for the 3° inner core (Figure 4.18) confirms a slight decrease in the lapse rate in the 1000–950 hPa layer as genesis nears. The observed anomaly appears to support a similar observation in an analysis by Raymond et al. (2011) for the pregenesis stage of TCS-08 cases. By analyzing a few of the same P-G-I developing systems as this dissertation (Karl, Matthew, and ex-Gaston), Smith and Montgomery (2012) dispute the anomaly in their analyses, while Davis and Ahijevych (2012) confirm it. As Davis and Ahijevych (2012)

note, Smith and Montgomery (2012) most likely do not detect the cool anomaly since they do not confine their analysis to the inner core (either 1 or 3°) and use a longer time-averaged reference profile.

A compilation of results from Raymond et al. (1998), Raymond and Sessions (2007), Raymond et al. (2007), and Raymond et al. (2011) indicate how, thermodynamically, a midlevel vortex is important for tropical cyclogenesis. Initially, a stronger midlevel circulation is observed; this translates to an upper-level warm temperature anomaly over a low-level cold anomaly, and thus increased stabilization in the low troposphere. The authors suggest that if the troposphere is moist and the saturation fraction (or column relative humidity – the fraction of precipitable water to saturation precipitable water) is sufficiently high (>0.80), a consequence of this thermodynamic profile is increased rainfall rates, and thus a preferentially bottom-heavy mass flux profile and a tendency for vorticity convergence (which must overcome frictional spin-down) to spin up the low-level (0–1km) circulation. Therefore, a bottom-heavy mass flux profile favors low-level convergence and spin-up. Although the authors do not explicitly relate the mass flux profile to precipitation characteristics, they suggest that the bottom-heavy mass flux profile is reminiscent of the profile expected in VHTs (Hendricks et al. 2004; Montgomery et al. 2006). Nonetheless, questions remain as to the consequence of lower tropospheric stabilization on precipitation characteristics (such as rainfall area, convective fraction, and intensity), as well as the reason for the bottom-heavy mass flux profile. So, according to the Raymond "chain of logic" (confirmed in numerical simulations of Nolan [2007]), the midlevel circulation in a moist, near-saturated environment intensifies before the low levels (predominantly stratiform

dynamics), and subsequently provides a favorable thermodynamic environment for low-level convergence and spin-up (predominantly convective dynamics).

Results from the composited dropsonde dataset support this pathway to genesis; an initially stronger midlevel (850–600 hPa) vortex (Figures 4.16 and 4.17), in an environment characterized by a low-level (1000–900 hPa) cold anomaly (Figures 4.8 and 4.11), increased static stability (Figure 4.18), and high relative humidity (Figures 4.14 and 4.15), precedes the low-level intensification (Figures 4.16 and 4.17). One could further speculate that the relatively cool, dry (according to θ_e, Figures 4.7 and 4.11, and water vapor mixing ratio, Figures 4.9 and 4.12) air observed within the inner core at low levels 1–3 days prior to genesis suggests that latent heat fluxes from the ocean are no longer able to maintain the boundary layer against the cumulative effect of convective downdrafts. However, given the positive feedback between surface wind speed and latent heat flux from the ocean, when the low-level wind speed (and relative vorticity) intensifies the day before formation, not coincidentally, the cool, dry air at low levels begins to recover, and by formation, is completely removed.

The reason for the low-level intensification in the 1–2 days prior to genesis has not yet been elucidated. Presumably during this period, low-level convergence replaces or overcomes competing low-level divergence expected from downdrafts. Although Raymond et al. (2011) suggest that the initiation of low-level vorticity convergence and the spin-up that follows is related to *convective-scale processes* (VHTs), another possible explanation is that on the *mesoscale*, warming aloft can produce, through hydrostatic adjustment, surface pressure falls that initiate low-level convergence. The initial formation, and subsequent downward extension, of an upper-level warm θ anomaly 3

days prior to genesis observed in the developing dropsonde composite (Figure 4.8) resembles a similar result presented in a numerical simulation (Penn State/NCAR MM5) of the formation of Typhoon Nari (2001) in Zhang and Zhu (2012). The authors conclude that upper-level warming, due to compensating subsidence from widespread deep convection, will hydrostatically induce meso-α-scale (> 200 km) surface pressure falls (in fact, compared to lower-level heating, accounts for more than 75% of MSLP changes), which subsequently enhances low-level convergence; in essence preconditioning the low-levels for bottom-up growth by smaller-scale cyclonic vorticity (such as VHTs).

It is important to note that the composite profiles 1–4 days before genesis are predominantly influenced by data from the five best-sampled pregenesis cases included in the dataset: Karl, Matthew, Nuri, Fay, and TD2 (all had three or more flights prior to genesis). Although the magnitude and depth differs in each case, the θ_e, θ and mixing ratio anomalies described in the composite time series are common among all the best-sampled cases in the dataset. The other, less-sampled cases, such as Danny, Bonnie, Gert, and Kyle, do exhibit some of these features; however, given the limited spatial and temporal sampling (in all cases, only 1–2 flights were dedicated to the pregenesis stage; all within a day of formation), no conclusion is made as to whether they support or differ from the genesis pathway exhibited by the composite. With the exception of Fay, a cool, dry anomaly is observed at low levels (below 850–900 hPa) in each of the best-sampled cases individually, while all of the cases exhibit a positive θ_e and mixing ratio (moisture) anomaly at middle to upper levels (above 850 hPa). Although a pregenesis warm anomaly at upper levels (above 500 hPa) is consistently observed in all cases, below 500

hPa, the θ anomaly is somewhat more variable. Some disturbances, such as TD2 and Karl, exhibit a warm core that extends to midlevels (850–500 hPa) prior to genesis, while others, such as Matthew and Nuri, are strictly cold core at midlevels until genesis. Regardless, not one of the best-sampled disturbances examined in this dissertation exhibits a maximum in relative vorticity below 850 hPa within 3 days before genesis.

4.3.3. Thermodynamic Evolution of Nondeveloping Disturbances

Four nondeveloping cases are included in the dropsonde dataset; ex-Gaston, PGI-27, PGI-30, and PGI-48. Although the sample size is significantly less than the developing cases, some conclusions can still be made regarding the essential differences between the time evolution of the inner core of developing disturbances compared to nondeveloping. Figure 4.19 shows the scatter of midlevel (700–400 hPa layer average) mixing ratio values for each nondeveloping dropsonde. (Note that in this figure, as before, the time on the abscissa is not related to genesis; Gaston is plotted "after genesis" and all other nondeveloping are plotted "before genesis"). The figure indicates that the midlevel mixing ratio at all radii (up to 5°) systematically decreases each day, until the disturbance is no longer tracked. The same tendency is observed in midlevel (600 hPa) relative humidity (Figure 4.20). Likewise, the difference between the surface θ_e and the midlevel θ_e minimum (Figure 14.21) shows a systematic *increase* over time. This result may not only be interpreted as a decrease in midlevel moisture, but also as a result of an increase in the surface θ_e (Figure 4.22).

4.3.4. Dropsonde Comparison with Model (Re)analyses

Given the robust sample size, the dropsonde dataset can be readily used to critically evaluate how well model analyses and reanalyses represent the nondeveloping, and pre- and postgenesis environments. The analyses and reanalyses from NCEP and ECMWF can also be compared with one another to reconcile which product best reproduces the observed thermodynamic and wind environment. Each dropsonde location has been corrected to the closest analysis and reanalysis time (00, 06, 12, 1800 UTC) according the zonal and meridional phase speed of the wave; the nearest neighbor grid point is then selected as the coincident analysis and reanalysis profile. All analyses shown will be for the 850 hPa VM locations only; with few exceptions, the differences computed for the pouch locations compare similarly to those computed for the VM in each analysis and reanalysis, and thus are not shown.

Figure 4.23 shows the mean and root mean square (RMS) for the difference between the dropsonde observations and the NCEP FNL analysis for potential temperature, equivalent potential temperature, relative humidity, water vapor mixing ratio, and u- and v-wind components. As before, the analyses are separated according to nondeveloping, developing pregenesis, and developing postgenesis (for this figure, no radius limit is applied). Figure 4.23 indicates two evident differences between the FNL analysis and dropsonde observations for water vapor mixing ratio and θ_e; at low levels (below 800 hPa), on average, the NCEP analysis mixing ratio is slightly lower than observed (approximately 1 g kg^{-1} at 1000 hPa), while at middle to upper levels (above 800 hPa), the FNL analysis tends to be somewhat too moist (approximately 0.5 g kg^{-1}); a contoured frequency by altitude diagram (CFAD; not shown) confirms that these results,

with few exceptions, are consistent among both developing and nondeveloping profiles. The RMS difference indicates the greatest differences are at low levels (approximately 4 K and 1.5 g kg^{-1}) and progressively decrease with increasing height. Similarly, the relative humidity at low levels in NCEP FNL is, on average, somewhat low compared to observed, while too high at midlevels (approximately 5%). The mean value is, however, somewhat misleading as the RMS difference is at least 10% (increases with height) at all levels, and a CFAD (not shown) indicates that, for both developing and nondeveloping profiles, positive differences (less humid than observations) exceeding 10% occur nearly as frequently as negative (more humid) differences exceeding 10%, particularly at midlevels (800–500 hPa). The NCEP appears to be, on average, warmer than observed at the surface and too cool aloft, however, the differences are small; the mean difference is less than 0.5 K, while the RMS difference is approximately 1–1.5 K at all levels. The distribution of θ differences (not shown) confirms that almost all profiles are within +2 (FNL is cooler) and -2 K (warmer) of the observations. Although, according to the mean difference, the FNL does not appear to differ significantly from the observed u- and v-component wind speeds (less than 0.5 m s^{-1}), the RMS difference is as high as 3 m s^{-1} for nondeveloping and pregenesis profiles, and as high as 10 m s^{-1} for postgenesis profiles. Overall, for moisture and humidity, results indicate that the FNL actually most differs from observations in nondeveloping cases, while for temperature and u- and v-wind speed, the differences are, as expected, distinguishably greatest for the postgenesis stage of developing disturbances.

To further clarify how well the FNL analysis represents the disturbance, the differences have also been computed for inner core-only (0–3°) and environment-only

(3–7°) dropsondes (Figures 4.24 and 4.25). While the mean and RMS differences for the inner core and environment are similar for θ_e and water vapor mixing ratio, more substantial differences appear for other variables. In both pre- and postgenesis samples, the relative humidity differences in the environment are, on average, greater than the inner core, meaning that the FNL tends to resolve the inner core relative humidity better than the environment's. For θ, the inner core is only distinguishably different than environment during the postgenesis stage; compared to the environment, the RMS difference is 1–1.5 K greater in the inner core. Although not consistent for all postgenesis profiles, the positive mean difference can be interpreted as meaning that the NCEP FNL's representation of the upper-level warm core is, on average, cooler than observed (approximately 0.75 K; RMS difference up to 2 K). As may be expected, the postgenesis profile exhibits the greatest RMS difference for the u- and v-wind (exceeding 10 m s^{-1} at low levels); the differences are not distinguishably greater in either the environment or inner core for pregenesis and nondeveloping profiles.

The differences between the dropsonde observations and the NCEP/NCAR reanalysis (hereafter, NNR) are *considerably* larger than NCEP FNL operational analysis differences (Figure 4.26). For a significant portion of developing and nondeveloping profiles, the reanalysis is too dry at low to midlevels (950–400 hPa); the RMS difference is in upwards of 4 g kg^{-1}, which well exceeds the 1.5 g kg^{-1} RMS difference seen in the FNL, while for relative humidity the RMS difference is up to 30% at midlevels (compared to ~15% RMSE for the FNL). Compared to the FNL, below 600 hPa, the mean and RMS difference for θ is greater in the NNR; the RMS difference is approximately 1–2.5 K in the NNR, compared to 0.5–1.5 K for the FNL. While, in both

developing and nondeveloping profiles, the reanalysis is consistently too warm below 600 hPa, above that level, the differences decrease, meaning that the NNR is closer to the observations at upper levels. In contrast to the thermodynamic variables, the u- and v-wind differences for the NNR are comparable to FNL; the RMS difference is approximately 3 m s^{-1} at all levels in the nondeveloping and pregenesis profiles, and is maximized at over 10 m s^{-1} at 900 hPa in the postgenesis profile. Similar to the FNL, the RMS differences for moisture and humidity in the NNR are slightly greater for nondeveloping, while for temperature and u- and v-wind, the postgenesis profile is distinguishably greater than both the pregenesis and nondeveloping profile.

Once again, the analyses are separated into those for the inner core (Figure 4.27) and the environment (Figure 4.28). Figures 4.27 and 4.28 indicate that the differences for mixing ratio and humidity are similar between the inner core and environment. In contrast, while the low-level (below 800 hPa) θ and θ_e differences are also similar for both the inner core and environment, at middle to upper levels (above 800 hPa), the inner core θ and θ_e differences are noticeably greater than the environment's in the postgenesis stage. The higher, positive θ (θ_e) difference is attributed to the reanalysis' representation of the inner warm core; on average, the reanalysis anomaly is *cooler* than observed (by, on average, up to 1.5 K). The distribution of θ differences, however, indicates that there are a number of occurrences where the NNR and FNL profiles are *warmer* than observed in the postgenesis inner core; the degree to which the NNR and FNL differ from observations in the postgenesis stage is most likely dependent on the strength of the tropical cyclone. Similar to the FNL, compared to the environment, the differences for the u- and v-wind in the NNR are significantly greater in the postgenesis inner core; the

RMS difference for u- and v-wind is over 10 m s^{-1} (3 m s^{-1} in the environment).

Compared to the NNR, the differences between the ERA Interim reanalysis and observations (Figure 4.29) are *considerably* smaller. In fact, despite the more coarse resolution (1.5°), the differences are somewhat *similar* to the FNL operational analysis (1°). For thermodynamic variables, on average, the ERA Interim appears to be somewhat too dry (less than 0.25 g kg^{-1}; RMS difference is approximately 1.5 g kg^{-1} at low levels and decreases with height), and slightly cooler than observed at all levels (less than 0.5 K; RMSE is 0.75 K for pregenesis and nondeveloping profiles, 1–2 K for postgenesis profiles). This, however, is not systematic among all developing and nondeveloping samples; the distributions indicate just as many occurrences where the ERA is somewhat too moist, and warmer than observed. Similar to the FNL, the small (less than 5%) mean relative humidity difference is misleading; the RMS difference exceeds 10% at nearly all levels (and increases with height), while the ERA is not systematically more or less humid than observed in either developing or nondeveloping profiles. In other words, positive differences (less humid than observations) exceeding 10% occur nearly as frequently as negative (more humid) differences exceeding 10%.

Once again, the ERA Interim profiles are separated into "inner core" (Figure 4.30) and "environment" (Figure 4.31). Overall, the nondeveloping and pregenesis developing profiles exhibit grossly similar differences in the inner core compared to environment; only the developing postgenesis profiles exhibit an increased difference. Figure 4.30 reveals that in the inner core, the ERA Interim representation of the warm core is too cool (on average, 0.5–1.5 K; RMS difference is up to 3 K) and too dry (on average, 0.25–0.5 g kg^{-1}; RMS difference is approximately 1–2 g kg^{-1}); however, as before, this may not be

representative of all developed cases investigated. The inner core u- and v-wind differences are also increased from the environment for postgenesis profiles; the RMS difference has increased up to 5–10 m s^{-1} at all levels in the inner core.

4.4. Summary and Conclusions

This chapter has presented results identifying the thermodynamic properties that distinguish developing from nondeveloping disturbances, as well as the temporal evolution of developing inner core thermodynamic characteristics, using a historical dropsonde dataset that not only includes P-G-I (2010) cases, but also many of the best-sampled genesis cases since 2005. Results indicate that the pregenesis stage of developing disturbances exhibit greater moisture and higher relative humidity at *midlevels* (above 800 hPa) than nondeveloping disturbances, while at low levels (below 800 hPa), the differences are less pronounced. Consistent with some previous observational and numerical tropical cyclogenesis studies (Montgomery et al. 2010; Montgomery and Smith 2012; Smith and Montgomery 2012; Wang et al. 2008), the developing inner core is characterized by a mean midlevel (700–400 hPa) θ_e (water vapor mixing ratio) that is higher than the surrounding environment, and that anomaly *increases slightly* each day before formation; "progressive moistening" quantitatively translates to an increase in mixing ratio at midlevels of approximately 0.5–1 g kg^{-1} per day (depending on the radius definition for inner core) from 4 to 2 days prior to formation, and even less within 2 days of genesis. These results suggest that, at least for the best-sampled developing cases included in the dataset (Karl, Matthew, Nuri, TD2, and Fay), the inner core appears primed (high moisture content and relative humidity) for genesis within 2 days of genesis. In addition, the developing inner core warm anomaly is observed as

many as 3 days prior to genesis at middle to upper levels (above 500 hPa), and extends downward each day through genesis. The time series of relative humidity indicates that, on average, just prior to genesis, the relative humidity reaches 80–85% in the low through mid-troposphere; a high humidity, but not necessarily a "near saturated" troposphere.

Results presented also support the conclusions of Raymond and Sessions (2007) and Raymond et al. (2011), who emphasize that, in a troposphere characterized by deep moisture and saturation, an initially stronger midlevel circulation supports a favorable thermodynamic environment for a bottom-heavy mass flux, and thus primarily low-level convergence and spin-up right before genesis. The composite results (also consistently observed in all of the best-sampled cases, individually) from the dropsonde dataset indicate that within 2 days of genesis, the inner core experiences a slight increase in midlevel moisture and relative humidity, a warm anomaly at upper levels (above 500 hPa), cool anomaly (approximately 1–1.5 K) at low levels (below 900 hPa), and increased low-tropospheric static stability. Within 24 hours of genesis, the low-level wind speed and vorticity increases more rapidly than midlevels, and perhaps as a result of increased latent heat fluxes due to the higher wind speeds, the low-level cool, dry anomaly is removed.

The dropsonde dataset is also utilized to analyze how well the NCEP/FNL analysis and NCEP/NCAR (NNR) and ERA Interim reanalyses, represent the wind and thermodynamic characteristics of nondeveloping, and pre- and postgenesis developing environments. The results indicate that the NCEP FNL operational analysis and ERA Interim reanalysis overall have the smallest differences (for both developing and nondeveloping disturbances), while the NNR reanalysis has substantially larger

differences. One possible explanation for the overall larger differences in the NNR reanalysis may be that the product has the coarsest resolution of the three analyzed (2.5°). Likewise, the FNL analysis may be superior to the NNR reanalysis given that the data assimilation system and dynamical core used to produce the analysis is continually improving, while the reanalysis is produced using a frozen model/data assimilation system. Given the choice between using the ERA Interim and the NNR reanalysis, however, no doubt one should use the ERA Interim since the ERA Interim reanalysis is actually comparable to the FNL analysis, despite a somewhat coarser resolution (1.5° versus 1°). In addition, unlike NCEP, ECMWF is known to have assimilated not only NOAA dropsondes, but also GRIP and PREDICT dropsondes during 2010. In general, for water vapor mixing ratio and humidity, the pregenesis profiles are the closest to observations in both the analysis and reanalyses, while in many cases, the nondeveloping profiles exhibit the greatest differences from observations. In comparison, for potential temperature, equivalent potential temperature, and u- and v-wind speed, the postgenesis profiles are distinguishably greater than the pregenesis and nondeveloping profiles. The differences for the inner core and environment are also compared to one another. In both the analysis and reanalyses, the inner core and environment differences (both developing and nondeveloping) for mixing ratio and humidity tend to be similar. However, for temperature and u- and v-wind speed, while the differences in the analyses and reanalyses in the inner core and environment for pregenesis and nondeveloping profiles are similar, they are distinguishably greater in the postgenesis profiles.

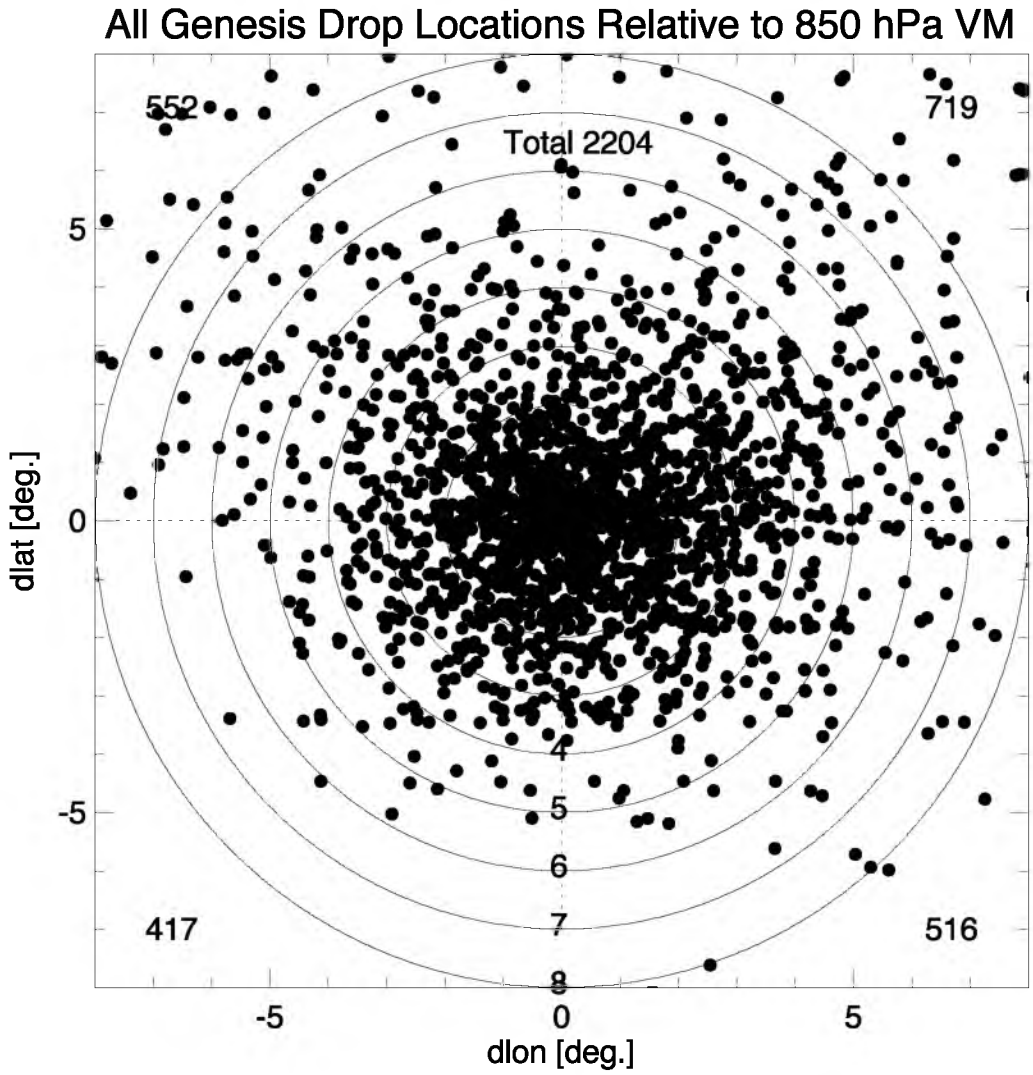

Figure 4.1. Dropsonde locations for developing cases; the total in each quadrant is indicated.

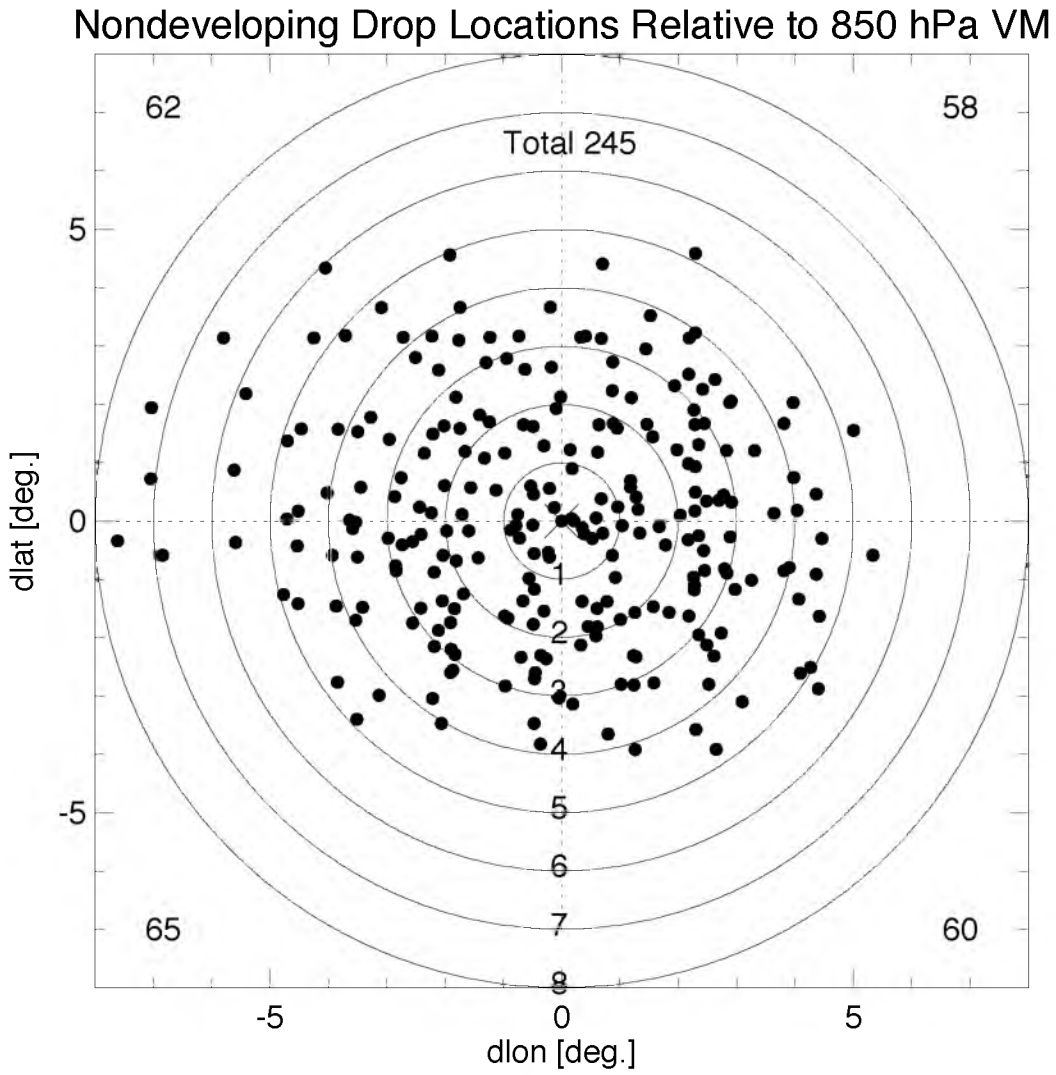

Figure 4.2. Dropsonde locations for nondeveloping cases; the total in each quadrant is indicated.

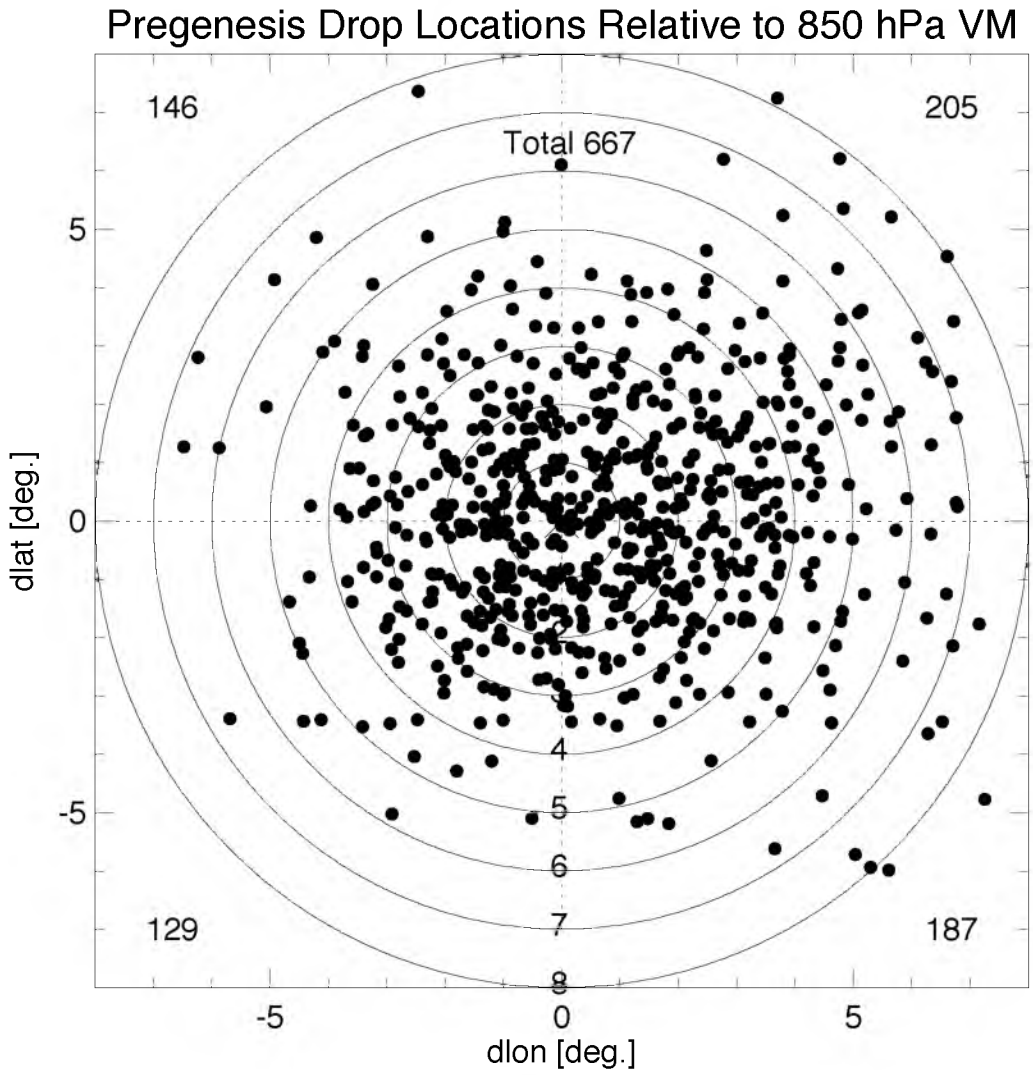

Figure 4.3. Dropsonde locations for the pregenesis stage of developing cases; the total in each quadrant is indicated.

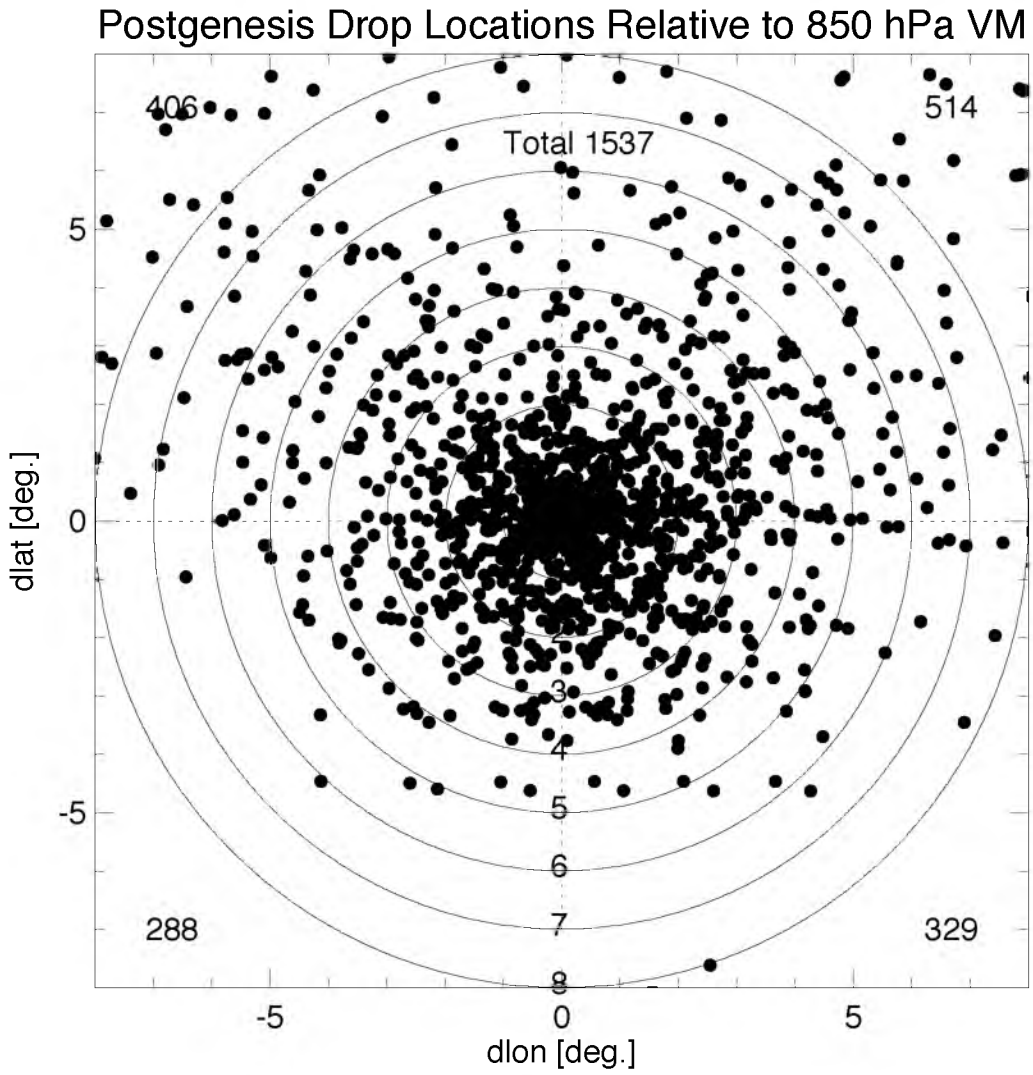

Figure 4.4. Dropsonde locations for the postgenesis stage of developing cases; the total in each quadrant is indicated.

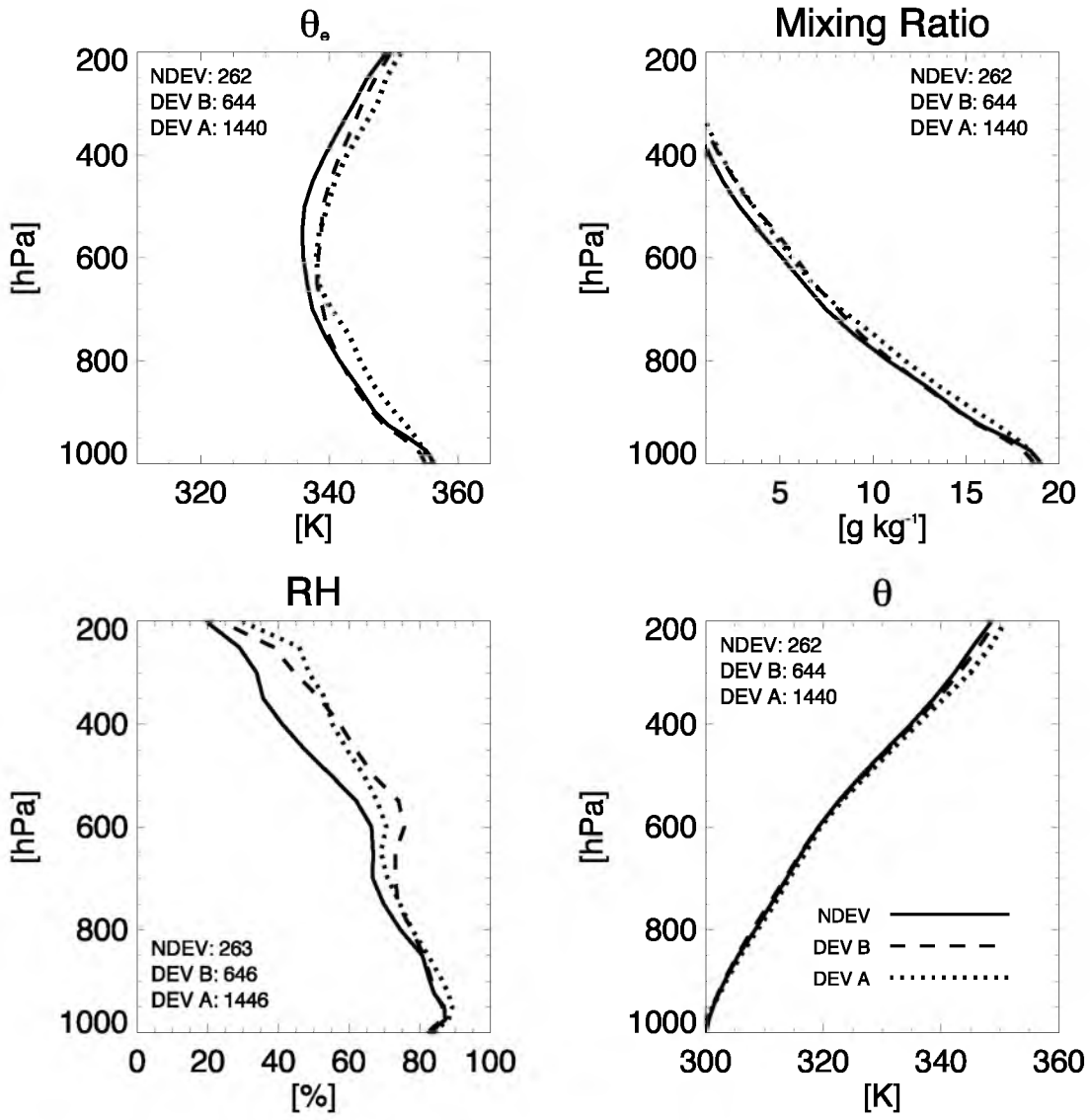

Figure 4.5. Mean vertical profiles of equivalent potential temperature (θ_e), water vapor mixing ratio, relative humidity (RH), and potential temperature (θ) for nondeveloping (solid), developing pregenesis (dashed), and developing postgenesis (dotted). The approximate number of samples for each profile indicated.

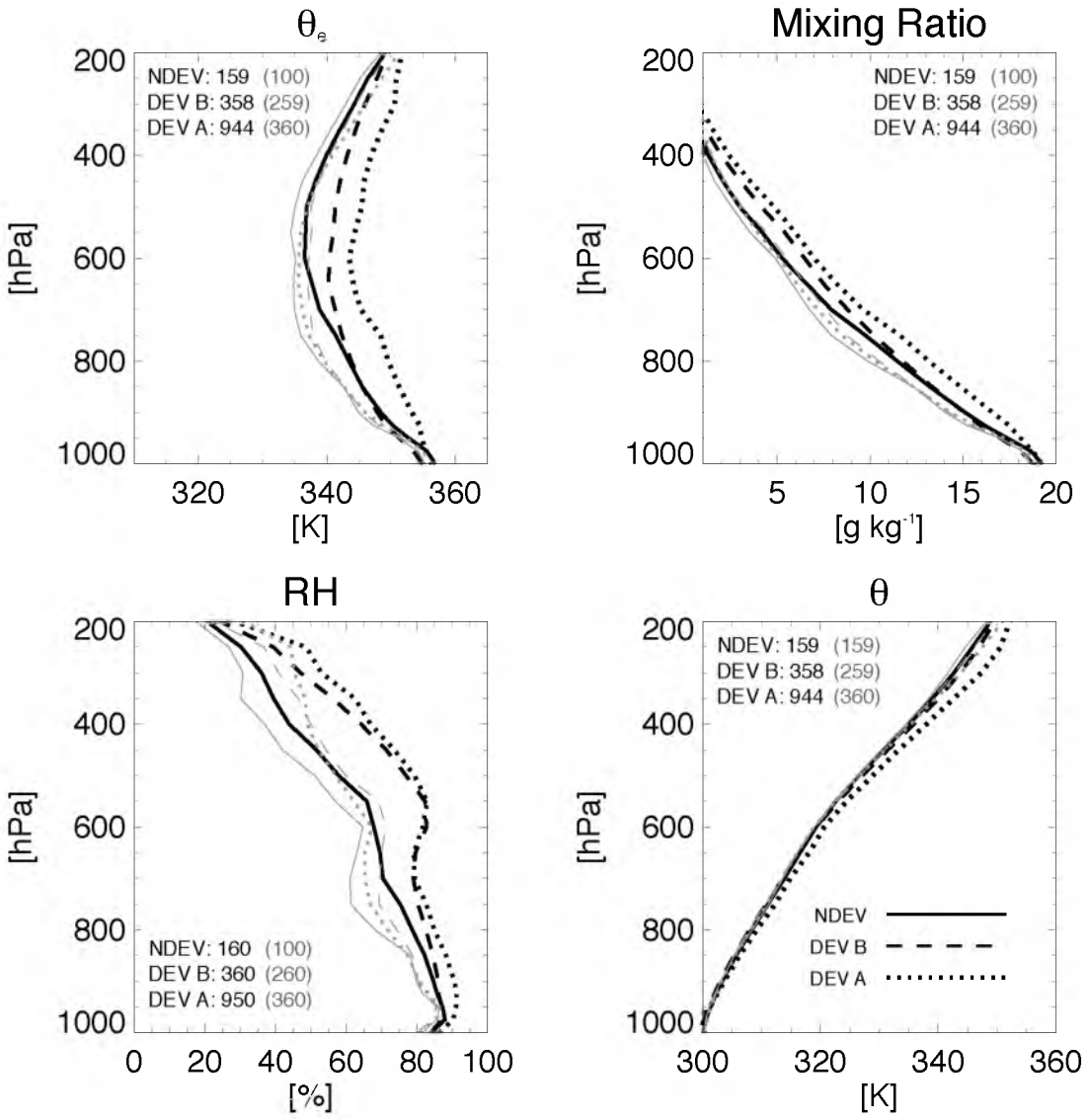

Figure 4.6. Mean vertical profiles of equivalent potential temperature (θ_e), water vapor mixing ratio, relative humidity (RH), and potential temperature (θ) for nondeveloping (solid), developing pregenesis (dashed), and developing postgenesis (dotted). The inner core (0–3°; black) and environment (3–7°; gray) are separated. The approximate number of samples for each profile indicated.

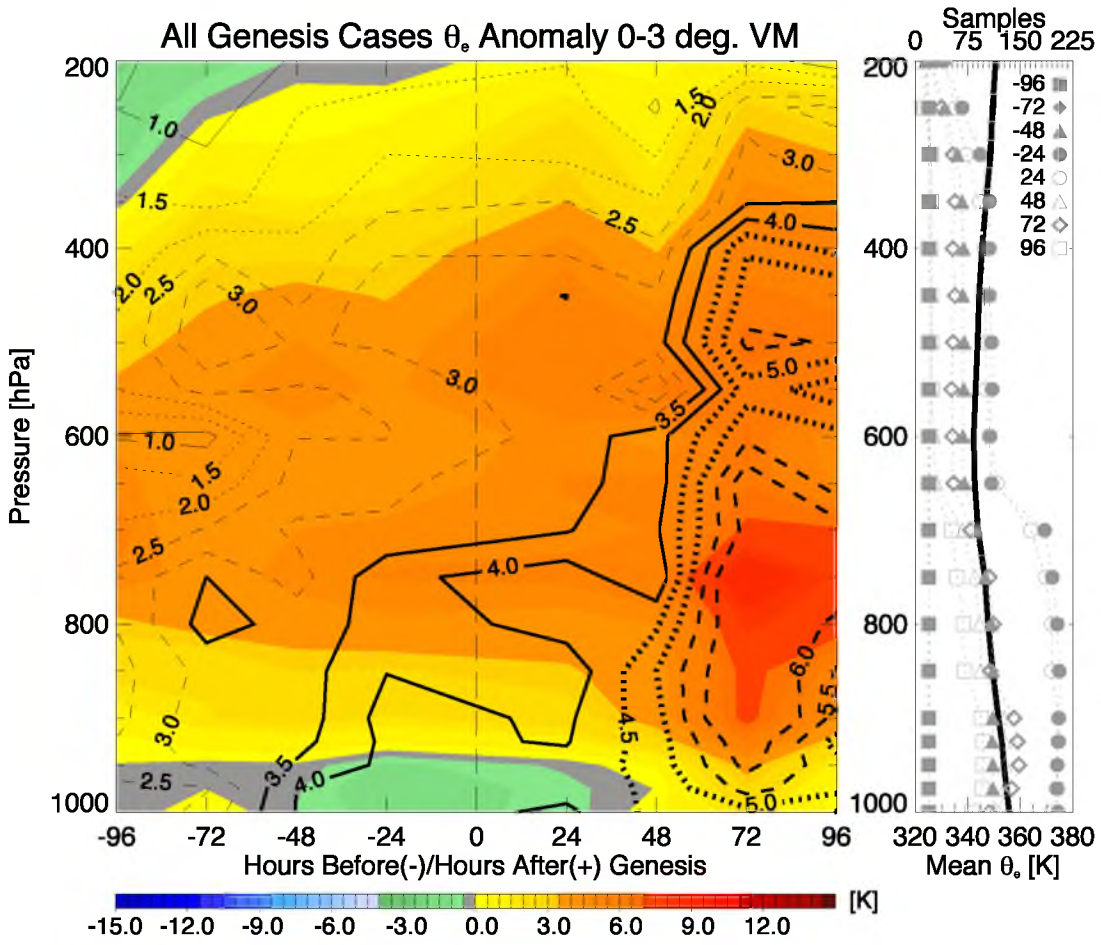

Figure 4.7. Composite θ_e anomaly (color shaded) of all dropsondes within 3° of the 850 hPa VM center for all genesis cases; black contours are standard deviation. Number of samples (gray) at each time, and the mean profile (black) are indicated on the right.

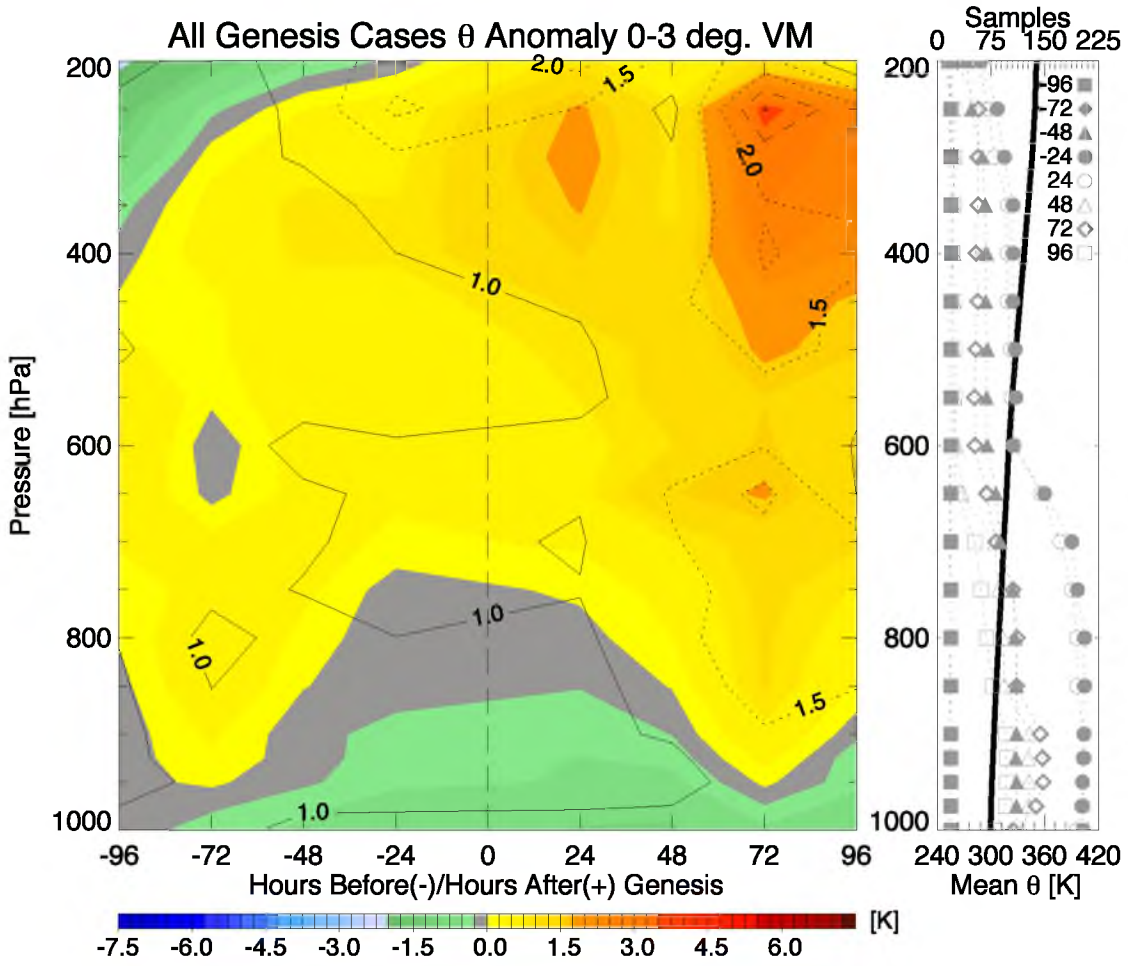

Figure 4.8. Composite θ anomaly (color shaded) of all dropsondes within 3° of the 850 hPa VM center for all genesis cases; black contours are standard deviation. Number of samples (gray) at each time, and the mean profile (black) are indicated on the right.

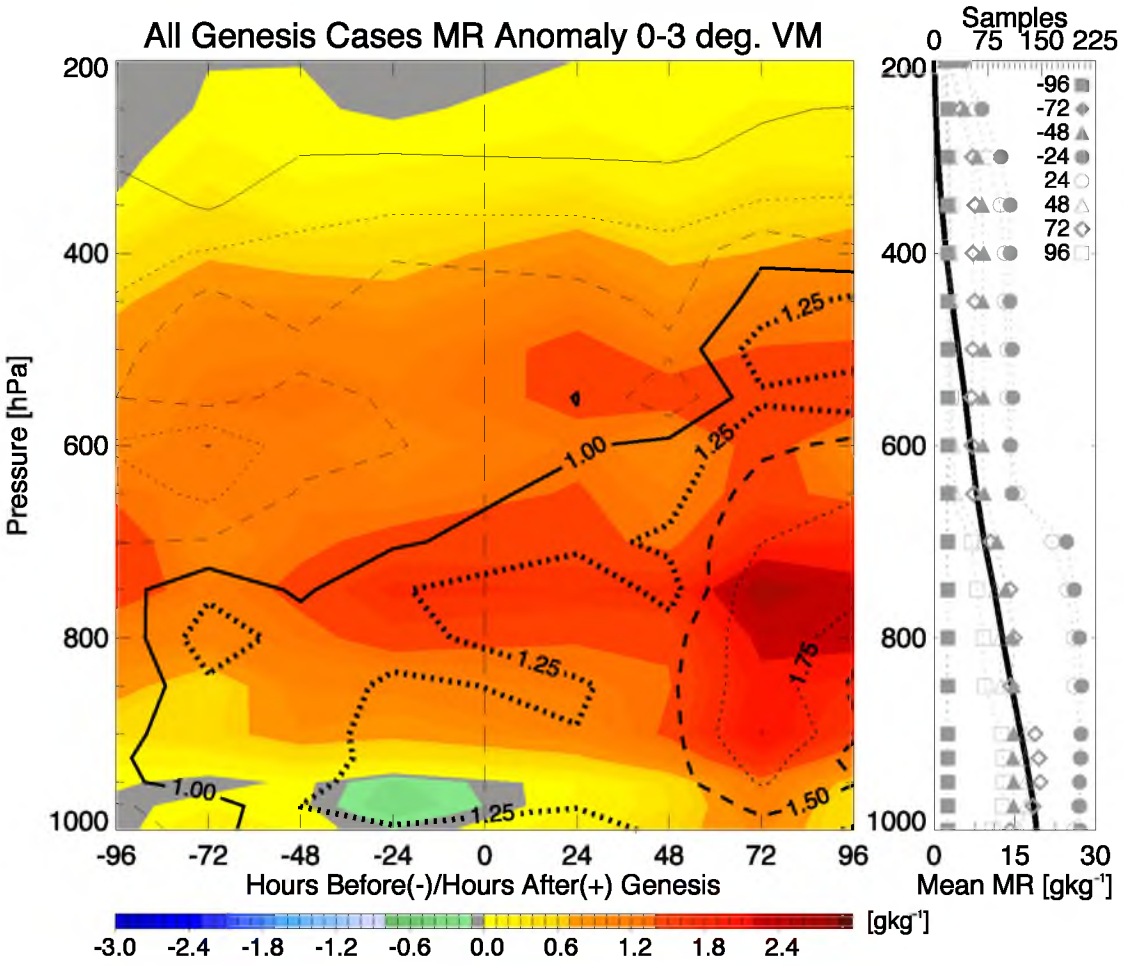

Figure 4.9. Composite water vapor mixing ratio anomaly (color shaded) of all dropsondes within 3° of the 850 hPa VM center for all genesis cases; black contours are standard deviation. Number of samples (gray) at each time, and the mean profile (black) are indicated on the right.

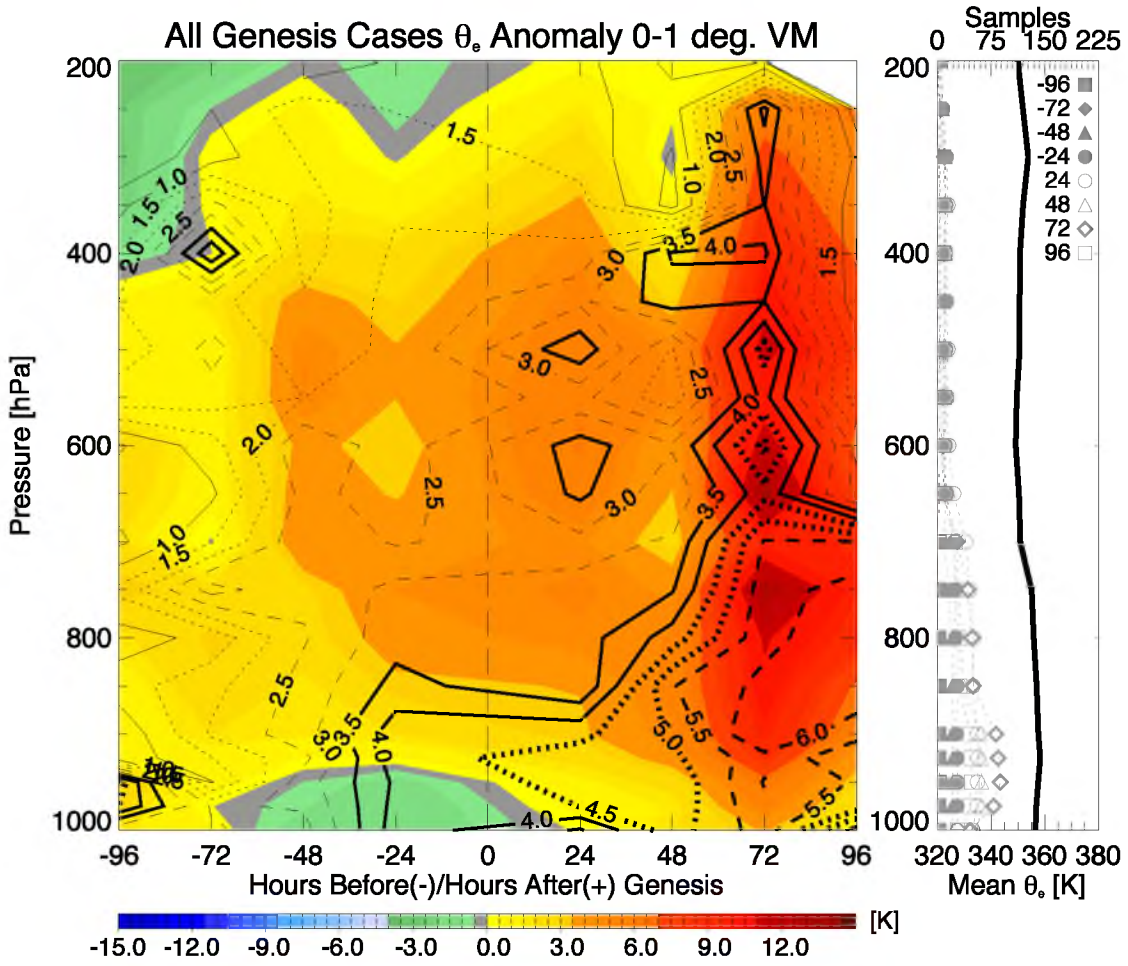

Figure 4.10. Composite θ_e anomaly (color shaded) of all dropsondes within 1° of the 850 hPa VM center for all genesis cases; black contours are standard deviation. Number of samples (gray) at each time, and the mean profile (black) are indicated on the right.

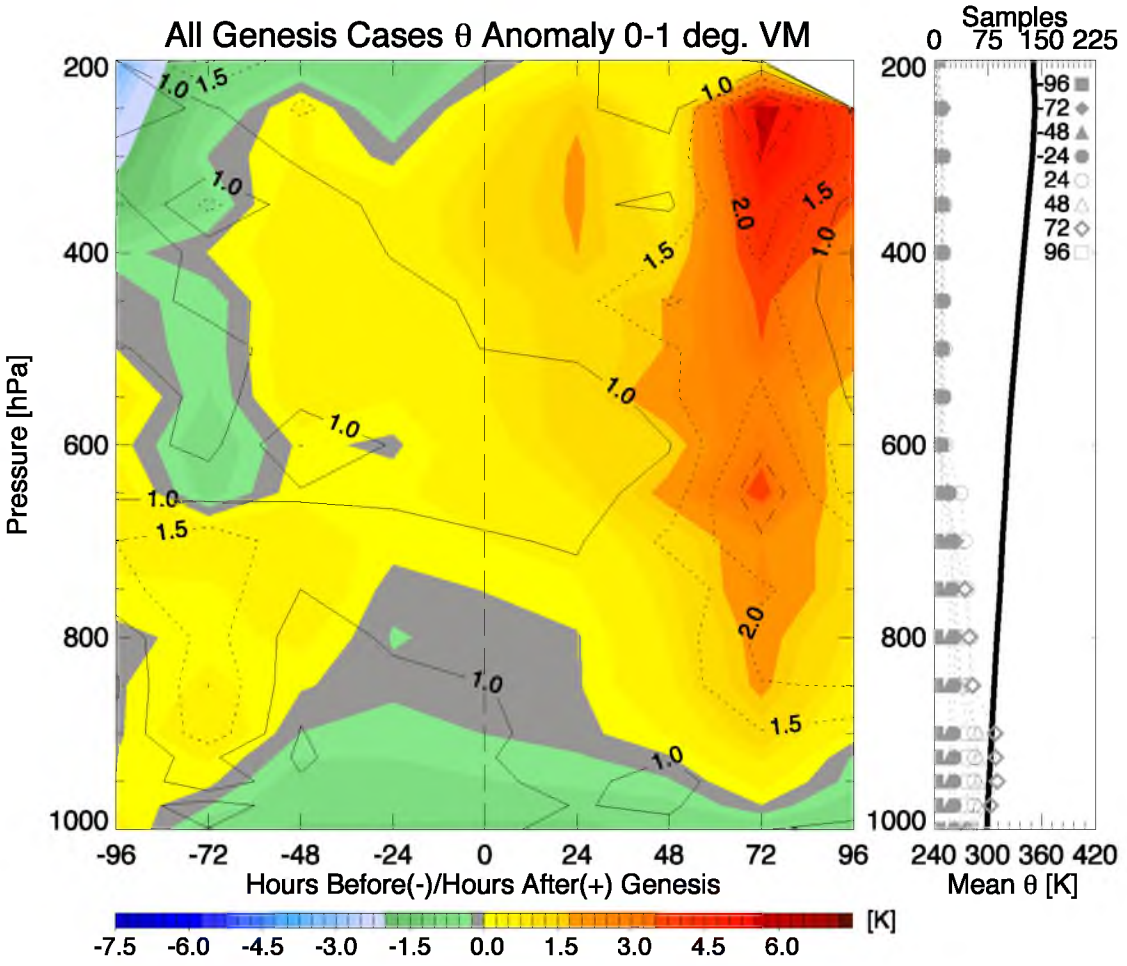

Figure 4.11. Composite θ anomaly (color shaded) of all dropsondes within 1° of the 850 hPa VM center for all genesis cases; black contours are standard deviation. Number of samples (gray) at each time, and the mean profile (black) are indicated on the right.

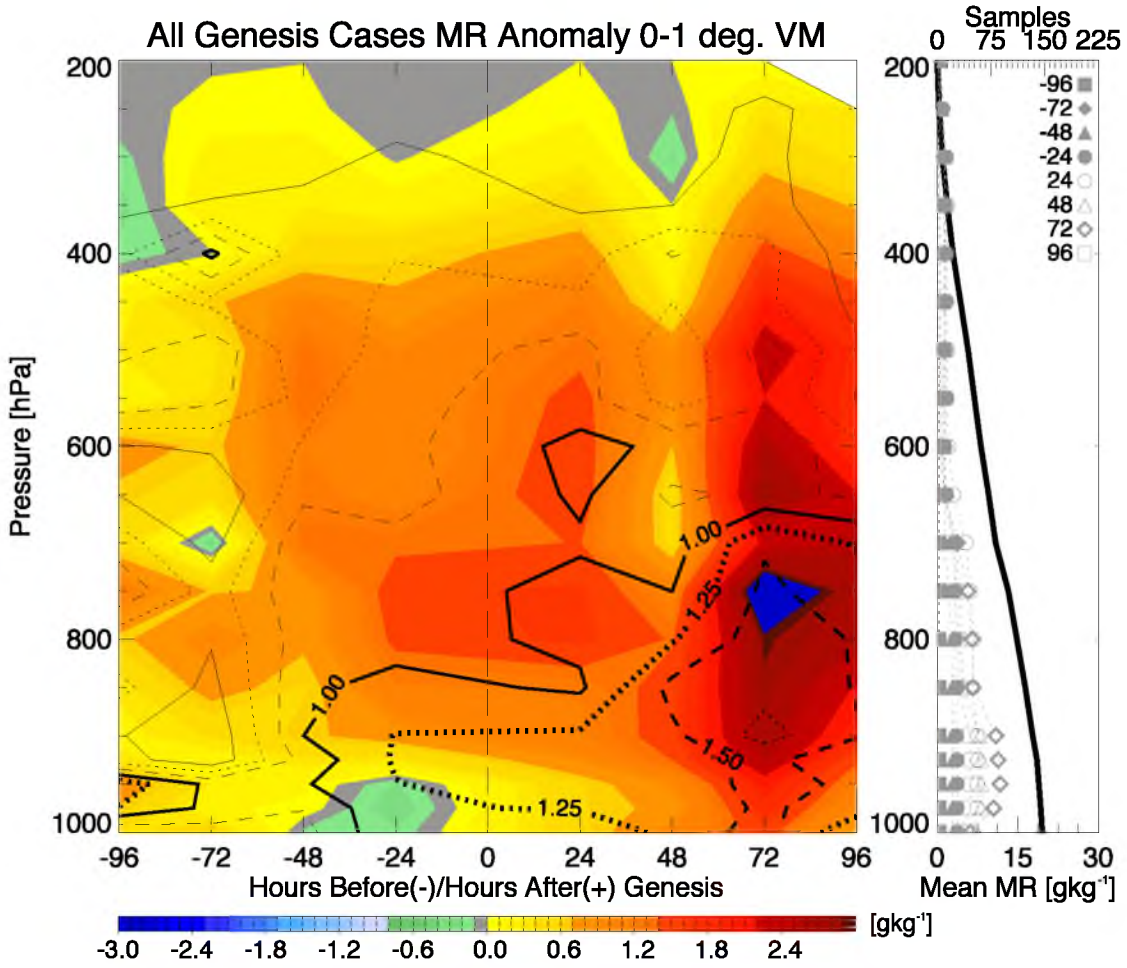

Figure 4.12. Composite water vapor mixing ratio anomaly (color shaded) of all dropsondes within 1° of the 850 hPa VM center for all genesis cases; black contours are standard deviation. Number of samples (gray) at each time, and the mean profile (black) are indicated on the right.

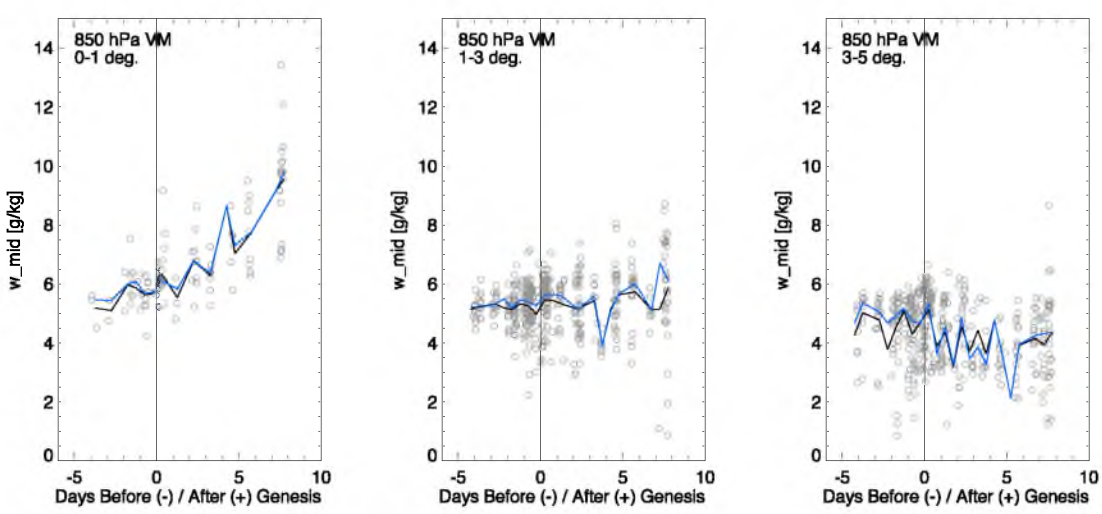

Figure 4.13. Dropsonde midlevel mean (700–400 hPa) mixing ratio within 1°, 1–3°, and 3–5° of the 850 hPa VM center for developing disturbances.

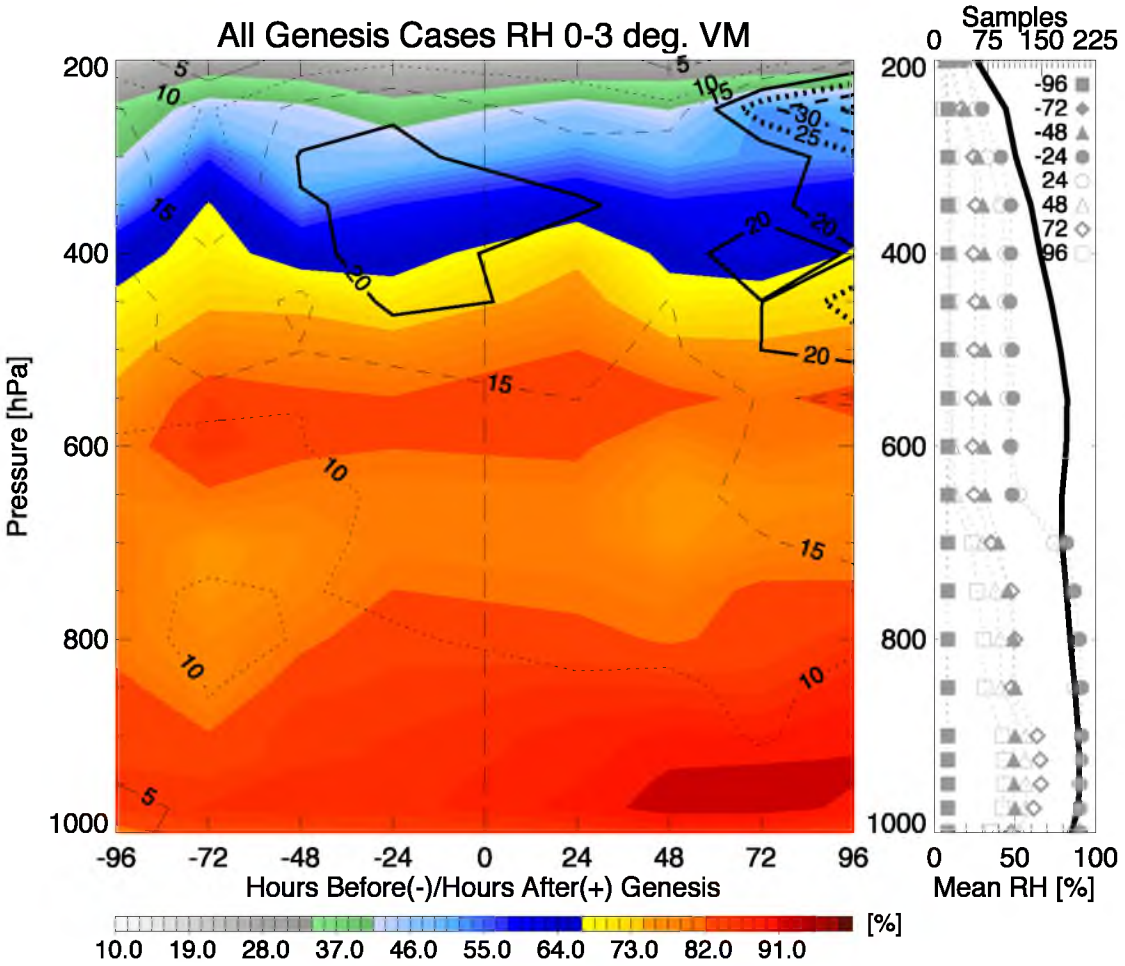

Figure 4.14. Composite relative humidity (color shaded) of all dropsondes within 3° of the 850 hPa VM center for all genesis cases; black contours are standard deviation. Number of samples (gray) at each time, and the mean profile (black) are indicated on the right.

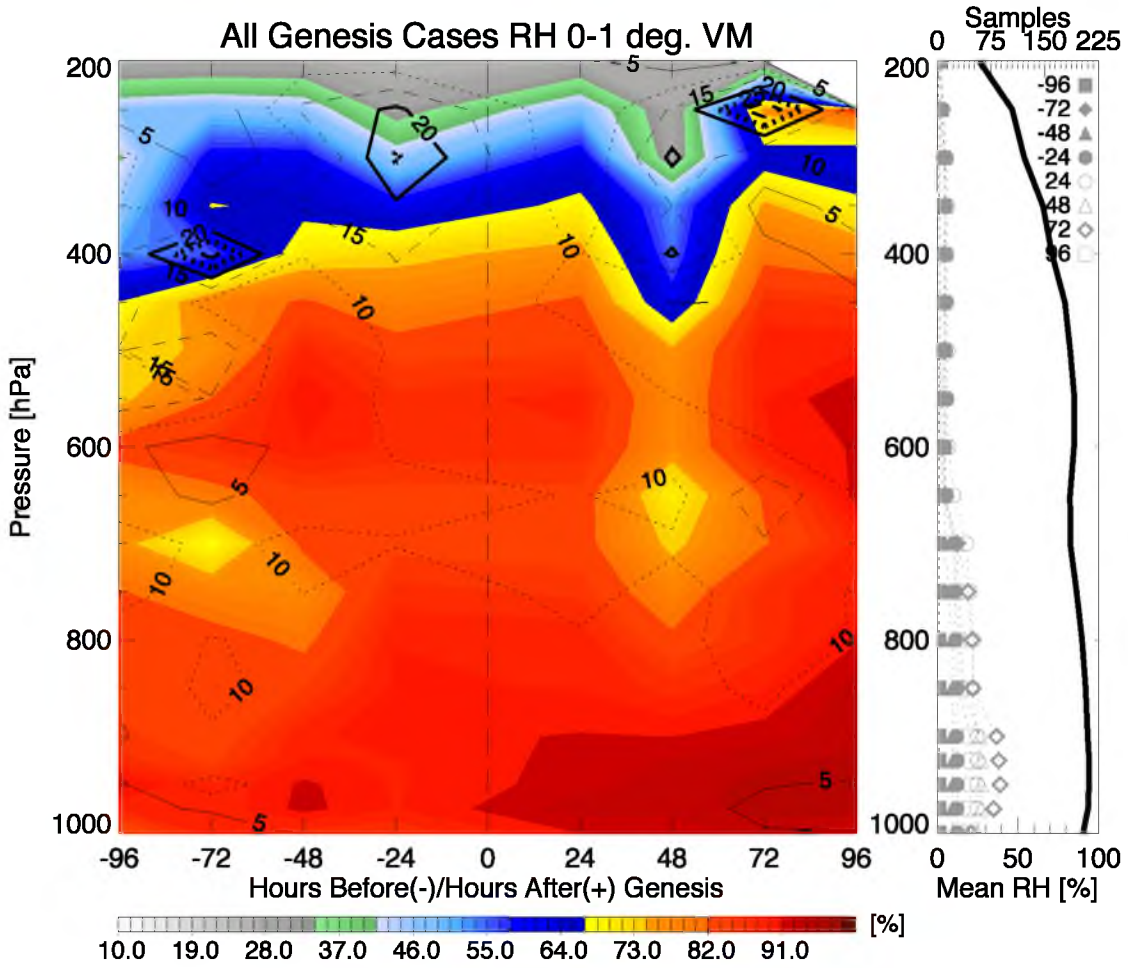

Figure 4.15. Composite relative humidity (color shaded) of all dropsondes within 1° of the 850 hPa VM center for all genesis cases; black contours are standard deviation. Number of samples (gray) at each time, and the mean profile (black) are indicated on the right.

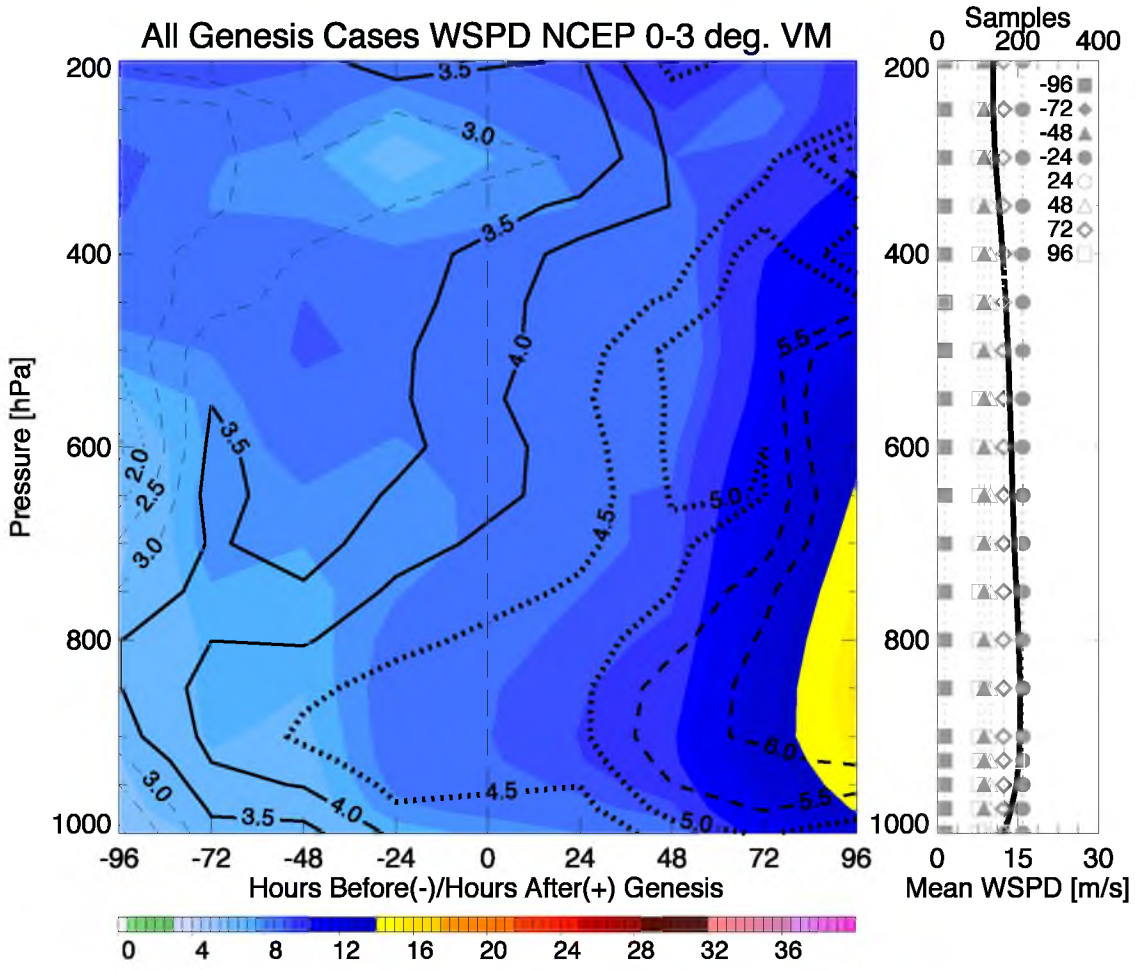

Figure 4.16. Composite wind speed (color shaded) of all dropsondes within 3° of the 850 hPa VM center for all genesis cases; black contours are standard deviation. Number of samples (gray) at each time, and the mean profile (black) are indicated on the right.

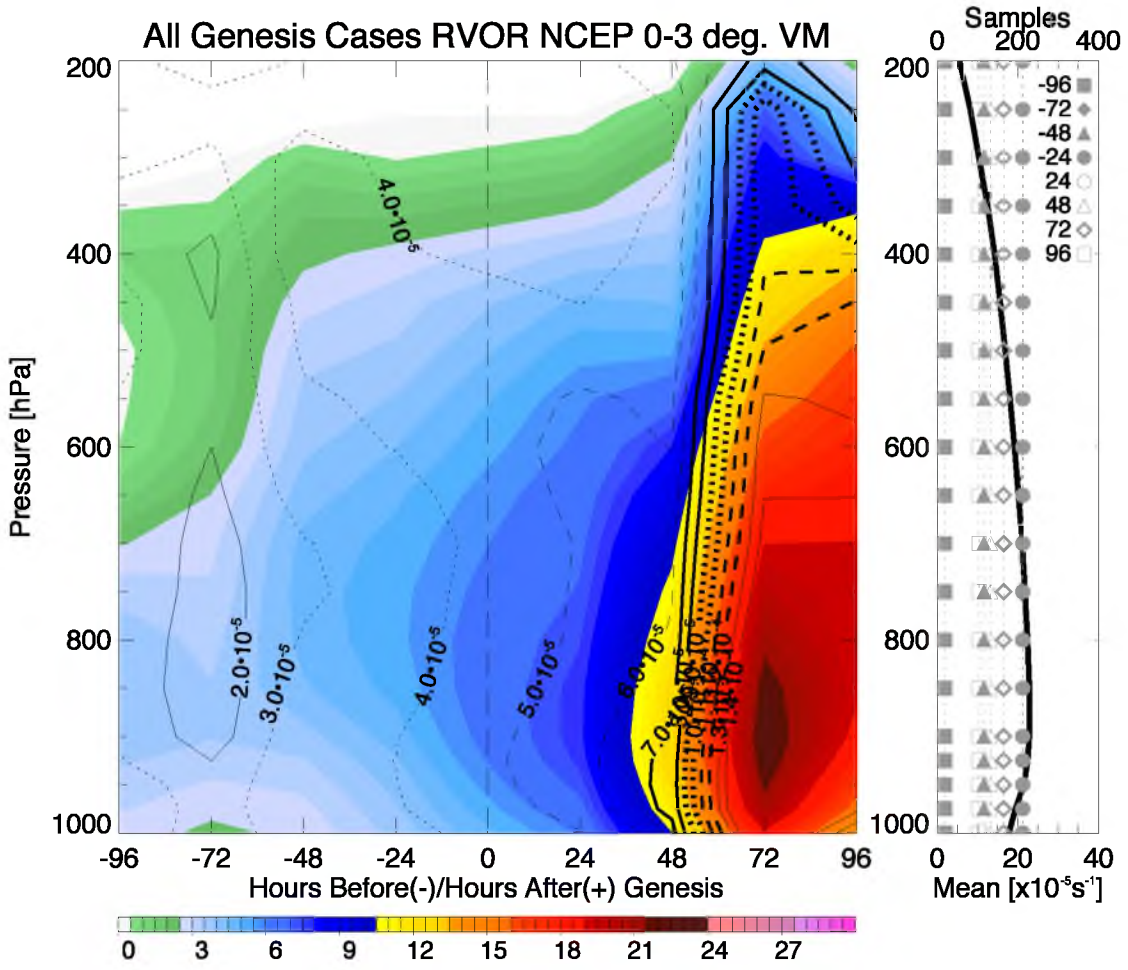

Figure 4.17. Composite NCEP relative vorticity (color shaded) of all dropsondes within 3° of the 850 hPa VM center for all genesis cases; black contours are standard deviation. Number of samples (gray) at each time, and the mean profile (black) are indicated on the right.

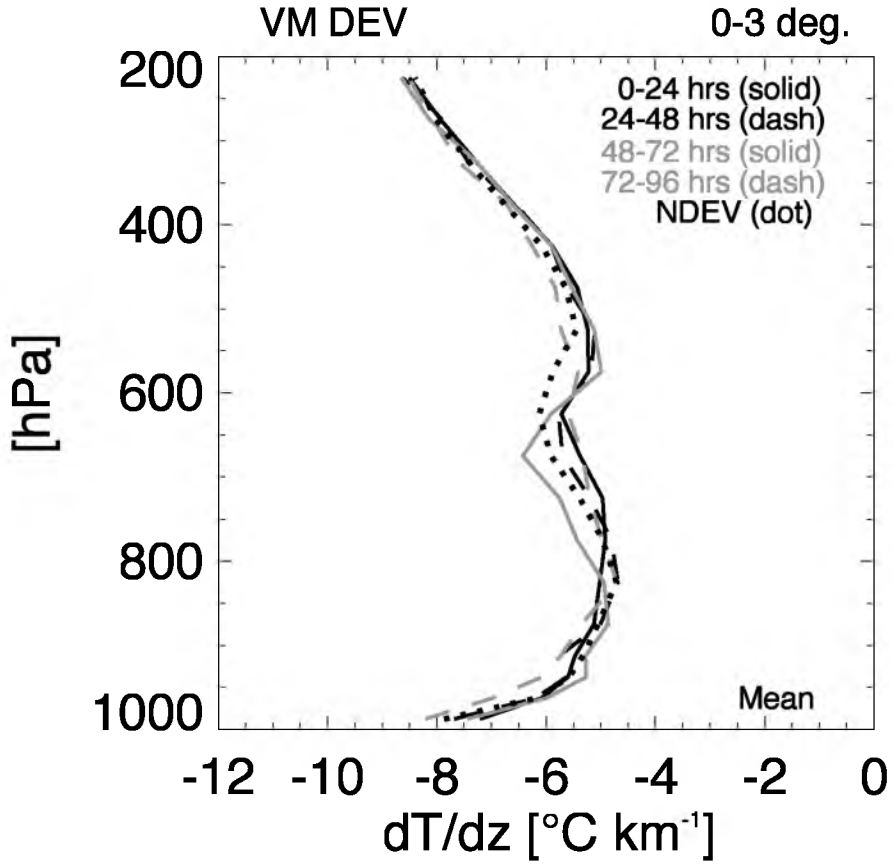

Figure 4.18. Mean temperature lapse rate profiles for developing disturbances for periods 0–24 hours before genesis (solid, black), 24–48 hours before (dashed, black), 48–72 hours before (solid, gray), 72–96 hours before (dashed, gray); the nondeveloping mean profile is also shown (dotted).

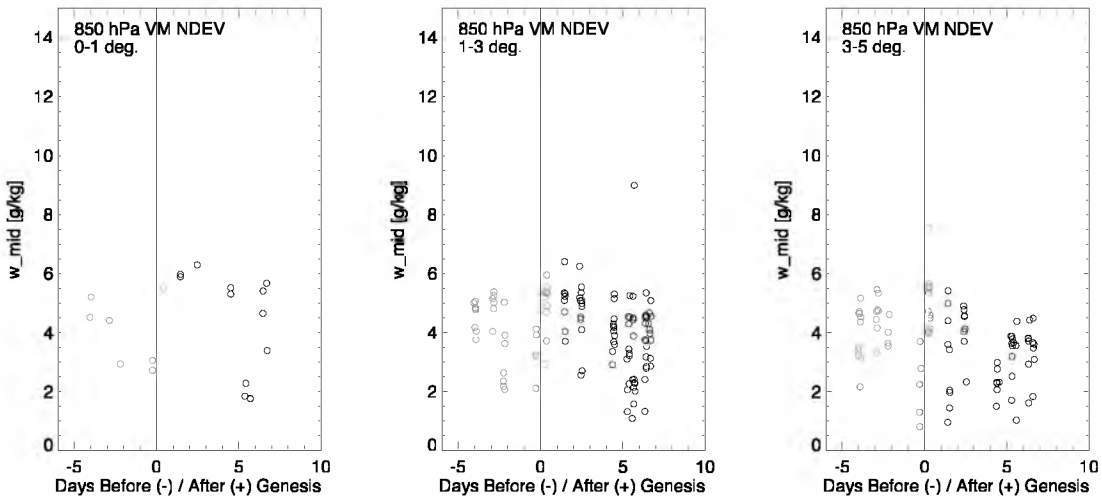

Figure 4.19. Dropsonde midlevel mean (700–400 hPa) mixing ratio within 1°, 1–3°, and 3–5° of the 850 hPa VM center for nondeveloping disturbances; black dots are ex-Gaston dropsondes, gray are all other nondeveloping disturbances.

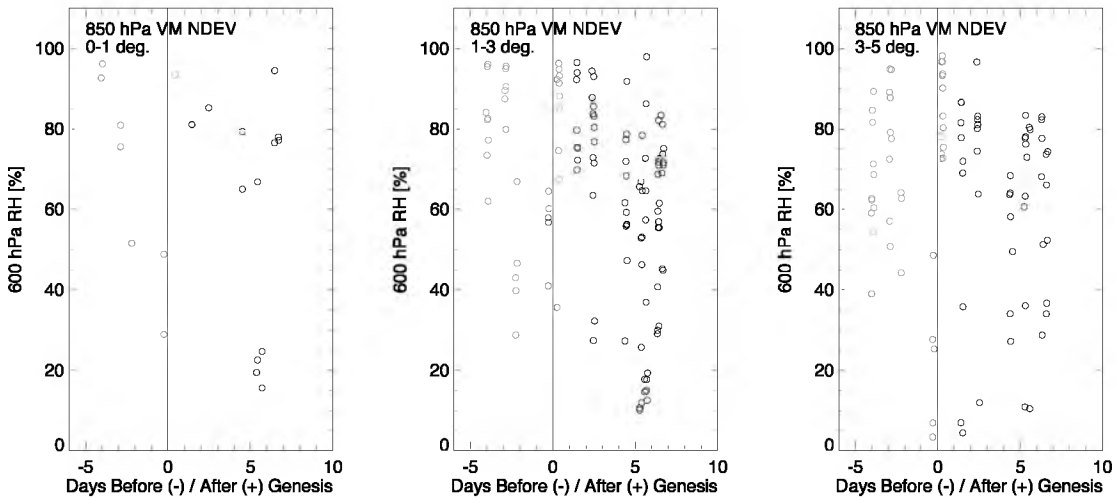

Figure 4.20. Dropsonde 600 hPa relative humidity within 1°, 1–3°, and 3–5° of the 850 hPa VM center for nondeveloping disturbances; black dots are ex-Gaston dropsondes, gray are all other nondeveloping disturbances.

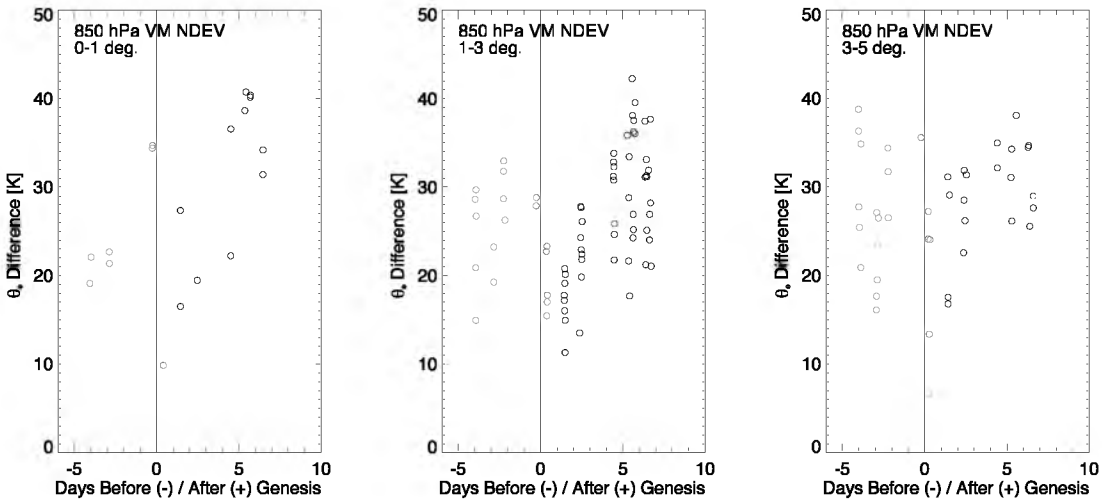

Figure 4.21. Dropsonde difference between the surface θ_e and midlevel θ_e minimum within 1°, 1–3°, and 3–5° of the 850 hPa VM center for nondeveloping disturbances; black dots are ex-Gaston dropsondes, gray are all other nondeveloping disturbances.

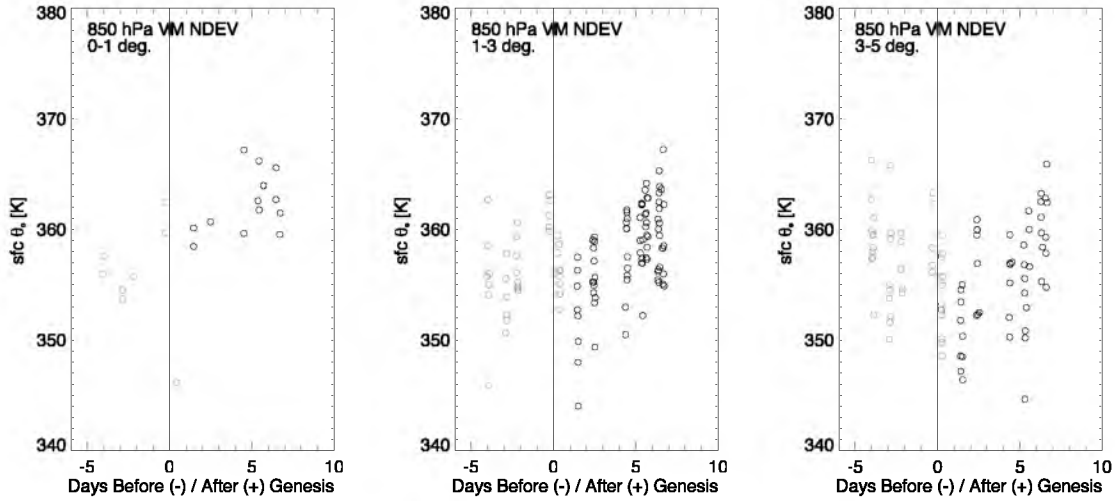

Figure 4.22. Dropsonde surface θ_e within 1°, 1–3°, and 3–5° of the 850 hPa VM center for nondeveloping disturbances; black dots are ex-Gaston dropsondes, gray are all other nondeveloping disturbances.

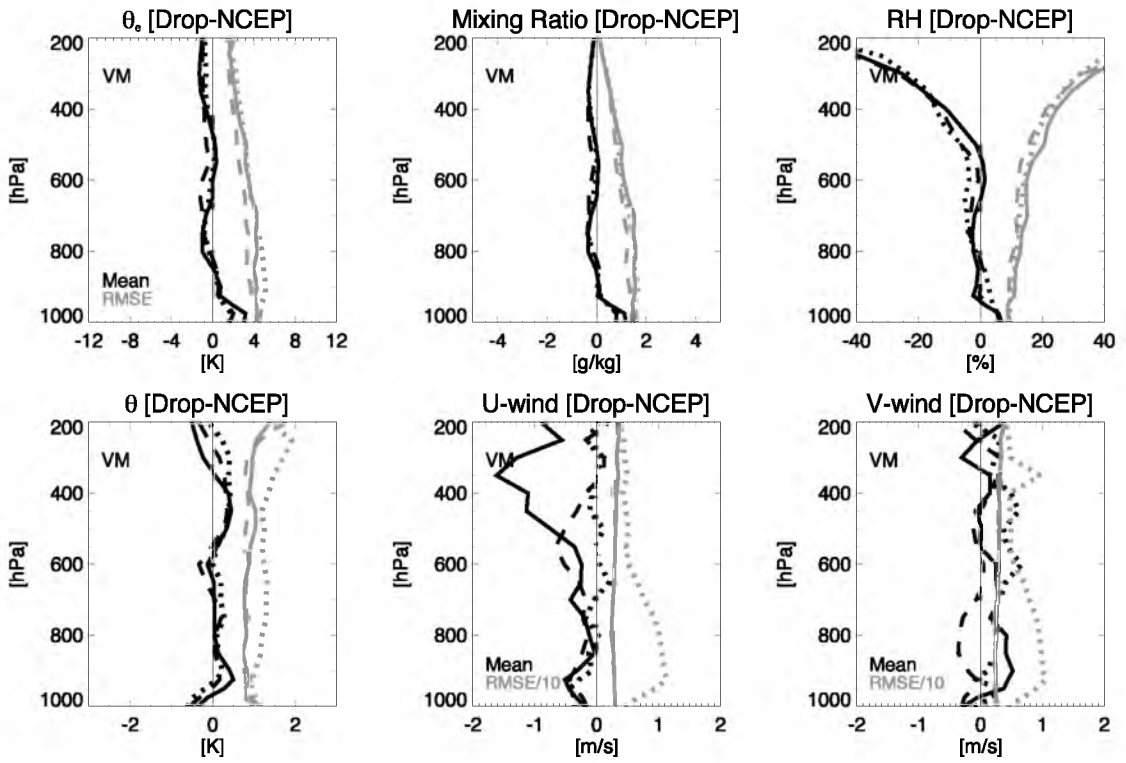

Figure 4.23. Mean (black) and RMS (gray) vertical profile of the difference between the dropsonde observations and NCEP FNL for equivalent potential temperature (θ_e), water vapor mixing ratio, relative humidity (RH), potential temperature (θ), u-wind speed, and v-wind wind speed for nondeveloping disturbances (solid), developing pregenesis (dashed), and developing postgenesis (dotted).

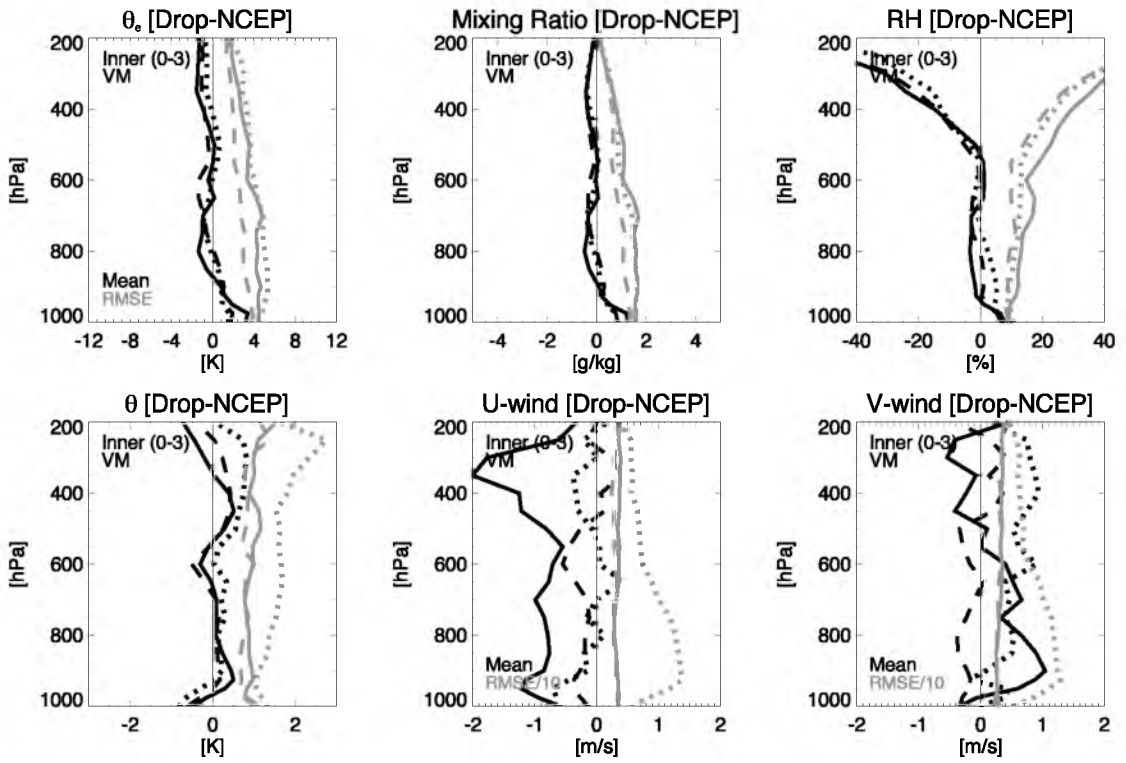

Figure 4.24. Mean (black) and RMS (gray) vertical profile of the difference between the inner core (0–3°) dropsonde observations and NCEP FNL for equivalent potential temperature (θ_e), water vapor mixing ratio, relative humidity (RH), potential temperature (θ), u-wind speed, and v-wind wind speed for nondeveloping disturbances (solid), developing pregenesis (dashed), and developing postgenesis (dotted).

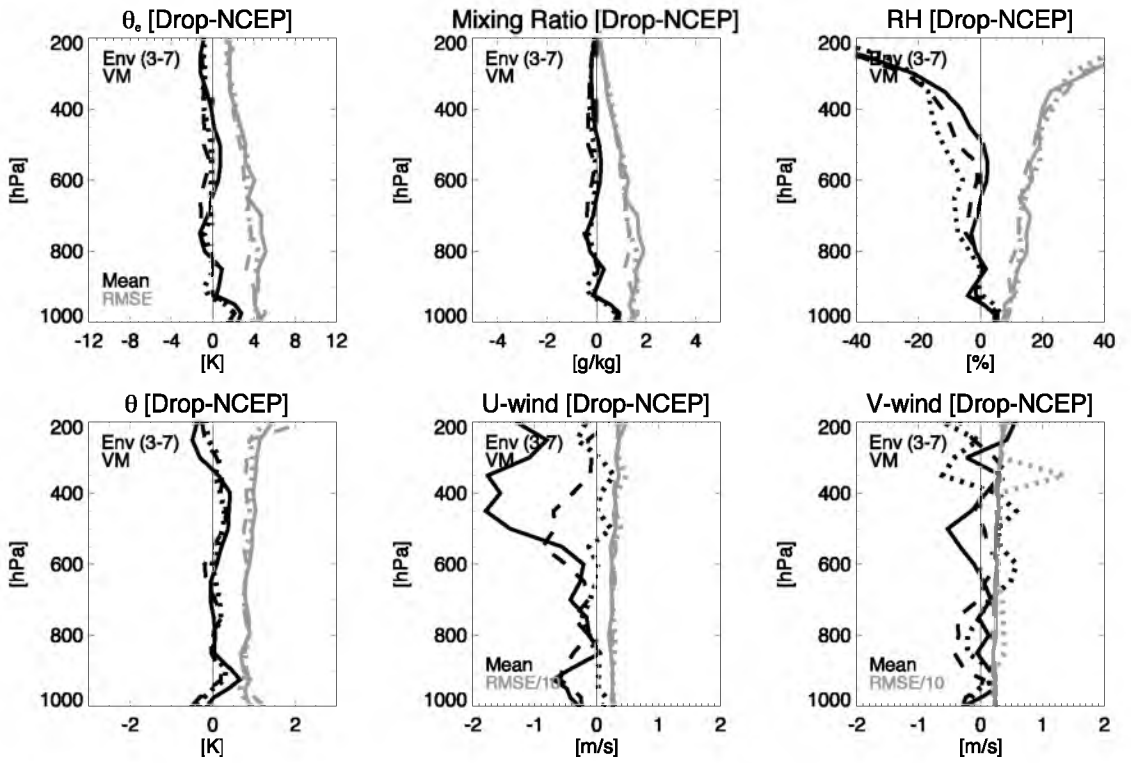

Figure 4.25. Mean (black) and RMS (gray) vertical profile of the difference between the environmental (3–7°) dropsonde observations and NCEP FNL for equivalent potential temperature (θ_e), water vapor mixing ratio, relative humidity (RH), potential temperature (θ), u-wind speed, and v-wind wind speed for nondeveloping disturbances (solid), developing pregenesis (dashed), and developing postgenesis (dotted).

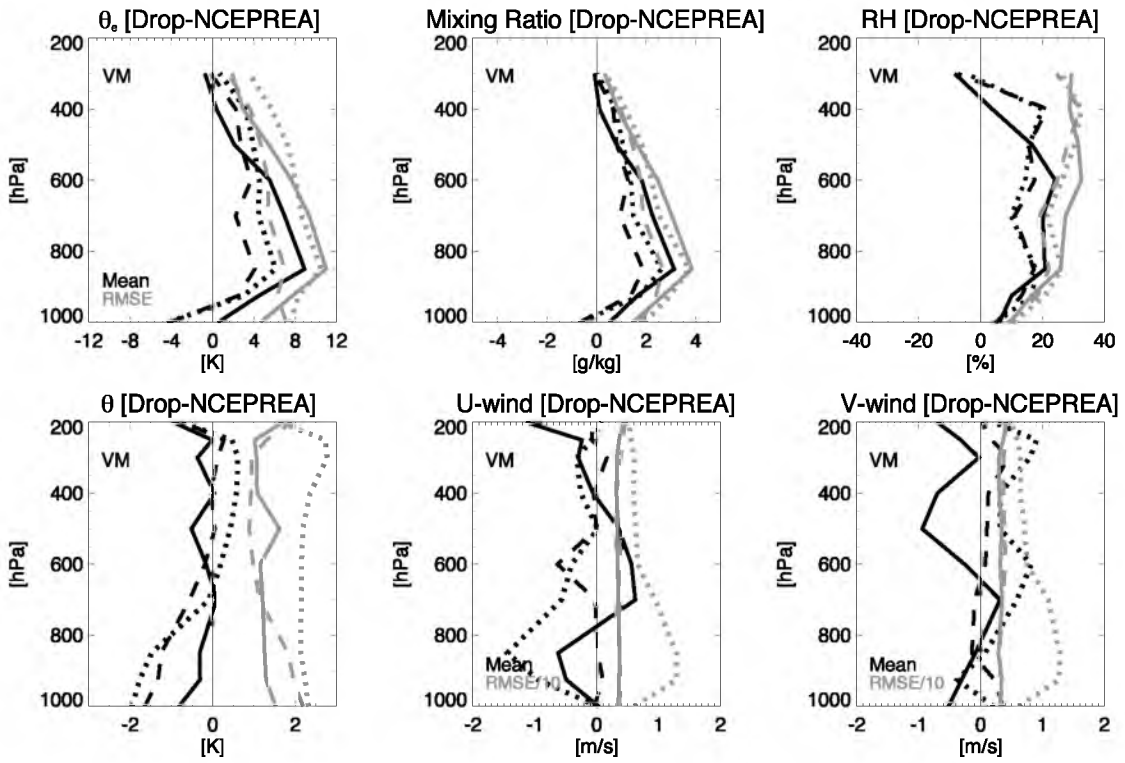

Figure 4.26. Mean (black) and RMS (gray) vertical profile of the difference between the dropsonde observations and NCEP/NCAR reanalysis for equivalent potential temperature (θ_e), water vapor mixing ratio, relative humidity (RH), potential temperature (θ), u-wind speed, and v-wind wind speed for nondeveloping disturbances (solid), developing pregenesis (dashed), and developing postgenesis (dotted).

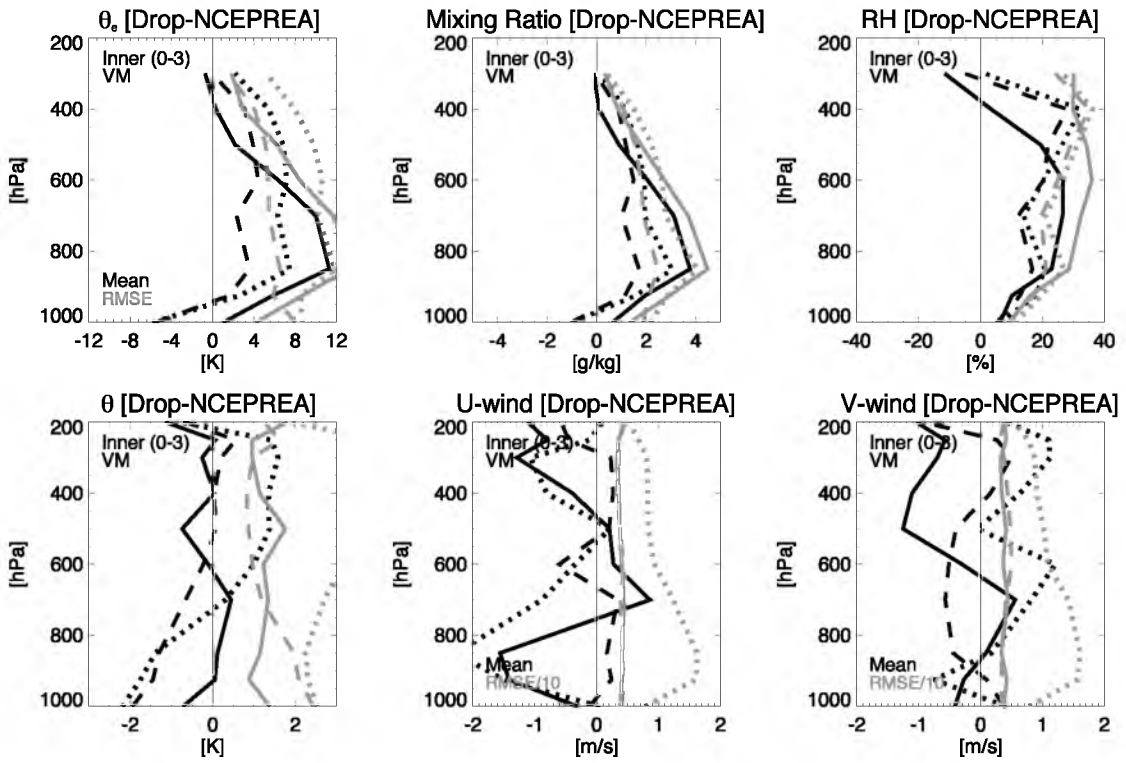

Figure 4.27. Mean (black) and RMS (gray) vertical profile of the difference between the inner core (0–3°) dropsonde observations and NCEP/NCAR reanalysis for equivalent potential temperature (θ_e), water vapor mixing ratio, relative humidity (RH), potential temperature (θ), u-wind speed, and v-wind wind speed for nondeveloping disturbances (solid), developing pregenesis (dashed), and developing postgenesis (dotted).

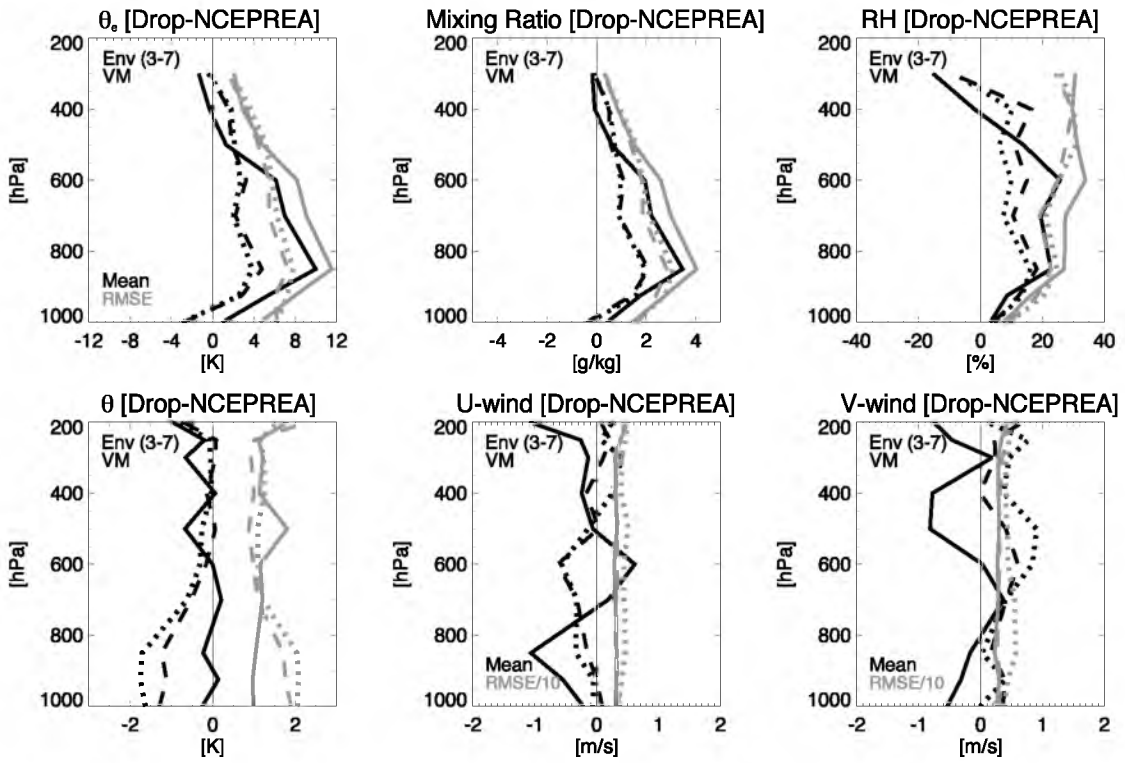

Figure 4.28. Mean (black) and RMS (gray) vertical profile of the difference between the environmental (3–7°) dropsonde observations and NCEP/NCAR reanalysis for equivalent potential temperature (θ_e), water vapor mixing ratio, relative humidity (RH), potential temperature (θ), u-wind speed, and v-wind wind speed for nondeveloping disturbances (solid), developing pregenesis (dashed), and developing postgenesis (dotted).

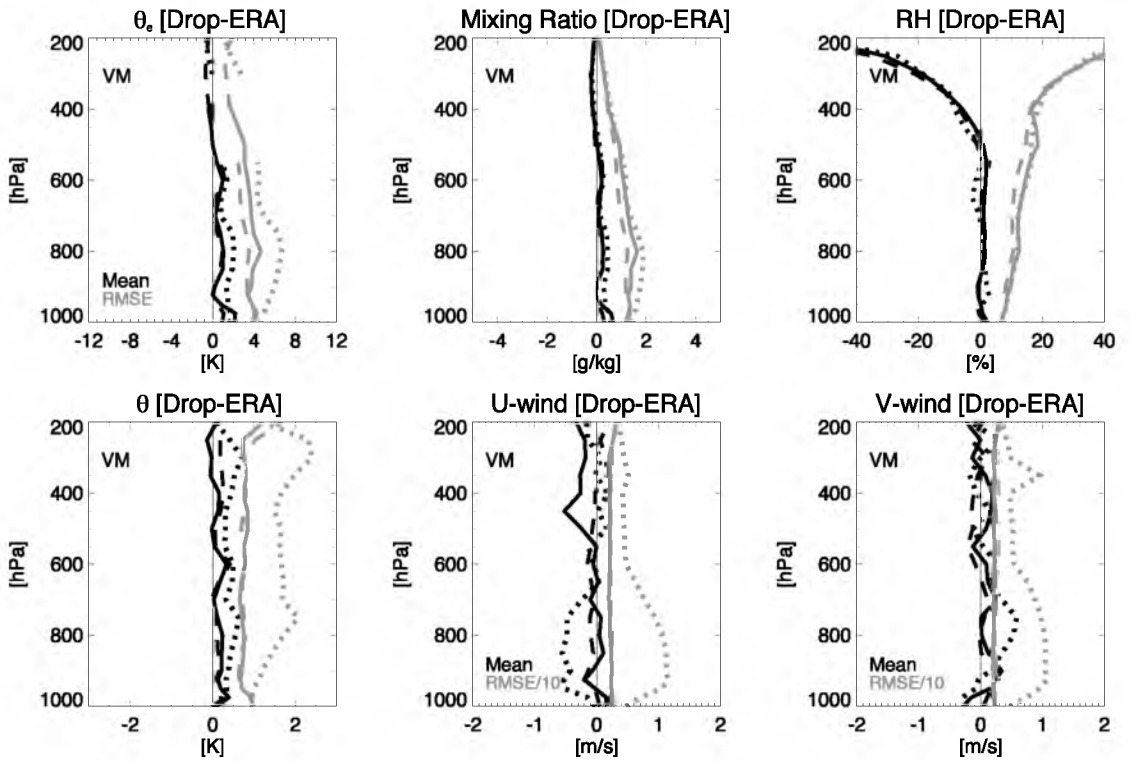

Figure 4.29. Mean (black) and RMS (gray) vertical profile of the difference between the dropsonde observations and ERA Interim reanalysis for equivalent potential temperature (θ_e), water vapor mixing ratio, relative humidity (RH), potential temperature (θ), u-wind speed, and v-wind wind speed for nondeveloping disturbances (solid), developing pregenesis (dashed), and developing postgenesis (dotted).

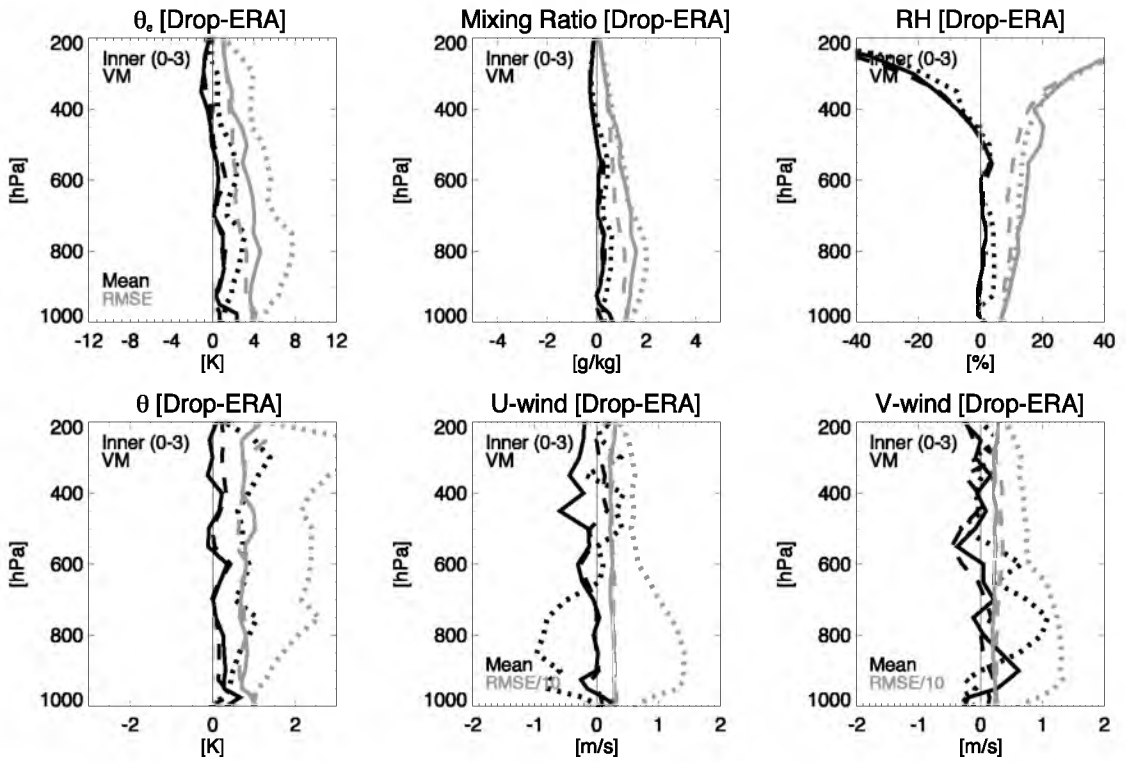

Figure 4.30. Mean (black) and RMS (gray) vertical profile of the difference between the inner core (0–3°) dropsonde observations and ERA Interim reanalysis for equivalent potential temperature (θ_e), water vapor mixing ratio, relative humidity (RH), potential temperature (θ), u-wind speed, and v-wind wind speed for nondeveloping disturbances (solid), developing pregenesis (dashed), and developing postgenesis (dotted).

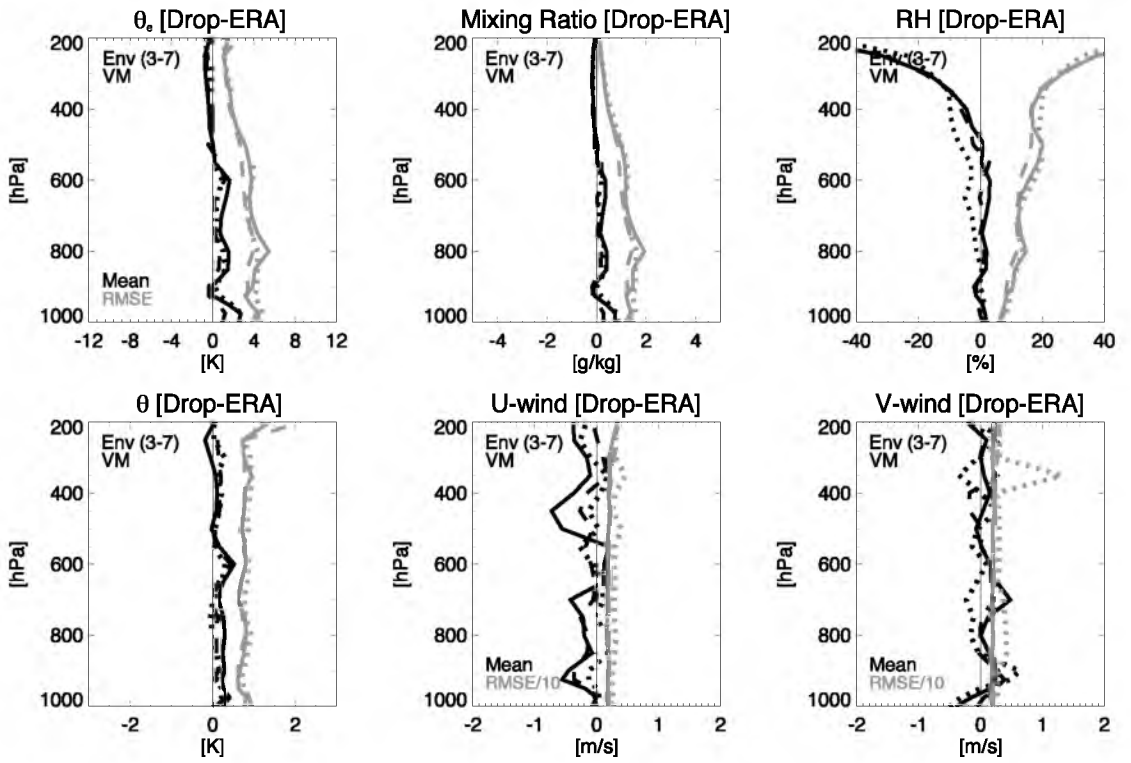

Figure 4.31. Mean (black) and RMS (gray) vertical profile of the difference between the inner core (3–7°) dropsonde observations and ERA Interim reanalysis for equivalent potential temperature (θ_e), water vapor mixing ratio, relative humidity (RH), potential temperature (θ), u-wind speed, and v-wind wind speed for nondeveloping disturbances (solid), developing pregenesis (dashed), and developing postgenesis (dotted).

CHAPTER 5

CASE STUDIES OF DEVELOPING AND NONDEVELOPING TROPICAL DISTURBANCES

5.1. Introduction

The previous chapter showed the evolution of the inner core moisture, relative humidity, and temperature during the genesis process through compositing dropsondes from multiple tropical cyclogenesis cases sampled by field campaigns, as well as reconnaissance and surveillance flights by NOAA and USAF aircraft. Composite results indicate that during the days before genesis, developing disturbances may already be primed for formation, the inner core is anomalously warm and moist at midlevels (which also distinguished the developing disturbance from nondevelopers), and quantitatively, there is only a slight "progressive moistening." This chapter seeks to build on describing the time evolution of thermodynamic properties, while also describing the time evolution of pregenesis convective systems examined by multiple satellite and aircraft platforms.

When combined with information on environmental variables from the NCEP FNL operational analysis, and the vortex evolution from in-situ measurements, the time evolution of convective and thermodynamic properties will offer insight into what ultimately determines the fate of disturbances with apparent genesis potential. Given the number of coincident and consecutive flights achieved in Karl, Matthew, and ex-Gaston, these cases represent the best opportunities to combine in-situ and satellite measurements

to relate precipitation to the thermodynamic and vortex evolution. Cases studies presented in this chapter will strategically combine data from *multiple* aircraft investigations with data from not only conventional infrared (IR), but also overpasses from *multiple* passive microwave (PMW) platforms. The continuity of observations from both aircraft and satellite platforms should help elucidate the properties of MCSs involved in organizing the circulation, as well as offer insight into where and when the vortex originates (low or midlevels) and how the timing of intensification relates to convective activity and thermodynamic changes occurring in the inner core environment. Although they do not provide nearly the same quantity of dropsonde data as the other cases, satellite data from cases such as Fiona, Fay, Nuri, and Danny will offer additional opportunities to compare and contrast properties of pregenesis convective systems, and determine which properties may be most necessary to genesis.

The following questions will be addressed in the compilation of 11 developing and four nondeveloping disturbances (Table 3.1; ex-TD5 and Nicole are not included for reasons explained in Chapter 3.1):

1) What properties of the large-scale environment are favorable for genesis? What is the time evolution of vorticity maxima and, in particular, how long prior to genesis does a midlevel vortex appear?

2) Is there is a systematic increase in moisture during the formation process? If so, by how much and at what levels? Quantitatively, does the inner core of the disturbance moisten after each convective episode?

3) What is the time evolution of the mesoscale convective systems and do they have credible connections to circulations at multiple scales?

4) What convective properties are most critical to the formation process? Convective properties will include raining area, intensity, area of intense convection, duration, and the proximity to the center.

In this chapter, section 2 will describe the datasets and additional methodology related to the case studies; sections 3 and 4 will offer results from individual developing and nondeveloping case studies, respectively; sections 5 and 6 will combine environmental and convective statistics for all cases; and finally, section 7 will offer a summary of the key findings.

5.2. Data and Methodology

As in the previous chapter, the center of the disturbance is defined by the vorticity maximum (VM) manually tracked in the 1°x1° NCEP FNL model analyses (see Chapter 3.2 for more information on tracking). Although 925, 700, and 600 hPa VMs are also tracked, the analyses presented are based on the 850 hPa VM center. Environmental parameters from the operational analysis will include relative humidity, relative vorticity, deep-layer (850–200 hPa) vertical wind shear, daily genesis potential, and the Rossby radius of deformation. With the exception of vertical wind shear, which is computed for a 2–8° annulus around the center, environmental parameters will be averages for the inner core (either 1 or 3°), which will be defined appropriately when presented.

As before, the results for the pouch (when actually present) do not differ significantly from those for the vorticity maxima, and therefore will not be shown. The pouch analysis can be less reliable, and certainly more difficult to interpret since in many cases, a coherent pouch is not tracked throughout the pregenesis period. Because this study computes a daily phase speed, rather than one that is representative of the entire

lifetime of the wave, disturbances often exhibit phase speeds outside of the "typical" range of 4–8 m s^{-1}, and the pouches are more difficult to identify in the co-moving framework. Other examples where pouches are difficult to identify are: waves that exhibit a highly tilted/elongated wave axis (not classically oriented north-south); disturbances that originate near monsoon circulations (such as off the West African coast) or the ITCZ, which appear as east-west elongated circulations; and waves with primarily north/northwestward movement (thus, small zonal phase speed) that do not already have a clear circulation. In the latter situation, since the meridional phase speed is not included in determining the co-moving framework, unless a closed circulation appears in the Eulerian framework, a closed pouch is most likely not present. Regardless, genesis is unfavorable to occur in many of these scenarios since wave vorticity is primarily from shear rather than curvature.

In-situ observations shown will come from dropsondes (from the dataset described in the previous chapter). TPW is also computed for dropsondes; to calculate TPW the dropsonde must reach a minimum pressure level of at least 400 hPa, a maximum of 975 hPa, and have a considerable fraction of data available between those levels. The case studies will also include brightness temperature (T_B) statistics from conventional IR, polarized corrected temperatures (PCT) and derived TPW from PMW satellites (including AMSR-E, TRMM, and SSM-I(S) 15–17), derived TPW from AIRS, and rainfall from TRMM 3B42 (see Chapter 3.4 for additional information on the satellite datasets). Given the limited width, not all swaths from PMW instruments will completely cover the inner core. To account for this in the analyses, the fractional coverage of data within the inner core is computed for each overpass. Overpasses are

only selected when brightness temperature data are available within 0.5° of the VM center; this ensures that for most overpasses included, the fractional coverage of data within the inner core is at least 40%. A similar threshold is required for the PMW-derived TPW product; although one additional difficulty for this dataset is that data do not exist over land, and thus gaps exist that are not otherwise present in the original brightness temperature data. The fractional coverage from AIRS is allowed to be lower since data in raining areas are excluded; as expected, because precipitation is prominent in developing disturbances, few AIRS overpasses are ultimately included.

The "proximity of rainfall" will be based on the radial distance of the raining pixel from the 850 hPa VM/pouch center. "Duration" is approximated by the percentage of the pregenesis stage where the total raining fraction within the inner core is above 40%. Convective intensity will be approximated from the minimum IR T_B and minimum/mean PCT (computed for pixels $\leq$ 250 K) from PMW overpasses of the center. The area of intense convection will be approximated by the fraction of pixels within the inner core that are below a certain IR threshold (such as 235 and 210 K IR T_B), below an 85–91 GHz PMW PCT threshold (such as 250 K), as well as from the fraction of "convective" rain rates (rain rate $\geq$ 5 mm hr^{-1}) from TRMM 3B42.

5.3. Individual Case Results: Developing Disturbances

5.3.1. Karl (2010)

Karl was classified a tropical depression at 1200 UTC on 14 September near 82°W, 17.5°N. Beginning on 9 September, the low (925–850 hPa) and midlevel (700–600 hPa) vorticity maxima tracks are shown in Figure 5.1. While the midlevel vorticity appears to originate from a wave over the central Atlantic, the low-level vorticity

originates in the monsoon region just off the South American coast. The tracks indicate a substantial misalignment of the low- and midlevel vorticity maxima in the NCEP FNL early in the track. By 13 September, low- and midlevel centers become better aligned, and remain so through formation. Seventeen total flights by dropsonde-equipped PGI and USAF aircraft investigated Karl in the 5 days up to, and including, formation. The evolution of the low-level (925 hPa) and midlevel (600 hPa) wind field from dropsonde observations, as well as accumulated rainfall (from 3B42), for the period between 10 and 15 September is shown in Figure 5.2. Days before genesis, on 9 and 10 September, a distinct low-level circulation is observed; however, formation is considered unlikely given the substantial misalignment (not collocated) of the low- and midlevel centers. By 12 September, the disturbance appears less organized; the low-level circulation is no longer apparent and the wave trough appears asymmetric since southeasterly winds on the east side of the trough axis are stronger than the northeasterly winds on the west side (the wave axis appears to have a SW-NE horizontal tilt). Only when the vorticity maxima align, and the winds became more symmetric on 13 September, did the wave vorticity come predominately from curvature, rather than from shear, and thus be more favorable for formation.

Figure 5.3 shows the time evolution of 235K IR cloud fraction as a function of the radius from 850 hPa VM center. This figure indicates that Karl's convection exhibits a distinct diurnal cycle before formation, and convection only persists through the diurnal cycle after reaching tropical storm intensity. In fact, as may be surmised in both Figures 5.3 and 5.4 (similar to Figure 5.3, except for azimuthally averaged rain rate), prior to formation, the most widespread, "intense" convective episode occurs *3 days* before

genesis (maximum around 1800 UTC on 11 September). Dropsonde observations (Figure 5.4) for the most recent PREDICT G-V flight (centered around 1200 UTC 12 September) after this episode suggest that convection did little to organize a circulation at low or midlevels. Each subsequent convective episode after 11 September, although still intense (mean rain rate $\geq$ 5 mm hr^{-1}), has *less* areal coverage and is *farther* from the VM center. The inner core statistics are consistent with these results as the time series of raining fraction ('RR' in Figure 5.3b) and "convective" raining fraction ('RR5' is the fraction of all pixels with an "convective" rain rate, $\geq$ 5 mm hr^{-1}; 'CRR5' is the fraction of all *raining* pixels that have an "convective" rain rate) indicates a *decrease* in areal coverage in each episode during the 3 days leading up to formation. Despite apparently less rainfall occurring near the center, dropsonde observations from flights on 13 and 14 September do indicate some organization at both low and midlevels; however, whether the convection is responsible for the circulation and alignment at low or midlevels is unclear.

To further characterize the intensity of each convective episode, PCT statistics from TMI, AMSR-E, and SSM-I(S) overpasses of the VM are computed (Figure 5.3c). According to the minimum and mean PCT (for pixels $\leq$ 250 K), no convective event is noticeably more intense than any other prior to formation. In fact, the final convective episode before formation (around 1800 UTC on 13 September) is characteristically the *least* intense; the fractional coverage of pixels $\leq$ 250 K is nearly 10% less, and minimum PCT as much as 40 K warmer, than previous episodes. Considering that the most "favorable" convective event (in terms of raining area, intensity, and proximity to the center) is 3 days prior to formation, and that the total raining/convective area in each

episode is decreasing in the days that follow, one may surmise that the formation of Karl is more closely tied to the low- and midlevel vorticity/pouch alignment than any single distinguishing characteristic in the convective episodes. Except for the fact that it occurs in a more organized disturbance, compared to previous episodes, there does not appear to be anything "special" about the convective episode occurring in the day prior to genesis.

Synthesizing the information given by the dropsondes, IR, and PMW overpasses, one can attempt to identify a relationship between convective episodes and moisture content in pre-Karl's inner core. Figure 5.5d shows the PMW-derived TPW from AMSR-E, TMI, SSM-I(S), and AIRS, as well as the median TPW computed from dropsondes for each DC-8 and G-V flight. Also shown in Figure 5.5d is the mean midlevel (700–400 hPa) water vapor mixing ratio from dropsondes, and for comparison, NCEP FNL model analysis. To truly evaluate if convection has increased moisture content, one must evaluate the properties during the minimum in the diurnal cycle. Figure 5.5d indicates that after an initial increase (~ 4 kg m^{-2}) in TPW on 10 September, the inner core exhibits only a slight increasing trend on subsequent days. Likewise, during each minimum in the diurnal cycle, the dropsonde-derived midlevel water vapor mixing ratio shows only a slight increase (approximately 0.25 g kg^{-1} per day) over the previous minimum. It appears that once the TPW of pre-Karl's inner core exceeds 55 kg m^{-2}, and the midlevel mean mixing ratio exceeds 5 g kg^{-1}, deep convection apparently does little to further moisten the inner core. These results suggest that the inner core of pre-Karl may, in terms of moisture, be thermodynamically primed for formation well in advance of genesis.

5.3.2. Matthew (2010)

Similar to Karl, the disturbance which eventually becomes Tropical Storm Matthew originates as a weak disturbance off the coast of South America, near 10°N, 55°W (Figure 5.6); no vorticity maxima are coherently tracked prior to 20 September. Although the vorticity maxima at low (925–850 hPa) and midlevels (700–600 hPa) appear to be better aligned than in Karl, dropsonde observations from DC-8 and G-V flights between 20 and 22 September indicate that the wave is similarly weak; winds in the trough are asymmetric as northerly winds are noticeably absent on the western side of the wave axis. Observations from flights on 22 September, however, indicate that a well-defined circulation has organized at midlevels (600 hPa), and perhaps even at low levels (925 hPa). Due to the flight restrictions in Venezuelan airspace and inability to launch dropsondes over land, no samples are available in the southern portion of the trough.

The accumulated precipitation shown in Figure 5.7 illustrates one apparent difference between Karl and Matthew; Matthew exhibits much greater rainfall throughout the pregenesis period than Karl. Likewise, in Matthew, compared to Karl, precipitation is more persistent near the center and the total raining fraction within the inner core is greater within 3 days of formation (Figure 5.8, azimuthally averaged rain rate, and Figure 5.9, 235 K IR cloud fraction). As with Karl, the most "favorable" convective burst (in terms of area, intensity, and "convective" rain fraction) appears to be 3 days prior to genesis; however unlike Karl, in the day following this episode, the disturbance exhibits a marked increase in organization. According to the dropsondes from the flights on 22 September (Figure 5.7), both the low- (925 hPa) and midlevel (600 hPa) trough has well-defined curvature, while a circulation may even have developed at both levels. Whether

the convection is directly responsible for this organization is unclear, particularly since the circulation seen in the G-V flight (approximately 15–18 hours after the event) is over 2° south of the latitude where the convection occurred the previous day; however, the timing is nonetheless intriguing.

In the 36 hours prior to genesis, even though the overall "convective" rain fraction (compared to the episode 2.5 days before formation) apparently is *decreased* within 3° (Figure 5.10b), when the inner core is redefined as 1° from the center, the "convective" fraction appears to be *increased* (approximated by the fraction of pixels with PCT $\leq$ 250 K in Figure 5.11c and also by the azimuthally averaged rain rate in Figure 5.8). This means that the precipitation – particularly the most intense areas – are primarily confined to within 1° of the VM center as Matthew approaches genesis. Considering that the overall intensity of deep convection does not seem to be distinguishable in any particular episode before genesis, one may speculate that the proximity of rainfall to the center is the most important convective property within 2 days of formation of Matthew. Finally, considering that the tracks of Karl and Matthew closely resemble one another, one may suggest that the "quicker" formation (72 hours tracked before genesis versus 114 hours for Karl) of Matthew may be related to the fact that all convective properties — raining fraction, fractional area of intense rainfall, duration, and proximity — are more favorable in Matthew.

Similar to Karl, the mean midlevel (700–400 hPa) mixing ratio and TPW exhibit little increasing trend during the pregenesis period (Figure 5.10d); in fact, one could argue that the midlevel mean mixing ratio has decreased somewhat from 1–2 days prior to formation. Given the mostly unchanged, elevated TPW (above 55 kg m^{-2}) and

midlevel water vapor mixing ratio (above 5 g kg^{-1}), the inner core thermodynamic properties appear to be sufficient for formation well in advance.

5.3.3. Nuri (2008)

During the TPARC/TCS-08 field program in the West Pacific, the USAF C-130 and NRL P-3 collaborated for two missions into pregenesis Nuri, as well as two additional investigations around the genesis time (1800 UTC on 16 August). Two days before genesis, the disturbance appears to be disorganized as the low- (925–850 hPa) and midlevel (700–600 hPa) vorticity maxima centers show substantial misalignment on 15 September (Figure 5.12), and no circulation is evident in the dropsonde observations from both C-130 and P-3 flights on 15–16 August (Figure 5.13; data are centered at 0000 UTC on 16 August). By 16 September, the vorticity alignment dramatically improves, and by 0000 UTC on 17 August, a tropical depression-strength vortex is clearly present in dropsondes from the C-130 and P-3 flights. Unlike Karl and Matthew, the mean midlevel mixing ratio (derived from dropsondes) and TPW (derived from PMW and dropsondes) do indicate an obvious increase prior to genesis (approximately 4–5 kg m^{-2} in 2 days). Although this could be attributed to moistening by convection, a more likely explanation is that the greater moisture is a consequence of the 5° southward movement of the midlevel VM on 15–16 August.

Rainfall is observed to be persistent and widespread within the inner core (Figure 5.14); raining fractions within 3° remain above 50% from 1200 UTC on 15 August, through genesis. The most "favorable" convective episode occurs around 1800 UTC on 15 August; this episode has the greatest raining fraction, and is the most intense of any before genesis. What effect, if any, this episode had on the intensification of the

circulation on 16 August is unclear; the C-130 and P-3 flights (centered around 0000 UTC on 16 August; Figure 5.13) sampled the disturbance while the convective episode was still active, and although dropsonde data do not indicate any clear circulation at midlevels, they do hint at a possible weak low-level circulation. The next, and final convective episode before formation (beginning around 1200 UTC on 16 August) is not as impressive; the most intense precipitation is outside of 1° (Figure 5.13) and does not appear near the center (within 0.5°) until right at genesis. In other words, despite the circulation apparently intensifying, the precipitation is primarily occurring *outside* the (1°) inner core. So the question remains: even though genesis is not directly attributed to the most "favorable" convective episode in Karl, Matthew, and Nuri, do changes in the thermodynamic environment, as a result of this episode, lessen the requirements (for intensity, proximity, area) of subsequent convective episodes to further intensify the vortex?

5.3.4. Fay (2008) and Fiona (2010)

For this subsection, Fay (10–24 Aug.) and Fiona (27 Aug.–4 Sept.) will be compared to one another. Fay and Fiona follow similar tracks (Figures 5.15 and 5.16, respectively) and appear to be embedded in similar environments; both exhibit favorable 850–200 hPa vertical wind shear (5–10 m s^{-1}), consistently high pregenesis inner core relative humidity (exceeding 70% at midlevels and 80% at low levels), moisture (TPW is 55 kg m^{-2}), and vorticity that is similar in magnitude and trend (gradual increase to formation during the pregenesis phase). One notable difference, and a possible reason for the characteristically more impressive convection in Fiona, SSTs along the Fiona track are 0.5–1°C greater than Fay. The difference of most interest is that Fay forms within 5.5

days of tracking, while Fiona forms more quickly, 4 days after the start of tracking. Comparing the precipitation characteristics between the two may offer the reason for this disparity.

While Fay does not exhibit any particularly impressive periods of deep convection (according to the azimuthally averaged rain rate, Figure 5.17) at any radius from the center, Fiona has two particularly impressive periods (Figure 5.18). Both episodes (around 0000 UTC on 28 and 29 August) are considered "favorable" among all proxies; the rainfall is intense (azimuthal mean rain rates exceed 7 mm hr^{-1}), widespread ("convective" rain rates span from the center to 1–2°), and is near the center (within 2°). Although few pregenesis in-situ observations exist within 24 hours to verify the direct impact of the convective episodes on the intensification of the pre-Fiona circulation, observations from the most recent G-V flight (midday on 30 August; Figure 5.19) after the 2nd episode indicates that at the time of formation, only a low-level circulation is present; no well-defined midlevel circulation is apparent. This seems to contradict the hypothesis that organization of a midlevel circulation prior to genesis is required. Like Nuri, Fiona does not develop immediately after the episode characteristically most "favorable" for genesis; in fact, the total raining fraction within the 1° inner core (Figure 5.20b) actually drops from 100% coverage to 30%, while according to 3B42 and PMW overpasses, the "convective" rain appears to be nearly nonexistent within in the inner core (Figure 5.20b,c). This time evolution suggests that by 30 August, the circulation is already primed for formation; widespread, intense precipitation may not be required to further intensify the circulation to tropical cyclone strength.

The inner core of Fay is experiencing persistent rainfall (Figure 5.17) as the

raining fraction within 3° (1°) remains at least 40% for 57% (73%) of the pregenesis period (Figure 5.21b; Table 5.1). Given the favorable environment (in terms of vertical wind shear, relative humidity, and moisture), and the lack distinguishing convective episodes like those observed in Fiona, the *persistence of rainfall near the center* may be more critical to formation of Fay than any widespread, intense convective episode. In comparing these two cases, one could speculate that widespread, "intense" convection, as observed in Fiona, may be favorable for more expeditious development.

5.3.5. Danny (2009)

Originating at 1200 UTC on 24 August, the pre-Danny vorticity maxima at low (925–850 hPa) and midlevels (700–600 hPa) quickly achieve decent alignment within 24 hours of the start of tracking (Figure 5.22); by 1200 UTC on 25 August, the low and midlevels are within 0.5°. With relative humidity exceeding 75% (Figure 5.23c), and 850–200 hPa vertical wind shear decreasing to around the 10 m s^{-1} (Figure 5.23b) by 26 August, the environment appears to be rapidly becoming more favorable for formation on 25 August. In fact, the relative vorticity (Figure 5.23a) at all levels in the NCEP FNL experiences a very dramatic spike late on 25 August, perhaps not coincidentally just as the vertical shear is significantly reduced. Unfortunately, the first aircraft to investigate the disturbance, the NOAA P-3, did not do so until two consecutive flights on 26–27 August (Danny is declared a TD at 0900 UTC on 26 August). According to the dropsondes on those flights (Figures 5.24a,b), the circulation has already been established and enough evidence exists for the NHC to upgrade Danny to a tropical storm. Similar to Fay, the rainfall within the inner core of Danny is persistent (the raining fraction within 3° is consistently greater than 60%), but not distinguishably "intense" as there are very

few instances where the azimuthally averaged rain rate exceeds 5 mm hr^{-1} (Figure 5.25). Therefore, although a direct link between the precipitation and the dramatic intensification of the circulation (or vorticity maxima in the operational analysis) can only be assumed, Danny (like Fay) is another example where formation occurs without intense convective episodes as impressive as those observed in Fiona; persistent, but not necessarily "intense" rainfall, is apparently sufficient for the genesis of Danny.

5.4. Individual Case Results: Nondeveloping Disturbances

5.4.1. Ex-Gaston (2010)

Gaston originated as an easterly wave that left the coast of Africa around 28 August. Vorticity maxima tracking begins on 29 August (Figure 5.26); two distinct tracks are observed, which are consistent with the climatology of easterly waves leaving Africa presented earlier (Chapter 2.1); a low-level track which originates to the north of the Sahel, and a southern track, which originates near the rainy region along 10°N (Burpee, 1974; Carlson, 1969a; Pytharoulis and Thorncroft, 1999; Reed et al. 1977, 1988a). The two tracks merge on 1 September, and perhaps not coincidentally, a tropical depression is declared at 0600 UTC. Gaston would briefly reach tropical storm strength, but by 1800 UTC on 2 September, Gaston weakened and was no longer a tropical depression. The vorticity maxima are, however, consistently tracked after 2 September as ex-Gaston progresses westward; tracking ends when the vorticity maxima make landfall in Central America on 11 September.

Given the potential for redevelopment, PREDICT and GRIP would focus their efforts on ex-Gaston between 3 and 8 September; however ex-Gaston never redeveloped. The reason for non-redevelopment is not attributed to vertical wind shear or even the

vertical alignment of vorticity. The low- and midlevel centers are within 1° between 2 and 8 September, while the NCEP FNL operational analysis indicates that the 850–200 hPa vertical wind shear (Figure 5.27b) is favorable throughout the life of Gaston (less than 10 m s^{-1}); yet the relative vorticity at low and midlevels is consistently decreasing from 3 to 8 September (Figure 5.27a). Instead, non-redevelopment appears to be related to the unfavorable relative humidity (Figure 5.27c); the midlevel relative humidity is systematically decreasing from 3 to 8 September. Likewise, the operational model analysis and dropsonde-derived midlevel (700–400 hPa) mean mixing ratio, and the satellite-derived TPW, all agree that the midlevels are drying during this period (5.28d). The decrease in midlevel relative humidity is confirmed in a similar analysis for 5 PREDICT flights into ex-Gaston by Smith and Montgomery (2012); they identify both a decrease in θ_e at midlevels and an increase in the difference between the surface θ_e and midlevel θ_e minimum. Consequently, the raining fraction within the inner core (for both 1 and 3° definitions) is also decreasing (Figure 15.28b), and is nearly non-existent within 1° of the center. Although, the "convective" raining fraction (Figure 5.28b) and fraction of cold pixels (Figure 5.26c; fraction of pixels ≤ 250K) do indicate periods of particularly "intense" convection, their radial distance from the center is often outside of 1° (azimuthally averaged rain rate; Figure 5.29).

5.4.2. PGI-27 (2010)

PGI-27 was the first disturbance sampled by the G-V during PREDICT; flights on 17 and 18 August sampled a weak easterly wave south of Puerto Rico and Hispaniola. Vorticity maxima at low (925–850 hPa) and midlevels (700–600 hPa) are coherently tracked from east of the Lesser Antilles, all the way to landfall in Mexico after passing

through the Bay of Campeche (Figure 5.30). While midlevel relative humidity (above 70%) and 850–200 hPa vertical wind shear (below 10 m s^{-1}) are apparently favorable (Figure 5.31b,c), and multiple periods of widespread rainfall exist (Figure 5.32), the most obvious reason for non-development between the start of the track (16 August) and 20 September appears to be related to the substantial misalignment of the low and midlevel vorticity maxima (Figure 5.30). Convection will not support intensification if the vorticity maxima are misaligned by as much as 4°, as observed in PGI-27. From 20 September until landfall, the alignment improves; however, now intensification may be limited by the fact that the disturbance is both interacting with land and the inner core is mostly void of precipitation (Figure 5.32).

5.4.3. PGI-30 (2010)

PGI-30 is the most obvious nondeveloping case among all disturbances studied in the dissertation. One obvious reason for nondevelopment is related to the substantial misalignment of the low- and midlevel vorticity maxima (approximately 2–5°; Figure 5.33). Even though the alignment improves (within 1°) after 22 August, and the midlevel relative humidity (Figure 5.34c) is somewhat favorable (above 70%), PGI-30 never develops. The other obvious reason for nondevelopment is the fact that the inner core (no matter what radial definition) is nearly void of precipitation (Figure 5.35).

5.5. Summary of Environmental Parameters

Case studies presented in sections 3 and 4 of this chapter indicate that the vertical alignment of VM and pouches (not shown) may be a necessary condition for genesis. To examine this possibility among all disturbances, the radial difference between the 925–

850 hPa, 925–700 hPa, and 925–600 hPa VM are presented in Figure 5.36. Nondeveloping disturbances are also provided for comparison. Figure 5.36 confirms that the *vertical alignment of the low- and midlevel vorticity maxima is a necessary condition for formation*. On average, the 925–600 hPa difference is as high as 2.5° as many as 4 days prior to genesis, and is reduced to less than 1° by genesis. The same tendency is observed for the low-level differences; the 925–700 hPa difference is reduced from 1.5° to 0.5°, while the 925–850 hPa difference is reduced from 0.5° to less than 0.25°. The same tendency is observed for the pouch locations (not shown). Vertical alignment, however, is not sufficient alone for formation; Figure 5.36 indicates that at low and midlevels, vorticity maxima in nondeveloping disturbances can also be vertically aligned.

McBride and Zehr (1981) identify an important genesis related parameter, the daily genesis potential (DGP), defined as the difference between the 925 and 200 hPa relative vorticity. Essentially, a high DGP represents a favorable superposition of upper level anticyclonic vorticity over low-level cyclonic vorticity. Kerns et al. (2009) determined that, in addition to the relative vorticity at 925 hPa, the DGP is a strong discriminator between developing and nondeveloping disturbances. Figure 5.37 summarizes the time series of DGP, averaged within 1° of VM center, for all cases. The time series indicates that within 2 days of genesis, the DGP for developing cases is consistently increasing; in contrast, nondeveloping disturbances tend to decrease over time. Note the nondeveloping spike in Figure 5.35 at day=0 is that of Gaston. Although considered nondeveloping in the PREDICT and GRIP programs, Gaston has been tracked and plotted during its developing phase as well; so Gaston should be considered developing from before genesis to 3 days after genesis, and nondeveloping from 3 days

after to genesis to the end of the track. The spike near genesis in Gaston is consistent with developing disturbances as the DGP increases dramatically as Gaston becomes a tropical storm; however, the DGP begins to rapidly decrease 2.5 days after formation as Gaston becomes more disorganized.

A summary of the time series of 850–200 hPa vertical wind shear is presented in Figure 5.38. Overwhelmingly cited as a necessary condition for formation, vertical wind shear must be low or moderate (less than 10 m s^{-1}) for genesis to occur. This figure indicates that, on average, the vertical wind shear of developing cases is below this threshold before genesis; however, nondeveloping disturbances can similarly exhibit low vertical wind shear. Therefore, at least for the cases presented, vertical wind shear is not a good separator of developing and nondeveloping cases.

As expected, the increase observed in DGP (Figure 5.37) is most closely linked to the increase of low-level relative vorticity (Figure 5.39; here the analysis for the 1° inner core is shown because the vorticity magnitude and tendency is more pronounced than for 3°); low- and midlevel relative vorticity increases prior to formation, and appears to, on average, reach a mean (1°) inner core magnitude of approximately $1x10^{-4}$ s^{-1}. Figure 5.39, however, also illustrates another important observation; while the 925 and 850 hPa (low-level) relative vorticities steadily increase within 2 days of genesis, prior to then the relative vorticity shows no increasing tendency. In contrast, at midlevels (700–600 hPa) the relative vorticity is steadily increasing beginning as many as 4 days prior to genesis. This could suggest that the midlevel spin-up (at least in terms of relative vorticity) may begin (or lead) low-level spin-up. Finally, at least for the cases included, the magnitude of the low-level vorticity of developing cases is typically greater for nondeveloping prior

to genesis.

Fundamental to tropical cyclogenesis is the formation of an inertially stable vortex, whereby latent heat release from deep convection remains within the disturbance, rather than be dispersed by gravity waves (Schubert and Hack, 1982). A measure of this effect, the Rossby radius of deformation (RROD) is a parameter that compares the relative importance of rotational effects compared to buoyancy. Fundamentally, when the disturbance length scale is less than the RROD, the latent heat from deep convection is not retained and the mass field adjusts to the wind field. On the other hand, when the scale of the disturbance approaches the RROD, latent heat from deep convection remains within the disturbance, the wind field adjusts to the mass field, and the incipient disturbance may intensify as a result of that latent heating. The RROD (L_R) is defined as:

$$L_R = NH / (\zeta + f_o) \qquad \text{(Equation 5.1)}$$

where ζ is the relative vorticity, f_o is the planetary vorticity, H is the depth of the system, (defined here as 10 km) and N is the Brunt Vaisala frequency:

$$N = \sqrt{((g / \theta) * d\theta/dz)} \qquad \text{(Equation 5.2)}$$

where g is gravity, which includes gravitational and centrifugal acceleration, and z is geometric height. The vertical gradient of potential temperature (static stability), $d\theta/dz$, has been computed for 1000–600 hPa; here 600 hPa is chosen to be the altitude for which maximum latent heat release occurs (defined similar to Papin and Hennon, 2011). From this calculation, Equation 5.1 clearly conveys the importance that latitude and relative vorticity play in reducing the RROD. At low latitudes, the absolute vorticity remains

small, and the RROD large; however, increasing the latitude favorably increases the absolute vorticity and decreases the RROD. Likewise, as relative vorticity increases, the RROD favorably decreases. In this study, the RROD has been computed using three different calculations of the mean relative vorticity:

(1) The mean relative vorticity at each location for the level only (925, 850, 700, 600 hPa),

(2) The mean relative vorticity is computed at each location (925, 850, 700, 600 hPa) for the entire 925–600 hPa column, and

(3) For the 925–600 hPa column at the average location from all levels (925, 850, 700, 600 hPa).

Figure 5.40 shows the RROD computed for methodology (1), averaged within 3° of the center. At all levels, the RROD consistently decreases for the developing cases within 2 days of genesis, while nondeveloping disturbances exhibit little reduction. At least for the cases presented, the results indicate that the RROD is reduced to approximately 1500 km (1000 km for the 1° average) by genesis. Although the magnitude differs slightly for some storms, results from methodology (2) (not shown) indicate a similar tendency. Figure 5.41 similarly shows (within 3° inner core) the RROD for methodology (3), the 925–600 hPa column-average vorticity for the mean location at 925, 850, 700, and 600 hPa. This figure similarly illustrates that within 3 days of genesis, the RROD in developing disturbances is decreasing, reaching, on average, 1500 km by genesis. Of course, the reduction of the RROD to these thresholds does not guarantee formation; only if the length scale of the developing disturbance nears this value can latent heat be contained within the disturbance, and positively support the

genesis process. Theoretically, for the cases presented, this condition is sufficiently met as genesis proceeds once the RROD has been reduced to approximately 1000–1500 km. Not surprisingly, these results mirror those observed in the relative vorticity; for the RROD calculation, the buoyancy term has little spatial variation and the RROD is predominantly influenced by the absolute vorticity.

The dropsonde mean midlevel relative humidity in developing disturbances has already been shown in Chapter 4.3 to be greater than that observed in nondeveloping disturbances. The time series of NCEP operational analysis relative humidity for the 3° inner core definition for each disturbance (Figure 5.42) confirms this same conclusion; nondeveloping disturbances, compared to developing, tend to be less humid at midlevels (700–600 hPa); at low levels (925–850 hPa), the difference between developing and nondeveloping humidity is less obvious. Figure 5.42 also indicates that the mean relative humidity within 3° (as well as for 1°, not shown) varies little with time at all levels prior to genesis; typically, the relative humidity at low levels remains above 80%, and at midlevels, above 70%.

5.6. Summary of Convective Parameters

The rainfall statistics for the 3° and 1° inner core definitions are provided in Figures 5.43 and 5.44, respectively. These results indicate that, on average, the total raining fraction within the inner core of developing cases shows no noticeable trend prior to genesis; high raining fractions are just as likely to be observed 3 days prior to genesis as 1 day prior to genesis. In fact, in only 3 of the 12 developing cases is the maximum raining fraction observed within 24 hours of genesis (Table 5.1). Although the "convective" rain fraction (Figures 5.43 and 5.44 b,c), shows no noticeable trend prior to

genesis, there appear to be a few disturbances that, within 1°, exhibit distinguishable, high "convective" rain fractions 1–2 days prior to genesis. This, however, appears to be more an exception than the rule; the mean "convective" fractions are noticeably less than the median, and therefore, the peaks 1–2 days before formation are not common among all developing disturbances included. Figures 5.43 and 5.44 also have one common feature; despite relatively persistent rainfall within the inner core 1–3 days before formation, in some cases (5 of the 12; Table 5.1), the *minimum* raining fraction of the pregenesis stage follows within a day of formation. In fact, in almost all cases, the "convective" rain fraction is *nearly 0% at some time within 24 hours of genesis* (Table 5.1).

Figures 5.43 and 5.44 demonstrate another important result; for the cases included, the nondeveloping disturbances exhibit lower raining fractions than developing disturbances. While the total raining fractions tend to be less (Figure 5.43b/5.44b), the "convective" rain fraction can be just as high in nondeveloping cases as developing. So, although nondeveloping disturbances may not have has much rainfall within the inner core, high "convective" rain fractions are not necessarily unique to developing disturbances.

Table 5.1 (last column) presents the duration of rainfall within 1° and 3° for all cases. Once again, the duration is defined as the percentage of hours before genesis where the raining fraction within the inner core exceeds 40%. In cases where the developing disturbance is tracked for at least 3 days during the pregenesis stage, the duration within 3° (1°) varies from 50%–75% (68–92%). Gaston is considered an exception at 8%; pre-Gaston is nearly absent of precipitation and seems to actually

develop after one convective episode, even though most of the intense precipitation is 3° from the center. Of the five developing disturbances that are tracked for less than 3 days, the duration within 3° (1°) of rainfall ranges from 56 to 83% (63–100%); in fact, in three of the five cases, the duration exceeds 80%. Overall, developing disturbances typically have rainfall covering at least 40% of the 3° (1°) inner core for at least 50% (60%) of the pregenesis stage, while nondeveloping disturbances typically have durations well below 50%.

IR data are only available for P-G-I cases and Gert; 2008–2009 cases are not yet included. The IR cloud fractions and minimum IR T_B for the 3° inner core are summarized in the time series in Figure 5.45. The fraction of IR pixels less than or equal to 270 (Figure 5.45a), 235 K (Figure 5.45b), and 210 K (Figure 5.45c) only show a slight increasing trend prior to formation. However, within a day of formation, the minimum in cold cloud fraction is actually *slightly less* than the minimums observed 1–3 days prior to genesis; this is consistent with the tendency observed in the rainfall within a day of formation. Similar conclusions can be made for the 1° analysis (Figure 5.46); however fractions are more pronounced, particularly right after genesis.

Statistics for high frequency (85–91 GHz) channels from PMW overpasses with swath data within the 3° inner core are summarized in Figure 5.47; (a) shows the mean PCT of all pixels that are less than or equal to 250 K (essentially, the mean PCT of all cold pixels); (b) shows the overall minimum PCT; (c) is the fraction of all pixels that are less than 250 K (in other words, the fraction of cold pixels). As defined in section 2 of this chapter, the relative size of the symbol represents the fraction of the swath that is within the radius indicated for the analysis; the larger the symbol, the greater the fraction,

and the more confidence that can be placed that the statistic is representative of the entire inner core. Although the *mean* PCT (Figure 5.45a) indicates no noticeable trend prior to formation, the overall *minimum* does show a slight decreasing trend (i.e., more intense); there are more occurrences of minimum PCT less than 150 K in overpasses within 3 days of formation. Likewise, the *fraction* of cold pixels (Figure 5.47c) has a slight increasing trend (i.e., greater "convective" fraction). These results are particularly distinguishable in the 1° inner core analysis (Figure 5.48); although once again the mean PCT does not differ through the pregenesis period, "intense" convection appears to cover a larger fraction of the (1°) inner core within 2 days of genesis. Nevertheless, such large fractions of cold pixels (greater than 20% within 1°) in episodes within 2–3 days of genesis are not common among all developing disturbances. Figures 5.47 and 5.48 also show overpasses of the nondeveloping VM centers; these overpasses indicate that nondeveloping disturbances have just as intense convection as developing disturbances. In fact, some overpasses of ex-Gaston indicate a convective intensity (mean and minimum PCT) that is comparable to the intensity seen in overpasses of mature tropical cyclones.

Figures 5.47d and 5.48d also show the time series of PMW-derived TPW for the 3° and 1° inner core, respectively. The mean and median TPW do not noticeably increase during the pregenesis period. Although overpasses that exhibit TPW above 60 kg m^{-2} appear more frequently during the period within 2 days of genesis, there are just as many observations where the TPW is below 55 kg m^{-2}. Overall, a few general conclusions can be made about TPW in developing cases; that the inner core TPW must be above 50 mm for genesis to proceed, that given the lack of any noticeable trend in TPW, developing disturbances appear to be thermodynamically primed (sufficient

moisture) for formation days in advance, and if 'progressive moistening' is occurring, it is not noticeable in TPW.

5.7. Summary and Conclusions

The time evolution of inner core environmental, thermodynamic, and convective properties from 11 developing and four nondeveloping disturbances have been investigated using the NCEP FNL operational analysis, in-situ dropsonde data, as well as conventional IR and numerous PMW overpasses. Developing disturbances exhibit a few common environmental characteristics; the inner core relative vorticity and daily genesis potential increase systematically prior to formation, the Rossby radius of deformation is subsequently reduced to around 1000–1500 km (depending on the inner core radial definition), the 850–200 hPa vertical wind shear magnitude is generally below 10 m s^{-1}, and relative humidity at low (925–850 hPa) and midlevels (700–600 hPa) remains at least 75% throughout the pregenesis stage (though no increase is observed). Although these conditions have already been well documented in a number of previous genesis studies (Gray 1968; Kerns et al. 2009; McBride and Zehr 1981; Ooyama 1982), an additional necessary condition has been revealed in this dissertation; the alignment of the low- (925 hPa) and midlevel (600 hPa) VM/pouch is critical for genesis; only when the centers are aligned within 1° is genesis observed (this result agrees with Davis and Ahijevych [2012], who investigated similar P-G-I cases). In contrast to developing cases, nondeveloping disturbances may be drier at midlevels, while the RVOR and RROD show no increasing tendency. Although the low- and midlevel centers are usually misaligned, nondeveloping disturbances can, at times, exhibit an alignment within 1°; thus vertical alignment is necessary, but not alone sufficient, for formation. Although the results

indicate distinct differences between developing and nondeveloping cases examined, since only four nondeveloping cases are examined (compared to 12 developing), these results should not be generalized for all null cases. Such small sample sizes may not sufficiently capture the variation of conditions observed among all nondeveloping disturbances. That being said, although null cases receive significantly less attention during field programs than developing disturbances, cases examined during P-G-I (PGI-27, 30, 48, and ex-Gaston) represent the best-sampled null cases to date and still offer an interesting contrast to the developing cases examined.

Similar to the conclusions from the composited dropsonde dataset (Chapter 4), according to PMW- and dropsonde-derived TPW and midlevel (700–400 hPa) mean mixing ratio, the developing inner core exhibits very little increase in moisture before formation; for the cases included, moisture and relative humidity in developing disturbances appear to be primed for formation days in advance. Although this moistening agrees with similar results from recent numerical and observational studies of tropical cyclogenesis (Montgomery et al. 2010; Smith and Montgomery 2012; Wang et al. 2008; Wang et al. 2010b), at least for the cases included, moisture content appears to be unaffected by convective events; results suggest that once the inner core is moist, convection does very little to add moisture to the environment. This conclusion is, however, only speculative; even with an impressive frequency of observations from satellites, it may be still difficult to directly attribute any moisture tendency to convection.

After a careful synthesis of IR and PMW satellite observations, results indicate the most "favorable" convective episode (in terms of raining area, intensity, area of

intense convection, and proximity to the center) *does not necessarily occur in the day prior to genesis*. While a few cases (such as Fiona, Nuri and TD2) exhibit the most "favorable" episode around 36 hours prior to genesis, in other cases, the episodes are observed as many as 3 days prior to formation (for example, in Karl and Matthew). Although episodes 2–4 days before formation do not directly result in formation, they may create a more favorable thermodynamic environment for the episodes that follow; even lessening the requirements (for intensity, area, and proximity) of those episodes that follow to further help intensify the disturbance. Although all developing cases exhibit some area of "convective" rain (as well as areas of 85–91 GHz PCT below 200 K) within 1–2 days of genesis, in all but four cases (Earl, TD2, Fiona, Nuri), those areas are outside of 1° and even as far as 2.5–3° from the center as genesis nears. Although not in close proximity to the center, these "convective" raining areas may still play an important role; they may still contribute to the organization and intensification of the circulation or perhaps be integral to the vertical alignment of vorticity. Overall, the results simply suggest that there are *no distinguishing characteristics of deep convection common among all cases studied*; in other words, no specific deep convective property (intensity, area, proximity) is consistently more important to genesis. Likewise, given the variability, the relative impact/role of convection during intensification/organization is likely dependent on the large-scale properties of the wave when the episode occurs. The case studies also indicate that intense convective bursts may not be necessary for formation, given that 'intense', widespread convective episodes in close proximity to the center are observed in less than half of the cases (here "intense" is defined when the PMW PCT is below 150 K and the azimuthally averaged rain rate exceeds 5 mm hr^{-1}, and

widespread when, within 1°, the fractional coverage of PCT $\leq$ 250K is at least 10-15% and 'convective' rain fractions exceed 50%). Therefore, MCSs such as those documented in Zipser and Gautier (1978) and Houze et al. (2009), that can alone support the mass flux and low-level convergence observed in the developing depression, are not consistently observed within a day of formation among the cases investigated.

Results also indicate that the overall raining fraction does not show an obvious trend during the pregenesis stage; large raining areas within 3° are just as likely to be observed days prior to genesis than right before genesis. In fact, similar to the "convective" fraction, in 8 of the 12 developing cases, the minimum raining area is observed within 36 hours of formation; one could speculate that the decrease in the overall intensity and area of rainfall during this period may be related to the stabilization from the cool, dry air observed in the dropsonde composite (Chapter 4) at low levels. While the duration or 'persistence' of precipitation varies among the developing cases (in most cases, duration is greater than 50% for the 3° inner core and 60% for 1°), results strongly suggest that persistence is a critical property of developing waves; not only does it differentiate developers from the nondevelopers, but it must be important for formation in cases such as Fay, Danny, and Matthew, which do not exhibit any distinguishing deep convective episodes, such as those observed in Fiona prior to genesis.

Results also suggest that the proximity of rainfall – though not necessarily "intense" rainfall - may be important for formation. In some cases, the timing of the organization of a low- and/or midlevel circulation, and vertical alignment of vorticity, appears coincidental with rainfall in close proximity to the center; however, whether the rainfall is responsible for, or simply a consequence of, this organization is still unclear.

Despite improved spatial and temporal coverage of in-situ data in a few of the cases presented, the ability to link organization of a low- and/or midlevel circulation to convective events remains a challenge. In Karl, observations from flights around 0000 UTC on 13 September hint at a low-level (925 hPa) circulation, which is perhaps not a coincidence given the convective activity observed between 0000 UTC 12 September and 0000 UTC 13 September. Likewise, in Matthew, it may not be a coincidence that well-defined low- (925 hPa) and midlevel circulations (600 hPa) are first observed in dropsonde observations from flights on 22 September, considering that the most impressive convective episode (in terms of intensity and fractional area of cold T_B/PCT and "convective" rain rates) occurs in the hours just prior to the flights.

Table 5.1
Summary of 3B42 rain statistics for the 3° (1°) inner core; bold indicates within 24 hours of genesis.

Name	Initial BT Intensity [kt]	Total Hours Before Genesis	Max. Raining Fraction	Hour Before Genesis	Min. Raining Fraction	Hour Before Genesis	Max. Conv. Fraction	Hour Before Genesis	Min. Conv. Fraction	Hour Before Genesis	Duration
Fay	30	132	0.77 (1.00)	114 (57)	0.04 (0.04)	60 (99)	0.23 (0.17)	**3** (90)	0.00 (0.00)	33 (**12**)	0.57 (0.73)
Kyle	30	120	0.66 (1.00)	39 (36)	0.15 (0.10)	114 (114)	0.18 (0.58)	33 (45)	0.00 (0.00)	99 (**6**)	0.73 (0.88)
Karl	30	114	0.89 (1.00)	66 (69)	0.06 (0.00)	57 (57)	0.20 (0.33)	72 (69)	0.00 (0.00)	**9** (**3**)	0.47 (0.71)
Fiona	30	84	0.71 (1.00)	27 (39)	0.21 (0.20)	**12** (**12**)	0.17 (0.59)	33 (30)	0.00 (0.00)	**12** (**3**)	0.68 (0.79)
Bonnie	30	84	0.69 (1.00)	57 (33)	0.08 (0.04)	**15** (**18**)	0.21 (0.26)	57 (63)	0.00 (0.00)	75 (**9**)	0.50 (0.68)
Matthew	30	72	0.81 (1.00)	39 (**3**)	0.31 (0.16)	72 (36)	0.27 (0.24)	51 (42)	0.00 (0.00)	**18** (**12**)	0.75 (0.92)
Gaston	30	72	0.50 (0.59)	**3** (**3**)	0.00 (0.00)	45 (**15**)	0.09 (0.00)	**24** (**3**)	0.00 (0.00)	39 (**3**)	0.08 (0.08)
Nuri	25	54	0.73 (1.00)	27 (36)	0.08 (0.00)	42 (42)	0.12 (0.48)	**24** (**18**)	0.00 (0.00)	42 (**9**)	0.56 (0.83)
Earl	30	54	0.89 (1.00)	30 (**24**)	0.25 (0.02)	**9** (**6**)	0.31 (0.61)	30 (30)	0.01 (0.00)	**6** (**3**)	0.83 (0.78)
Gert	25	48	0.59 (0.82)	42 (27)	0.17 (0.00)	**6** (36)	0.08 (0.12)	33 (27)	0.00 (0.00)	**12** (**12**)	0.31 (0.63)
Danny	40	45	0.77 (1.00)	**18** (**3**)	0.29 (0.57)	**6** (33)	0.20 (0.14)	**24** (**21**)	0.00 (0.00)	42 (30)	0.80 (1.00)
TD2	30	36	0.76 (1.00)	**3** (33)	0.27 (0.18)	36 (**18**)	0.15 (0.64)	33 (33)	0.01 (0.00)	42 (**12**)	0.83 (0.92)
PGI27	-	120	0.77 (1.00)	63 (45)	0.01 (0.00)	81 (**21**)	0.15 (0.15)	66 (117)	0.00 (0.00)	**15** (**3**)	0.35 (0.50)
PGI30	-	163	0.52 (0.79)	33 (153)	0.00 (0.00)	87 (36)	0.03 (0.13)	162 (153)	0.00 (0.00)	**6** (**3**)	0.06 (0.19)

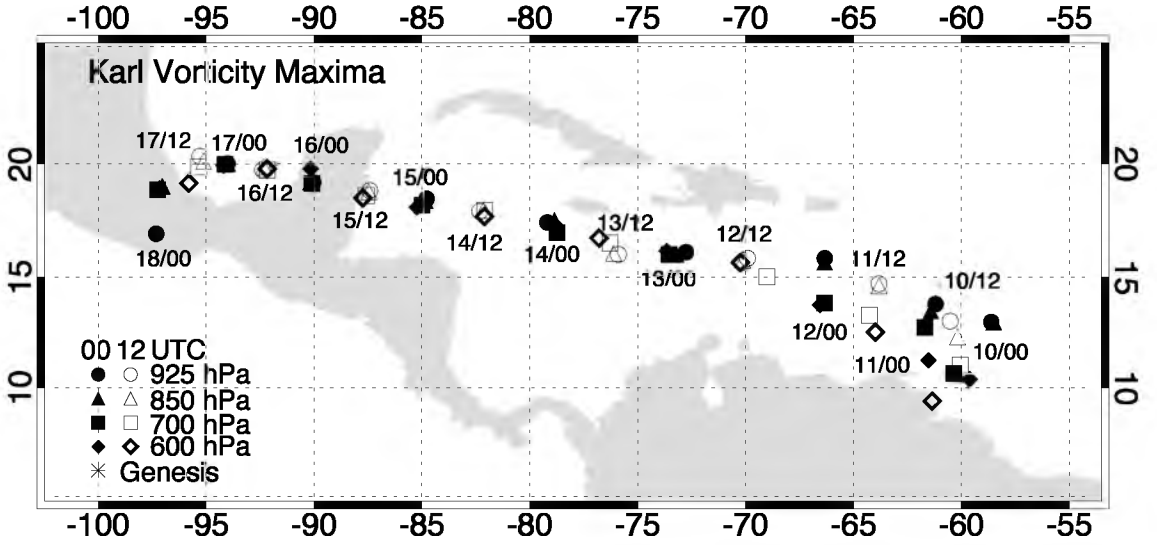

Figure 5.1. Karl 0000 (closed symbol) and 1200 UTC (open) vorticity maxima locations in the NCEP FNL analysis for 925 (circle), 850 (triangle), 700 (square), and 600 (diamond) hPa.

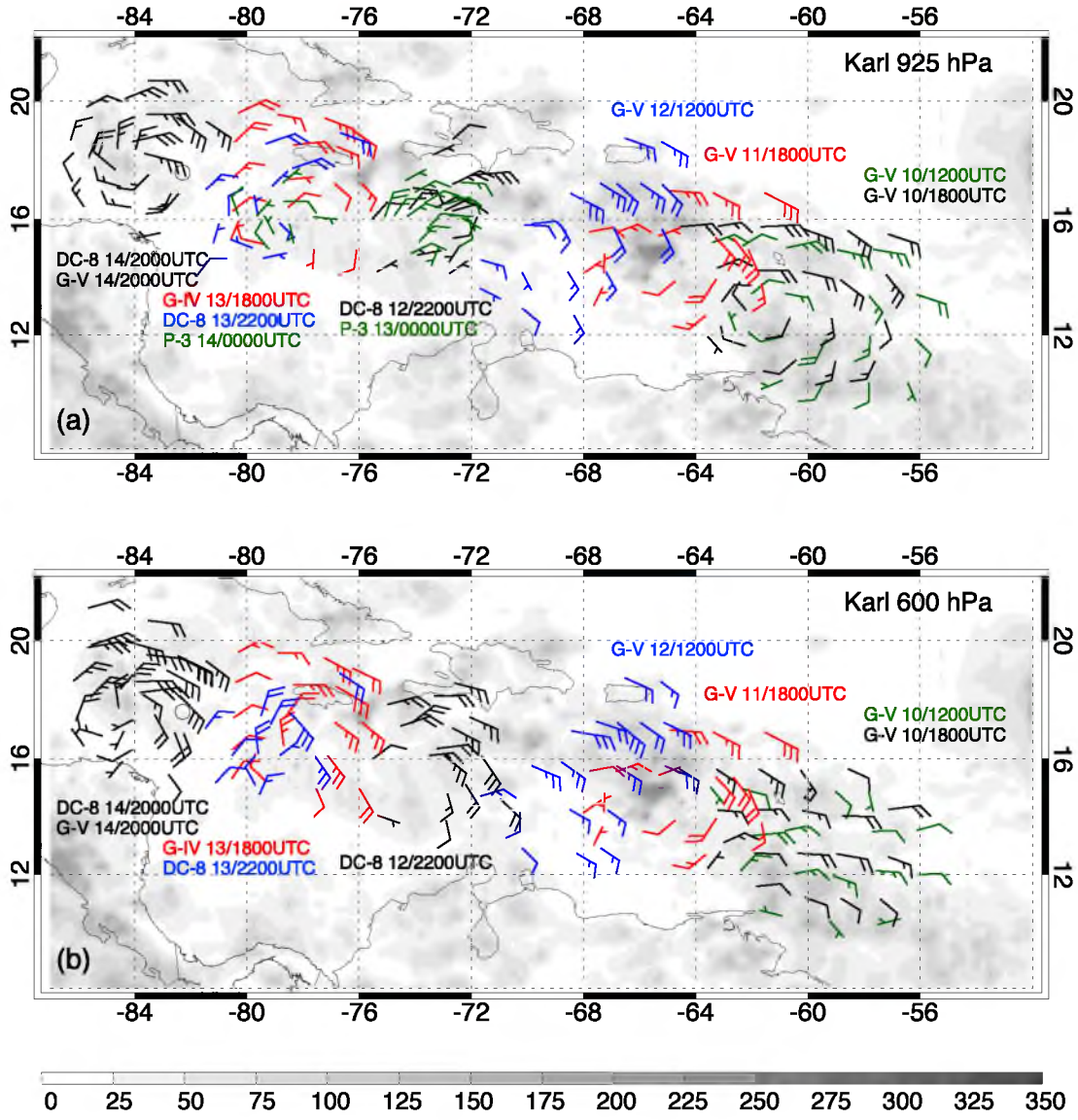

Figure 5.2. Select dropsonde observations at low (a, 925 hPa) and midlevels (b, 600 hPa) of Karl from 10–14 September. Flights are separated by color and dropsonde locations are time-space adjusted, based on the zonal phase speed of Karl, to the time indicated. Accumulated rainfall (mm) from TRMM 3B42 is contoured (period is from 0000 UTC 10 September to 0000 UTC 15 September). The open circle is the genesis location at 1200 UTC 14 September (adapted from Braun et al. 2013).

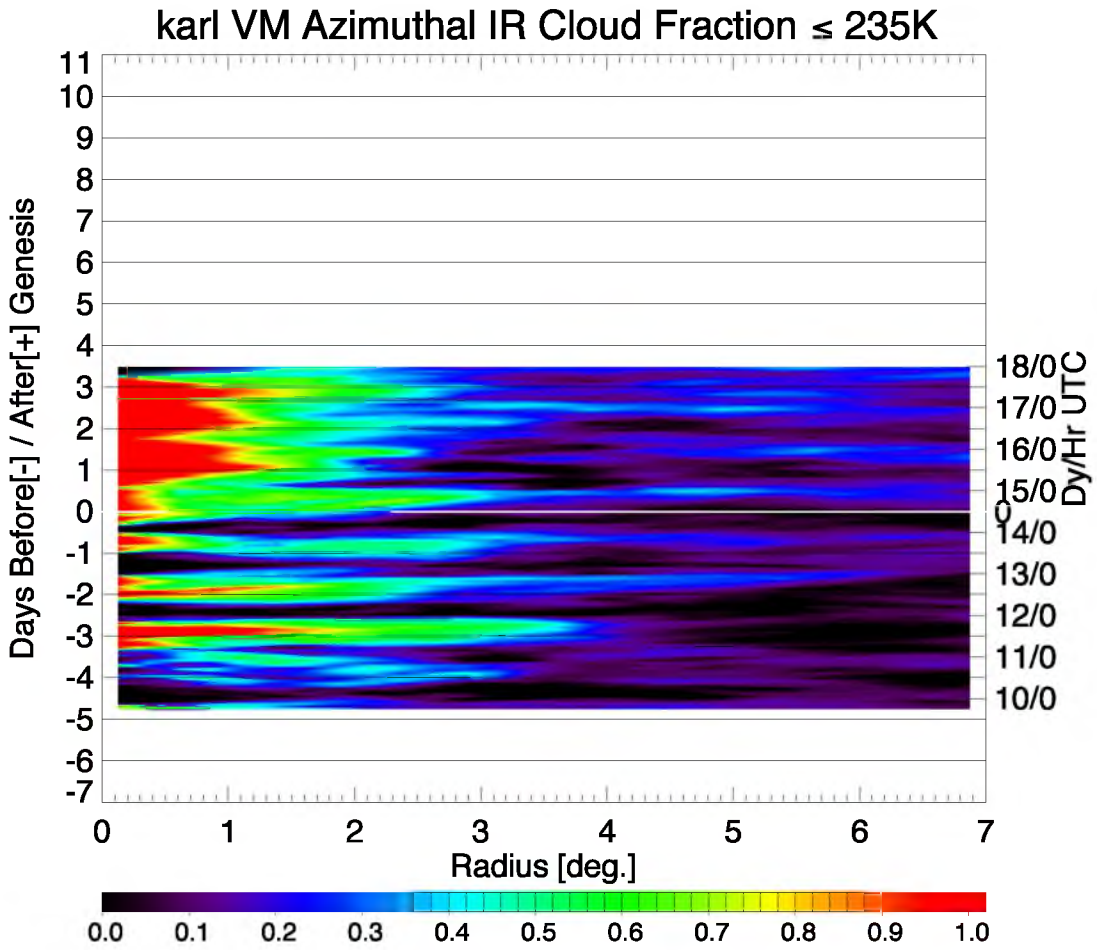

Figure 5.3. Time series of IR cloud fraction for $T_b \leq 235$ K as a function of radial distance from the 850 hPa VM center for Karl.

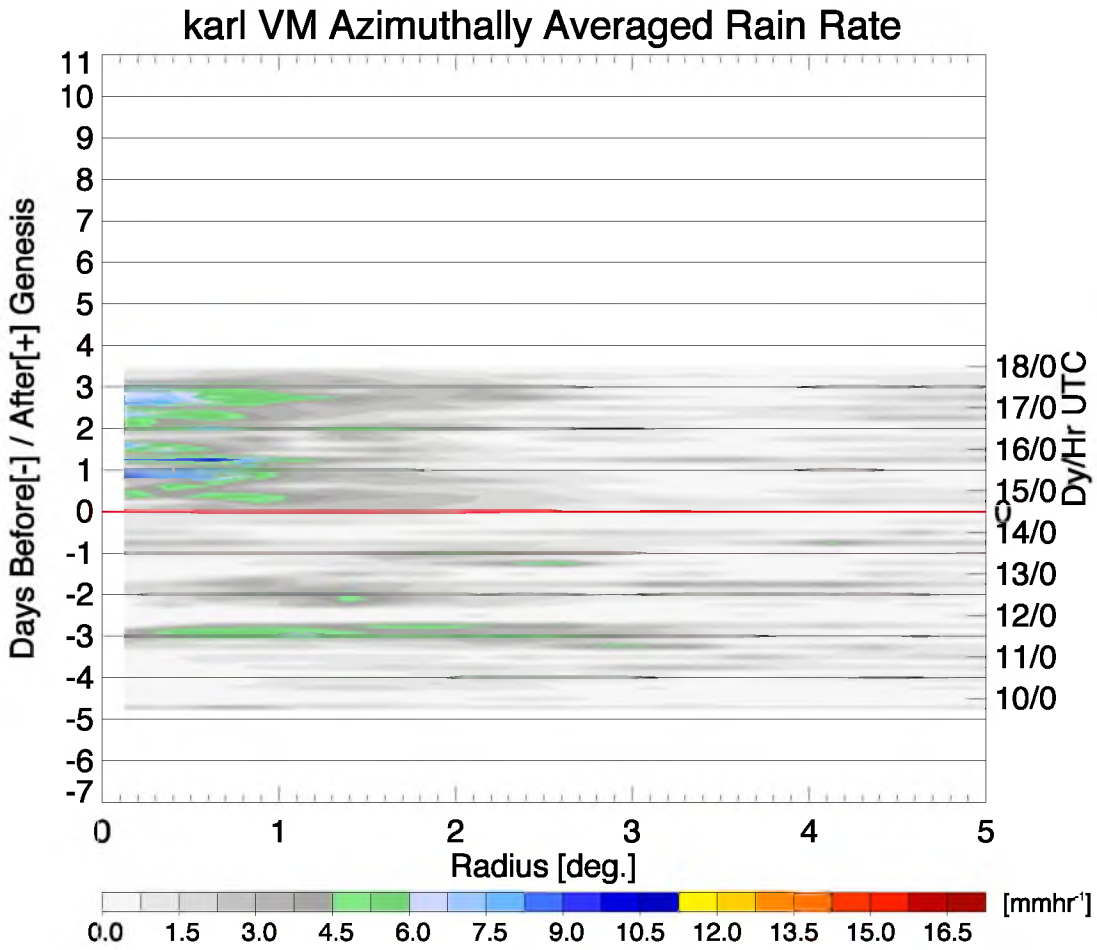

Figure 5.4. Time series of mean rain rate (from TRMM 3B42) as a function of radial distance from the 850 hPa VM center for Karl.

Figure 5.5. For Karl, within 3° of 850 hPa VM center: Time series of (a) fraction of IR pixels with $T_b \leq 210$ (black, solid), 235 (dashed), 210 K (dash-dotted), and minimum IR T_b (gray, solid); (b) fraction of raining pixels (solid, black), fraction of total pixels within 3° with rain rate $\geq$ 5 mm hr^{-1} (dashed), and "convective" fraction, i.e., the fraction of raining pixels with rain rate $\geq$ 5 mm hr^{-1} (gray, solid); (c) mean PCT of pixels $\leq$ 250 K (filled black), minimum PCT (filled gray), and fraction of pixels within 3° that are $\leq$ 250 K (open symbols). (d) TPW from satellites (filled, black) and aircraft (filled, gray), 700–400 hPa mean water vapor mixing ratio from aircraft (open) and NCEP FNL (solid line). For (c) and (d), the size of the symbol indicates the fractional coverage of swath data within the 3° radial circle around the 850 hPa VM center; the larger symbol, the higher the fractional swath data coverage within the radial circle. Upper axis represents the day, as well as the longitude.

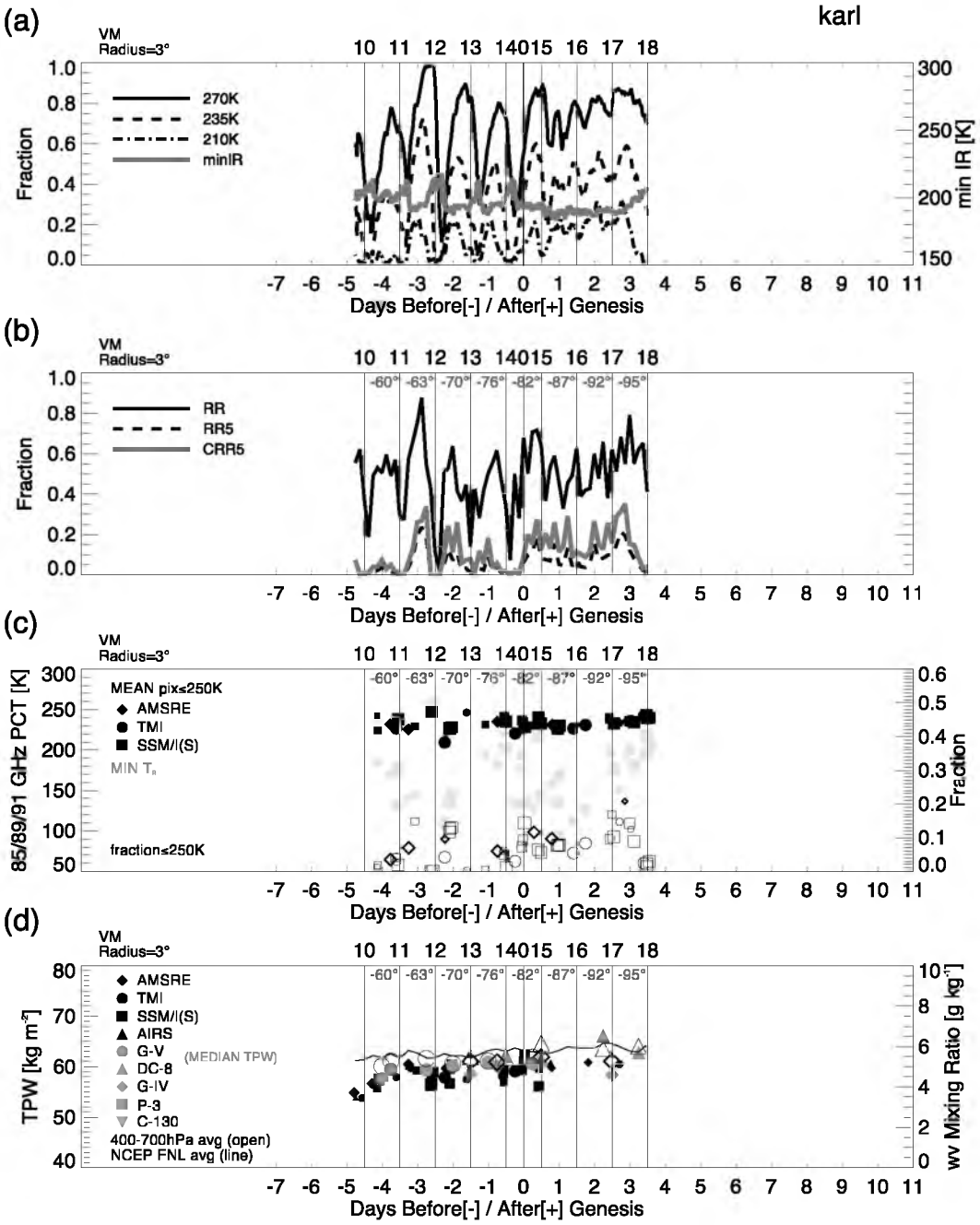
(a)
karl
VM
Radius=3°
10 11 12 13 14 15 16 17 18
Fraction
270K
235K
210K
minIR
min IR [K]
Days Before[-] / After[+] Genesis
(b)
RR
RR5
CRR5
-60° -63° -70° -76° -82° -87° -92° -95°
(c)
85/89/91 GHz PCT [K]
MEAN pix≤250K
AMSRE
TMI
SSM/I(S)
MIN T_b
fraction≤250K
Fraction
(d)
TPW [kg m⁻²]
AIRS
G-V
DC-8
G-IV
P-3
C-130
(MEDIAN TPW)
400-700hPa avg (open)
NCEP FNL avg (line)
wv Mixing Ratio [g kg⁻¹]

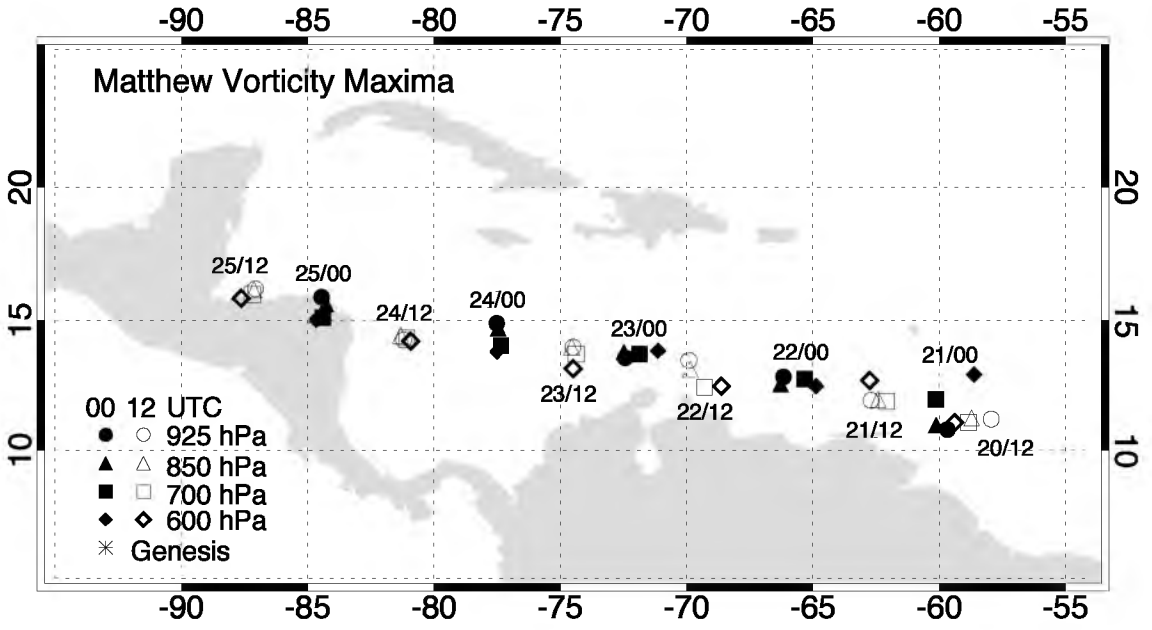

Figure 5.6. Matthew 0000 (closed symbol) and 1200 UTC (open) vorticity maxima locations in the NCEP FNL analysis for 925 (circle), 850 (triangle), 700 (square), and 600 (diamond) hPa.

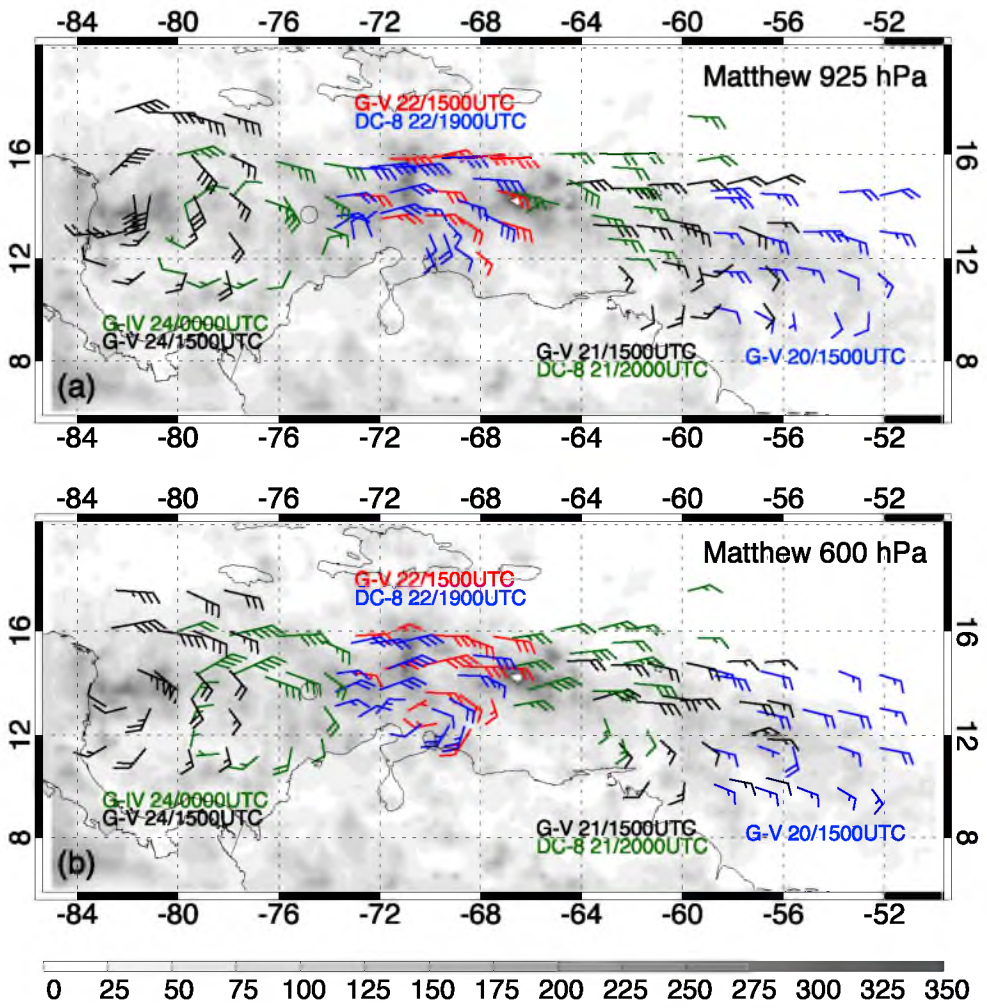

Figure 5.7. Select dropsonde observations at low (a, 925 hPa) and midlevels (b, 600 hPa) of Matthew from 20–24 September. Flights are separated by color and dropsonde locations are time-space adjusted, based on the zonal phase speed of Karl, to the time indicated. Accumulated rainfall (mm) from TRMM 3B42 is contoured (period is from 0000 UTC 20 September to 0000 UTC 24 September). The open circle is the genesis location at 1800 UTC 23 September (adapted from Braun et al. 2013).

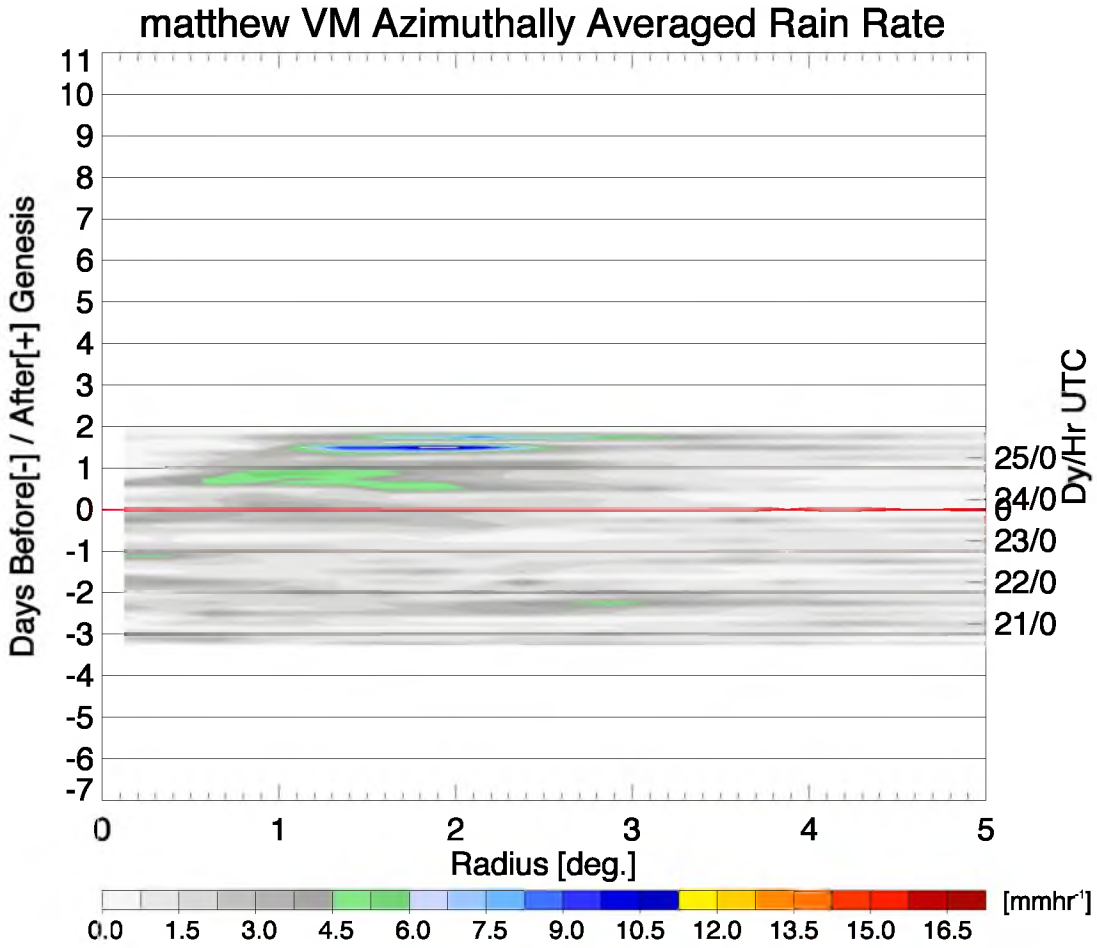

Figure 5.8. Time series of mean rain rate (from TRMM 3B42) as a function of radial distance from the 850 hPa VM center for Matthew.

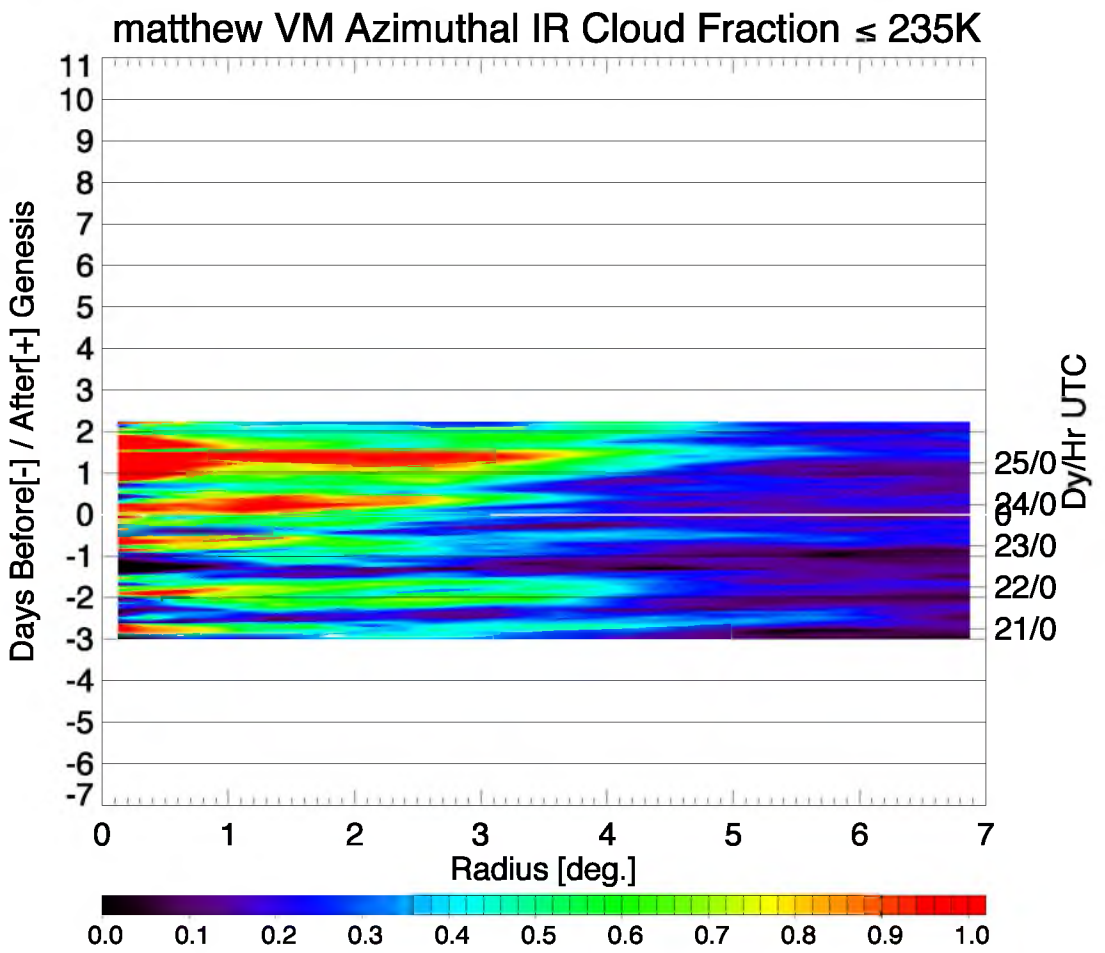

Figure 5.9. Time series of IR cloud fraction for $T_b \leq 235$ K as a function of radial distance from the 850 hPa VM center for Matthew.

Figure 5.10. For Matthew, within 3° of 850 hPa VM center: Time series of (a) fraction of IR pixels with $T_b \leq 210$ (black, solid), 235 (dashed), 210 K (dash-dotted), and minimum IR T_b (gray, solid); (b) fraction of raining pixels (solid, black), fraction of total pixels within 3° with rain rate ≥ 5 mm hr^{-1} (dashed), and "convective" fraction, i.e., the fraction of raining pixels with rain rate ≥ 5 mm hr^{-1} (gray, solid); (c) mean PCT of pixels ≤ 250 K (filled black), minimum PCT (filled gray), and fraction of pixels within 3° that are ≤ 250 K (open symbols). (d) TPW from satellites (filled, black) and aircraft (filled, gray), 700–400 hPa mean water vapor mixing ratio from aircraft (open) and NCEP FNL (solid line). For (c) and (d), the size of the symbol indicates the fractional coverage of swath data within the 3° radial circle around the 850 hPa VM center; the larger symbol, the higher the fractional swath data coverage within the radial circle. Upper axis represents the day, as well as the longitude.

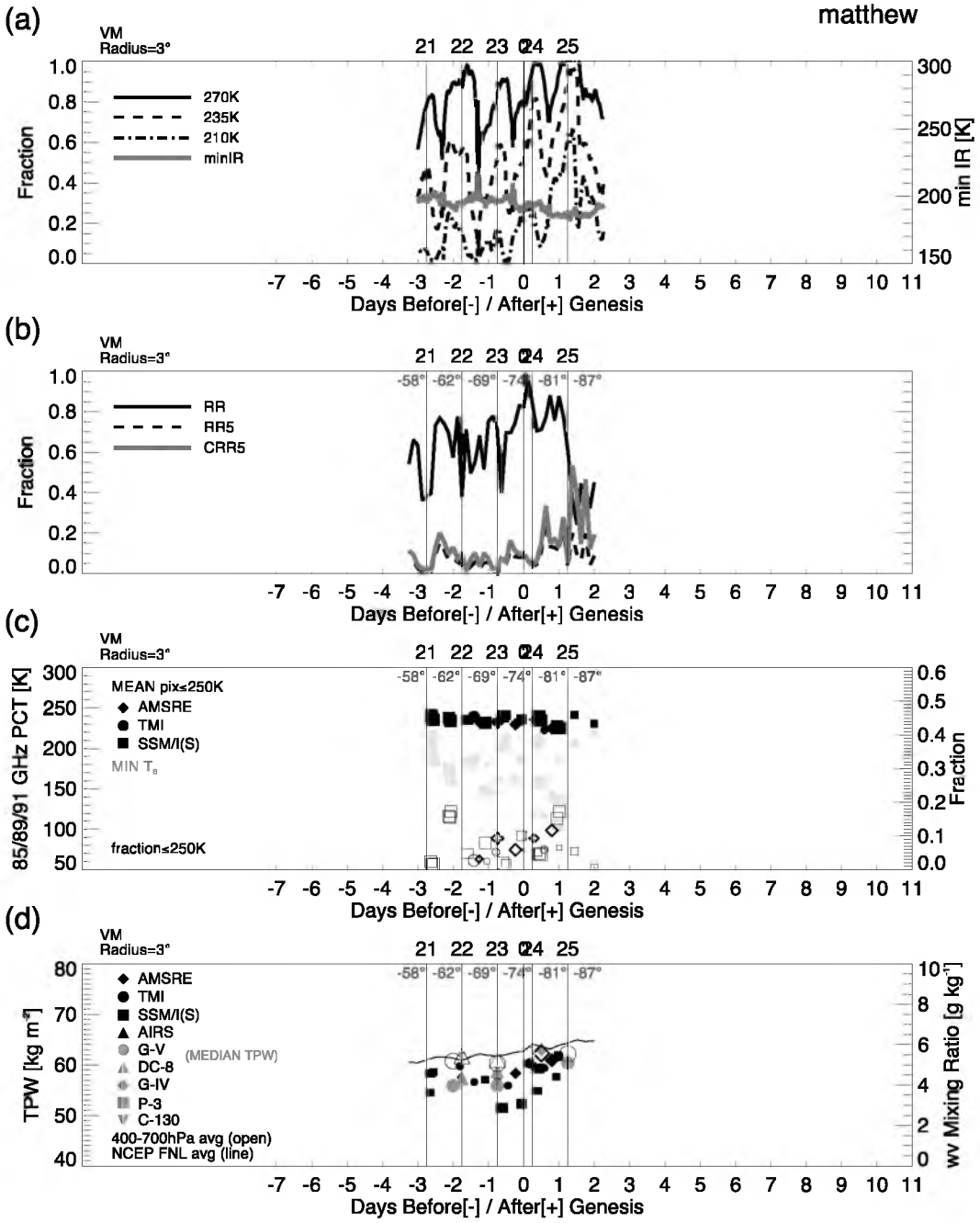
(a)
matthew
VM
Radius=3°
21 22 23 24 25
270K
235K
210K
minIR
Fraction
min IR [K]
Days Before[-] / After[+] Genesis
(b)
RR
RR5
CRR5
-58° -62° -69° -74° -81° -87°
(c)
MEAN pix≤250K
AMSRE
TMI
SSM/I(S)
MIN T_B
fraction≤250K
85/89/91 GHz PCT [K]
Fraction
(d)
AIRS
G-V
DC-8
G-IV
P-3
C-130
(MEDIAN TPW)
400-700hPa avg (open)
NCEP FNL avg (line)
TPW [kg m⁻²]
wv Mixing Ratio [g kg⁻¹]

Figure 5.11. For Matthew, within 1° of 850 hPa VM center: Time series of (a) fraction of IR pixels with $T_b \leq 210$ (black, solid), 235 (dashed), 210 K (dash-dotted), and minimum IR T_b (gray, solid); (b) fraction of raining pixels (solid, black), fraction of total pixels within 3° with rain rate ≥ 5 mm hr^{-1} (dashed), and "convective" fraction, i.e., the fraction of raining pixels with rain rate ≥ 5 mm hr^{-1} (gray, solid); (c) mean PCT of pixels ≤ 250 K (filled black), minimum PCT (filled gray), and fraction of pixels within 3° that are ≤ 250 K (open symbols). (d) TPW from satellites (filled, black) and aircraft (filled, gray), 700–400 hPa mean water vapor mixing ratio from aircraft (open) and NCEP FNL (solid line). For (c) and (d), the size of the symbol indicates the fractional coverage of swath data within the 3° radial circle around the 850 hPa VM center; the larger symbol, the higher the fractional swath data coverage within the radial circle. Upper axis represents the day, as well as the longitude.

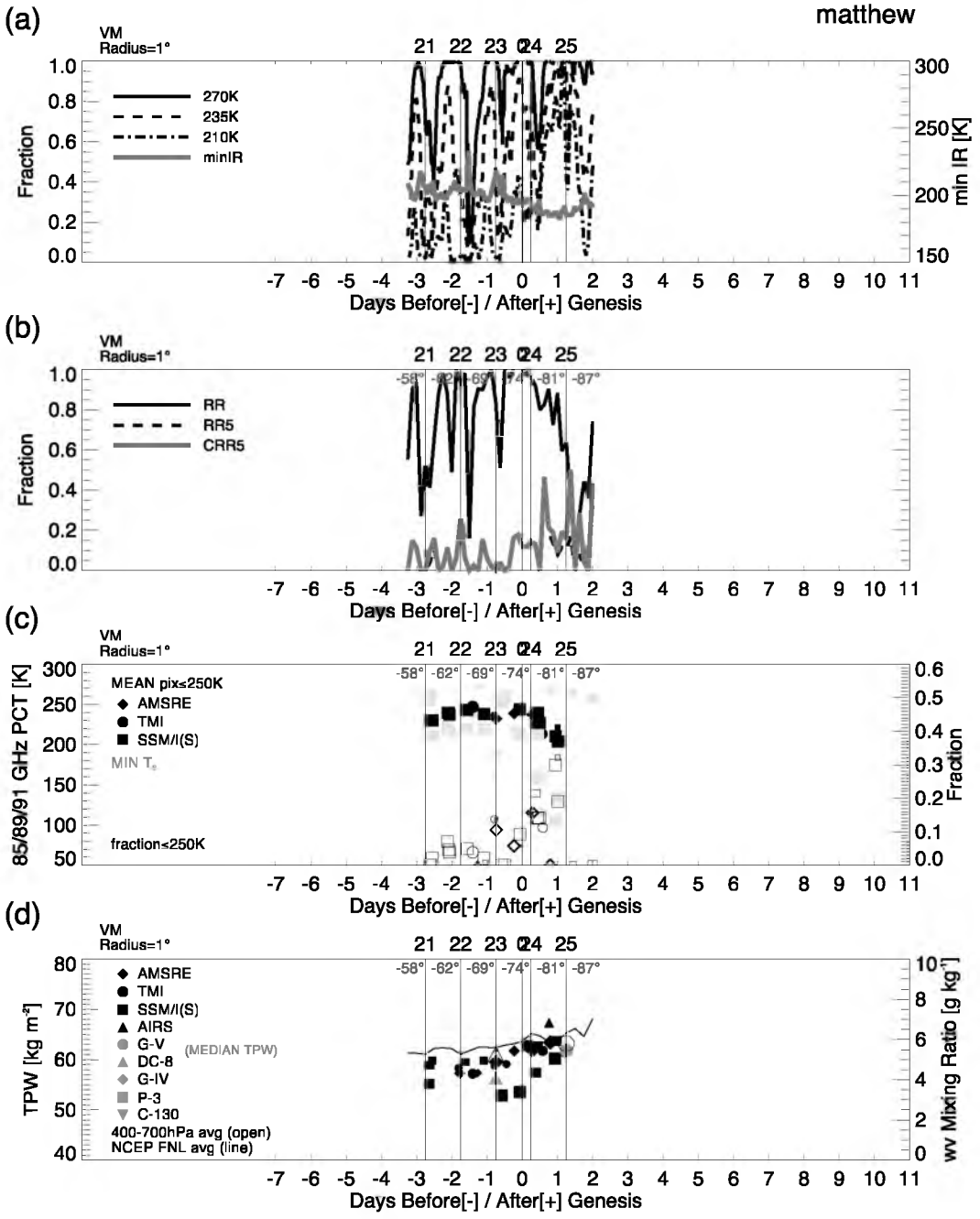
(a)
matthew
VM
Radius=1°
21 22 23 24 25
270K
235K
210K
minIR
Fraction
min IR [K]
Days Before[-] / After[+] Genesis
(b)
RR
RR5
CRR5
(c)
MEAN pix≤250K
AMSRE
TMI
SSM/I(S)
MIN T
fraction≤250K
85/89/91 GHz PCT [K]
(d)
AIRS
G-V
DC-8
G-IV
P-3
C-130
(MEDIAN TPW)
400-700hPa avg (open)
NCEP FNL avg (line)
TPW [kg m⁻²]
wv Mixing Ratio [g kg⁻¹]

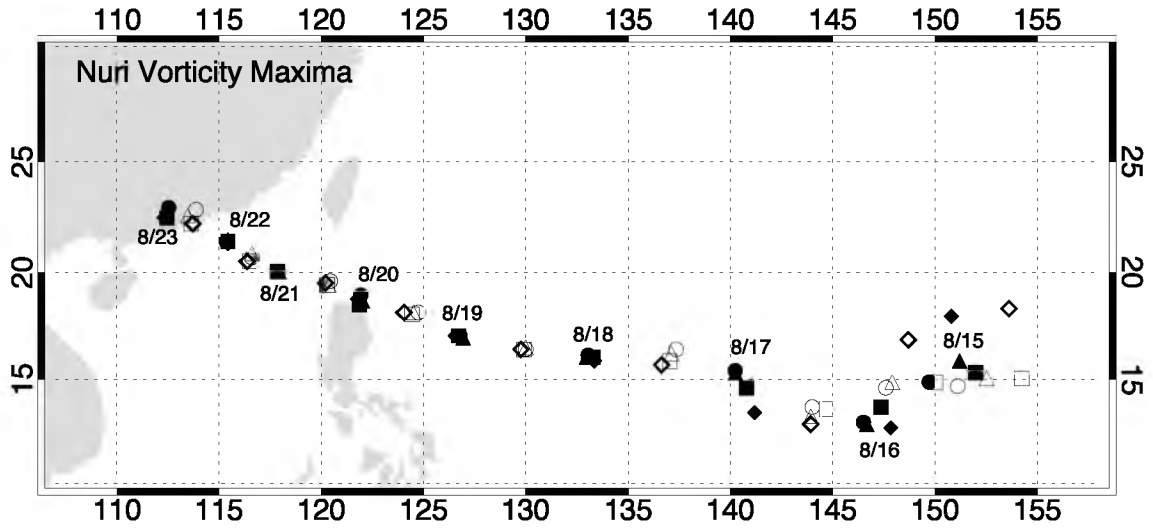

Figure 5.12. Nuri 0000 (closed symbol) and 1200 UTC (open) vorticity maxima locations in the NCEP FNL analysis for 925 (circle), 850 (triangle), 700 (square), and 600 (diamond) hPa.

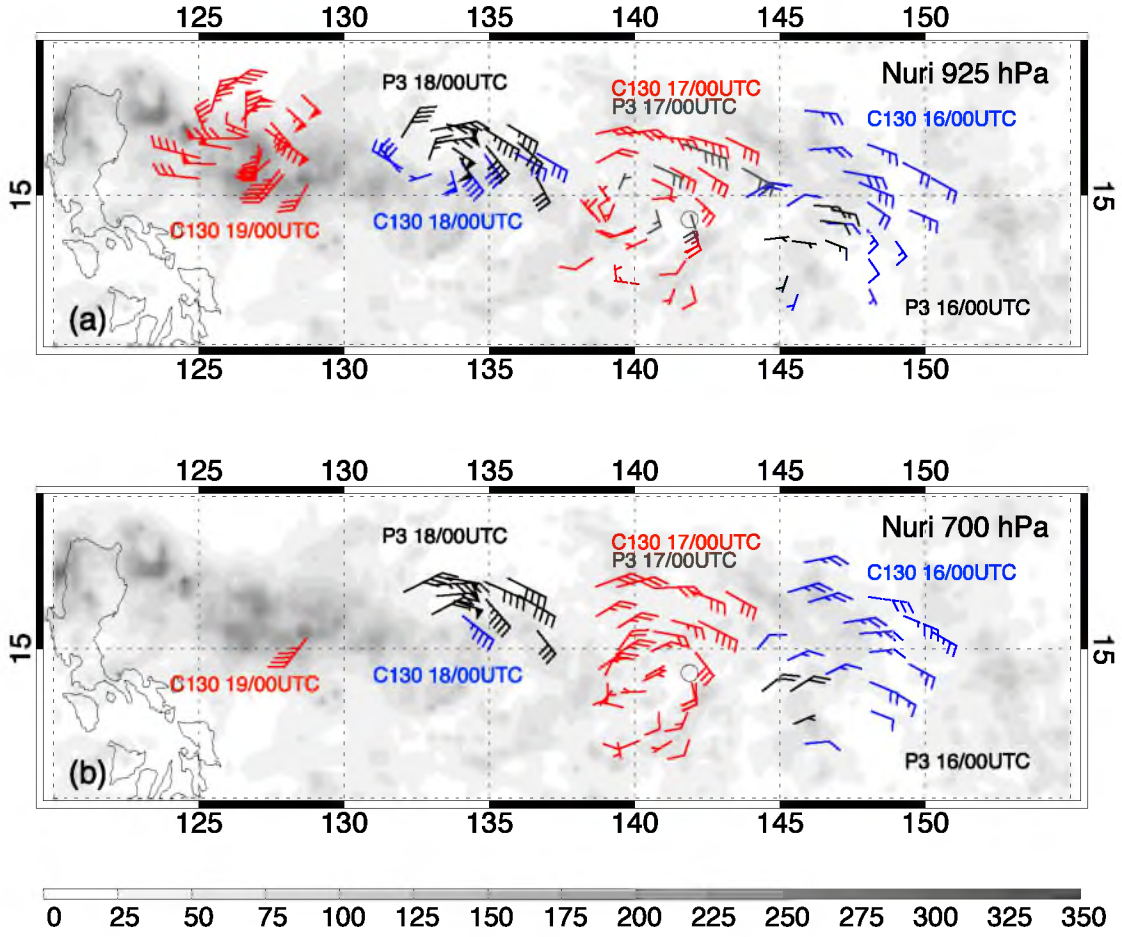

Figure 5.13. Select dropsonde observations at low (a, 925 hPa) and midlevels (b, 600 hPa) of Nuri from 16–19 August. Flights are separated by color and dropsonde locations are time-space adjusted, based on the zonal phase speed of Nuri, to the time indicated. Accumulated rainfall (mm) from TRMM 3B42 is contoured (period is from 0000 UTC 16 August to 0000 UTC 20 August). The open circle is the genesis location at 1800 UTC 16 August.

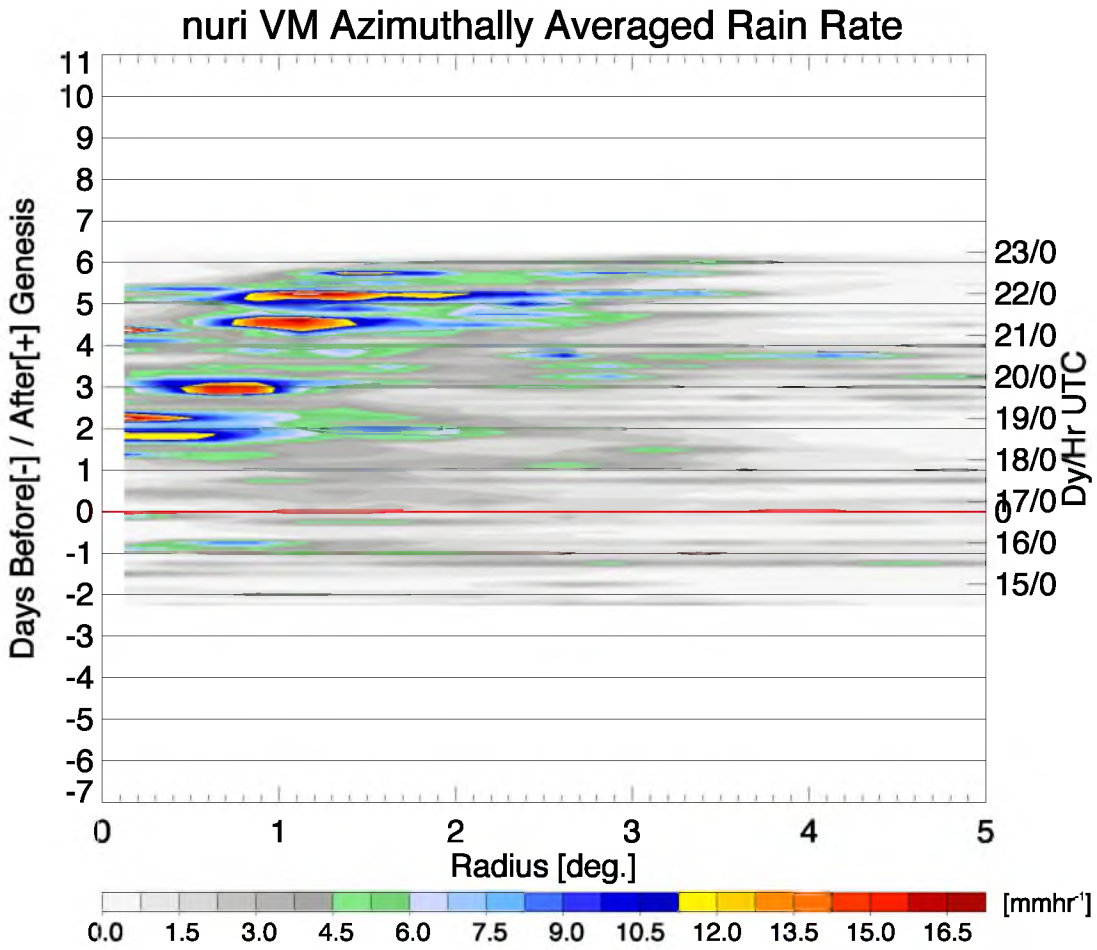

Figure 5.14. Time series of mean rain rate (from TRMM 3B42) as a function of radial distance from the 850 hPa VM center for Nuri.

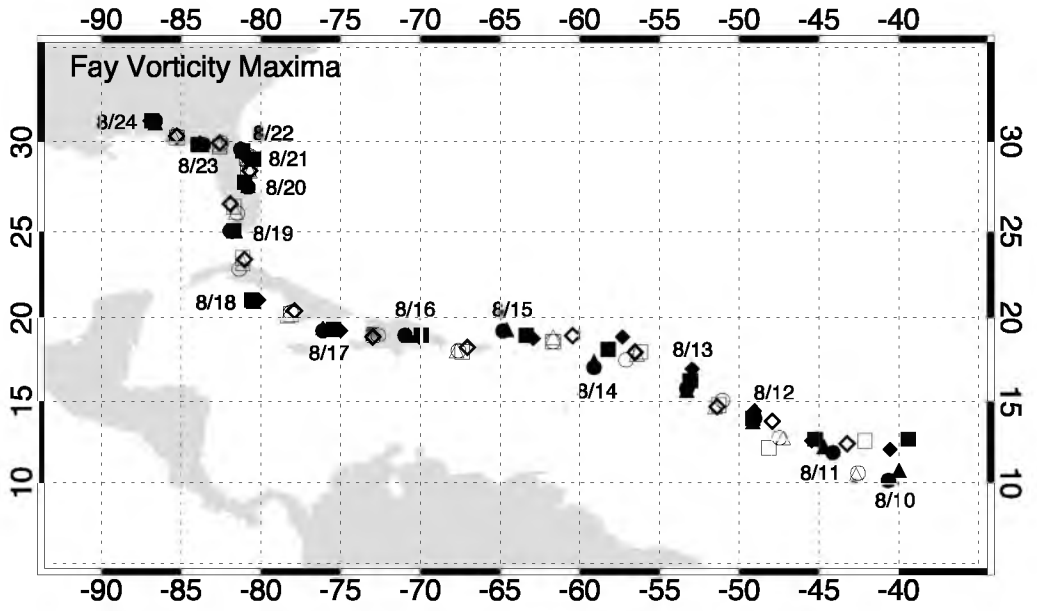

Figure 5.15. Fay 0000 (closed symbol) and 1200 UTC (open) vorticity maxima locations in the NCEP FNL analysis for 925 (circle), 850 (triangle), 700 (square), and 600 (diamond) hPa.

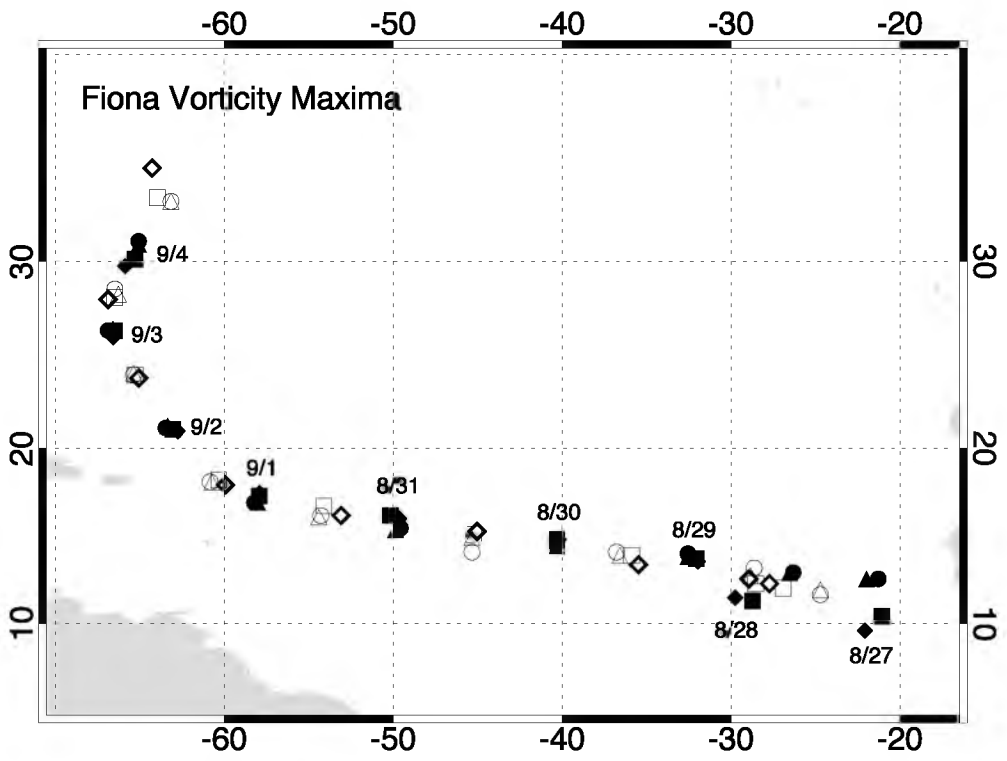

Figure 5.16. Fiona 0000 (closed symbol) and 1200 UTC (open) vorticity maxima locations in the NCEP FNL analysis for 925 (circle), 850 (triangle), 700 (square), and 600 (diamond) hPa.

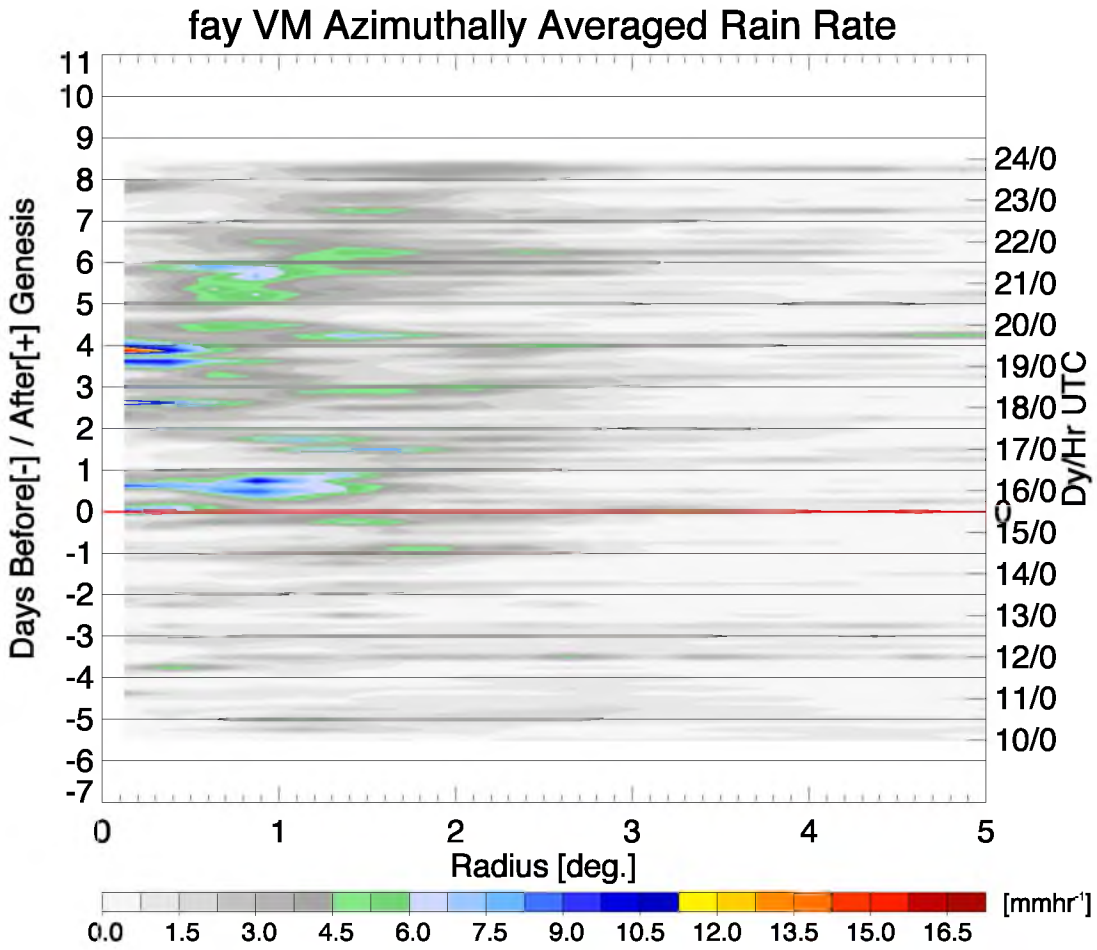

Figure 5.17. Time series of mean rain rate (from TRMM 3B42) as a function of radial distance from the 850 hPa VM center for Fay.

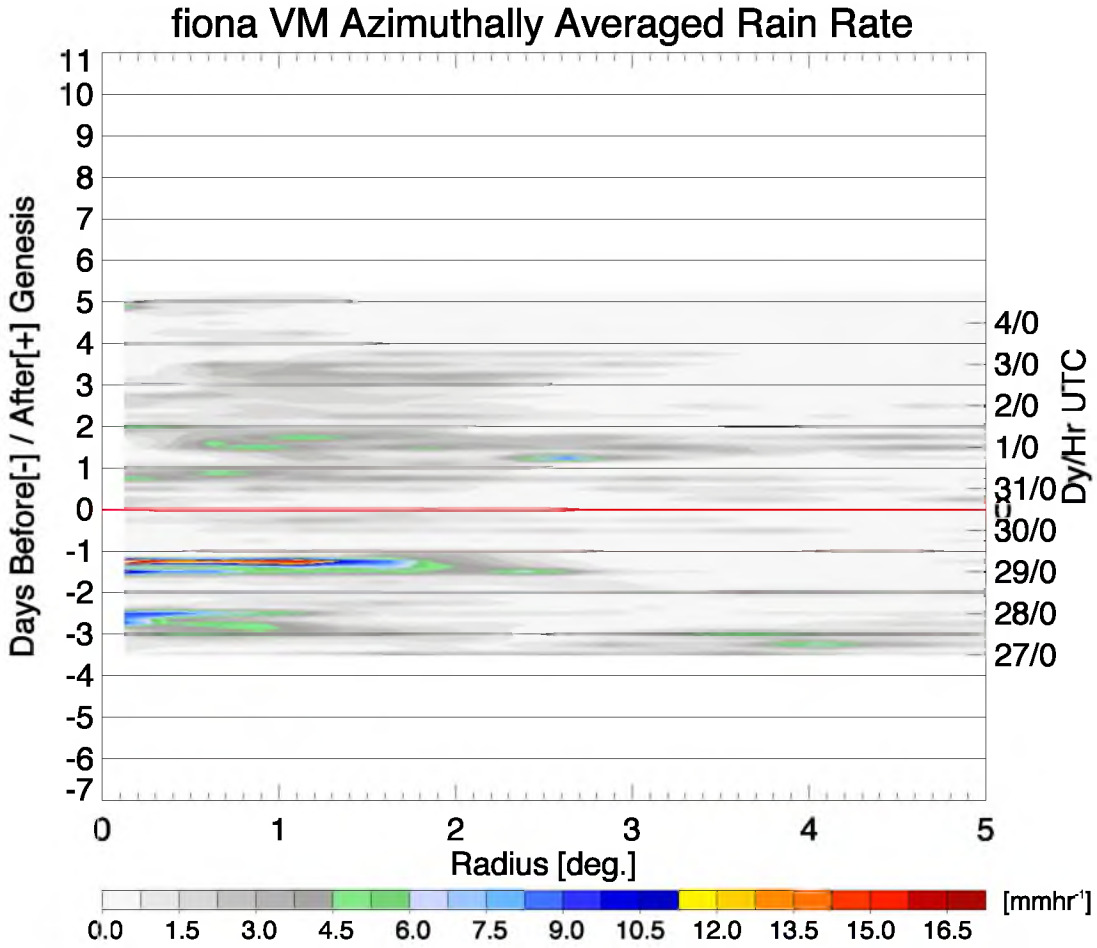

Figure 5.18. Time series of mean rain rate (from TRMM 3B42) as a function of radial distance from the 850 hPa VM center for Fiona.

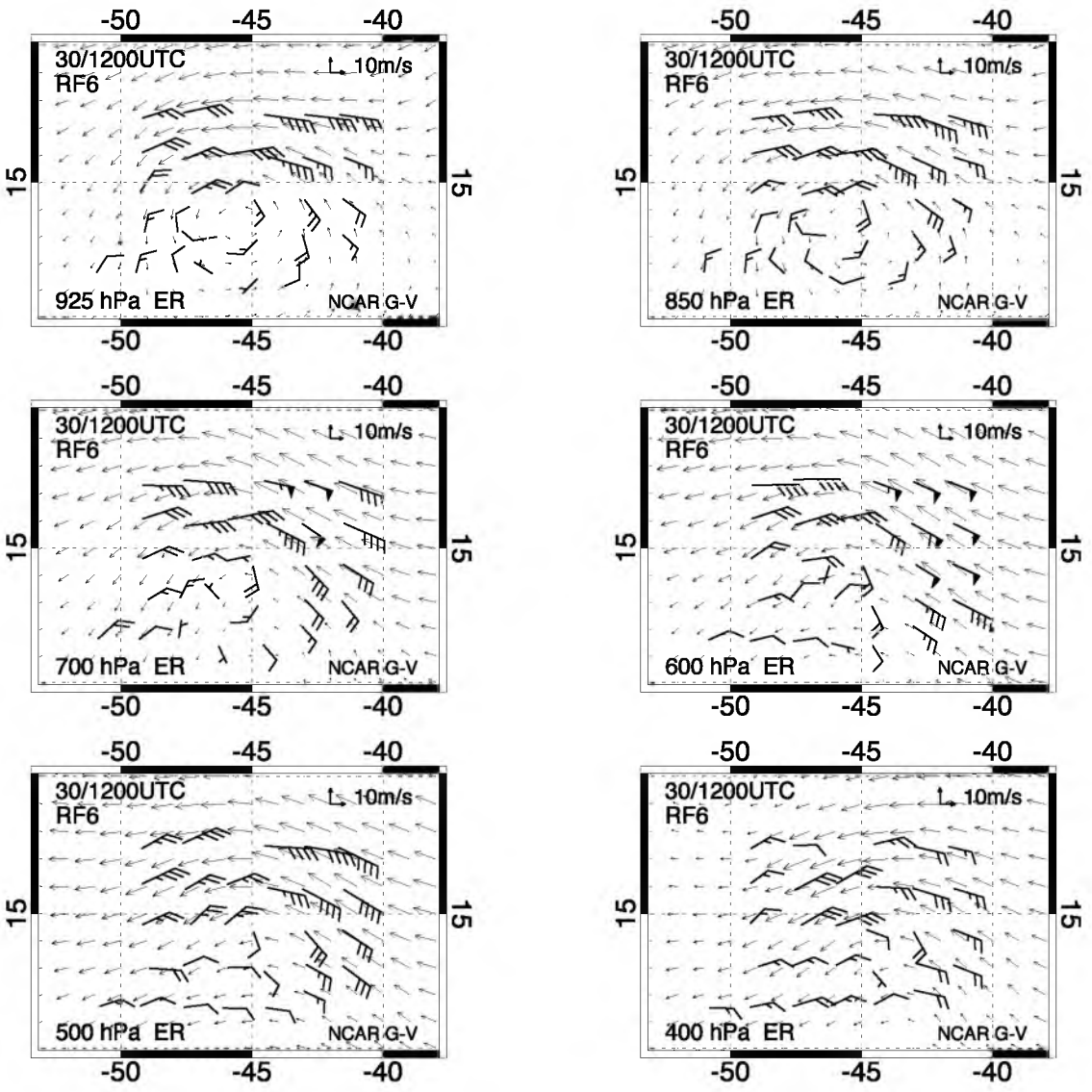

Figure 5.19. Dropsonde observations (barbs; full barb is 10 kt) from the NCAR/NSF G-V research flight on 30 August into Fiona at 925, 850, 700, 600, 500, and 400 hPa; locations are corrected using the disturbance phase speeds to 1200 UTC 30 August. Vectors are from NCEP FNL operational analysis.

Figure 5.20. For Fiona, within 1° of 850 hPa VM center: Time series of (a) fraction of IR pixels with $T_b \leq 210$ (black, solid), 235 (dashed), 210 K (dash-dotted), and minimum IR T_b (gray, solid); (b) fraction of raining pixels (solid, black), fraction of total pixels within 3° with rain rate $\geq$ 5 mm hr^{-1} (dashed), and "convective" fraction, i.e., the fraction of raining pixels with rain rate $\geq$ 5 mm hr^{-1} (gray, solid); (c) mean PCT of pixels $\leq$ 250 K (filled black), minimum PCT (filled gray), and fraction of pixels within 3° that are $\leq$ 250 K (open symbols). (d) TPW from satellites (filled, black) and aircraft (filled, gray), 700–400 hPa mean water vapor mixing ratio from aircraft (open) and NCEP FNL (solid line). For (c) and (d), the size of the symbol indicates the fractional coverage of swath data within the 3° radial circle around the 850 hPa VM center; the larger symbol, the higher the fractional swath data coverage within the radial circle. Upper axis represents the day, as well as the longitude.

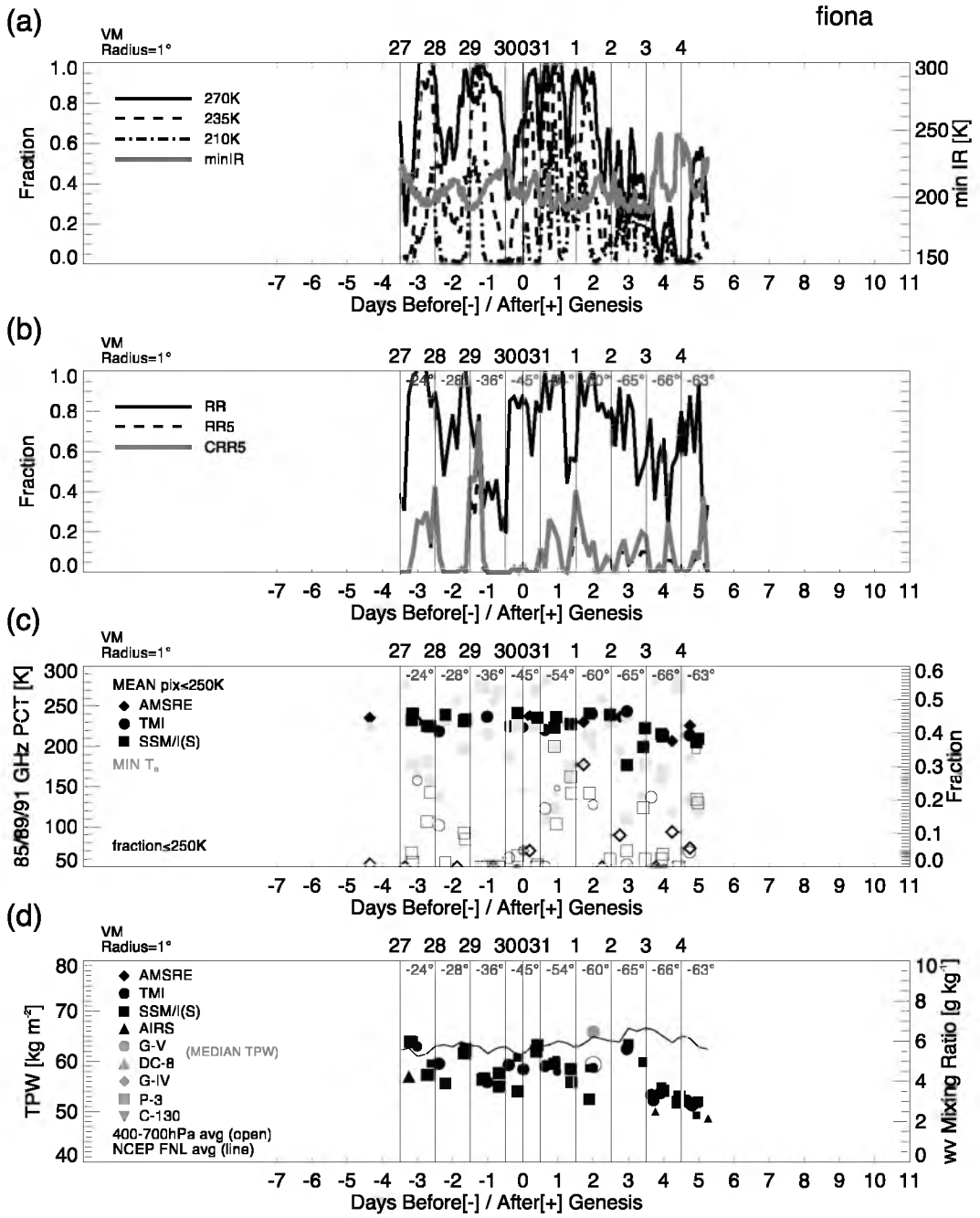
(a)
fiona
VM
Radius=1°
27 28 29 30031 1 2 3 4
270K
235K
210K
minIR
Fraction
min IR [K]
Days Before[-] / After[+] Genesis
(b)
RR
RR5
CRR5
(c)
MEAN pix≤250K
AMSRE
TMI
SSM/I(S)
MIN T_B
fraction≤250K
85/89/91 GHz PCT [K]
Fraction
(d)
AIRS
G-V
DC-8
G-IV
P-3
C-130
(MEDIAN TPW)
400-700hPa avg (open)
NCEP FNL avg (line)
TPW [kg m^-2]
wv Mixing Ratio [g kg^-1]

Figure 5.21. For Fay, within 3° of 850 hPa VM center: Time series of (a) fraction of IR pixels with $T_b \leq 210$ (black, solid), 235 (dashed), 210 K (dash-dotted), and minimum IR T_b (gray, solid); (b) fraction of raining pixels (solid, black), fraction of total pixels within 3° with rain rate $\geq$ 5 mm hr^{-1} (dashed), and "convective" fraction, i.e., the fraction of raining pixels with rain rate $\geq$ 5 mm hr^{-1} (gray, solid); (c) mean PCT of pixels $\leq$ 250 K (filled black), minimum PCT (filled gray), and fraction of pixels within 3° that are $\leq$ 250 K (open symbols). (d) TPW from satellites (filled, black) and aircraft (filled, gray), 700–400 hPa mean water vapor mixing ratio from aircraft (open) and NCEP FNL (solid line). For (c) and (d), the size of the symbol indicates the fractional coverage of swath data within the 3° radial circle around the 850 hPa VM center; the larger symbol, the higher the fractional swath data coverage within the radial circle. Upper axis represents the day, as well as the longitude.

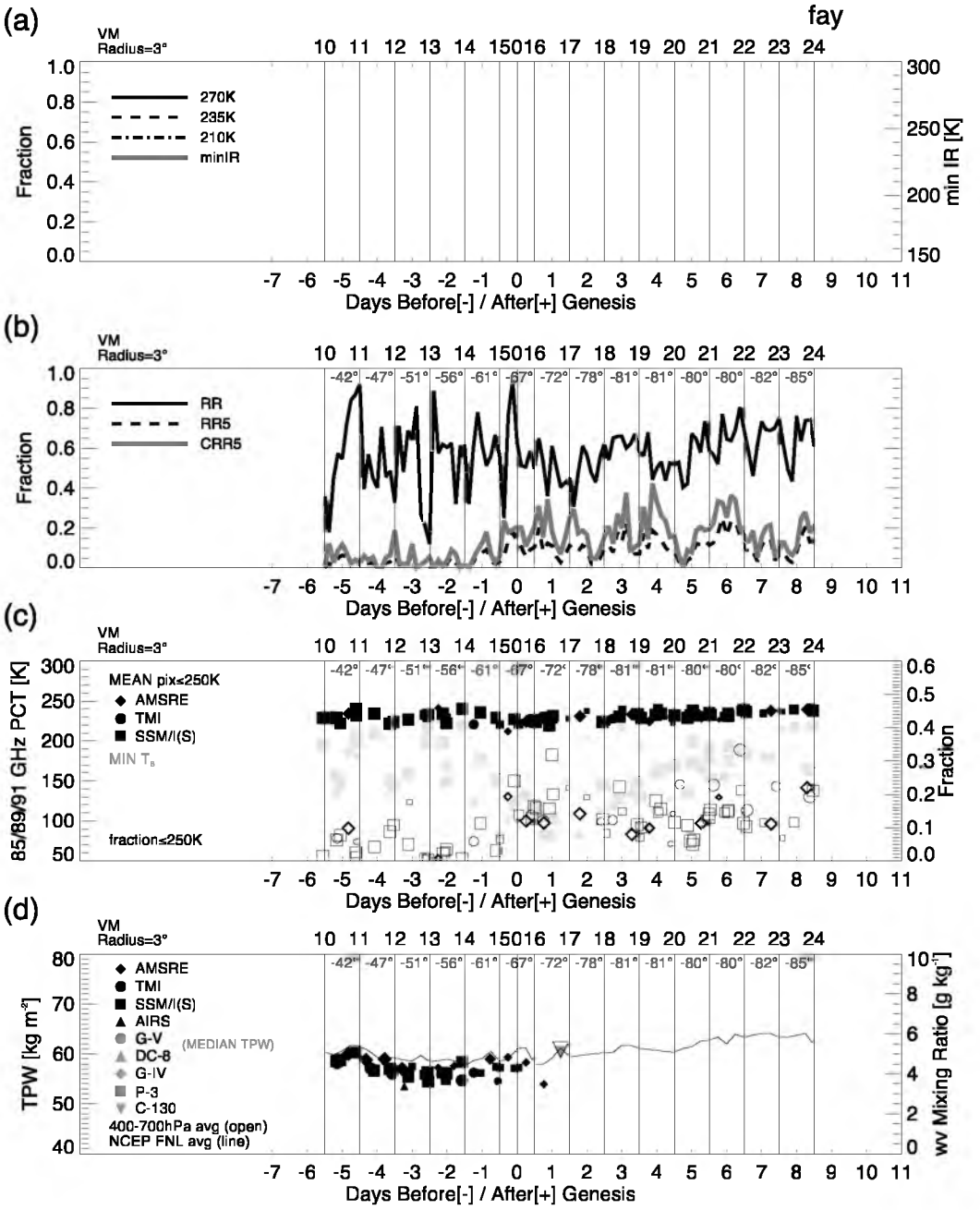
(a)
fay
VM
Radius=3°
10 11 12 13 14 15016 17 18 19 20 21 22 23 24
270K
235K
210K
minIR
Fraction
min IR [K]
(b)
RR
RR5
CRR5
-42° -47° -51° -56° -61° -67° -72° -78° -81° -81° -80° -80° -82° -85°
(c)
MEAN pix≤250K
AMSRE
TMI
SSM/I(S)
MIN Tb
fraction≤250K
85/89/91 GHz PCT [K]
(d)
AMSRE
TMI
SSM/I(S)
AIRS
G-V
DC-8
G-IV
P-3
C-130
(MEDIAN TPW)
400-700hPa avg (open)
NCEP FNL avg (line)
TPW [kg m-2]
wv Mixing Ratio [g kg-1]
-7 -6 -5 -4 -3 -2 -1 0 1 2 3 4 5 6 7 8 9 10 11
Days Before[-] / After[+] Genesis

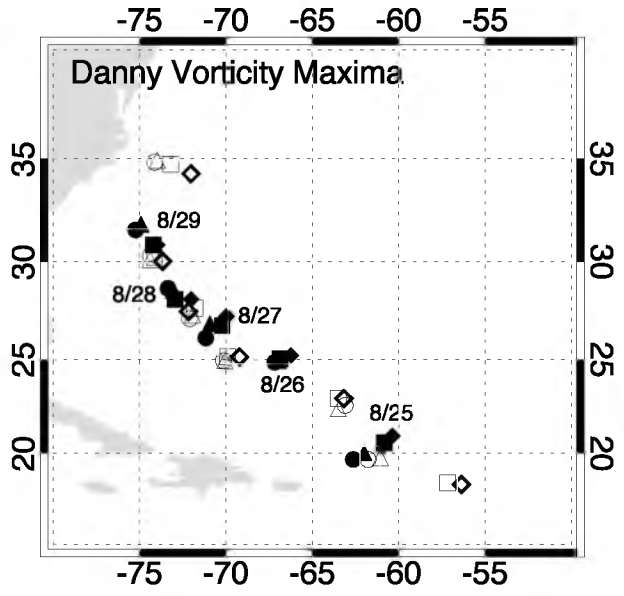

Figure 5.22. Danny 0000 (closed symbol) and 1200 UTC (open) vorticity maxima locations in the NCEP FNL analysis for 925 (circle), 850 (triangle), 700 (square), and 600 (diamond) hPa.

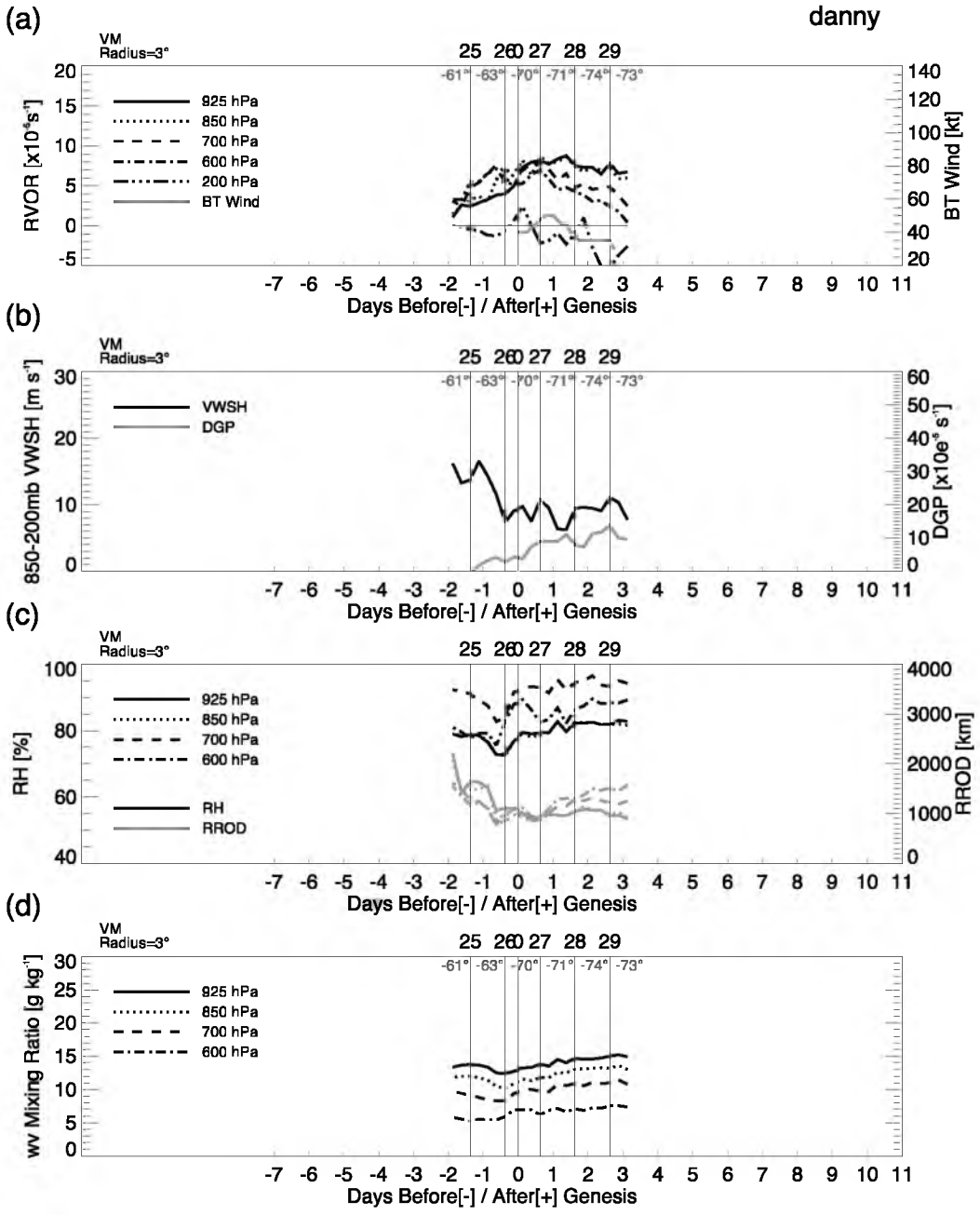

Figure 5.23. For Danny, within 3° of 850 hPa VM center in NCEP FNL analysis: Time series of (a) 925 (black, solid), 850 (dotted), 700 (dashed), and 600 (dash-dotted) hPa relative vorticity, as well as the NHC advisory intensity (gray); (b) deep layer (850–200 hPa) vertical wind shear (VWSH; black) and daily genesis potential (DGP; gray); (c) 925 (solid), 850 (dotted), 700 (dashed), and 600 (dotted-dashed) hPa relative humidity (black) and Rossby radius of deformation (gray); (d) 925 (solid), 850 (dotted), 700 (dashed), 600 (dotted-dashed) hPa water vapor mixing ratio. Upper axis represents the day, as well as the longitude (gray).

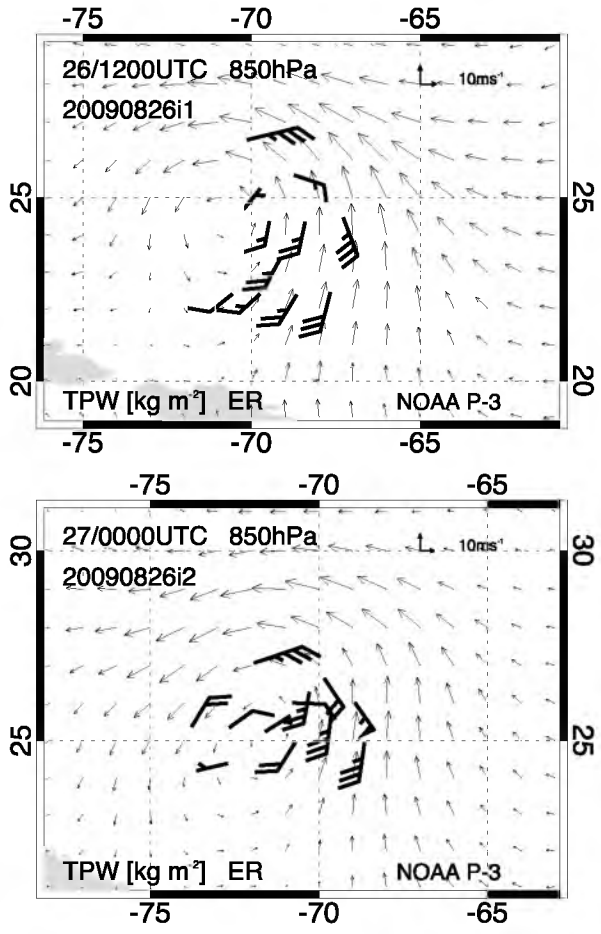

Figure 5.24. Dropsonde observations (barbs; full barb is 10 kt) from the NOAA P-3 research flight on 26 August (top) and 27 August (bottom) into Danny at 850 hPa; locations are corrected using the disturbance phase speeds to 1200 UTC 26 August and 27 August, respectively. Vectors are from NCEP FNL operational analysis.

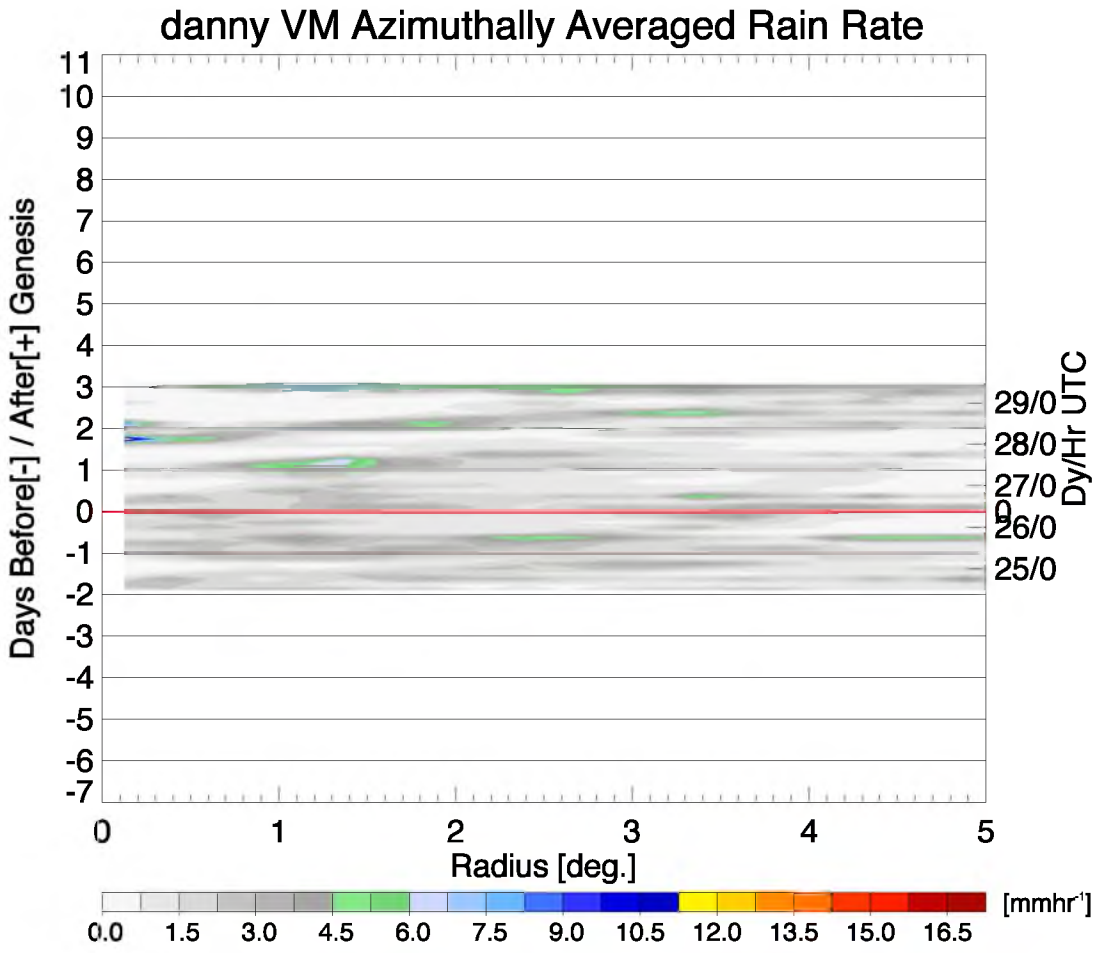

Figure 5.25. Time series of mean rain rate (from TRMM 3B42) as a function of radial distance from the 850 hPa VM center for Danny.

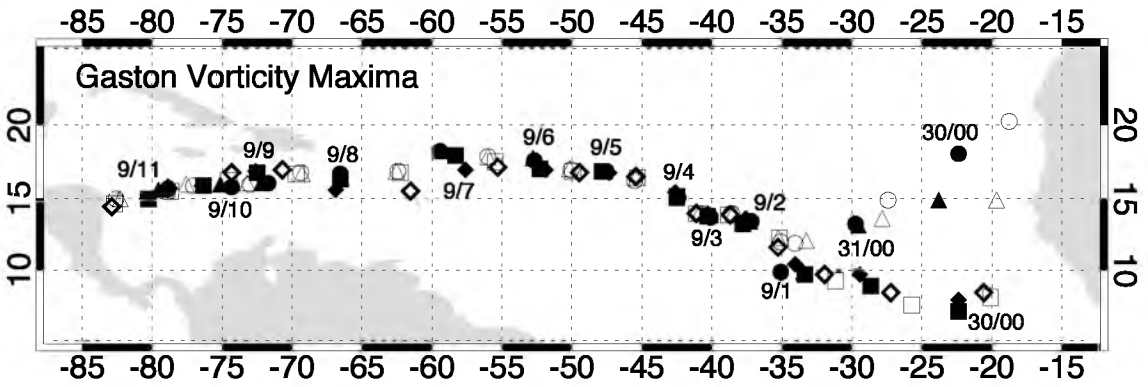

Figure 5.26. Gaston 0000 (closed symbol) and 1200 UTC (open) vorticity maxima locations in the NCEP FNL analysis for 925 (circle), 850 (triangle), 700 (square), and 600 (diamond) hPa.

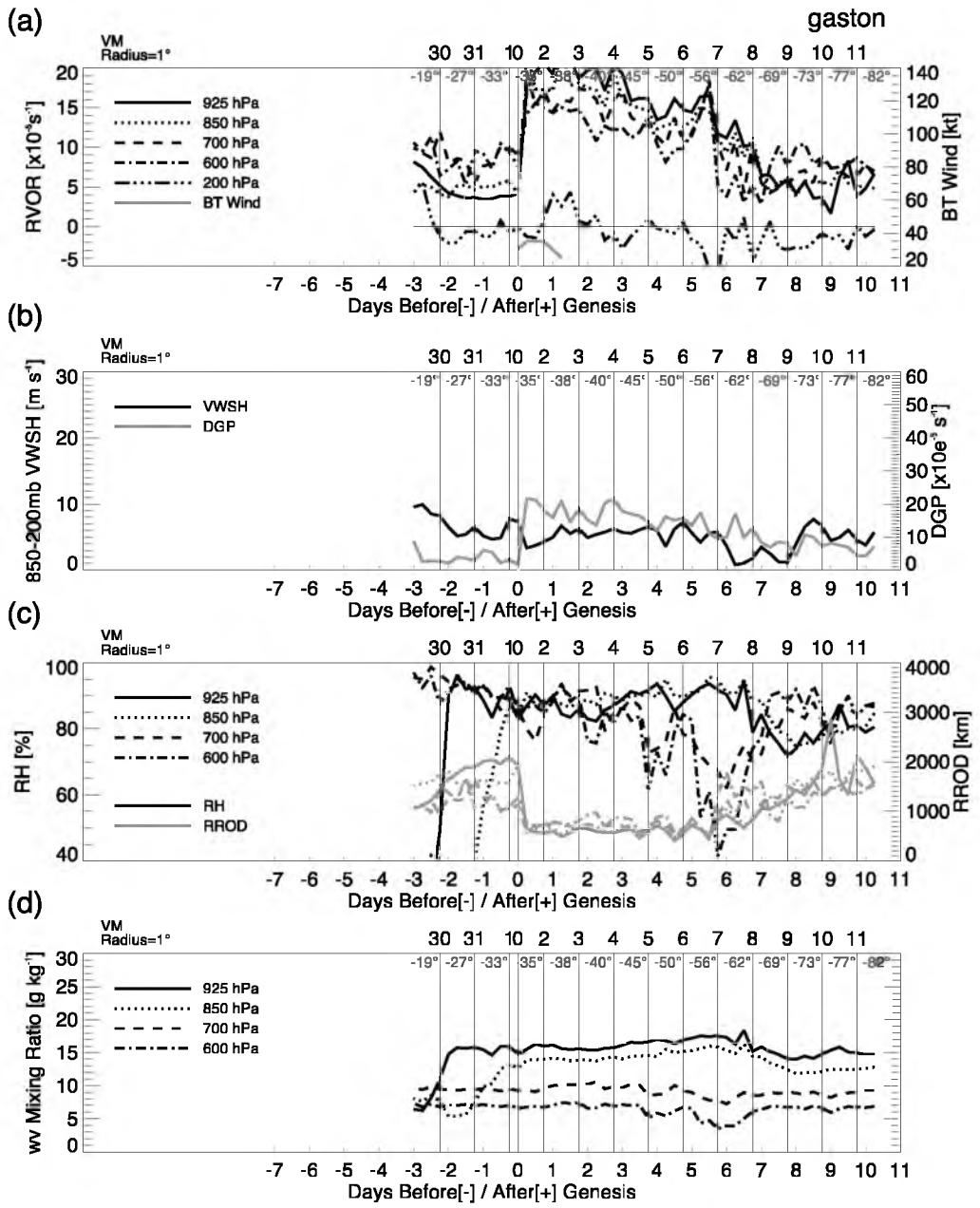

Figure 5.27. For Gaston, within 1° of 850 hPa VM center in NCEP FNL analysis: Time series of (a) 925 (black, solid), 850 (dotted), 700 (dashed), and 600 (dash-dotted) hPa relative vorticity, as well as the NHC advisory intensity (gray); (b) deep layer (850–200 hPa) vertical wind shear (VWSH; black) and daily genesis potential (DGP; gray); (c) 925 (solid), 850 (dotted), 700 (dashed), and 600 (dotted-dashed) hPa relative humidity (black) and Rossby radius of deformation (gray); (d) 925 (solid), 850 (dotted), 700 (dashed), 600 (dotted-dashed) hPa water vapor mixing ratio. Upper axis represents the day, as well as the longitude (gray).

Figure 5.28. For Gaston, within 3° of 850 hPa VM center: Time series of (a) fraction of IR pixels with $T_b \leq 210$ (black, solid), 235 (dashed), 210 K (dash-dotted), and minimum IR T_b (gray, solid); (b) fraction of raining pixels (solid, black), fraction of total pixels within 3° with rain rate ≥ 5 mm hr^{-1} (dashed), and "convective" fraction, i.e., the fraction of raining pixels with rain rate ≥ 5 mm hr^{-1} (gray, solid); (c) mean PCT of pixels ≤ 250 K (filled black), minimum PCT (filled gray), and fraction of pixels within 3° that are ≤ 250 K (open symbols). (d) TPW from satellites (filled, black) and aircraft (filled, gray), 700–400 hPa mean water vapor mixing ratio from aircraft (open) and NCEP FNL (solid line). For (c) and (d), the size of the symbol indicates the fractional coverage of swath data within the 3° radial circle around the 850 hPa VM center; the larger symbol, the higher the fractional swath data coverage within the radial circle. Upper axis represents the day, as well as the longitude.

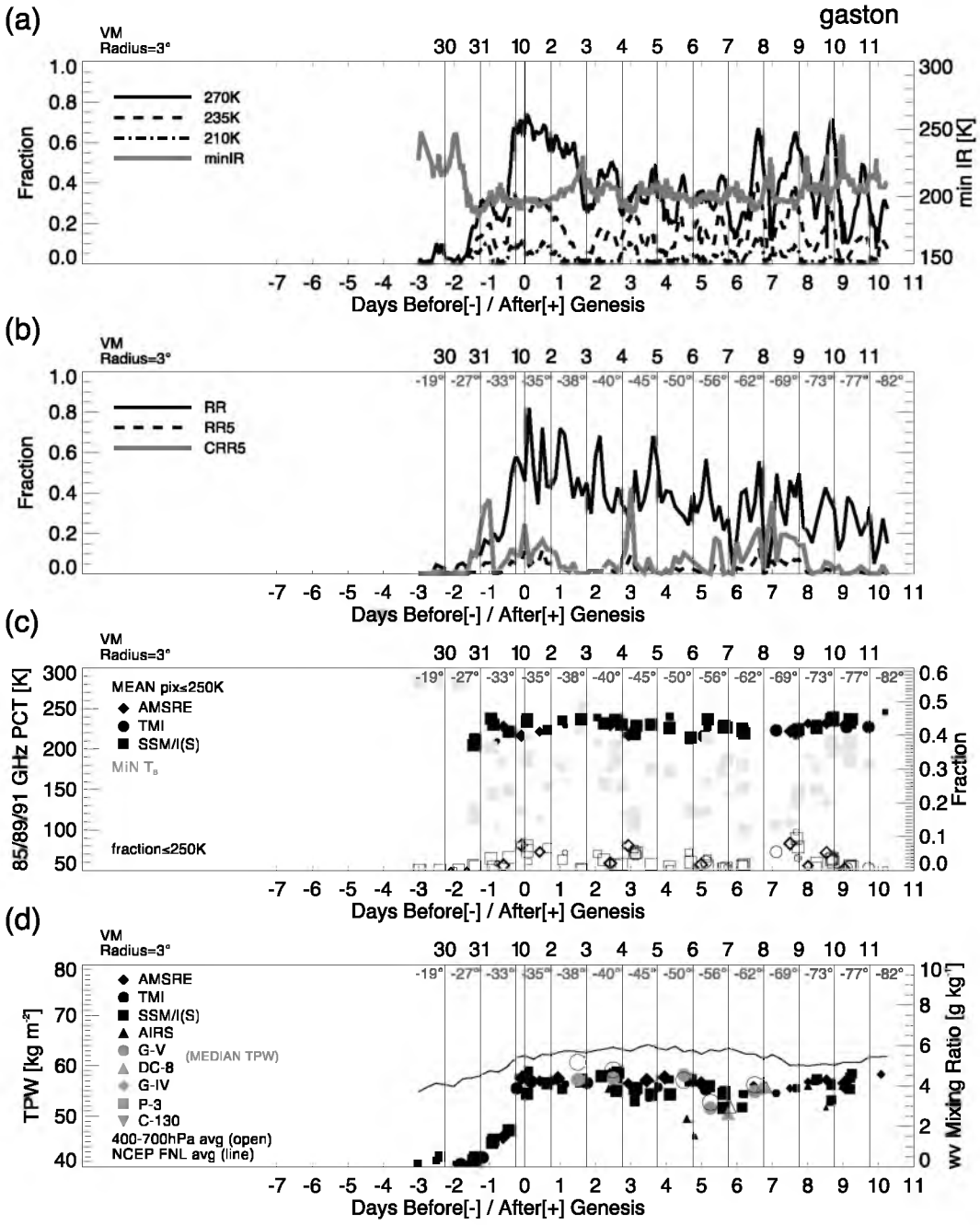
(a)
gaston
VM
Radius=3°
30 31 10 2 3 4 5 6 7 8 9 10 11
270K
235K
210K
minIR
Fraction
min IR [K]
-7 -6 -5 -4 -3 -2 -1 0 1 2 3 4 5 6 7 8 9 10 11
Days Before[-] / After[+] Genesis
(b)
VM
Radius=3°
RR
RR5
CRR5
Fraction
-19° -27° -33° -35° -38° -40° -45° -50° -56° -62° -69° -73° -77° -82°
Days Before[-] / After[+] Genesis
(c)
VM
Radius=3°
MEAN pix≤250K
AMSRE
TMI
SSM/I(S)
MiN Ts
fraction≤250K
85/89/91 GHz PCT [K]
Fraction
Days Before[-] / After[+] Genesis
(d)
VM
Radius=3°
AMSRE
TMI
SSM/I(S)
AIRS
G-V
DC-8
G-IV
P-3
C-130
(MEDIAN TPW)
400-700hPa avg (open)
NCEP FNL avg (line)
TPW [kg m-2]
wv Mixing Ratio [g kg-1]
Days Before[-] / After[+] Genesis

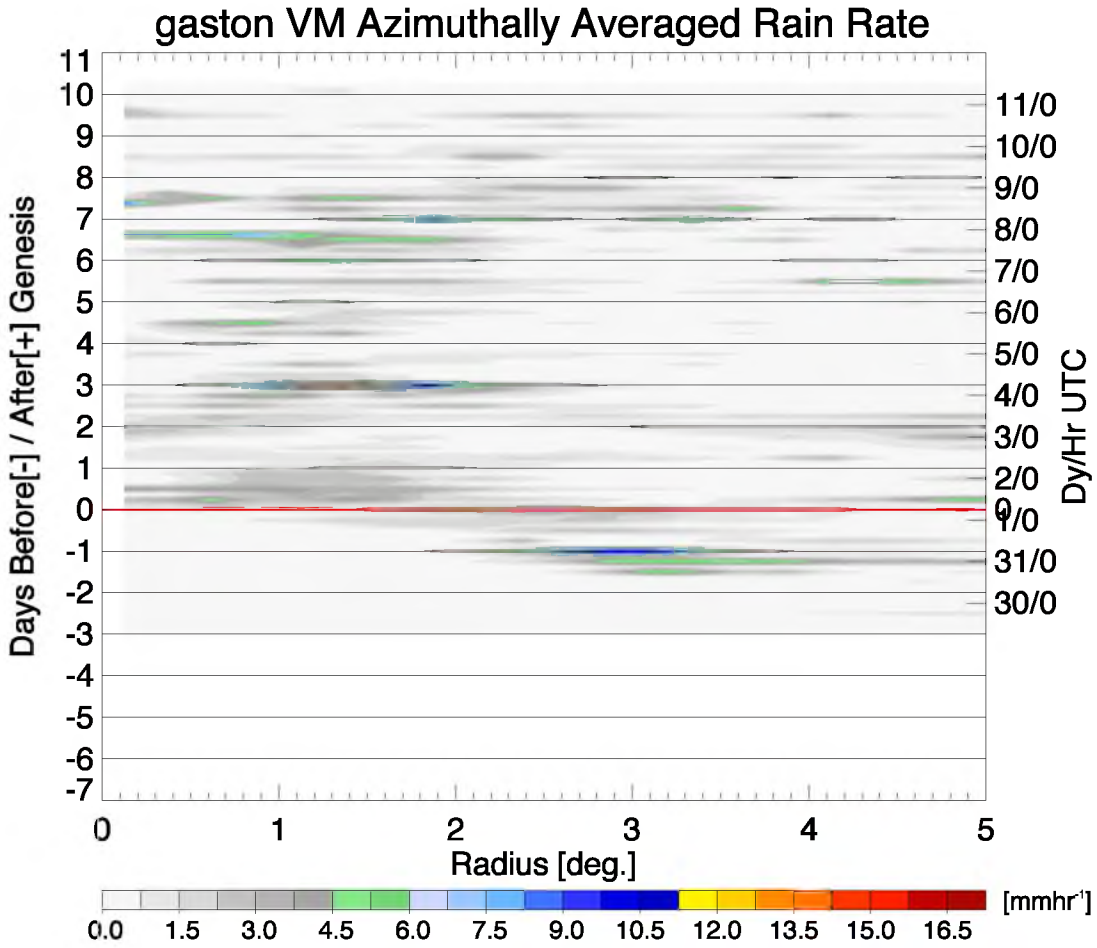

Figure 5.29. Time series of mean rain rate (from TRMM 3B42) as a function of radial distance from the 850 hPa VM center for Gaston.

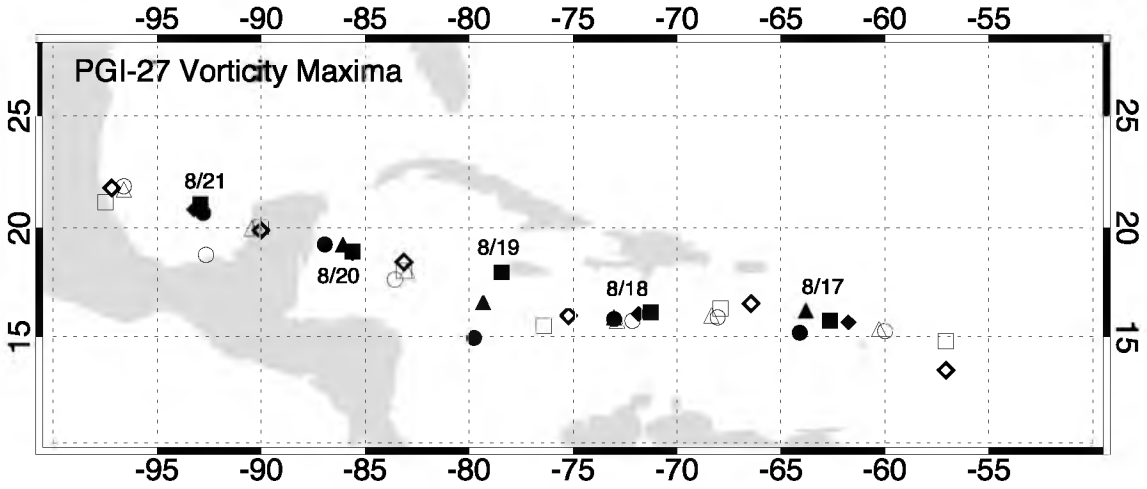

Figure 5.30. PGI-27 0000 (closed symbol) and 1200 UTC (open) vorticity maxima locations in the NCEP FNL analysis for 925 (circle), 850 (triangle), 700 (square), and 600 (diamond) hPa.

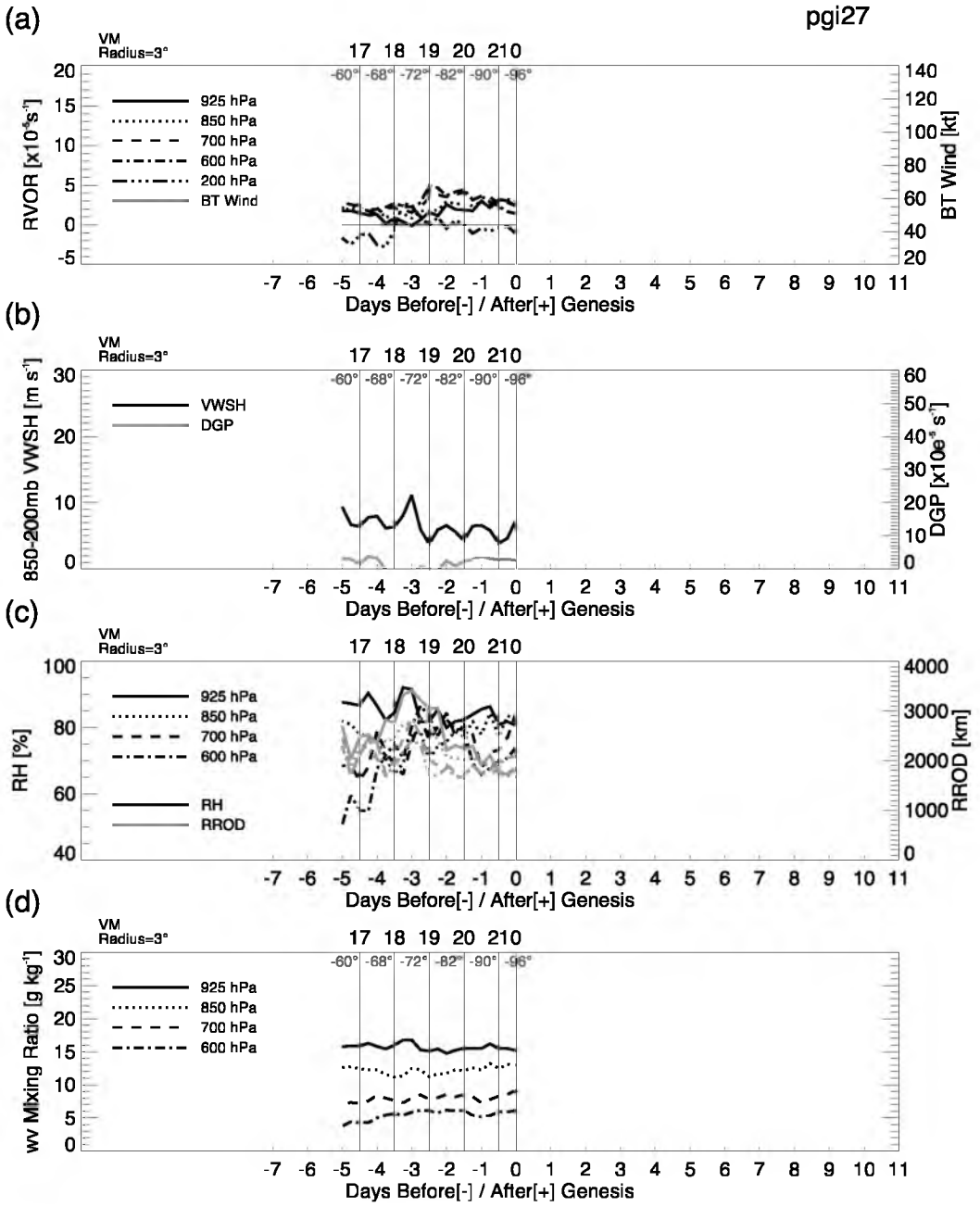

Figure 5.31. For PGI-27, within 3° of 850 hPa VM center in NCEP FNL analysis: Time series of (a) 925 (black, solid), 850 (dotted), 700 (dashed), and 600 (dash-dotted) hPa relative vorticity, as well as the NHC advisory intensity (gray); (b) deep layer (850–200 hPa) vertical wind shear (VWSH; black) and daily genesis potential (DGP; gray); (c) 925 (solid), 850 (dotted), 700 (dashed), and 600 (dotted-dashed) hPa relative humidity (black) and Rossby radius of deformation (gray); (d) 925 (solid), 850 (dotted), 700 (dashed), 600 (dotted-dashed) hPa water vapor mixing ratio. Upper axis represents the day, as well as the longitude (gray).

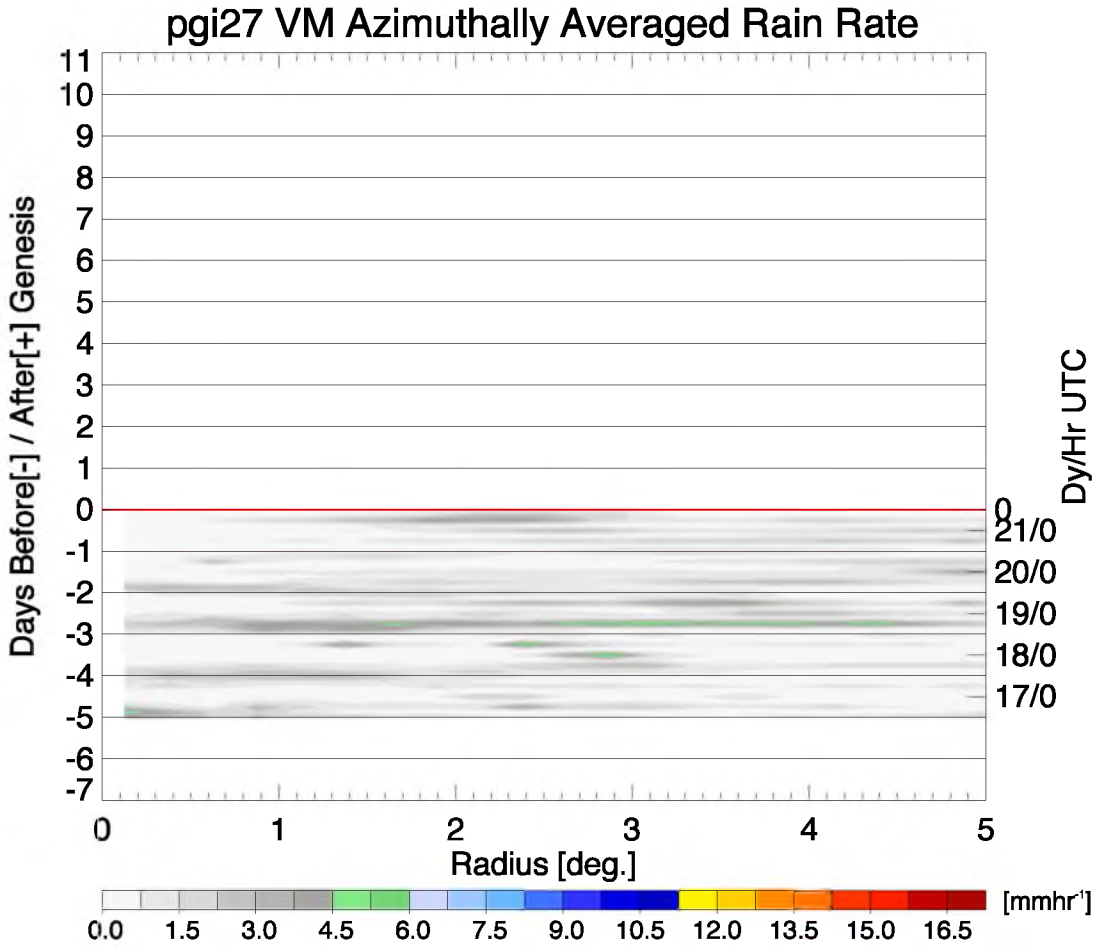

Figure 5.32. Time series of mean rain rate (from TRMM 3B42) as a function of radial distance from the 850 hPa VM center for PGI-27.

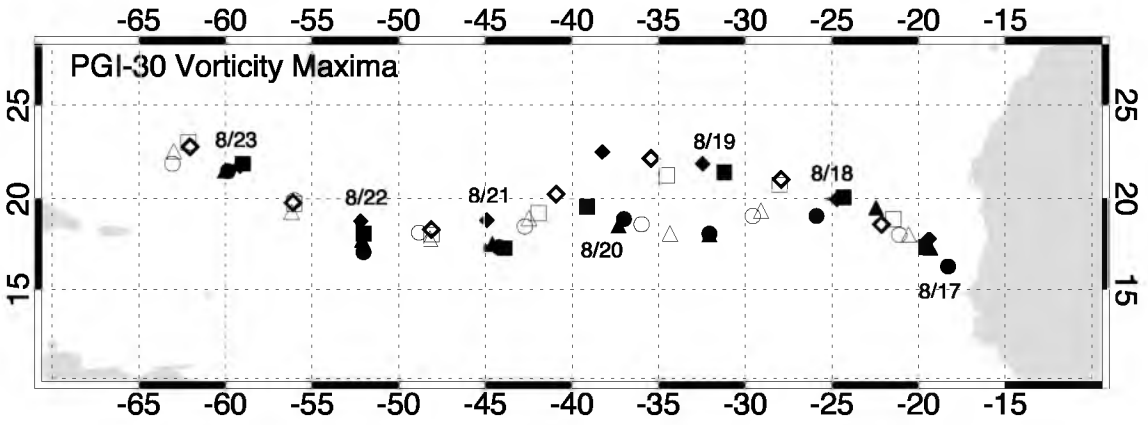

Figure 5.33. PGI-30 0000 (closed symbol) and 1200 UTC (open) vorticity maxima locations in the NCEP FNL analysis for 925 (circle), 850 (triangle), 700 (square), and 600 (diamond) hPa.

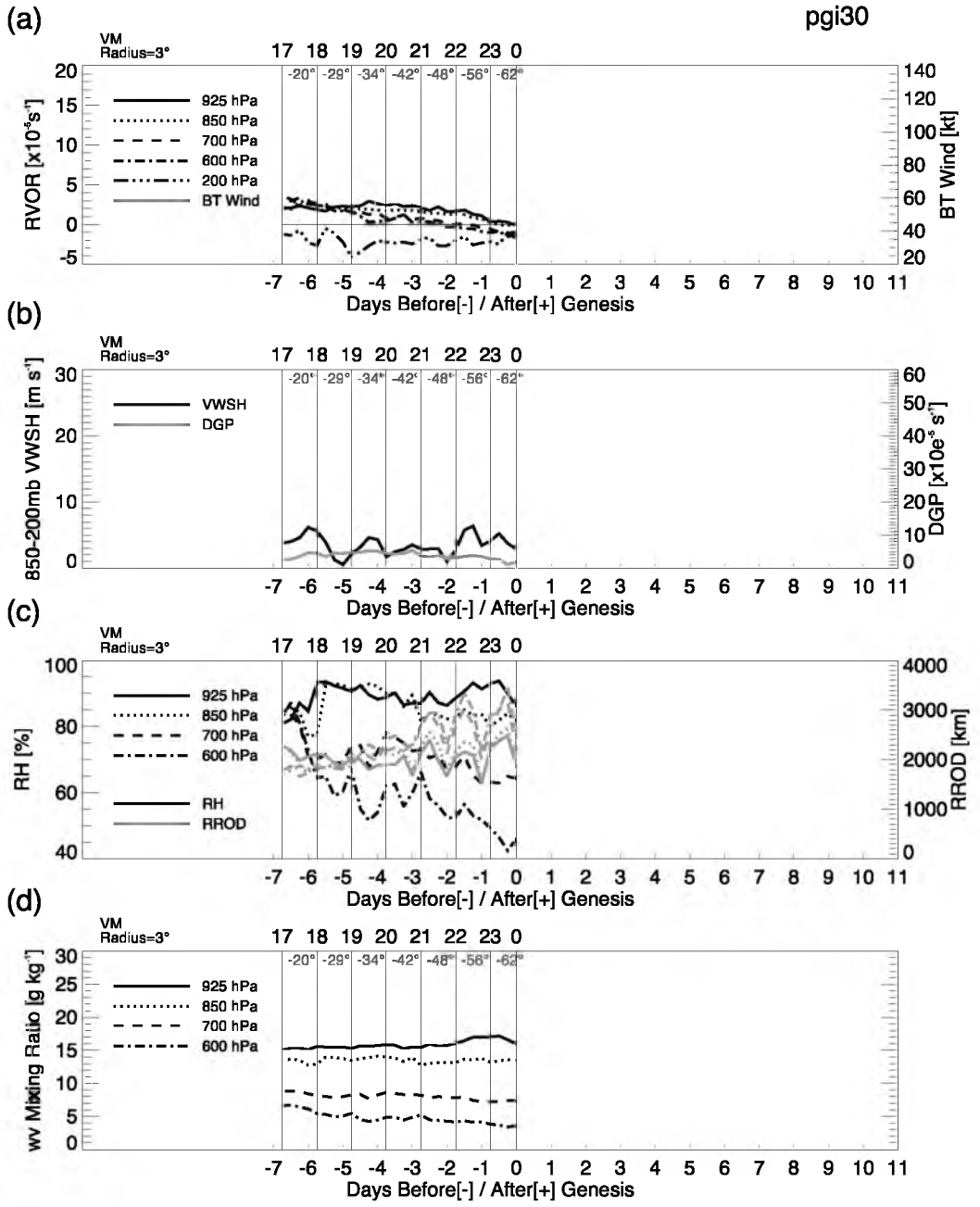

Figure 5.34. For PGI-30, within 3° of 850 hPa VM center in NCEP FNL analysis: Time series of (a) 925 (black, solid), 850 (dotted), 700 (dashed), and 600 (dash-dotted) hPa relative vorticity, as well as the NHC advisory intensity (gray); (b) deep layer (850–200 hPa) vertical wind shear (VWSH; black) and daily genesis potential (DGP; gray); (c) 925 (solid), 850 (dotted), 700 (dashed), and 600 (dotted-dashed) hPa relative humidity (black) and Rossby radius of deformation (gray); (d) 925 (solid), 850 (dotted), 700 (dashed), 600 (dotted-dashed) hPa water vapor mixing ratio. Upper axis represents the day, as well as the longitude (gray).

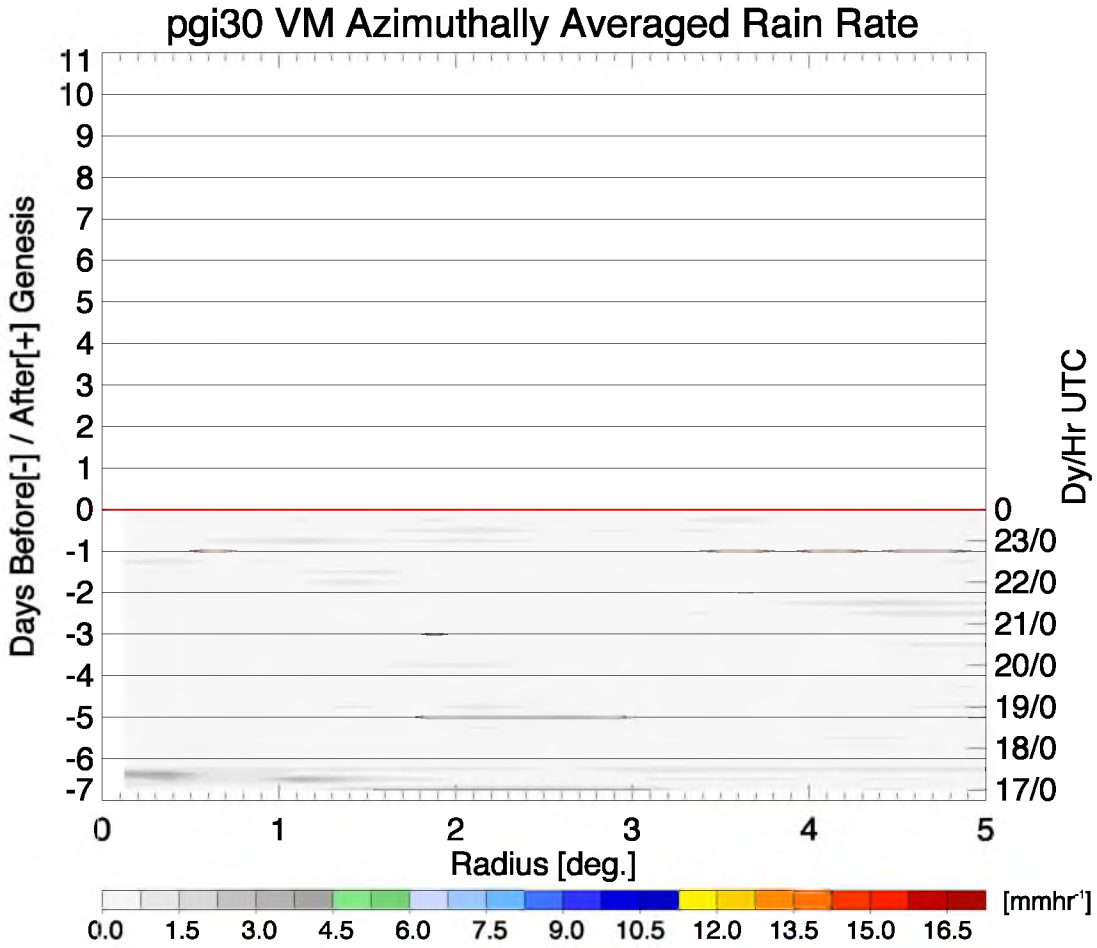

Figure 5.35. Time series of mean rain rate (from TRMM 3B42) as a function of radial distance from the 850 hPa VM center for PGI-30.

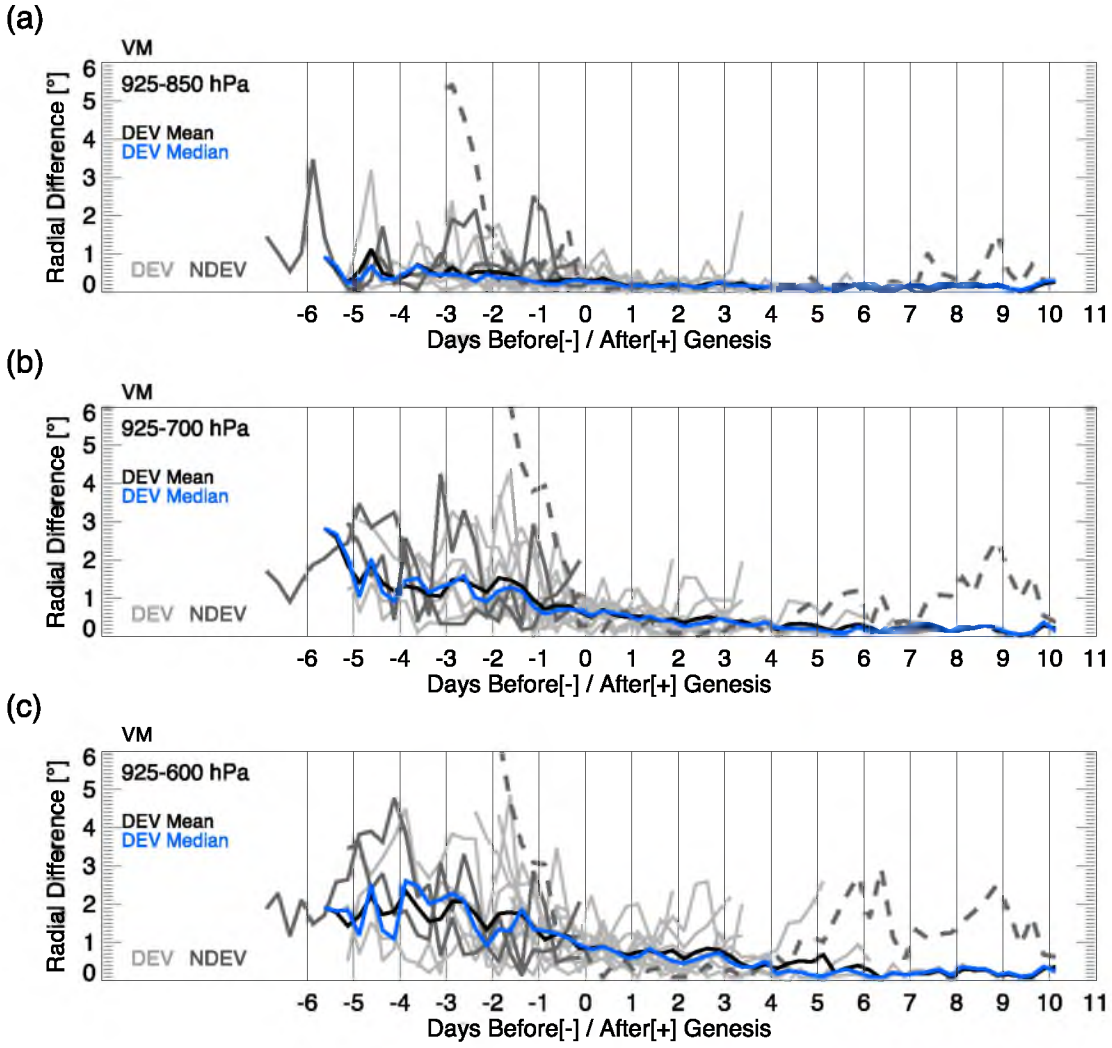

Figure 5.36. Time series of the radial difference between the VM location at 925–850 hPa (a), 925–700 hPa (b), and 925–600 hPa (c) for developing disturbances (solid, light gray), nondeveloping (solid, dark gray), and Gaston (dashed, dark gray); the developing mean (black) and developing median (blue) are also shown.

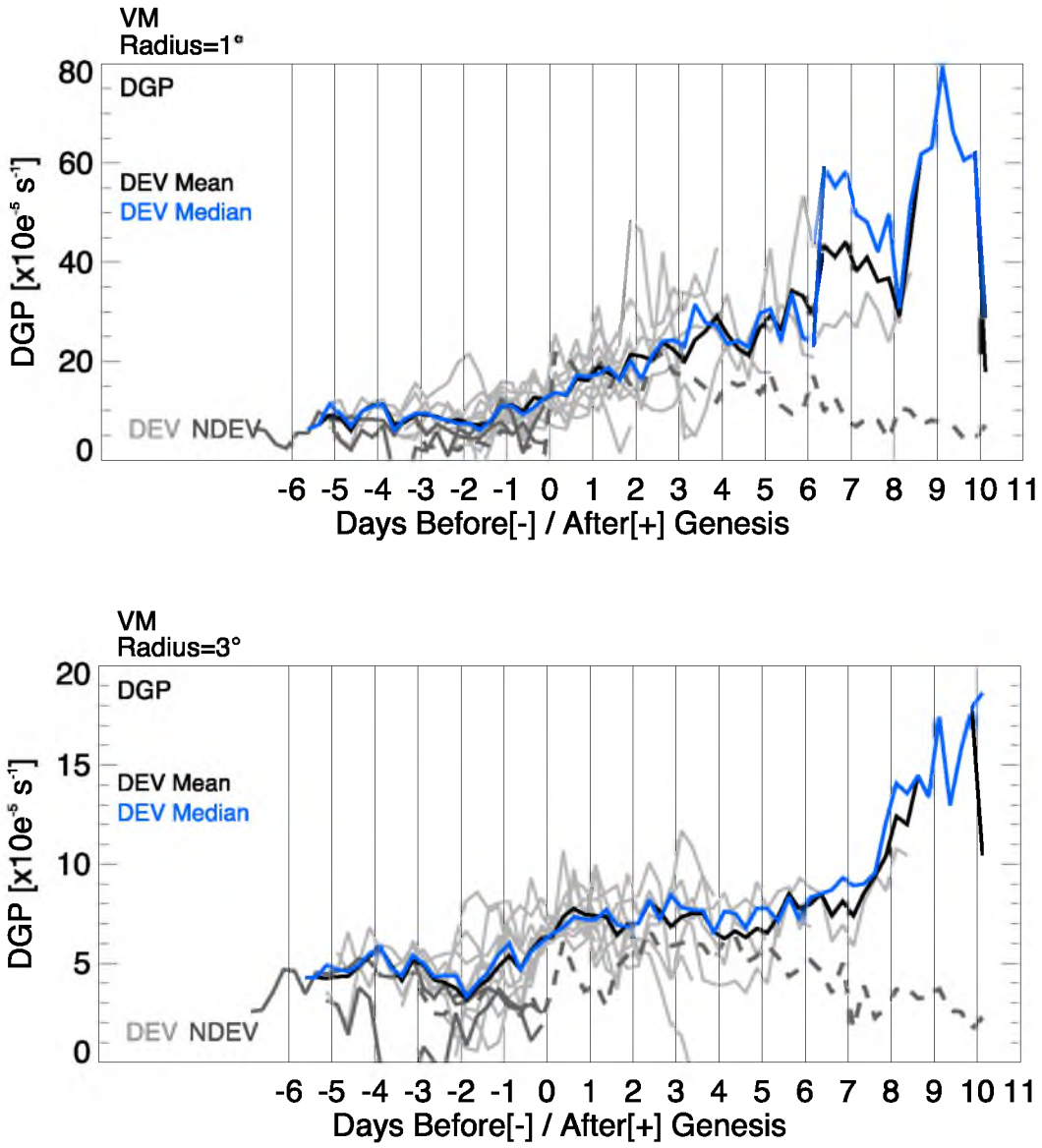

Figure 5.37. Time series of the daily genesis potential (DGP) within 1° (top) and 3° (bottom) of the 850 hPa VM center for developing disturbances (solid, light gray), nondeveloping (solid, dark gray), and Gaston (dashed, dark gray); the developing mean (black) and developing median (blue) are also shown.

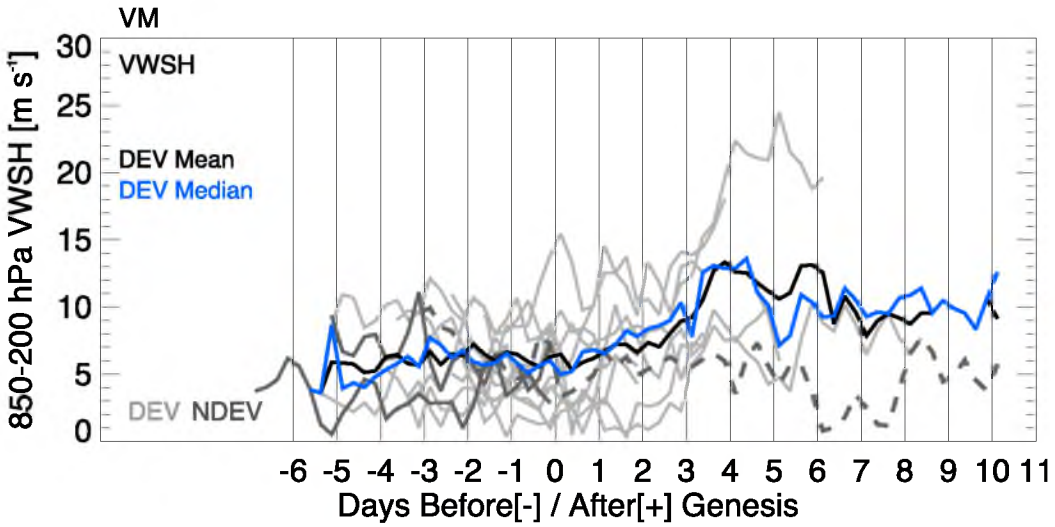

Figure 5.38. Time series of the mean deep layer (850–200 hPa) vertical wind shear within a 2–8° annulus of the 850 hPa VM center for developing disturbances (solid, light gray), nondeveloping (solid, dark gray), and Gaston (dashed, dark gray); the developing mean (black) and developing median (blue) are also shown.

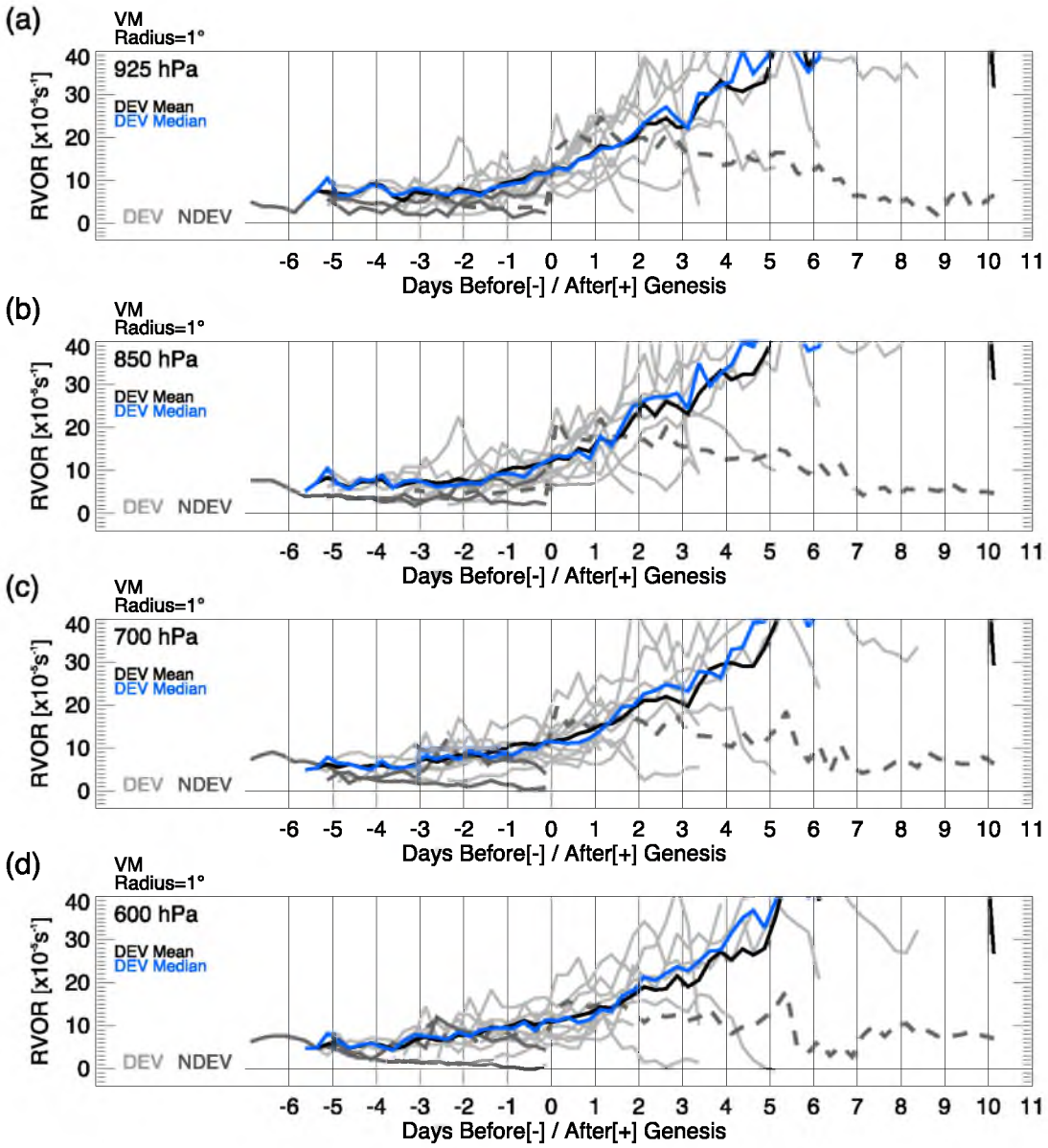

Figure 5.39. Time series of the mean relative vorticity at 925 (a), 850 (b), 700 (c), and 600 (d) hPa within 1° of the 850 hPa VM center for developing disturbances (solid, light gray), nondeveloping (solid, dark gray), and Gaston (dashed, dark gray); the developing mean (black) and developing median (blue) are also shown.

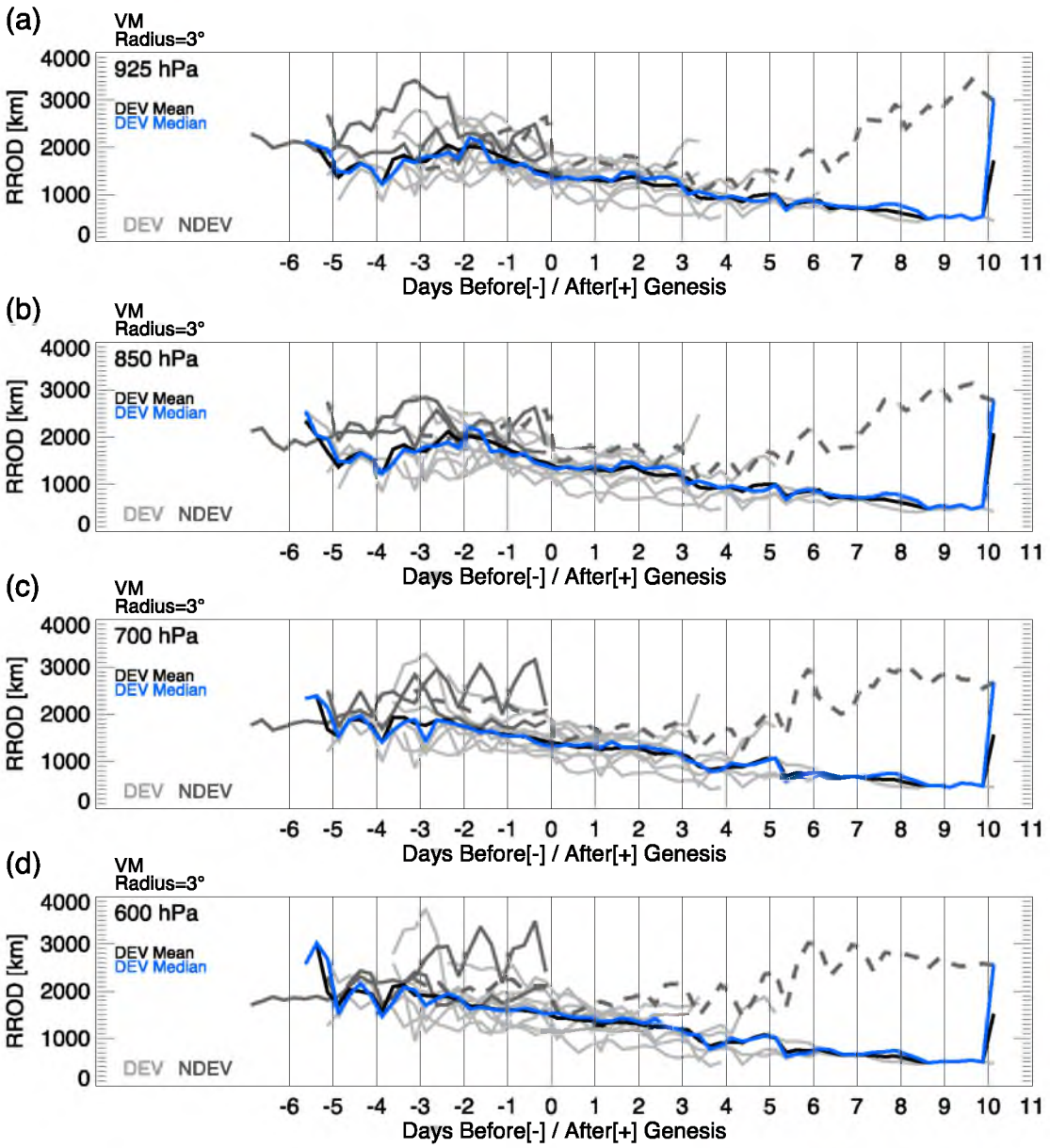

Figure 5.40. Time series of the mean Rossby radius of deformation (RROD) at 925 (a), 850 (b), 700 (c), and 600 (d) hPa within 3° of the 850 hPa VM center for developing disturbances (solid, light gray), nondeveloping (solid, dark gray), and Gaston (dashed, dark gray); the developing mean (black) and developing median (blue) are also shown.

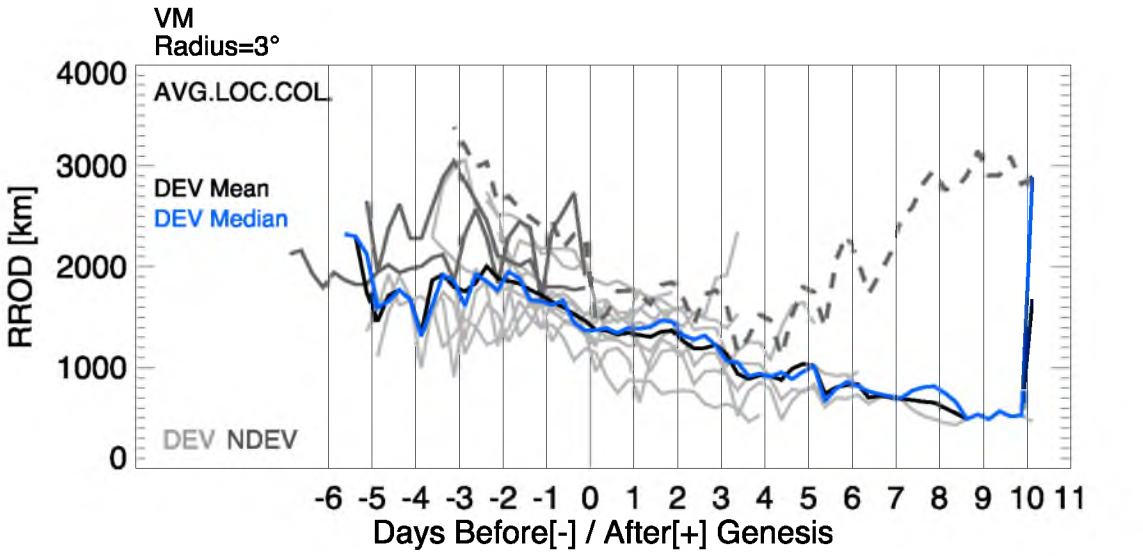

Figure 5.41. Time series of the 925–600 hPa column mean Rossby radius of deformation (RROD) computed for the mean location within 3° of 925, 850, 700, and 600 hPa locations for developing disturbances (solid, light gray), nondeveloping (solid, dark gray), and Gaston (dashed, dark gray); the developing mean (black) and developing median (blue) are also shown.

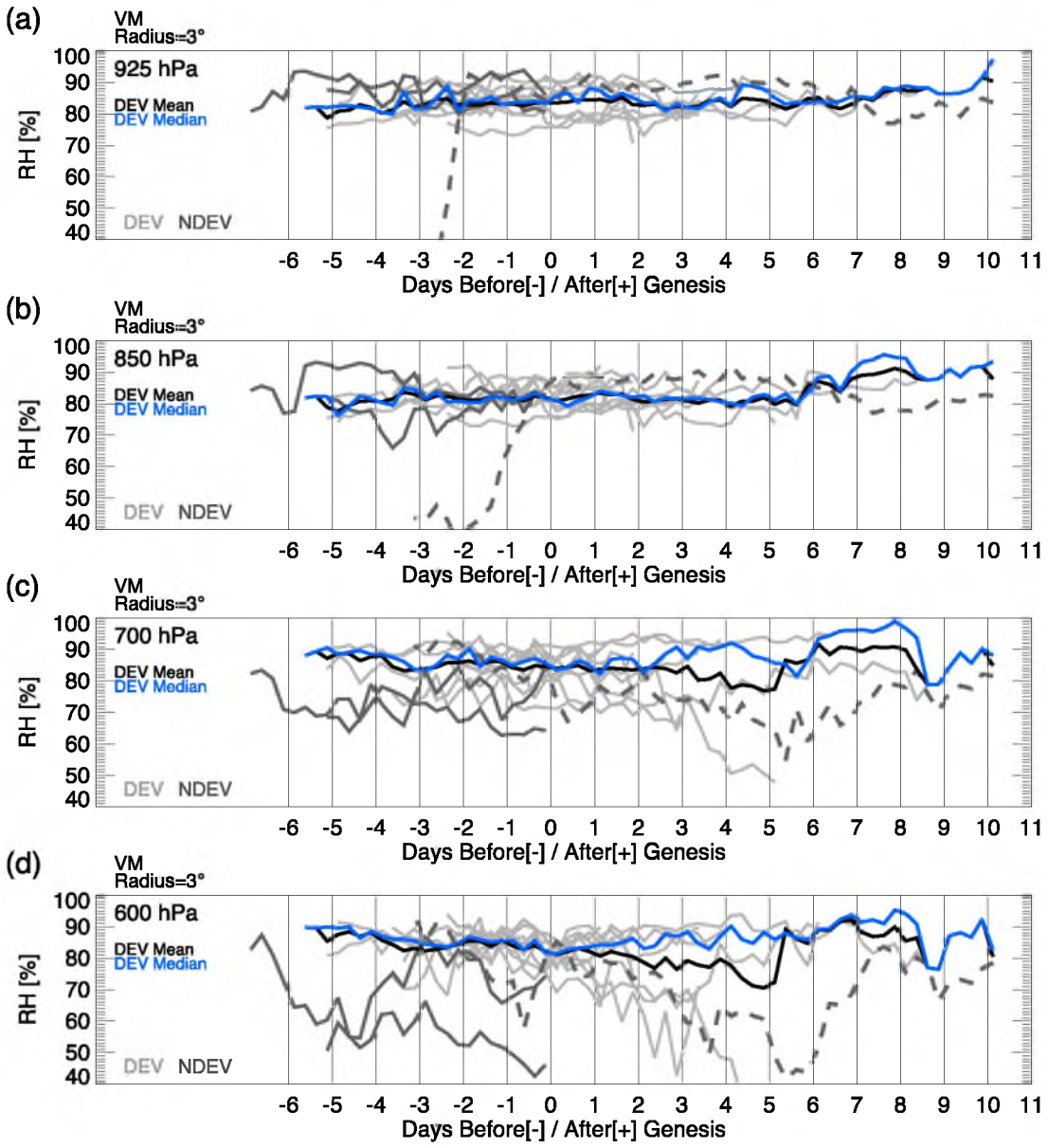

Figure 5.42. Time series of the mean relative humidity at 925 (a), 850 (b), 700 (c), and 600 (d) hPa within 3° of the 850 hPa VM center for developing disturbances (solid, light gray), nondeveloping (solid, dark gray), and Gaston (dashed, dark gray); the developing mean (black) and developing median (blue) are also shown.

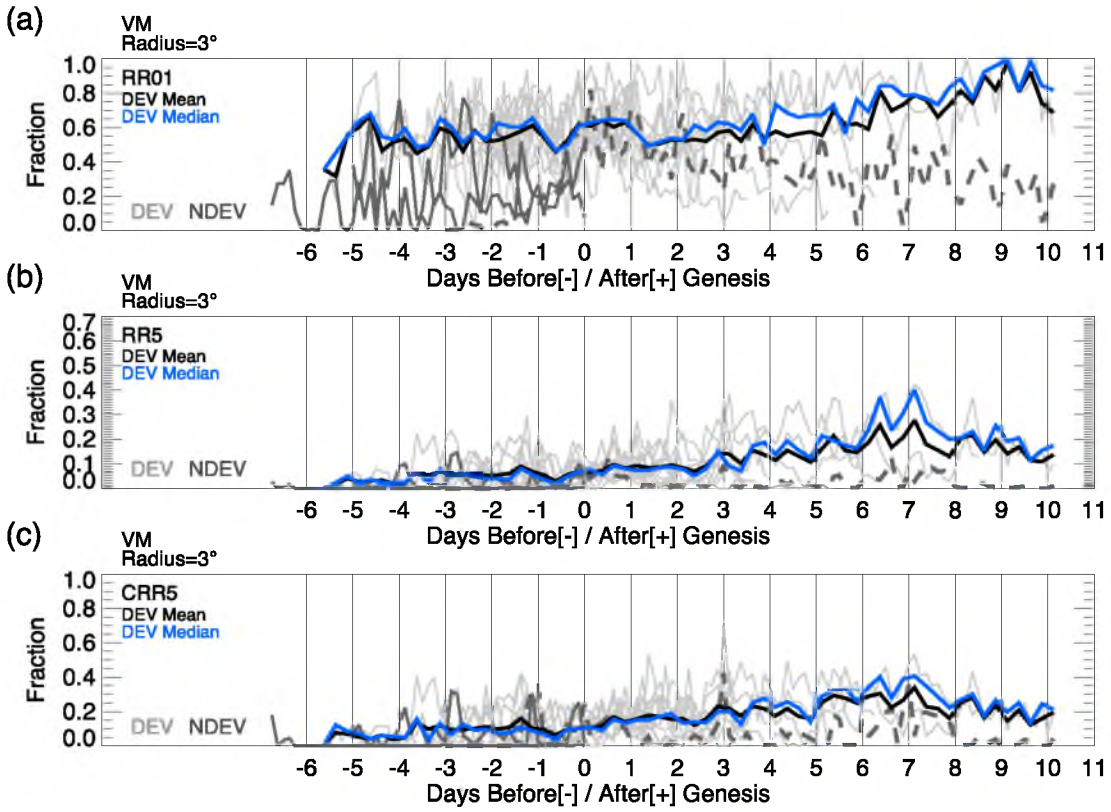

Figure 5.43. Time series of the (a) the total raining fraction (RR01), (b) fraction of all pixels with "convective" rain rate ($\geq$ 5mm hr^{-1}; RR5), and (c) fraction of raining pixels with "convective" rain rate (CRR5), within 3° of the 850 hPa VM center for developing disturbances (solid, light gray), nondeveloping (solid, dark gray), and Gaston (dashed, dark gray); the developing mean (black) and developing median (blue) are also shown.

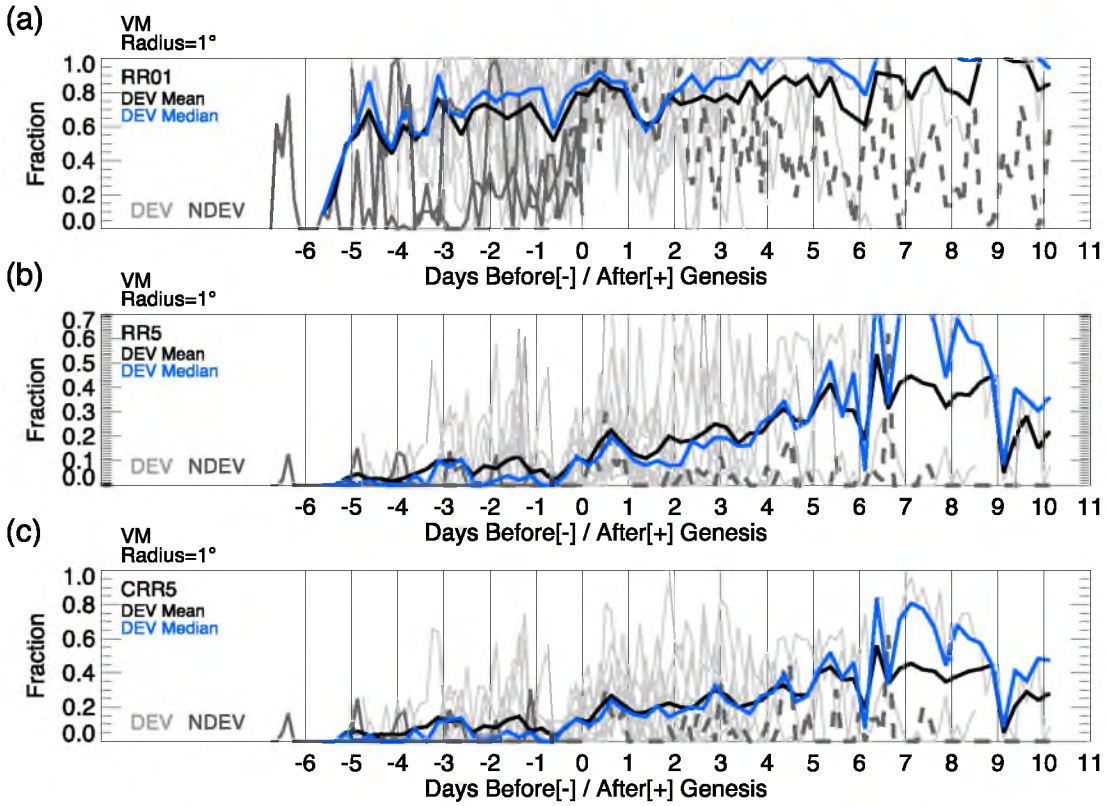

Figure 5.44. Time series of the (a) the total raining fraction (RR01), (b) fraction of all pixels with "convective" rain rate ($\geq$ 5mm hr^{-1}; RR5), and (c) fraction of raining pixels with "convective" rain rate (CRR5), within 1° of the 850 hPa VM center for developing disturbances (solid, light gray), nondeveloping (solid, dark gray), and Gaston (dashed, dark gray); the developing mean (black) and developing median (blue) are also shown.

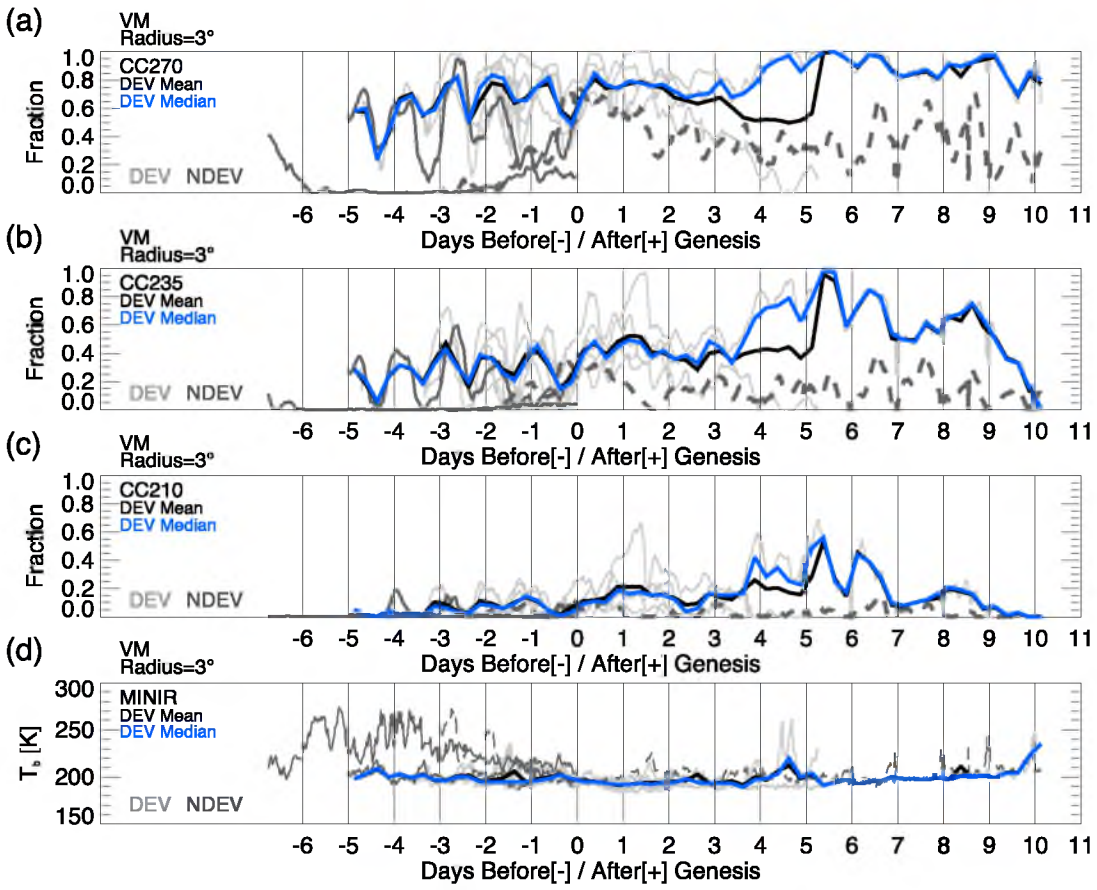

Figure 5.45. Time series of the IR cloud fractions within 3° of the 850 hPa VM for (a) IR $T_B \leq 270$ K, (b) IR $T_B \leq 235$ K, (c) IR $T_B \leq 210$ K, and (d) the minimum IR T_B for developing disturbances (solid, light gray), nondeveloping (solid, dark gray), and Gaston (dashed, dark gray); the developing mean (black) and developing median (blue) are also shown.

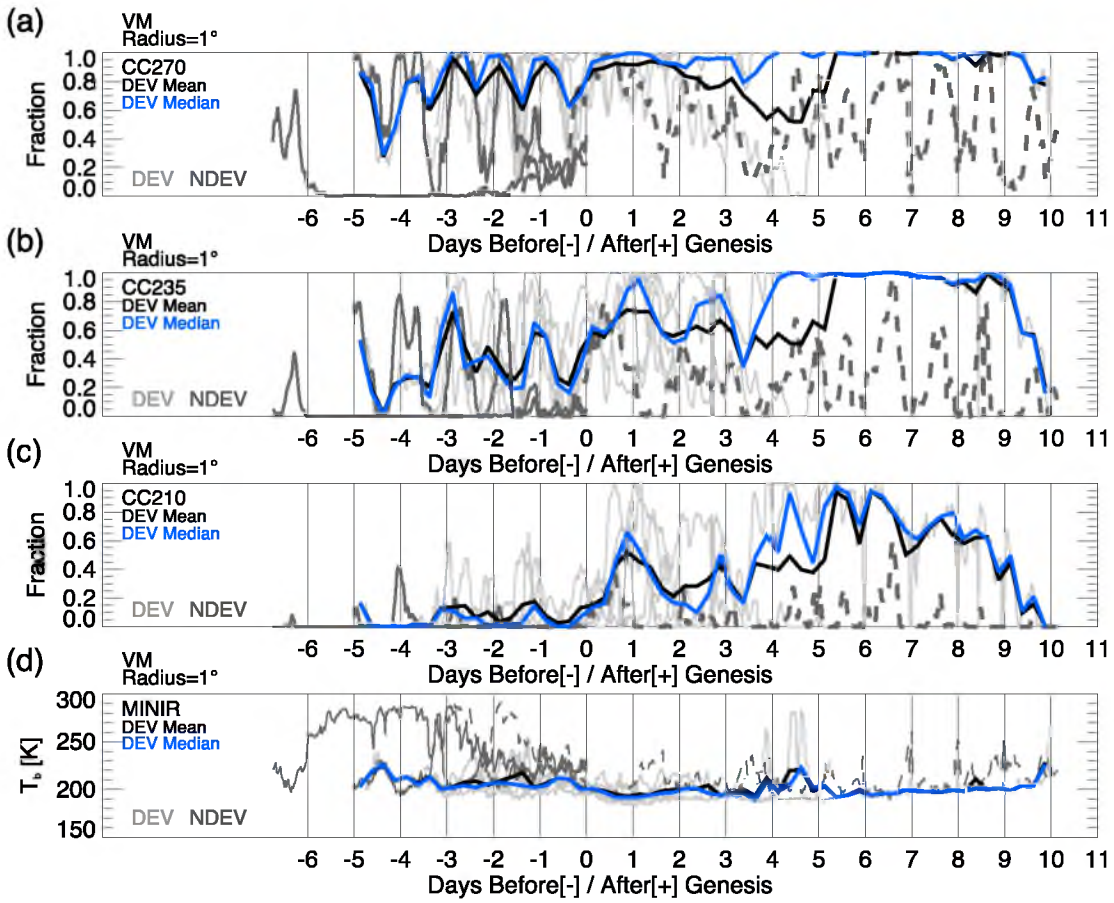

Figure 5.46. Time series of the IR cloud fractions within 1° of the 850 hPa VM for (a) IR $T_B \leq 270$ K, (b) IR $T_B \leq 235$ K, (c) IR $T_B \leq 210$ K, and (d) the minimum IR T_B for developing disturbances (solid, light gray), nondeveloping (solid, dark gray), and Gaston (dashed, dark gray); the developing mean (black) and developing median (blue) are also shown.

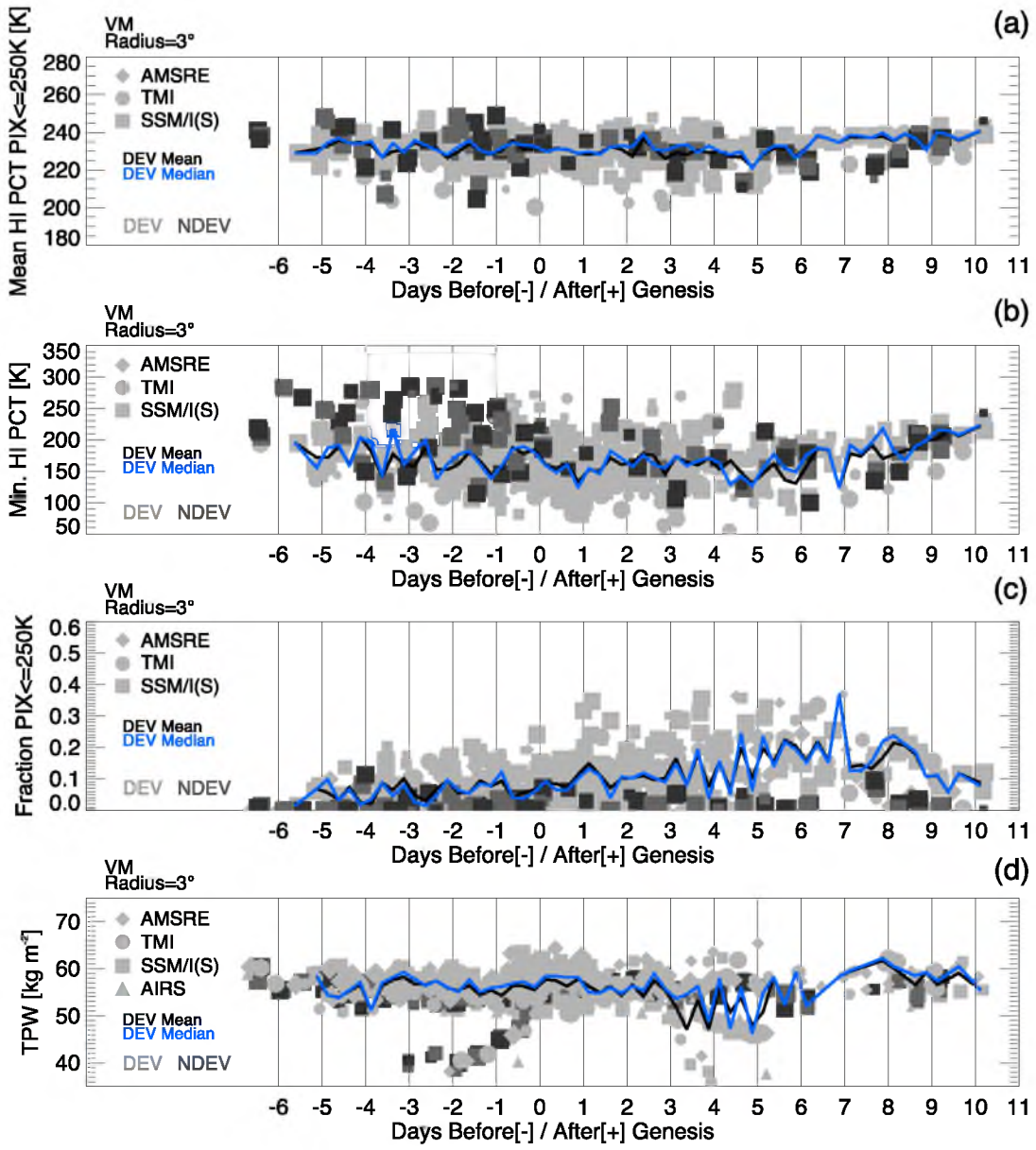

Figure 5.47. Within 3° of the 850 hPa VM center, (a) mean 85–91 GHz (HI) PCT for all pixels with PCT ≤ 250 K; (b) minimum 85-91 GHz (HI) PCT; (c) fraction of pixels with PCT ≤ 250 K; and (d) PMW-derived total precipitable water (TPW) for developing (gray symbol), nondeveloping (dark gray), and Gaston (black). The size of the symbol indicates the fractional coverage of swath data within the 3° radial circle around the 850 hPa VM center; the larger symbol, the higher the fractional swath data coverage within the radial circle. The mean (black) and median (blue) of developing samples are also included.

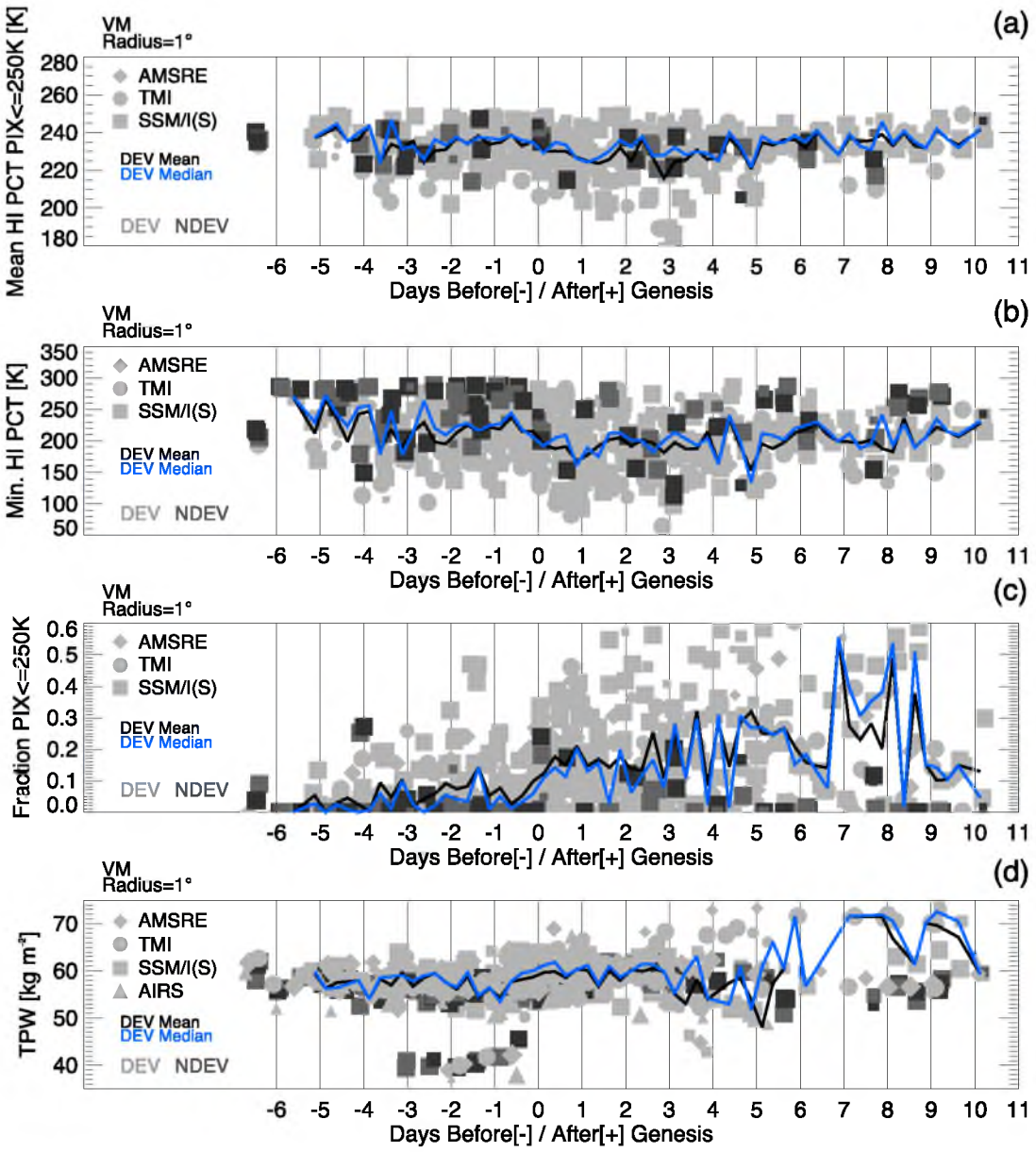

Figure 5.48. Within 1° of the 850 hPa VM center, (a) mean 85–91 GHz (HI) PCT for all pixels with PCT ≤ 250 K; (b) minimum 85-91 GHz (HI) PCT; (c) fraction of pixels with PCT ≤ 250 K; and (d) PMW-derived total precipitable water (TPW) for developing (gray symbol), nondeveloping (dark gray), and Gaston (black). The size of the symbol indicates the fractional coverage of swath data within the 3° radial circle around the 850 hPa VM center; the larger symbol, the higher the fractional swath data coverage within the radial circle. The mean (black) and median (blue) of developing samples are also included.

CHAPTER 6

CONCLUSIONS

6.1 Necessary Conditions for Tropical Cyclogenesis

The objective of this dissertation was to identify the necessary and sufficient conditions for tropical cyclogenesis; specifically those environmental, convective, and thermodynamic properties that may determine the fate of disturbances with apparent genesis potential. To address this objective, 12 developing and four nondeveloping disturbances — half of which are from the PREDICT-GRIP-IFEX (2010) field campaigns — were analyzed for environmental variables (relative vorticity, Rossby radius of deformation, daily genesis potential, vertical wind shear, relative humidity, temperature, wind, and moisture) from the NCEP FNL operational analysis and an extensive dataset of dropsondes, as well as convective properties from IR and multiple PMW instruments. The synthesis of model analysis, dropsonde, and satellite data allowed for an unparalleled opportunity to examine the time evolution of environmental and convective properties of the developing inner core. To achieve the main goals, five questions were outlined in the introduction; their key findings are presented here.

1) Developing disturbances tend to exhibit greater midlevel (700–400 hPa) moisture and humidity than nondeveloping disturbances. While the midlevel moisture and humidity can increase during the pregenesis stage, nondeveloping disturbances examined in this dissertation are observed to become drier over time. Likewise,

their surface θ_e, as well as the difference between the surface θ_e and midlevel θ_e minimum, is increased over time; an indication that the low troposphere may be becoming more convectively unstable in nondeveloping disturbances. (Although the differences between developing and nondeveloping disturbances appear to be pronounced for the cases examined, one should heed caution in generalizing the comparison between developing and nondeveloping since the nondeveloping cases included may not be representative of the variations observed across all null cases, and because the samples examined [4] is much less than the developing cases examined [12].)

2) The inner core of developing disturbances also exhibit some unique qualities as genesis nears; in the composite (and also in individual analyses of the best-sampled cases: Karl, Matthew, Nuri, Fay, and TD2), the midlevel moisture and θ_e are anomalously greater than the surrounding environment and slightly increase as genesis approaches, while at upper levels (above 500 hPa) a warm anomaly is observed as many as 3 days in advance and is observed to progressively reach lower levels through genesis.

    a. In the inner core, "progressive moistening" translates to about a 0.5–1.0 g kg^{-1} day^{-1} (depending on the inner core definition). Whether these changes are attributable to deep convective events is still unclear. Based on the dropsonde and PMW-derived observations presented, changes in the midlevel (700–400 hPa) moisture do not appear to be coherent with individual convective episodes; however, spatial and temporal sampling may still be too limited to confidently identify, or rule out, this

relationship.

b. The relative humidity in the low to mid-troposphere (1000–500 hPa) in developing cases is above 75% for much of the pregenesis stage; although in the composite, the humidity is high, the tropospheric column is not necessarily described as being "near-saturation" (above 90%). While the composited relative humidity for the 1° inner core indicates an initially larger increase 2–4 days prior to genesis, within 2 days, little increase is observed in relative humidity.

c. In all developing cases, TPW is above 50 mm, and mean midlevel (700–400 hPa) mixing ratio is above 4 g kg^{-1} throughout the pregenesis stage. Given that only small increases are observed, in most cases, the inner core moisture is already thermodynamically favorable as many as 3–4 days prior to formation.

3) The large-scale environment of developing disturbances exhibits a few common necessary conditions for genesis to proceed; the low- (925 hPa) and midlevel (600 hPa) VM/pouch must be aligned within 1°, the midlevels must be moist (700–400 hPa mean mixing ratio is above 4 g kg^{-1}) and humid (above 80%), the relative vorticity and DGP must increase, the Rossby radius of deformation (through an increase in relative vorticity and latitude) must decrease, the scale of the disturbance must be greater than or equal to the RROD, and 850–200 hPa vertical wind shear must be low to moderate (10 m s^{-1}).

a. In the dropsonde composite, a cool, dry anomaly develops at low levels (1000–900 hPa) within 48 hours of genesis, and reaches its maximum

vertical depth (around 900 hPa) at 24 hours prior. The anomaly is preceded by relative vorticity maximized near midlevels (850–600 hPa, which is also steadily increasing), and is coincident with a more rapid increase in low-level (below 850 hPa) vorticity and windspeed within 48 hours of genesis.

b. Dropsonde observations from the better-documented cases, Karl, Matthew, and Nuri, indicate that a midlevel circulation precedes formation; only Fiona appears to form in the absence of a well-defined midlevel circulation. Results presented for the dropsonde dataset, as well as for individual case studies generally support the hypothesis that a midlevel vortex in an already moist, humid environment may be necessary for formation, but suggest that this is only one of the pathways to formation.

4) Among all the convective properties examined (raining area, intensity, area of intense convection, duration, and proximity), the results suggest that proximity and duration of rainfall within 3° of the center may be two of the most important properties; almost all developing disturbances exhibit total raining fractions above 40% for at least half of the hours tracked before genesis. The total raining area is only distinguishable when comparing developing disturbances to nondeveloping disturbances.

a. The most "favorable" convective episodes do not necessarily occur within 24–36 hours of genesis. Although not directly responsible for formation, their locations in close proximity to the center may modify the

thermodynamic environment in such a way that convective episodes that follow are not required to be as intense, widespread, or close to the center to further organize the disturbance.

b. In terms of deep convection, the developing cases presented do not indicate any common distinguishing deep convective characteristics before formation. The convective intensity shows no increasing tendency before genesis, and is not consistently greater until after genesis, and convective intensity in the pregenesis stage of developing cases is not noticeably greater than nondeveloping cases. Given the variability in the timing, location, and area of deep convection among the cases studied, its specific role in the formation process remains difficult to ascertain.

c. Dropsonde observations from research flights following convective episodes in Karl and Matthew suggest that convection may have played a role in organizing both low- (925 hPa) and midlevel (600 hPa) circulations; however, distinguishing this relationship from other (perhaps large-scale) reasons for increased organization is still difficult.

In the composite, the results of this dissertation support a pathway to tropical cyclogenesis presented by Raymond et al. (2011) and Raymond and Sessions (2007), in which a midlevel vortex in an already moist, humid environment is favorable thermodynamically for a bottom-heavy mass flux profile and low-level convergence and spin-up right before genesis. The results from the rainfall analysis (Chapter 5) suggest that the low-level cool anomaly (1000–900 hPa) observed 1–2 days before formation may be caused by the cumulative effect of convective precipitation 2–4 days before genesis, in

which the low levels are eventually unable to completely recover from cooling and drying effects of convective precipitation. Perhaps as a consequence of the stabilization at low levels, the raining area and intensity are observed to, on average, decrease in the day before formation. One can then speculate that, with less convective precipitation, the ocean latent heat fluxes — already increased by the higher surface wind speeds — remove the cool, dry low-level anomaly. Considering the subsequent increase in total raining area and the high "convective" rain fraction observed near the center after genesis, over that observed prior to formation, the results suggest that once the low levels have recovered, the low-level convergence increases, the circulation quickly achieves at least tropical depression strength, and the secondary circulation becomes well-established.

Although generally consistent among the better-sampled cases in this dissertation, the tropical cyclogenesis pathway previously described is not necessarily the only pathway to formation. Given the variability observed in the timing, location, and proximity of precipitation to the center, within the context of the organization of the wave, one must concede that multiple pathways could exist to formation. Although this dissertation did not specifically address each case as being "top-down" or "bottom-up" development, one pathway, however, is not well supported by the observations. Although the spatial and temporal resolution of the satellite observations may not be sufficient to identify VHTs, results tend not to support the VHT route to cyclogenesis that has been documented in numerical studies such as Hendricks et al. (2004) and Montgomery et al. (2006). In no case examined does precipitation, in the form of particularly deep, intense towers appear to aggregate to organize a low-level circulation.

In agreement with Houze et al. (2009), convective and stratiform areas near the center most likely *both* contribute to genesis; while active convection supports intensification at low levels, at the same time, stratiform rain regions (from old convective cells) contribute to intensification at midlevels.

6.2. Analysis and Reanalyses

The NCEP FNL operational analysis was an integral part of the dissertation. Given the small differences found when NCEP FNL is compared to dropsonde observations, one should have some confidence in the ability of the analysis to replicate the thermodynamic and wind environment in developing and nondeveloping disturbances. Given a choice between the ERA Interim and the NCEP/NCAR reanalysis, the choice is clear; compared to observations, the ERA Interim is by far the better reanalysis. In fact, the ERA Interim reanalysis differences from the dropsonde observations are actually comparable to the NCEP FNL operational analysis, despite a somewhat lower resolution (1.5° versus 1.0°).

6.3. Vorticity Maxima and Pouches

Although all the analyses in this dissertation were also done for the pouch, only analyses for the vorticity maxima were shown. With few exceptions, the analyses do not differ between the VM and pouch (when present). Despite the difficulties encountered in tracking vorticity maxima — such as when multiple vorticity maxima are present or the vorticity maximum is elongated — this dissertation concludes that vorticity maxima in the Eulerian framework is still preferred when tracking the pregenesis disturbance center. Tracking pouch centers in the co-moving (Lagrangian) framework is complicated by the

fact that the appropriate methodology for calculating the phase speed of the wave has not been well defined. The traditional methodology is to compute a phase speed that is representative of the entire lifetime of the wave (Dunkerton et al. 2009; Montgomery et al. 2010); this results in an "ideal" phase speed, around 5–7 m s^{-1}, for identifying a pouch in the co-moving framework. If one wants to define a pouch every 6 hours, it makes more sense that co-moving wind field is determined by a phase speed representative of that day, rather than one representative of the entire lifetime of the wave. If the daily variations in phase speed are considered, such as was done in this dissertation, the phase speeds can be well below and above this range, and a pouch is often not identifiable in the co-moving framework. A more rigorous evaluation of the wave phase speed methodology is still required; the goal, to identify the appropriate averaging time and to characterize the sensitivity of the resulting pouch location to the phase speed.

REFERENCES

Aberson, S.D., M.L. Black, R.A. Black, J.J. Cione, C.W. Landsea, F.D. Marks, Jr., and R.W. Burpee, 2006: Thirty years of tropical cyclone research with the NOAA P-3 aircraft. *Bull. Amer. Meteor. Soc.*, **87**, 1039-1055.

Bister, M., and K.A. Emanuel, 1997: The genesis of Hurricane Guillermo: TEXMEX analyses and a modeling study. *Mon. Wea. Rev.*, **125**, 2662-2682.

Bell, M. M., and M.T. Montgomery, 2010: Sheared deep vortical convection in pre-depression Hagupit during TCS08. *Geo. Res. Lett.*, 37, L06802, 5 pp., doi:10.1029/2009GL042313.

Berry, G.J, and C. Thorncorft, 2005: Case study of an intense African easterly wave. *Mon. Wea. Rev.*, **133**, 752-766.

Bolton, D., 1980: The computation of equivalent potential temperature. *Mon. Wea. Rev.*, **108**, 1046-1053.

Braun, S.A., M.T. Montgomery, K.J. Mallen, and P.D. Reasor, 2010: Simulation and interpretation of the genesis of Tropical Storm Gert (2005) as part of the NASA Tropical Cloud Systems and Processes Experiment. *J. Atmos. Sci.*, **67**, 999–1025.

Braun, S.A., 2010: Reevaluating the role of the Saharan air layer in Atlantic tropical cyclogenesis and evolution. *Mon. Wea. Rev.*, **138**, 2007-2037.

Braun, S.A, and Coauthors, 2013: NASA's Genesis and Rapid Intensification Processes (GRIP) field experiment – bringing new technologies to the hurricane intensity problem. *Bull. Amer. Meteo. Soc.*, **94**, 345-363.

Burpee, R.W., 1974: Characteristics of Northern African easterly waves during the summers of 1968-1969. *J. of Atmos. Sci.*, **31**, 1556-1570.

Carlson, T.N., 1969a: Some remarks on tropical disturbances and their progress over the tropical Atlantic. *Mon. Wea. Rev.*, **97**, 716-726.

Carlson, T.N., 1969b: Synoptic histories of three African disturbances that developed into Atlantic hurricanes. *Mon. Wea. Rev.*, **97**, 256-276.

Chen, S. S., and W. M. Frank, 1993: A numerical study of the genesis of extratropical

convective mesovortices. Part I: Evolution and dynamics. *J. Atmos. Sci.*, **50**, 2401–2426.

Davis, C. A., and L. F. Bosart, 2001: Numerical simulations of the genesis of Hurricane Diana (1984). Part I: Control simulation. *Mon. Wea. Rev.*, **129**, 1859–1881.

Dunion, J.P., and C.S. Velden, 2004: The impact of the Saharan air layer on tropical cyclone activity, *Bull. Amer. Meteo. Soc.*, **85**, 353-365.

Erickson, C.O., 1963: An incipient hurricane near the West African coast. *Mon. Wea. Rev.*, **91**, 61-68.

Evans, C., and coauthors, 2012: The Pre-Depression Investigation of Cloud-Systems in the Tropics (PREDICT) field campaign: Perspectives of early career scientists. *Bull. Amer. Meteor. Soc.*, **93**, 173–187.

Fang, J., and F. Zhang, 2011: Evolution of multiscale vortices in the development of Hurricane Dolly (2008). *J. Atmos. Sci.*, **68**, 103–122.

Frank, N., 1970: Atlantic tropical systems of 1969. *Mon. Wea. Rev.*, **98**, 307-314.

Fritsch, J.M., and C.F. Chappell, 1980: Numerical prediction of convectively driven mesoscale pressure systems. Part II: Mesoscale model. *J. Atmos. Sci.*, **37**, 1734-1762.

Gray, W. M., 1968: Global view of the origin of tropical disturbance and storms. *Mon. Wea. Rev.*, **96**, 669–700.

Gray, W.M., 1975: Tropical cyclone genesis. Colorado State University Dept. of Atmos. Sci. Paper No. 232, 121 pp.

Gray, W.M., 1984a: Atlantic seasonal hurricane frequency. Part I: El Nino and 30 mb quasi-biennial oscillation influences. *Mon. Wea. Rev.*, **112**, 1649-1668.

Guinn, T.A., and W.H. Schubert, 1993: Hurricane spiral bands. *J. Atmos. Sci.*, **50**, 3380–3403.

Davis, C. A., and D. A. Ahijevych, 2012: Mesoscale structural evolution of three tropical weather systems observed during PREDICT. *J. Atmos. Sci.*, **69**, 1284–1305.

DeMaria, M., J.-J. Baik, and J. Kaplan, 1993: Upper-level eddy angular momentum fluxes and tropical cyclone intensity change. *J. Atmos. Sci.*, **50,** 1133–1147.

DeMaria, M., and J.M. Gross, 2003: Evolution of tropical cyclone forecast models. *Hurricane! Coping with Disaster*, R. Simpson, Ed., Amer. Geophys. Union, 103-126.

DeMaria, M., M. Mainelli, L.K. Shay, J.A. Knaff, and J. Kaplan, 2005: Further improvements to the Statistical Hurricane Intensity Prediction Scheme (SHIPS). *Wea. Forecasting*, **20**, 531-543.

Dunkerton, T.J., M.T. Montgomery, and Z. Wang, 2009: Tropical cyclogenesis in a tropical wave critical layer: easterly waves. *Atmos. Chem. Phys.*, **9**, 5587-5646.

Harr, P. A., M. S. Kalafsky, and R. L. Elsberry, 1996a: Environmental conditions prior to formation of a midget tropical cyclone during TCM-93. *Mon. Wea. Rev.*, **124**, 1693-1710.

Harr, P. A., R. L. Elsberry, and J. C. L. Chan, 1996b: Transformation of a large monsoon depression to a tropical storm during TCM-93. *Mon. Wea. Rev.*, **124**, 2625-2643.

Halverson, J., and Coauthors, 2007: NASA's Tropical Cloud Systems and Processes experiment. *Bull. Amer. Meteor. Soc.*, **88**, 867-882.

Holland, G.J., and R. T. Merrill, 1984: On the dynamics of tropical cyclone structure changes. *Quart. J. Roy. Meteor. Soc.*, **110,** 723–745.

Holland, G.J., 1995: Scale interaction in the western Pacific monsoon, *Meteor. and Atmos. Phys.*, **56**, 57-80.

Hopsch, S.B., C.D. Thorncroft, K. Hodges, and A. Aiyyer, 2007: West African storm tracks and their relationship to Atlantic tropical cyclones. *J. of Climate,* **20**, 2468–2483.

Hendricks, E. A., M. T. Montgomery, and C.A. Davis, 2004: The role of "vortical" hot towers in the formation of Tropical Cyclone Diana (1984). *J. Atmos. Sci.*, **61**, 1209–1232.

Houze**,** R.A., Jr., 2004: Mesoscale convective systems. *Rev. Geophys.*, **42**, 10.1029/2004RG000150, 43 pp.

Houze, R. A., W.-C. Lee, and M. M. Bell, 2009: Convective contribution to the genesis of Hurricane Ophelia (2005). *Mon. Wea. Rev.*, **137**, 2778–2800.

Jiang, H., C. Liu, and E. J. Zipser, 2011: A TRMM-based tropical cyclone cloud and precipitation feature database. *J. Appl. Meteor. Climatol.*, **50**, 1255–1274.

Kakar, R., M. Goodman, R. Hood, and A. Guillory, 2006: Overview of the Convection and Moisture Experiment (CAMEX). *J. Atmos, Sci.*, **63**, 5-18.

Karyampudi, V. M., and H.F. Pierce, 2002: Synoptic-scale influence of the Saharan air layer on tropical cyclogenesis over the Eastern Atlantic. *Mon. Wea. Rev.*, **130**, 3100–3128.

Kerns, B.K. K.G. Greene, and E. Zipser, 2008: Four years of tropical ERA-40 vorticity maxima tracks, Part 1: Climatology and vertical vorticity structure. *Mon. Wea. Rev.*, 136, 4301-4319.

Kerns, B., and E. Zipser, 2009: Four years of tropical ERA-40 vorticity maxima tracks. Part II: Differences between developing and non-developing disturbances. *Mon. Wea. Rev.*, **137**, 2576–2591.

Kieu, C.Q., and D.-L. Zhang, 2009: Genesis of Tropical Storm Eugene (2005) from merging vortices associated with ITCZ breakdowns. Part II: Roles of vortex merger and ambient potential vorticity. *J. Atmos. Sci.*, **66**, 1980–1996.

Landsea, C.W., 1993: A climatology of intense (or major) Atlantic hurricanes. *Mon. Wea. Rev.*, **121**, 1703–1713.

Lee, C.S., 1989: Observational analysis of tropical cyclogenesis in the Western North Pacific. Part I: Structural evolution of cloud clusters. *J. Atmos. Sci.*, **46**, 2580–2598.

McBride, J.L., and R. Zehr, 1981: Observational analysis of tropical cyclone formation. Part II: Comparison of non-developing versus developing systems. *J. Atmos. Sci.*, **38**, 1132-1151.

Molinari, J., and D. Vollaro, 1989: External influences on hurricane intensity. Part I: Outflow layer eddy angular momentum fluxes. *J. Atmos. Sci.*, **46,** 1093–1105.

Molinari, J., D. Vollaro, and K. L. Corbosiero, 2004: Tropical cyclone formation in a sheared environment: A case study. *J. Atmos. Sci.*, **61,** 2493–2509.

Montgomery, M. T., and J. Enagonio, 1998: Tropical cyclogenesis via convectively forced vrtex rossby waves in a three-dimensional quasigeostrophic model. *J. Atmos. Sci.*, **55**, 3176–3207.

Montgomery, M.T., M.E. Nicholls, T.A. Cram, and A.B. Saunders, 2006: A vortical hot tower route to tropical cyclogenesis. *J. Atmos. Sci.*, **63**, 355–386.

Montgomery, M.T., Z. Wang, and T.J. Dunkerton, 2010: Coarse, intermediate, and high resolution numerical simulations of the transition of a tropical wave critical layer to a tropical storm. *Atmos. Chem. Phys.*, **10**, 10803-10827.

Montgomery, M.T., and R.K. Smith, 2012: The genesis of Typhoon Nuri as observed during the Tropical Cyclone Structure 2008 (TCS08) field experiment – Part 2: Observations of the convective environment. *Atmos. Chem. Phys.*, **11**, 31115-31136.

Montgomery, M.T., and Coauthors, 2012: The Pre-Depression Investigation of Cloud-

Systems in the Tropics (PREDICT) Experiment: Scientific basis, new analysis tools, and some first results. *Bull. Amer. Meteor. Soc.*, **93**, 153–172.

Möller, J. D., and M.T. Montgomery, 2000: Tropical cyclone evolution via potential vorticity anomalies in a three-dimensional balance model. *J. Atmos. Sci.*, **57**, 3366–3387.

Nolan, D. S., E. D. Rappin, and K. A. Emanuel, 2007: Tropical cyclogenesis sensitivity to environmental parameters in radiative-convective equilibrium. *Q. J. Royal Meteor. Soc.*, **133**, 2085-2107.

Ooyama, K.V., 1982: Conceptual evolution of the theory and modeling of the tropical cyclone. *J. Meteor. Soc. Japan*, **60**, 369-379.

Papin, P., and C. Hennon, 2011: Using the Rossby radius of deformation as a forecasting tool for tropical cyclogenesis. *Proceedings of the National Conference on Undergraduate Research*, Ithaca College, NY, 2011.

Pfeffer, R. L., and M. Challa, 1981: A numerical study of the role of eddy fluxes of momentum in the development of Atlantic hurricanes. *J. Atmos. Sci.*, **38,** 2392–2398.

Pytharoulis I., and C. D. Thorncroft, 1999: The low-level structure of African easterly waves in 1995. *Mon. Wea. Rev.*, **127**, 2266–2280.

Raymond, D. J., C. López-Carrillo, and L. López Cavazos, 1998: Case-studies of developing east Pacific easterly waves. *Quart. J. Roy. Meteor. Soc.*, **124**, 2005-2034.

Raymond, D. J., and S. L. Sessions (2007), Evolution of convection during tropical cyclogenesis, *Geophys. Res. Lett.*, 34, L06811, doi:10.1029/2006GL028607.

Raymond, D. J., and C. Lopez, 2010: The vorticity budget of developing Typhoon Nuri (2008). *Atmos. Chem. Phys. Discuss.*, **10**, 16,589 – 16,635, doi: 10.5194/acpd-10-16589-2010.

Raymond, D. J., S. L. Sessions, and C. Lopez-Carillo, 2011: Thermodynamics of tropical cyclogenesis in the northwest Pacific. *J. of Geophy. Res.*, **116**, D18101, 18 pp., doi:10.1029/2011JD015624.

Riehl, H., 1948: On the formation of typhoons. *J. Meteor.*, **5**, 247-264.

Riehl, H., 1954: *Tropical meteorology*. McGraw-Hill, New York, 392 pp.

Ritchie, E. A., and G. J. Holland, 1997: Scale interactions during the formation of Typhoon Irving. *Mon. Wea. Rev.*, **125**, 1377-1396.

Rogers, R., S. Aberson, M. Black, P. Black, J. Cione, P. Dodge, J. Gamache, J. Kaplan,

M. Powell, J. Dunion, E. Uhlhorn, N. Shay, and N. Surgi, 2006: The intensity forecast experiment: A NOAA multi-year field program for improving tropical cyclone intensity forecasts. *Bull. Amer. Meteor. Soc.*, **87**, 1523-1537.

Rogers, R. F., and J. M. Fritsch, 2001: Surface cyclogenesis from convectively driven amplification of midlevel mesoscale convective vortices. *Mon. Wea. Rev.*, **129**, 605–637.

Reasor, P. D., M. T. Montgomery, and L. F. Bosart. 2005: Mesoscale observations of the genesis of Hurricane Dolly (1996). *J. Atmos. Sci.*, **62**, 3151–3171.

Reed R. J., D. C. Norquist, and E. E. Recker, 1977: The structure and properties of African wave disturbances as observed during phase III of GATE. *Mon. Wea. Rev.*, **105**, 317–333.

Reed R. J., E. Klinker, and A. Hollingsworth, 1988: The structure and characteristics of African easterly wave disturbances determined from ECMWF operational analysis/forecast system. *Meteor. Atmos. Phys.*, **38**, 22–33.

Sadler, J.C., 1976: A role of the tropical upper tropospheric trough in early season typhoon development. *Mon. Wea. Rev.*, **104**, 1266–1278.

Sadler, J.C., 1978: Mid-season typhoon development and intensity changes and the tropical upper tropospheric trough. *Mon. Wea. Rev.*, **106**, 1137–1152.

Schubert, W. H., and J. J. Hack, 1982: Inertial stability and tropical cyclone development. *J. Atmos. Sci.*, **39**, 1687–1697.

Sears, J., 2011: Investigating the role of the upper-levels in tropical cyclogenesis. Masters Thesis, University of Wisconsin - Madison, 2011.

Simpson, J., J.B. Halverson, B.S. Ferrier, W.A. Petersen, R.H. Simpson, R. Blakeslee, and S.L. Durden, 1997: On the role of "hot towers" in tropical cyclone formation. *Meteo. Atmos. Phys.*, **67**, 15-35.

Sippel, J. A., J. W. Nielsen-Gammon, and S. E. Allen, 2006: The multiple-vortex nature of tropical cyclogenesis. *Mon. Wea. Rev.*, **134**, 1796–1814.

Smith, R. K., and M. T. Montgomery, 2012: Observations of the convective environment in developing and non-developing tropical disturbances. *Q. J. Royal Meteor. Soc.*, doi:10.1002/qj.1910.

Spencer, R. W., H. M. Goodman, and R. E. Hood, 1989: Precipitation retrieval over land and ocean with the SSM/I: Identification and characteristics of the scattering signal. *J. Atmos. Oceanic Technol.*, **6**, 254–273.

Thorncroft C. D., and K. I. Hodges, 2001: African easterly wave variability and its

relationship to Atlantic tropical cyclone activity. *J. Climate*, **14**, 1166–1179.

Tory, K.J., and M.T. Montgomery, 2006: Internal influences on tropical cyclone formation. World Meteorological Organization. Report on the 6th International Workshop on Tropical Cyclones, San Jose, Costa Rica, Nov. 2006.

Tory, K. J., M. T. Montgomery, and N. E. Davidson, 2006: Prediction and diagnosis of tropical cyclone formation in an NWP system. Part I: The critical role of vortex enhancement in deep convection. *J. Atmos. Sci.*, **63**, 3077–3090.

Tory, K. J., M. T. Montgomery, N. E. Davidson, and J. D. Kepert, 2006: Prediction and diagnosis of tropical cyclone formation in an NWP system. Part II: A diagnosis of tropical cyclone Chris formation. *J. Atmos. Sci.*, **63**, 3091–3113.

Wang, L., K.-H. Lau, Q.-H. Zhang, and C.-H. Fung, 2008: Observation of non-developing and developing disturbances over the South China Sea using SSM/I satellite. *Geo. Res. Lett.*, **35**, L10801, 5 pp., doi:10.1029/2008GL033446.

Wang, Z., M. T. Montgomery, and T. J. Dunkerton, 2010a: Genesis of pre–Hurricane Felix (2007). Part I: The role of the easterly wave critical layer. *J. Atmos. Sci.*, **67**, 1711–1729.

Wang, Z., M. T. Montgomery, and T. J. Dunkerton, 2010b: Genesis of pre–Hurricane Felix (2007). Part II: Warm core formation, precipitation evolution, and predictability. *J. Atmos. Sci.*, **67**, 1730–1744.

Wang, Z., M.T. Montgomery, and C. Fritz, 2012: A first look at the structure of the wave pouch during the 2009 PREDICT–GRIP dry runs over the Atlantic. *Mon. Wea. Rev.*, **140**, 1144–1163.

Wang, Z., T.J. Dunkerton, and M.T. Montgomery, 2012: Application of the marsupial paradigm to tropical cyclone formation from northwestward-propagating disturbances. *Mon. Wea. Rev.*, **140**, 66–76.

Wilson, S.G., and T.R. Fischetti, 2010: Coastline population trends in the United States: 1960 – 2008. *U.S. Census Bureau Report*. P25-1139.

Whitehead, J.C., 2003: One million dollars per mile? The opportunity costs of Hurricane evacuation. *Ocean Coastal Manage.*, **46**, 1069-1083.

Wu, C-C., and H-J. Cheng, 1999: An observational study of environmental influences on the intensity changes of Typhoons Flo (1990) and Gene (1990). *Mon. Wea. Rev.*, **127**, 3003–3031.

Zawislak, J., and E.J. Zipser, 2010: Observations of seven African easterly waves in the East Atlantic during 2006. *J. Atmos. Sci.*, **67**, 26-43.

Zhang, D-L., and L. Zhu, 2012: Roles of upper-level processes in tropical cyclogenesis. *Geo. Res. Lett.*, **39**, L17804, doi:10.1029/2012GL053140.

Zipser, E.J., and C. Gautier, 1978: Mesoscale events within a GATE tropical depression. *Mon. Wea. Rev.*, **106**, 789–805.

Zipser, E.J., and Coauthors, 2009: The Saharan air layer and the fate of African easterly waves. NASA's AMMA field study of tropical cyclogenesis. *Bull. Amer. Meteor. Soc.*, **90**, 1137-1156.

Zehr, R.M., 1992: Tropical cyclogenesis in the western North Pacific. NOAA Tech. Rep. NESDIS 61, 181 pp.